



Deliverable No. 6.4

Clinical adaptation and partial validation of hypermodels

Grant Agreement No.: 600841
 Deliverable No.: D6.4
 Deliverable Name: Clinical adaptation and partial validation of hypermodels
 Contractual Submission Date: 31/01/2017
 Actual Submission Date: 09/05/2017

Dissemination Level		
PU	Public	
PP	Restricted to other programme participants (including the Commission Services)	
RE	Restricted to a group specified by the consortium (including the Commission Services)	
CO	Confidential, only for members of the consortium (including the Commission Services)	X



COVER AND CONTROL PAGE OF DOCUMENT	
Project Acronym:	CHIC
Project Full Name:	Computational Horizons In Cancer (CHIC): Developing Meta- and Hyper-Multiscale Models and Repositories for <i>In Silico</i> Oncology
Deliverable No.:	D6.4
Document name:	Clinical adaptation and partial validation of hypermodels
Nature (R, P, D, O) ¹	R
Dissemination Level (PU, PP, RE, CO) ²	CO
Version:	I (Final)
Actual Submission Date:	09/05/2017
Editor:	Georgios S. Stamatakos
Institution:	Institute of Communication and Computer Systems (ICCS) School of Electrical and Computer Engineering National Technical University of Athens (NTUA)
E-Mail:	<i>In Silico</i> Oncology and <i>In Silico</i> Medicine Group gestam@central.ntua.gr

ABSTRACT

This document outlines the methods developed and/or adopted by CHIC in order to carry out clinical adaptation and partial clinical validation of its highly innovative multiscale cancer hypermodels. It also provides important and extensive pertinent results, findings and remarks of special value for both the fundamental/basic science and the clinical communities. The document concerns all four exemplary cancer types addressed by CHIC in conjunction with a variety of treatment modalities including chemotherapy, radiation therapy, immunotherapy and hormone therapy. Three out of the four CHIC multiscale hypermodels i.e the nephroblastoma, the non small cell lung cancer and the prostate cancer ones have been collectively developed by three up to six modelling partners each. World leading cancer modelling partners have been geographically distributed in both EU and US and have been supported by the technological infrastructure developed by CHIC. The preliminary partial clinical validation of the developed hypermodels, largely based on retrospective imaging, histological, molecular and clinical data has demonstrated the great potential of cancer hypermodels and Oncosimulators as candidates for clinical decision support systems (CDS) and/or as cores of future *in silico* trial platforms. However, additional retrospective validation work for the developed hypermodels and Oncosimulators is needed in order to more

¹ R=Report, P=Prototype, D=Demonstrator, O=Other

² PU=Public, PP=Restricted to other programme participants (including the Commission Services), RE=Restricted to a group specified by the consortium (including the Commission Services), CO=Confidential, only for members of the consortium (including the Commission Services)

fully substantiate and support their “candidacy” for undergoing validation through prospective clinical trials. Prospective clinical trial based validation is a necessary step in order to definitely assess both their clinical validity and clinical value. Further retrospective validation work will be carried out by specific former CHIC partners on a bilateral or small partner group basis. Regarding the eventual prospective clinical validation of the hypermodels, certain exploratory steps have already been taken, including focused discussions within the framework of the International Society for Pediatric Oncology (SIOP).

KEYWORD LIST

cancer modelling, multiscale cancer modelling, hypermodelling, CHIC project, hypermodel, hypomodel, component model, tumour growth, angiogenesis, cancer biomechanics, cancer metabolism, molecular cancer modelling, integrated cancer model, Oncosimulator, hypermodel based oncosimulator, *in silico* oncology, *in silico* medicine, systems medicine, computational oncology, computational medicine, systems oncology, finite element method, discrete event, discrete entity, partial differential equation, ordinary differential equation, semantics, model repository, clinical research application framework, CRAF, hypermodelling editor, hypermodel execution, nephroblastoma, non small cell lung cancer, glioblastoma multiforme, prostate cancer

The research leading to these results has received funding from the European Community's Seventh Framework Programme (FP7/2007-2013) under grant agreement n° 600841.

The author is solely responsible for its content, it does not represent the opinion of the European Community and the Community is not responsible for any use that might be made of data appearing therein.

MODIFICATION CONTROL

Version	Date	Status	Author
1.0	26/03/2017	Draft	G. Stamatakis, ICCS-NTUA
2.0	11/04/2017	Draft	G. Stamatakis, ICCS-NTUA
3.0	27/04/2017	Draft	G. Stamatakis, ICCS-NTUA
4.0	29/04/2017	Draft	G. Stamatakis, ICCS-NTUA
5.0	02/05/2017	Revision	G. Stamatakis, ICCS-NTUA
6.0	07/05/2017	Clinical Check	N. Graf, USAAR
7.0→ 1 (Final)	09/05/2017	Revision	G. Stamatakis, ICCS-NTUA

List of additional contributors (see next page)

List of additional contributors

E. Kolokotroni, ICCS	D. Dionysiou, ICCS	I. Karatzanis, FORTH	R. Bohle, USAAR
E. Georgiadi, ICCS	D. Abler, UBERN	S.Sfakianakis, FORTH	D. Shouka, USAAR
K. Argyri, ICCS	J. Grogan, UOXF	R.Radhakrishnan, UPENN	S. van Gool, KUL
M. Antonopoulos, ICCS	H. Byrne, UOXF	A. Ghosh, UPENN	Lien Solie, KUL
E.Ouzounoglou, ICCS	E. Tzamali, FORTH	I. Stura, UNITO	J. Dejaegher, KUL
N. Tousert, ICCS	V. Sakkalis, FORTH	C. Guiot, UNITO	N. Mcfarlane, BED
N. Christodoulou, ICCS	K. Nikiforaki, FORTH	E. Ebert, USAAR	

EXECUTIVE SUMMARY

This deliverable outlines the methods developed and/or adopted by CHIC in order to carry out clinical adaptation and partial clinical validation of its highly innovative multiscale cancer hypermodels. It also provides important and extensive pertinent results, findings and remarks of special value for both the fundamental/basic science and the clinical communities. The document concerns all four exemplary cancer types addressed by CHIC in conjunction with a variety of treatment modalities, including chemotherapy, radiation therapy, immunotherapy and hormone therapy. Three out of the four CHIC multiscale hypermodels i.e the nephroblastoma, the non small cell lung cancer and the prostate cancer ones have been collectively developed by three up to six modelling partners each. World leading cancer modelling partners have been geographically distributed in both EU and US and supported by the technological infrastructure developed by CHIC. Regarding nephroblastoma, a study on the corresponding Oncosimulator hypomodel adaptation has been conducted and the produced results are reported. A second study regarding the molecular model adaptation is outlined. mRNA expression data has been used in order to generate patient specific predictions. A third study regarding the adaptation of the coupling of the nephroblastoma (or lung cancer) Oncosimulators with the Biomechanics hypomodel is delineated. The simulated evolution of tumour shape and position is assessed. A fourth study concerns the adaptation and initial partial validation of the coupling of the molecular hypomodel with the nephroblastoma Oncosimulator. A fifth study focuses on the adaptation and the partial validation of the integrated nephroblastoma hypermodel. Regarding non small cell lung cancer, the angiogenesis hypomodel, the lung cancer molecular model, the metabolic hypomodel and the biomechanical hypomodel are outlined. The clinical adaptation and the partial clinical validation of the Oncosimulator and the lung cancer multimodeller hypermodel along with the methods developed and applied are presented. Details on the static and dynamic interaction of the component models (or hypomodels) during execution are also provided. Concerning the statistical model for lung cancer, the validation of two developed classifiers is presented.

Regarding the glioblastoma statistical and machine learning model developed, the principles of the approach along with correlation results for various categories of patients are presented. Arguments supporting the credence of the model, despite the limited number of patient data sets available are formulated. Concerning prostate cancer, an outline of the corresponding multimodeller hypermodel along with a description of its component (or hypo-) models, including the prostate cancer hypomodel, the pharmacokinetics hypomodel, the pharmacodynamics hypomodel and the molecular hypomodel are presented. Clinical adaptation and clinical validation of the hypermodel in various contexts is reported. The presented partial clinical validation of the developed hypomodels, largely based on retrospective imaging, histological, molecular and clinical data has demonstrated the great potential of cancer hypermodels and Oncosimulators to serve as clinical decision support systems (CDS) and/or cores of future *in silico* trial platforms. However, additional retrospective validation work for the developed hypermodels is needed in order to more fully substantiate and support their “candidacy” for undergoing validation through prospective clinical trials. This is a necessary step in order to definitely assess both their clinical validity and clinical value. Further retrospective validation work will be carried out by specific former CHIC partners on a bilateral or small partner group basis. Regarding the eventual prospective clinical validation of the hypermodels, certain exploratory steps have already been taken, including focused discussions within the framework of the International Society for Pediatric Oncology (SIOP).

Contents

Executive Summary	5
IN. INTRODUCTION	8
NB: THE NEPHROBLASTOMA HYPERMODEL: CLINICAL ADAPTATION AND PARTIAL VALIDATION	10
LC: THE NON SMALL CELL LUNG CANCER HYPERMODEL: CLINICAL ADAPTATION AND PARTIAL VALIDATION	53
GB: THE GLIOBLASTOMA HYPERMODEL: CLINICAL ADAPTATION AND PARTIAL VALIDATION	139
PC: THE PROSTATE CANCER HYPERMODEL: CLINICAL ADAPTATION AND PARTIAL VALIDATION	172
DI: DISCUSSION	203
CO: CONCLUSIONS	204
APPENDIX I (ABBREVIATIONS AND ACRONYMS)	205

CHAPTER IN: INTRODUCTION

(Please note that the numbering of sections, subsections, equations, figures and references within this chapter refers exclusively to the latter and is not applicable to other chapters of the document. If any of the above entities of another chapter is to be referred to, the chapter under consideration should also be mentioned through its two capital letter code)

This document outlines the methods developed and/or adopted by CHIC in order to carry out clinical adaptation and partial clinical validation of its highly innovative multiscale cancer hypermodels. It also provides important and extensive results, findings and remarks of special value for both the fundamental/basic science and the clinical communities.

The document addresses all four exemplary cancer types addressed by CHIC in conjunction with a variety of treatment modalities, including chemotherapy, radiation therapy, immunotherapy and hormone therapy. Three out of the four CHIC multiscale hypermodels i.e the nephroblastoma, the non small cell lung cancer and the prostate cancer ones have been collectively developed by three up to six modelling partners each. World leading cancer modelling partners have been geographically distributed in both EU and US and supported by the technological infrastructure developed by CHIC.

Regarding nephroblastoma (Chapter NB), a study on the corresponding Oncosimulator hypomodel adaptation has been conducted and the produced results are reported. A second study regarding the molecular model adaptation is outlined. mRNA expression data has been used in order to generate patient specific predictions. A third study regarding the adaptation of the coupling of the nephroblastoma (or lung cancer) Oncosimulators with the Biomechanics hypomodel is delineated. The simulated evolution of tumour shape and position is assessed. A fourth study concerns the adaptation and initial partial validation of the coupling of the molecular hypomodel with the nephroblastoma Oncosimulator. A fifth study outlines the adaptation and the partial validation of the integrated nephroblastoma hypermodel.

Regarding non small cell lung cancer (Chapter LC), the angiogenesis hypomodel, the lung cancer molecular model, the metabolic hypomodel and the biomechanical hypomodel are outlined. The clinical adaptation and the partial clinical validation of the Oncosimulator and the lung cancer multimodeller hypermodel along with the methods developed and applied are presented. Details on the static and dynamic interaction of the component models (or hypomodels) during execution are also provided.

Concerning the statistical model for lung cancer, the validation of two developed classifiers is presented. Regarding the glioblastoma statistical and machine learning model developed, the principles of the approach along with correlation results for various categories of patients are presented. Arguments supporting the credence of the model, despite the limited number of patient data sets available are formulated.

Concerning prostate cancer (Chapter PC), an outline of the corresponding multimodeller hypermodel along with a description of its component (or hypo-) models, including the prostate cancer hypomodel, the pharmacokinetics hypomodel, the pharmacodynamics hypomodel and the molecular hypomodel are presented. Clinical adaptation and clinical validation of the hypermodel in various contexts is reported.

The presented partial clinical validation of the developed hypemodells, largely based on retrospective imaging, histological, molecular and clinical data has demonstrated the great potential of cancer hypermodels and Oncosimulators to serve as clinical decision support systems (CDS) and/or cores of future *in silico* trial platforms. However, additional retrospective validation work for the developed hypermodels is needed in order to more fully substantiate and support their “candidacy” for undergoing validation through prospective clinical trials. This is a necessary step in order to definitely assess both their clinical validity and clinical value. Further retrospective validation work will be carried out by specific former CHIC partners on a bilateral or small partner group basis. Regarding the eventual prospective clinical validation of the hypermodels, certain exploratory steps have already been taken, including focused discussions within the framework of the International Society for Pediatric Oncology (SIOP).

CHAPTER NB: THE NEPHROBLASTOMA HYPERMODEL: CLINICAL ADAPTATION AND PARTIAL VALIDATION

(Please note that the numbering of sections, subsections, equations, figures and references within this chapter refers exclusively to the latter or even a section of it and is not applicable to other chapters of the document. If any of the above entities of another chapter is to be referred to, the chapter under consideration should also be mentioned through its two capital letter code)

Introduction

Wilms integrated hypermodel (fig 1) as described analytically in D6.3 is an integrated software system incorporating five biological hypomodels and an image processing tool simulating the growth of nephroblastoma tumours and their *in vivo* response to chemotherapeutic modalities within the clinical trials environment. It aims at supporting clinical decision making in individual patients by addressing the clinical question whether a Wilms tumour patient will respond to pre-operative chemotherapy through tumour shrinkage or not.

Due to the complexity of the biological phenomenon of cancer, simulation hypomodels utilize a large number of parameters. Nevertheless, the nature of oncosimulator discrete model makes it possible to define the values of the parameters from quantitative experimental data. It is widely accepted that the more experimental data available to define or constrain the parameter values, the more likely it is for the models to describe accurately the observed behaviours (Sible, 2007). However, not all of the model parameters can be directly defined by current experimental techniques or experiments that could serve for this purpose are not included in the framework of ongoing clinical trials. Therefore, some parameters must be estimated by comparing model results with clinical data. To constrain these models and thereby improve predictive power, modelers must integrate insights from numerical parameter studies, direct experimental data from collaborators and any information that can be gleaned from the experimental and theoretical biology literature.

The outcome of an initial step towards the clinical adaptation and partial validation of the integrated software system of the Wilms Multimodeler Hypermodel is presented in this deliverable and discussed.

Several studies are formed in order to set the adaptation procedure for each hypomodel, to test the coupling between individual hypomodels but also based on the input data availability.

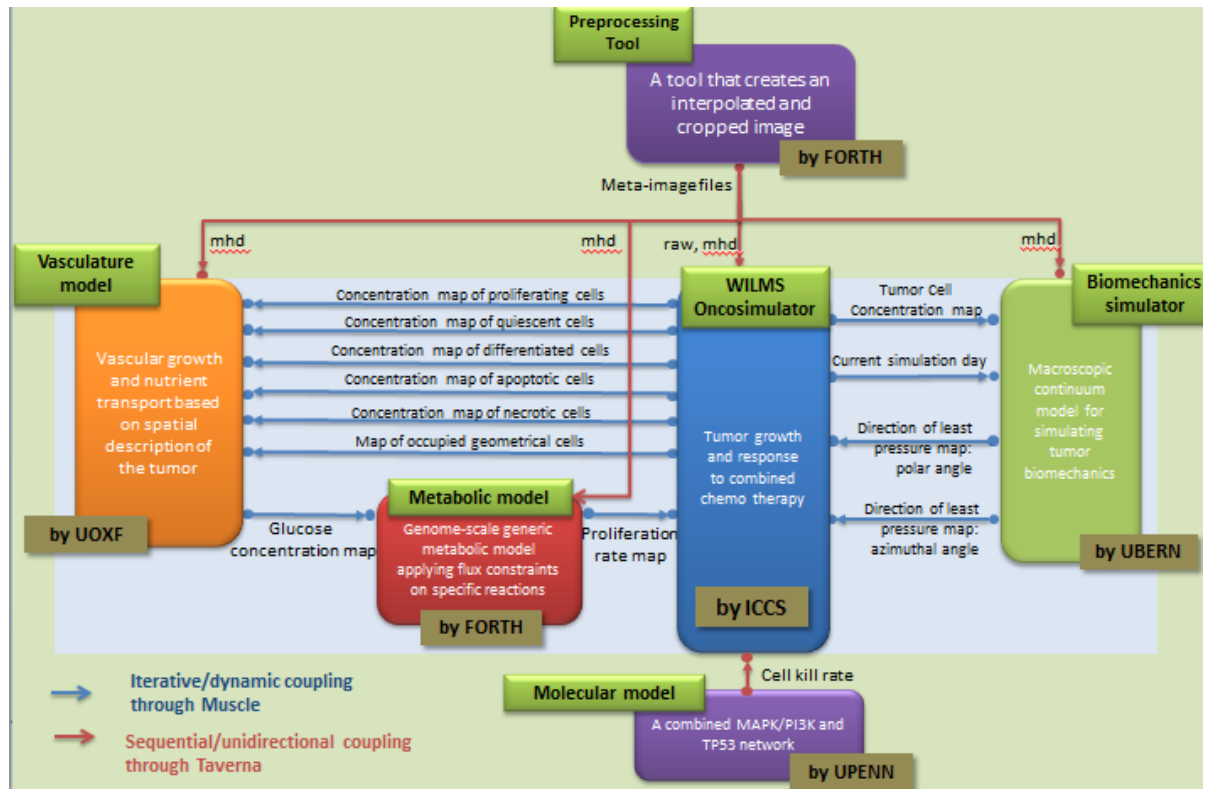


Figure 1 [D6.3]: Wilms Multimodeler Hypermodel: integration scheme of Wilms oncosimulator, preprocessing tool, metabolic, molecular, vasculature and biomechanic hypomodels

Reference

Sible JC, Tyson JJ. Mathematical modeling as a tool for investigating cell cycle control networks. *Methods*. 2007;41:238–47.

Study 1: The Nephroblastoma (Wilms Tumour) Oncosimulator Component adaptation

A thorough sensitivity analysis of the model parameters (Table 1, table 2) has been performed previously (Georgiadi, 2012; Stamatakis, 2011), leading to a sorting of the model parameters according to the magnitude of their effect on virtual tumour characteristics, and has unveiled the

relative importance of the corresponding biological mechanisms. Since the results of this sensitivity analysis are important for the presented clinical adaptation process, a brief summary is given below.

TABLE I: Definition of the model parameters describing tumour dynamics

Symbol (units)	Definition
T_c (h)	Cell cycle duration
T_{G0} (h)	G0 (dormant phase) duration, i.e. time interval before a dormant cell dies through necrosis
T_N (h)	Time needed for necrosis to be completed and its lysis products to be eliminated from the tumour
T_A (h)	Time needed for apoptosis to be completed and its products to be eliminated from the tumour
R_A (h^{-1})	Apoptosis rate of living stem and LIMP tumour cells (fraction of non-differentiated cells dying through apoptosis per hour)
R_{ADiff} (h^{-1})	Apoptosis rate of differentiated tumour cells per hour
R_{NDiff} (h^{-1})	Necrosis rate of differentiated tumour cells per hour
P_{G0toG1}	The fraction of stem or LIMP cells having just left the G0 compartment that re-enter the cell cycle
N_{LIMP}	The maximum number of mitoses that a LIMP cell can perform before becoming terminally differentiated
P_{sym}	Fraction of stem cells that perform symmetric division.
P_{sleep}	Fraction of cells that enter G0 phase following mitosis
CKR_{VCR}	Cell kill rate for the specific vincristine dose
CKR_{ACT}	Cell kill rate for the specific actinomycin-D dose
CKR_{TOTAL}^*	Combined cell kill rate of the two drugs (dependent parameter)

TABLE 2: Miscellaneous model parameters (unrelated to tumour dynamics). GC: geometrical cell.

Other model parameters			
Input_image	The initial tumour volume area defined by the annotated imaging data of the patient at time of diagnosis	**.raw file	Imaging data
NBC	Number of biological cells typically contained within a GC of the mesh (assigned in relation to the GC's volume)	10^6 (for GC volume=1 mm ³)	Based on typical tumour cell densities. [12]
Margin percent	Acceptable temporary over-loading or under-loading of each geometrical cell as a fraction of unity	0.1	Based on exploratory runs
T _{init} (h)	Time interval between the pre-treatment imaging data acquisition and the first drugs' administration	-	Clinical data or exploratory simulation data
T _{pt_scan} (h)	Time interval between the last drug administration and the post-treatment imaging data acquisition	-	Clinical data or exploratory simulation data
T _{admin,i}	Drug administration instants	-	Treatment protocol/clinical data

• Growth rate – Tumour doubling time

The virtual tumour growth rate depends only on the population of stem cells which preserve the tumour population as these are the only cells with unlimited mitotic potential. The growth fraction of a biologically accepted tumour is defined according to the equation (Kolokotroni, 2011):

$$\left(1 + P_{sym}\right) \left(1 - P_{sleep} + P_{sleep} \frac{P_{G0toG1} / T_{G0}}{R_A + 1 / T_{G0}}\right) e^{-R_A T_C} \geq 1 \quad \text{Equation 1}$$

As depicted in eq.1 and based on the sensitivity analysis of the model (Georgiadi, 2012; Stamatakis, 2011), the most determinant model parameters on the growth fraction of virtual tumours are:

- Cell cycle duration (T_c)
- The fraction of stem cells that perform symmetric division (P_{sym}).
- The fraction of cells that enter G0 phase following mitosis (P_{sleep})
- Apoptosis rate of living stem and LIMP tumour cells (fraction of non-differentiated cells dying through apoptosis per hour) (R_A)

Other parameters that play a role in the value of the growth fraction of the virtual tumour modeled, but with significantly reduced impact on it, are:

- The fraction of stem or LIMP cells having just left the G0 compartment that re-enter the cell cycle (P_{G0toG1})
- G0 (dormant phase) duration (T_{GO})

Decrease in parameters T_c , P_{sleep} , R_A and T_{GO} and/or increase in parameters P_{sym} , P_{G0toG1} lead to virtual tumours with higher growth fractions and lower doubling times, i.e. more aggressive tumours.

• Cell constitution of virtual tumours

The percentage of proliferating stem cells in the total population is increased for higher fractions of stem cells that perform symmetric division (P_{sym}), prolonged cell cycle durations (T_c) and lower loss rates due to spontaneous apoptosis (R_A).

The fraction of proliferating LIMP cells depends on two competitive mechanisms: the pool of the producers (stem cells - P_{sym}) and the rate of the production of LIMP cells from this pool ($1-P_{sym}$). The duration of cell cycle (T_c) and the loss rate (R_A) also define the proliferating LIMP cell population in a similar way to proliferating stem cells.

The fraction of the dormant stem and LIMP cells depends on the rate of quiescence (P_{sleep}), the rate of recycling (P_{G0toG1}) and the remaining time in dormant state before necrosis.

The relative percentages of stem and committed progenitor cells are defined by the maximum number of mitoses that a LIMP cell can perform before becoming terminally differentiated (N_{LIMP}). The differentiated population is increased for a high percentage of LIMP cells and low rates of loss due to necrosis (R_{NDiff}) and apoptosis (R_{ADiff}).

The fraction of dead cells in the total population is increased if the loss rates (R_A , R_{ADiff} , R_{NDiff}) of the other populations are increased or/and the time during which cell death products remain in the tumour bulk is prolonged (T_N , T_A).

• Chemotherapy induced tumour volume reduction

The chemotherapy induced volume reduction depends upon the growth rate of the virtual tumour and the cell kill rate of the chemotherapeutic drugs in use.

Subsequently the model parameters that play an important role in the simulated tumour reduction are T_c , P_{sym} , P_{sleep} , R_A and CKR_{TOTAL} .

More aggressive tumours have a worse response to chemotherapy due to the fast repopulation of the cancer cells.

Increased effectiveness of chemotherapeutic drugs, leads to a better therapeutic outcome.

1.1 Adaptation of model parameters based on real clinical nephroblastoma tumour cases. - General Methodology

First of all, the miscellaneous model parameters (Table 2) are adapted to the specific patient data. The patient's imaging data is used to initialize the tumour area and the clinical data to set the chemotherapeutic scheme which is administered to the specific patient.

Subsequently, the model parameters describing the free growth tumour dynamics (table 1) are to be adapted. Primarily, the model parameters that are determinative of the tumour rate should be adapted. In case histological data of the patients are available and provide information on the tumour cell constitution (initial or/and final), further parameters (e.g. cell cycle phases durations) defining the cell subclasses population fractions have to be adapted accordingly as well.

Finally, the therapy tumour dynamics parameters, defining the effect of the chemotherapeutic drugs are to be adapted based on the clinical chemo-induced tumour volume reduction.

1.2 Nephroblastoma Clinical Data

Seventeen (17) nephroblastoma tumour cases have been collected and analyzed in this study. The histological data of the patients were also available and presented in table 3.

TABLE 3: The histological data of nephroblastoma tumour cases selected in the context of SIOP 2001/GPOH trial. Histological information derived after the surgical excision of the tumours. Regression/necrosis left/right: percentage of chemotherapy induced regression/necrosis in the left/right kidney. (*Bilateral nephroblastoma. **Not known.)

Case no	Histology			Subpopulations			Histological type
	Regression/ Necrosis left	Regression/ Necrosis right	Metastasis	Blastema	Epithelial	Stroma	Staging
1	30%		None	85%	10%	5%	Blastemal predominant, high risk
2		20%	None				Mixed type, intermediate risk
3		15%	None				Mixed type with focal Anaplasia, intermediate risk
4		40%	None	5%	60%	35%	Mixed type, intermediate malignancy
5		30%	None	5%	25%	70%	Stromal Type, intermediate Malignancy
6	50%		None	0%	90%	10%	Regressive Type, intermediate Malignancy
7	<65%		None				Stromal Type, intermediate Malignancy
8		<65%	None		30%	70%	Stromal Type, Intermediate malignancy
9	<65%		None	60%	25%	15%	Mixed type, intermediate malignancy.
10	<65%			100%			Blastemal type, high malignancy
11		<25%	None				Mixed type, intermediate malignancy.
12		<65%	None				Mixed type, intermediate

							malignancy.
13	90%		None	70%	20%	10%	Regressive Type, intermediate Malignancy.
14	80%		Lymphnodes				Diffuse anaplasia, high Malignancy,
15	5%		None				Epithelial type, intermediate malignancy.
16		<65%	None	20%	40%	40%	Mixed type, intermediate malignancy.
17		80%	None				Regressive Type, intermediate Malignancy.

As depicted in the above table cases where blastemal predominant, 7 mixed type, 3 stromal, 3 regressive, 1 diffuse anaplasia and 1 epithelial nephroblastoma

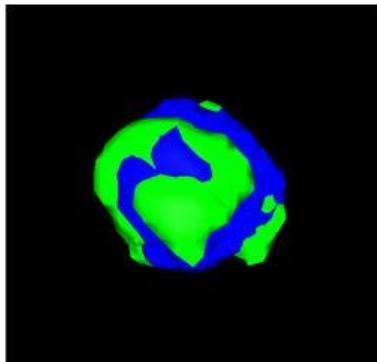
TABLE 4: Clinical data of the selected SIO P 2001/GPOH trial nephroblastoma tumour cases

Case no	Date of diagnosis	Start Chemotherapy	Cycle I (ACT:µg, VCR:mg)	Cycle II (VCR: mg)	Cycle III (ACT: µg, VCR: mg)	Cycle IV (VCR: mg)
1	9/20/2005	9/29/2005	ACT: 931 VCR: 1,2	VCR: 1,2	ACT: 931 VCR: 1,2	VCR: 1,2
2	8/30/2006	9/6/2006	ACT: 570 VCR: 0,85	VCR: 0,85	ACT: 570 VCR: 0,85	VCR: 0,85
3	11/10/2006	11/10/2006	ACT: 900 VCR: 1,2	VCR: 1,2	ACT: 900 VCR: 1,2	VCR: 1,2
4	2/5/2007	2/8/2007	ACT: 610 VCR: 0,9	VCR: 0,9	ACT: 610 VCR: 0,9	VCR: 0,9
5	2/5/2007	2/9/2007	ACT: 880 VCR: 1,2	VCR: 1,2	ACT:880 VCR: 1,2	VCR: 1,2
6	3/21/2007	3/23/2007	ACT: 740 VCR: 1	VCR: 1	ACT:740 VCR: 1	VCR: 1
7	7/18/2008	7/18/2008	ACT: 605 VCR: 0,89	VCR: 0,89	ACT: 605 VCR: 0,89	VCR: 0,89
8	6/13/2006	6/15/2006	ACT: 870 VCR: 1,2	VCR: 1,2	ACT: 870 VCR: 1,2	VCR: 1,2
9	10/24/2007	10/25/2007	ACT: 350 VCR: 0,49	VCR: 0,49	ACT: 350 VCR: 0,49	VCR: 0,49
10	12/6/2007	12/10/2007	ACT: 730 VCR: 1	VCR: 1	ACT: 730 VCR: 1	VCR: 1

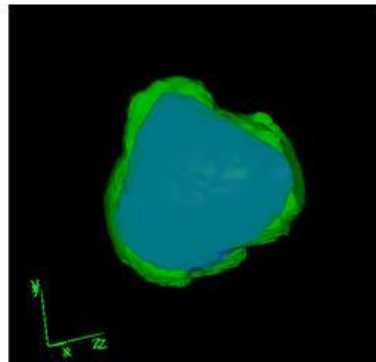
11	12/18/2007	12/19/2007	ACT: 310 VCR: 0,47	VCR: 0,47	ACT: 300 VCR: 0,47	VCR: 0,47
12	8/21/2008	8/23/2008	ACT: 850 VCR: 1,15	VCR: 1,15	ACT: 850 VCR: 1,15	VCR: 1,15
13	9/23/2008	9/25/2008	ACT: 1224 VCR: 1,53	VCR: 1,53	ACT: 1224 VCR: 1,53	VCR: 1,53
14	11/25/2008	11/25/2008	ACT: 1200 VCR: 1,50	VCR: 1,50	ACT: 1200 VCR: 1,50	VCR: 1,50
15	1/14/2009	1/19/2009	ACT: 267 VCR: 0,42	V: 0,42	ACT: 267 VCR: 0,42	VCR: 0,42
16	1/30/2009	2/4/2009	ACT: 810 VCR: 1,1	VCR: 1,1	ACT: 810 VCR: 1,1	VCR: 1,1
17	3/10/2009	3/11/2009	ACT: 399 VCR: 0,55	VCR: 0,82	ACT: 581 VCR: 0,82	VCR: 0,82

The anonymized imaging and clinical data have been collected by the clinicians in the framework of SIOP 2001/GPOH trial and selected to be modeled by the 'Oncosimulator'. The clinical data of the nephroblastoma cases describing the chemotherapeutic scheme administered are presented in table 4.

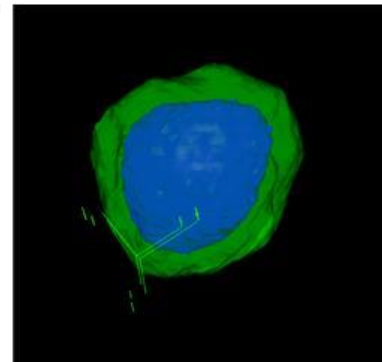
The initial and final virtual tumours have been spatiotemporally initialized based on MRI images of the clinical tumours collected at two time instants: before the start of chemotherapy and after its completion, respectively (fig. 2).



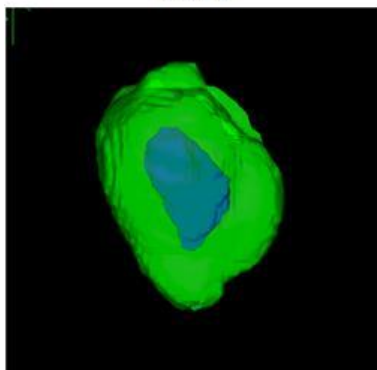
Case 1



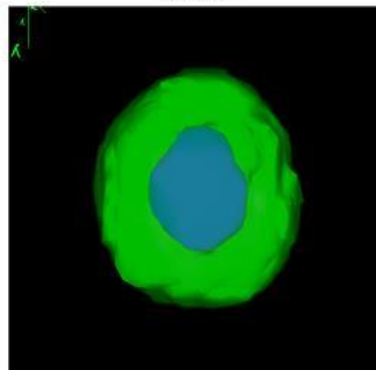
Case 2



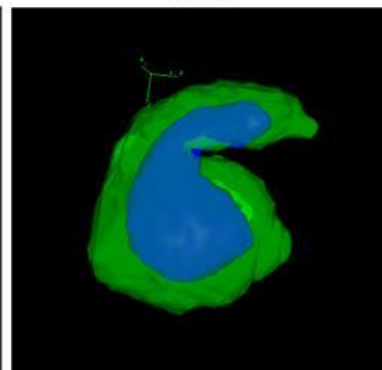
Case 3



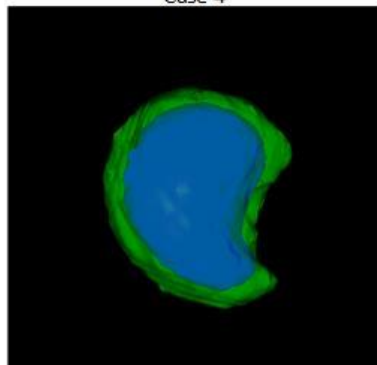
Case 4



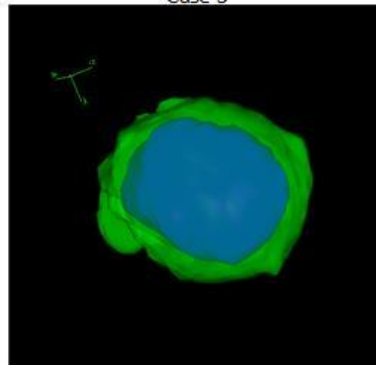
Case 5



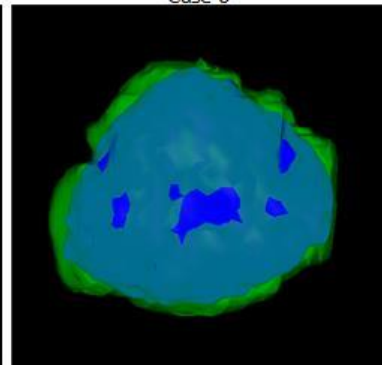
Case 6



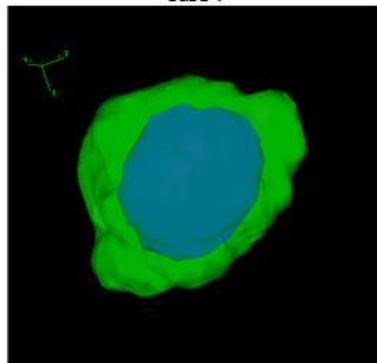
Case 7



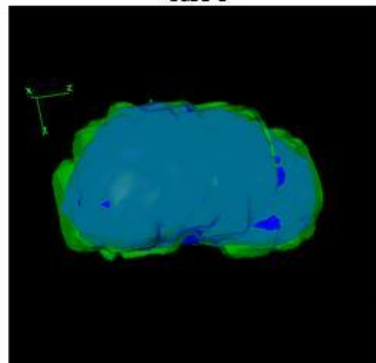
Case 8



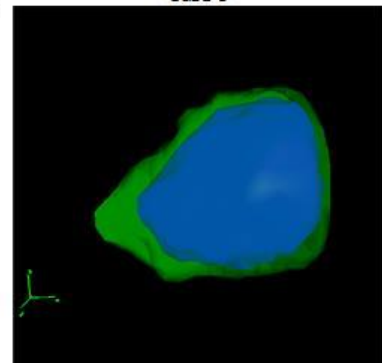
Case 9



Case 10



Case 11



Case 12

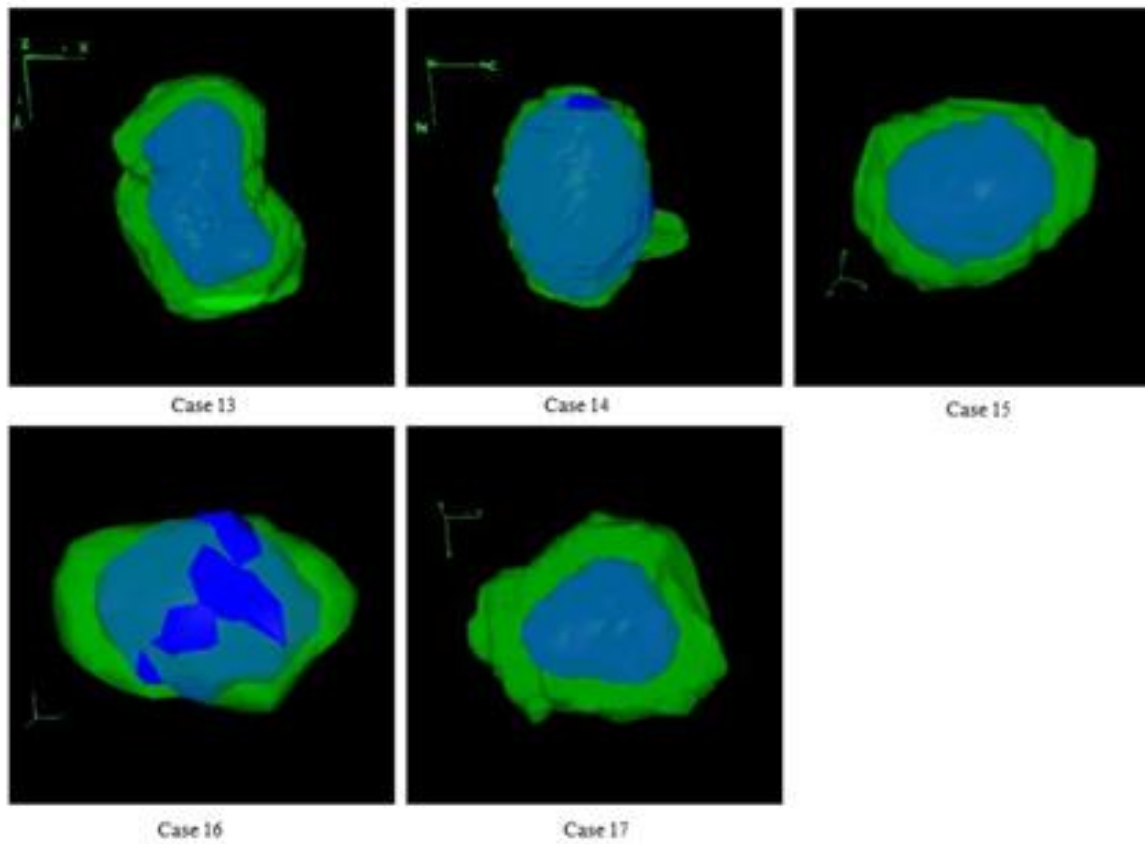


Figure 2: Apposition of the initial (green) and the final (blue) virtual tumours that have been spatiotemporally initialized based on MRI image datasets of 17 clinical tumours collected at two time instants before the start of chemotherapy and after the completion of the treatment.

1.3 Adaptation assumptions for the nephroblastoma cases

The three histological components of nephroblastoma (blastemal, epithelial and stromal) have different proliferating potential.

The nuclear antigen Ki-67 is associated with cell proliferation, as it is present throughout the cell cycle and absent in resting cells (Berrebi et al., 2008), and is studied as a tumour proliferation marker.

In (Berrebi et al., 2008) the marker ki-67 SI was evaluated in the three components of nephroblastoma and its highest values were found in the blastemal and epithelial components of the tumours.

The median ki-67 SI was determined to be 33% in blastemal cells, 10% in stromal cells and 29.5% in epithelial cells. The study included postchemotherapy nephroblastomas, treated with neoadjuvant chemotherapy before nephrectomy. These values will be used as an assumption for the adaptation of the growth fraction of the final tumour.

For mixed type nephroblastoma, the growth fraction will be computed according to the equation 2 :

$$GF_{TOTAL} = p_{BLASTEMAL} * GF_{BLASTEMAL} + p_{EPITHELIAL} * GF_{EPITHELIAL} + p_{STROMAL} * GF_{STROMAL}$$

(Equation 2)

Where:

GF: Growth fraction

p: percentage of the component

In case the histological subpopulation is not defined, the percentages of the three components are considered equal. For anaplastic nephroblastomas, the median ki-67 SI in the blastemal component was 70%, 24% in stromal and 43% in epithelial cells. For regressive type nephroblastomas a median ki-67 Si of 9.5 % is considered.

According to the above assumptions, the calculated growth fraction of the final tumour to be adapted for the 17 cases, is noted in table 5.

Another assumption for the adaptation of the nephroblastoma cases is a doubling time in the range of 11–40 days (Shackney, 1978; Craft, 1999; Zoubek, 1999; Carre', 2005; Steel, 2002).

The imaging data-specified volume reduction is calculated for each nephroblastoma case (table 5).

TABLE 5: The chemotherapy induced tumour volume reduction for the nephroblastoma cases under study as calculated according to their imaging data before and after therapy.

Case No	Relative Clinical Tumour Volume reduction (%)	Growth fraction of final Clinical tumour (%)
1	-9	33
2	35	24
3	63	24
4	80	18
5	82	10
6	71	10
7	39	10
8	32	10
9	2	27
10	73	33
11	25	24
12	44	24
13	70	10
14	34	58
15	71	30
16	41	22
17	73	10

1.4 Adaptation results

All the cases undergo the chemotherapeutic treatment for Wilms tumour preoperative chemotherapy as defined by SIOP trial treatment protocol and depicted in figure 3.

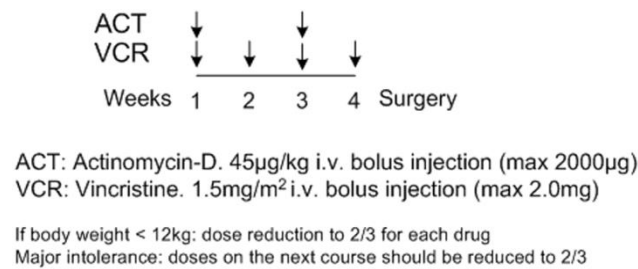


Figure 3: The simulated Wilms tumour preoperative chemotherapy treatment protocol of the SIOP/GPOH clinical trial (see also Table 6).

The time interval between the pre-treatment imaging data acquisition and the first drugs administration and the time interval between the last drug administration and the post-treatment imaging data acquisition per case are defined by the clinical data and presented in table 6.

The adaptation values of model parameters are presented in table 7. The resultant initial and final virtual tumour characteristics as well as the resultant tumour reduction are given in table 8. In figure 4 the time evolution of the simulated tumour volumes for the 17 cases are depicted.

TABLE 6: The time interval between the pre-treatment imaging data acquisition and the first drugs' administration and the time interval between the last drug administration and the post-treatment imaging data acquisition for 17 cases of nephroblastoma

Case No	T _{init} (h)	T _{pt_scan} (h)
1	144	0
2	168	120
3	72	96
4	72	24
5	24	144
6	48	96
7	144	240
8	144	0
9	24	312
10	72	96
11	24	120
12	48	96
13	48	96
14	96	48
15	120	216
16	120	192
17	24	120

TABLE 7: Dynamic model parameters' values assigned for the implementation of virtual tumours adapted in 17 clinical nephroblastoma cases.

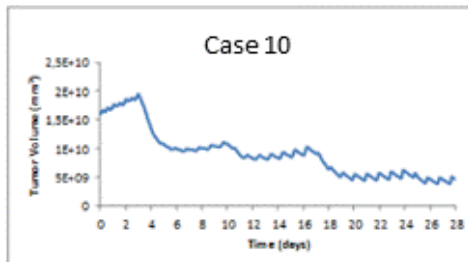
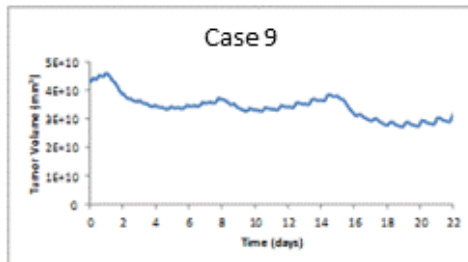
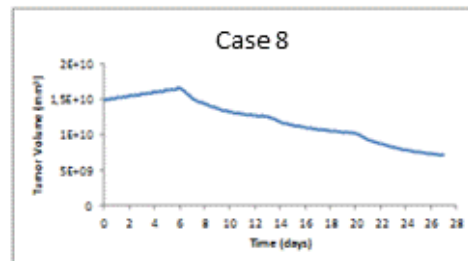
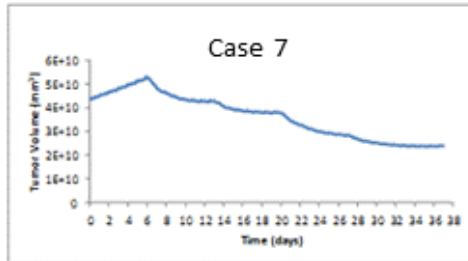
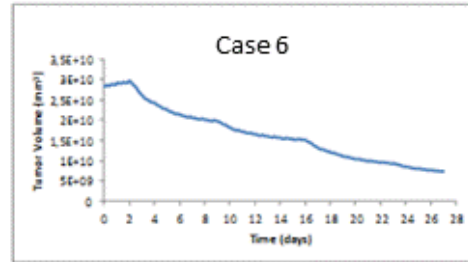
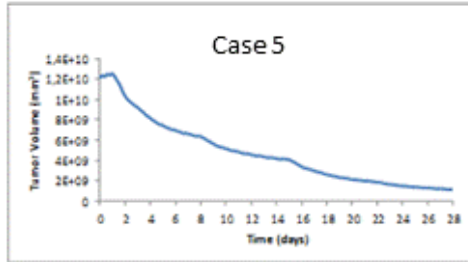
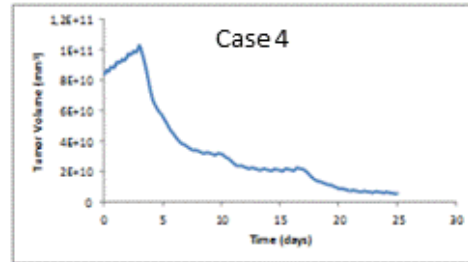
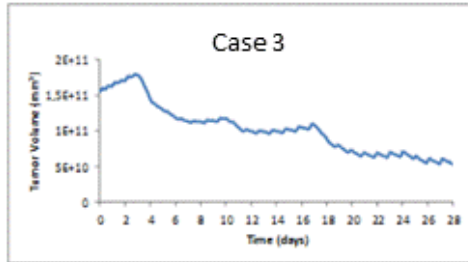
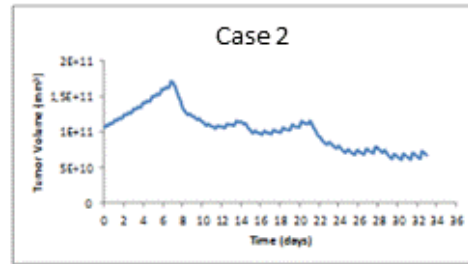
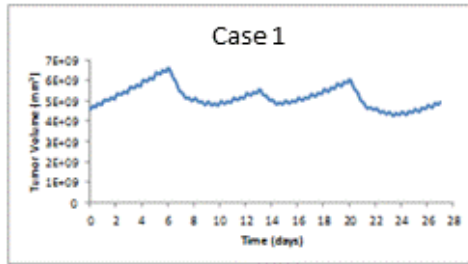
Symbol (units)	Adaptation values								
Case No	1	2	3	4	5	6	7	8	9
T_c (h)	24	23	25	23	23	23	23	23	23
T_{G0} (h)	96	120	96	96	96	96	96	96	96
T_N (h)	20	20	20	20	20	20	20	20	20
T_A (h)	6	6	6	6	6	6	6	6	6
R_A (h^{-1})	0.001	0.001	0.001	0.001	0.001	0.001	0.001	0.001	0.001
R_{ADiff} (h^{-1})	0.045	0.02	0.015	0.015	0.005	0.005	0.003	0.003	0.018
R_{NDiff} (h^{-1})	0.001	0.001	0.001	0.001	0.001	0.001	0.001	0.001	0.001
P_{G0toG1}	0.02	0.01	0.01	0.01	0.01	0.01	0.01	0.01	0.01
N_{LIMP}	7	7	7	7	7	7	7	7	7
P_{sym}	0.50	0.51	0.49	0.5	0.45	0.44	0.46	0.44	0.49
P_{sleep}	0.28	0.28	0.28	0.28	0.28	0.28	0.28	0.28	0.28
CKR_{VCR}	0.28	0.362	0.334	0.5	0.43	0.31	0.29	0.2	0.277
CKR_{ACT}	0.19	0.241	0.223	0.33	0.28	0.21	0.19	0.13	0.185
CKR_{TOTAL}^*	0.47	0.603	0.557	0.83	0.71	0.52	0.48	0.33	0.462

Symbol (units)	Adaptation values							
Case No	10	11	12	13	14	15	16	17
T_c (h)	23	23	23	23	50	23	23	20
T_{G0} (h)	50	96	96	50	50	96	96	96
T_N (h)	20	20	20	20	10	10	20	10
T_A (h)	6	6	6	6	6	6	6	6
R_A (h^{-1})	0.001	0.001	0.001	0.001	0.0005	0.001	0.001	0.001
R_{ADiff} (h^{-1})	0.03	0.018	0.018	0.004	0.06	0.01	0.01	0.005
R_{NDiff} (h^{-1})	0.001	0.001	0.001	0.001	0.001	0.01	0.001	0.001
P_{G0toG1}	0.01	0.01	0.01	0.01	0.1	0.01	0.01	0.01
N_{LIMP}	7	7	7	7	7	7	7	7
P_{sym}	0.49	0.46	0.48	0.46	0.5	0.45	0.47	0.48
P_{sleep}	0.28	0.28	0.28	0.28	0.28	0.28	0.28	0.28
CKR_{VCR}	0.37	0.19	0.28	0.35	0.19	0.28	0.28	0.41
CKR_{ACT}	0.25	0.13	0.19	0.23	0.13	0.19	0.19	0.27
CKR_{TOTAL}^*	0.62	0.32	0.47	0.58	0.32	0.47	0.47	0.68

TABLE 8: Initial and final virtual tumours' characteristics, and tumour volume reduction defined by the model parameters' values in table 7.

Case	1	2	3	4	5	6	7	8	9
Volume Doubling Time	11.8	10.5	14.96	11.69	28.52	40.38	22.08	40.38	13.23
Initial percentage of proliferating cells (Growth Fraction) (%)	33.98	27.35	27.23	26.47	17.5	14.49	12.67	11.05	27.21
Initial percentage of dormant cells (%)	40.54	39.41	32.34	32.98	23.96	20.24	17	15.44	34.5
Initial percentage of differentiated cells (%)	13.88	24.2	31.21	31.27	50.95	59.34	65.61	69.03	28.44
Initial percentage of dead cells (%)	11.6	9.04	9.23	9.43	9.28	5.94	4.72	4.48	9.85
Tumour volume reduction percentage (%)	-9.78	35.66	63.84	79.82	80.17	71.63	38.86	32.06	2.58
Final percentage of proliferating cells (Growth Fraction) (%)	32.68	24.79	24.55	17.38	17.1	9.3	9.12	9.32	26.99
Final percentage of dormant cells (%)	42.12	42.47	34.14	43.84	36.51	15.68	12.63	13.07	34.64
Final percentage of differentiated cells (%)	13.22	23.09	31.35	20.82	32.69	69.73	74.31	73.54	28.54
Final percentage of dead cells (%)	11.98	9.65	9.97	17.96	13.7	5.3	3.94	4.08	9.83

Case	I0	I1	I2	I3	I4	I5	I6	I7
Volume Doubling Time	13.13	22.08	15.25	21.86	25.97	11.69	18.03	12.44
Initial percentage of proliferating cells (Growth Fraction) (%)	36.02	25.87	26.92	17.22	61.1	30.93	21.76	16.1
Initial percentage of dormant cells (%)	26.35	34.7	34.76	12.97	22.21	38.52	28.62	23.17
Initial percentage of differentiated cells (%)	23.4	28.9	27.96	62.12	9.12	19.52	41.42	54.45
Initial percentage of dead cells (%)	14.23	10.53	10.36	7.69	7.56	11.03	8.2	6.28
Tumour volume reduction percentage (%)	72.81	25.01	24.56	70.49	34.06	70.21	41.75	73.61
Final percentage of proliferating cells (Growth Fraction) (%)	33.93	24.52	43.53	10.31	59.39	30.07	20.79	9.99
Final percentage of dormant cells (%)	27.48	35.72	36.66	8.66	22.77	39.38	28.65	16.86
Final percentage of differentiated cells (%)	24.05	29.23	28.12	74.56	8.74	19.35	42.3	67.6
Final percentage of dead cells (%)	14.53	10.53	10.66	6.46	9.11	11.2	8.26	5.55



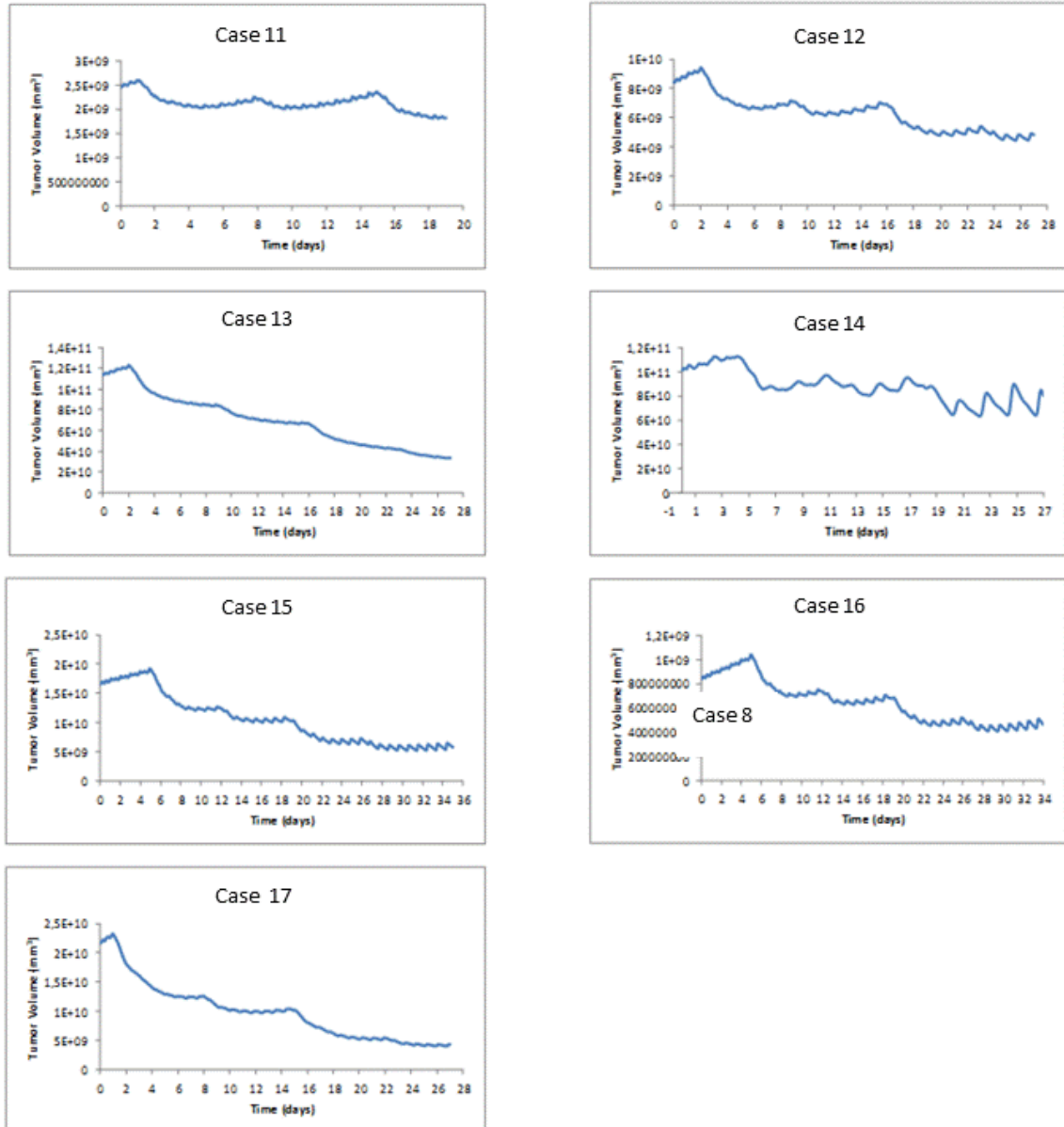


Figure 4: The evolution of tumour volume over time for 17 virtual tumours defined in table 7.

I.5 Discussion

The fitting of Wilms Oncosimulator hypomodel on the selected 17 nephroblastoma cases to the clinical data demonstrates the basic philosophy of model adaptation, based on the combined use of the available multiscale clinical and literature data. Availability of multiscale medical data imposes constraints on model parameter values. A possible set of model parameters have been assigned at each case leading to virtual tumours with resulting characteristics in accordance to the available data. As the available information regarding a particular tumour's characteristics increases, a narrowing of the window of possible virtual scenarios is to be expected. Contrarily, after adequate "tuning" the simulation results could give valuable hints concerning tumour characteristics for which actual estimations might be missing in each case considered.

References

- Deisboeck TS, Wang Z, Macklin P, Cristini V, "Multiscale cancer modeling.", *Annu Rev Biomed Eng.* 2011 Aug 15;13:127-55. doi: 10.1146/annurev-bioeng-071910-124729
- E.C.Georgiadi, D.D.Dionysiou, N.Graf, G.Stamatakis, "Towards In Silico Oncology: Adapting a Four Dimensional Nephroblastoma Treatment Model to a Clinical Trial Case Based on Multi-Method Sensitivity Analysis." *Computers in Biology and Medicine*, in press, doi: 10.1016/j.compbimed.2012.08.008. Epub 2012 Oct 10. vol.42 (11) pp. 1064-1078 2012
- G.S.Stamatakis, E.Ch.Georgiadi, N.Graf, E.A.Kolokotroni, and D.D.Dionysiou, "Exploiting Clinical Trial Data Drastically Narrows the Window of Possible Solutions to the Problem of Clinical Adaptation of a Multiscale Cancer Model", *PLOS ONE* 6(3), e17594, 2011
- N. Graf, A. Hoppe , E. Georgiadi, R. Belleman, C. Desmedt, D. Dionysiou, M. Erdt , J. Jacques, E. Kolokotroni, A. Lunzer, M. Tsiknakis, G. Stamatakis "In Silico Oncology" for Clinical Decision Making in the Context of Nephroblastoma. [Die Bedeutung von ‚in silico Onkologie‘ zur klinischen Entscheidungsfindung am Beispiel des Nephroblastoms] *Klin. Paediatr. (Klinische Paediatric)* 221, 141-149, 2009
- G Stamatakis, D Dionysiou, A Lunzer, R Belleman, E Kolokotroni, E Georgiadi, M Erdt, J Pukacki, S Rueping, S Giatili, A d'Onofrio, S Sfakianakis, K Marias, C Desmedt, M Tsiknakis, and N Graf "The Technologically Integrated Oncosimulator: Combining Multiscale Cancer Modeling with Information Technology in the In Silico Oncology Context" *IEEE J Biomed Health Inform* 2013
- Othersen BH., Jr . In: *Nephroblastoma*. Hays DM, editor. Published by Grune and Stratton, California: Pediatric Surgical Oncology; 1986. pp. 139–50.
- E.A. Kolokotroni, D.D. Dionysiou, N.K. Uzunoglu, G.S. Stamatakis, "Studying the growth kinetics of untreated clinical tumours by using an advanced discrete simulation model", *Mathematical and Computer Modelling*, 54 1989-2006 2011

Berrebi D, Leclerc J, Schleiermacher G, Zaccaria I, Boccon-Gibod L, et al. (2008) High cyclin-E staining index in blastemal, stromal or epithelial cells is correlated with tumour aggressiveness in patients with nephroblastoma. *PLoS ONE* 3(5): e2216. doi:10.1371/journal.pone.0002216.

Shackney SE, McCormack GW, Cuchural GJ (1978) Growth rate patterns of solid tumours and their relation to responsiveness to therapy. *Ann Intern Med* 89: 107–121.

Craft AW (1999) Growth rate of Wilms' tumour. *The Lancet* 354(9184): 1127.

Zoubek A, Slavc I, Mann G, Trittenwein G, Gadner H (1999) Natural course of a Wilms' tumour. *Lancet* 354: 344.

Carre' A, Frantz CN, Weksberg R, Nicholson L, Ciarlo L, et al. (2005) Wilms tumour in an 11-year old with hemihyperplasia. *Am J Med Genetics* 139A:165–166

Steel GG (2002) *Basic Clinical Radiobiology*. London: Arnold. pp 9–10.

Popel AS, Hunter PJ. *Systems Biology and Physiome Projects*. Wiley Interdisciplinary Reviews: Systems Biology and Medicine. 2009;1:153–8.

Study 2: Molecular Model adaptation: Using miRNA expression data to generate patient specific predictions

2.1 Model Description

The UPENN model is composed of two main signaling modules – ErbB receptor mediated Ras-MAPK and PI3K/AKT signaling module and TP53 mediated DNA damage response module. The main features of model are summarized below

Input

1. Patient microRNA from tissue or serum; oncogene mutation
2. Treatment conditions- Radiation: dose and regimen

Model

1. Tumour microenvironment- growth factor level, temporal growth factor availability, receptor expression, heterogeneity of the tumour microenvironment
2. Integration of cell cycle, DNA damage response, mitogenic and survival signals, drugs

Output

Patient-specific cell kill probability, cell growth probability, and cell senescence probability in the presence and absence of specific drug/combinations, radiation treatment

2.2 Using miRNA expression data to generate patient specific predictions

Micro-RNAs are short non-coding RNAs that regulate gene expression post-transcriptionally by either inhibiting translation or promoting mRNA degradation. Hence not surprisingly these miRNAs have been found to play critical role in various forms of cancer. For CHIC lung and nephroblastoma demo normalized tissue and serum miRNA expression data are available in minml format. We were able to utilize this expression data by identifying the specific targets of top 20 miRNAs using miRTarBase [5]. For those mRNAs which are present in our network we adjusted the initial expression level accordingly before each model run. Hence the final outcomes were tailored to the particular expression profile of the patients to generate clinically useful outcomes. An example table is shown below indicating some top expressed miRNA and their corresponding mRNA targets obtained from miRTarBase [6].

The molecular hypermodel takes as an input, the miRNA profiles of a given patient from the CHIC data repository and then uses a database mapping (miRTARbase) to map the enriched miRNA in either tissue or serum of a patient to the corresponding mRNA, see Fig. 6. The mRNA information is then used to constrain the nodes of our network in order to capture the molecular effect; similarly, nodes are constrained based on the drug interactions. In total, we consider doxorubicin, vincristine, and actinomycin as the three drugs for nephroblastoma. The model is run based on the input miRNA and drug treatment and averages over several tissue conditions such as growthfactor levels and receptor expression. An average as well as a distribution of cell kill, cell senescence, and cell growth probabilities are obtained for a given patient, which are then passed on to the multi-modeler framework.

miRNA	WT vs. control	*Targets in Combined Network†
miR-223-3p		9.63 STAT5A, ATM, E2F1, TP53, MDM2
miR-143-3p		6.87 KRAS, MAPK, HRAS, AKT, MDM2, BCL2, MAP3K, CASP5
miR-130b-3p		6.47 RB, PTP, E2F, CASP, PTEN, MAP3K, WIP, CDK4
miR-17-5p		6.2
miR-100-5p		5.29 ATM, MTOR, MAPK(ERK), BCL, PTP, GRB2, RB, AKT
miR-24-3p		4.37 E2F1, MDM2, MAP3K, MAP2K, MAPK, CDK, ATF, PTP, BCL2
miR-3651		3.58
let-7f-5p		3.35
miR-18a-5p		2.91 PTEN, ATM, BCL2, ARF6, TP53
miR-181-b-5p		2.86 BCL2, MAP3K, E2F1, PTEN, MTOR, ATM, ARF6, MAP2K, PDK3
let-7a-5p		2.75
miR-335-5p		2.29
miR-320a		1.71
miR-126-3p		1.68 *miRNA Expression data from Ludwig, Nicole, et al.
miR-195-5p		1.67 "Circulating serum miRNAs as potential biomarkers
miR-101-3p		1.31 for nephroblastoma." Pediatric blood & cancer
miR-638		1.15 (2015).
miR-572		†Target genes obtained from miRTarBase:
miR-1825		-1.29 (http://mirtarbase.mbc.nctu.edu.tw)
		-2.55

How will the miRNA data be combined with network model?

- Identify top 5-10 miRNA which are overexpressed in particular patient data pre and post CT
- Use miRTarBase to obtain a list of top target proteins (can be automated using a simple Perl/Python script)
- Run combined model with lower levels of activity or concentration (determined based on the expression levels of miRNA with respect to control) for the target proteins
- Report observed cell fate/cell kill rate

Fig. 6: Algorithm for miRNA implementation in the molecular model.

2.3 Results - Application to the Nephroblastoma scenario

In Fig. 10, we describe the results of our model for a given patient in the nephroblastoma scenario selected from the CHIC data repository. The Table in Fig. 10 shows the cell death probabilities predicted by the model under the action of different chemotherapeutic drugs (A: doxorubicin; V: vincristine; A: actinomycin). The panels below show the cell state transitions and the time evolution of key transcriptional activators.

Results Summary for Patient 5XIHQGQZ2GDYMIT55KON

Table 1: Cell Fate Probabilities

mirna-source	Drug(D,V,A) [†]	Cell-Death($\mu \pm \sigma$)	Cell-Growth($\mu \pm \sigma$)	Cell-Senescence($\mu \pm \sigma$)
tissue	(D-,V-,A-)	0.18(± 0.03)	0.51(± 0.15)	0.32(± 0.13)
tissue	(D+,V+,A+)	0.63(± 0.08)	0.08(± 0.07)	0.29(± 0.14)
tissue	(D-,V+,A+)	0.53(± 0.18)	0.12(± 0.15)	0.35(± 0.1)

[†] D-Doxorubicin, V-Vincristine, A-Actinomycin

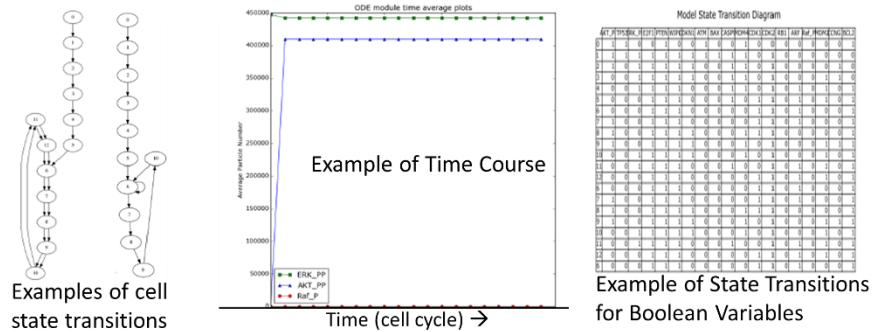


Fig. 10: Demonstration of the molecular model for a patient in the nephroblastoma scenario.

The approach has been further exploited in the case of 7 patients. For each patient, an adjusted cell kill ratio based on the molecular profile and the drug dosage of the patient is calculated. The results are provided below:

Table I: Patient-specific adjusted cell kill ratio for different drug combinations.

The adjusted cell kill ratio is to be utilized by the oncosimulator of the multimodeller framework as described below. Further details of how the adjusted CKR has been computed by combining the UPENN model results with literature data is available in the attached excel document.

Control				
Vincristine (mg/m ²)	Dox (mg/m ²)	Actinomycin (ug/kg)	Cell-Death-Mean	CKR Adjusted
0	0	0	0.148809524	N/A
can test the additivity assumption				
LADYMBZY4K262EJRR3V				
Vincristine (mg/m ²)	Dox (mg/m ²)	Actinomycin (ug/kg)	Cell-Death-Mean	CKR Adjusted
1	0	0	0.074404762	0.28
1	0	730	0.148809524	0.813376
KOLQXCKDRWLYVCATQAMF				
Vincristine (mg/m ²)	Dox (mg/m ²)	Actinomycin (ug/kg)	Cell-Death-Mean	CKR Adjusted
1	0	0	0.077380952	0.28
1	0	730	0.148809524	0.800929363
1	34	730	0.142857143	0.92957668
M2Z4XCTXSR3NCW454E5E				
Vincristine (mg/m ²)	Dox (mg/m ²)	Actinomycin (ug/kg)	Cell-Death-Mean	CKR Adjusted
0.9	0	0	0.110119048	0.28
0.9	0	650	0.145833333	0.670949724
XEON5ZV5NZIIKEAQHY4M				
Vincristine (mg/m ²)	Dox (mg/m ²)	Actinomycin (ug/kg)	Cell-Death-Mean	CKR Adjusted
0.83	0	0	0.111607143	0.28
0.83	0	540	0.148809524	0.673428464
5XIHQQZ2GDYMIT5KON				
Vincristine (mg/m ²)	Dox (mg/m ²)	Actinomycin (ug/kg)	Cell-Death-Mean	CKR Adjusted
0	0	0	0.178571429	N/A
1	0	650	0.526785714	0.91592303
6Z34IQAMEOQ2YZTU3SOE				
Vincristine (mg/m ²)	Dox (mg/m ²)	Actinomycin (ug/kg)	Cell-Death-Mean	CKR Adjusted
0	0	0	0.142857143	N/A
1	0	650	0.386904762	0.897016302
1	34	650	0.43452381	0.987366232
4L3YB6HMD3LK52ZVLCF				
Vincristine (mg/m ²)	Dox (mg/m ²)	Actinomycin (ug/kg)	Cell-Death-Mean	CKR Adjusted
0	0	0	0.116071429	N/A
1	0	650	0.511904762	0.97531746
1	34	650	0.523809524	0.99847487

2.5 Conclusions and future work

The present work we describe an integrated cellular framework to model key cell signaling pathways operating at different time scales – a well-recognized challenge in the field. Here we model the ErbB receptor mediated Ras-MAPK and PI3K/AKT pathway and integrate it with p53 mediated DNA damage response pathway to obtain a cell kill rate under specific drug dosing and patient specific miRNA expression levels. The obtained cell kill rate was directly used as an input to phenomenological tumour growth models. The aim of such integrated molecular model is to provide a mechanistic foundation to the more empirical models used in the field to obtain cell kill and growth rates under particular dosage conditions. The integration of the models was accomplished by identifying model interfaces and passing information between runs of the two models. This framework has been tested for the lung cancer and the nephroblastoma scenarios and the future work will be focused on performing a detailed sensitivity analysis to simulate the inherent tumour heterogeneity and also the effect of various mutations and subject the framework to clinical validation. The integration of the UPENN molecular model with the multimodeler framework of CHIC is shown in Fig. 11.

Integration of UPENN Model in the CHIC Multimodeler

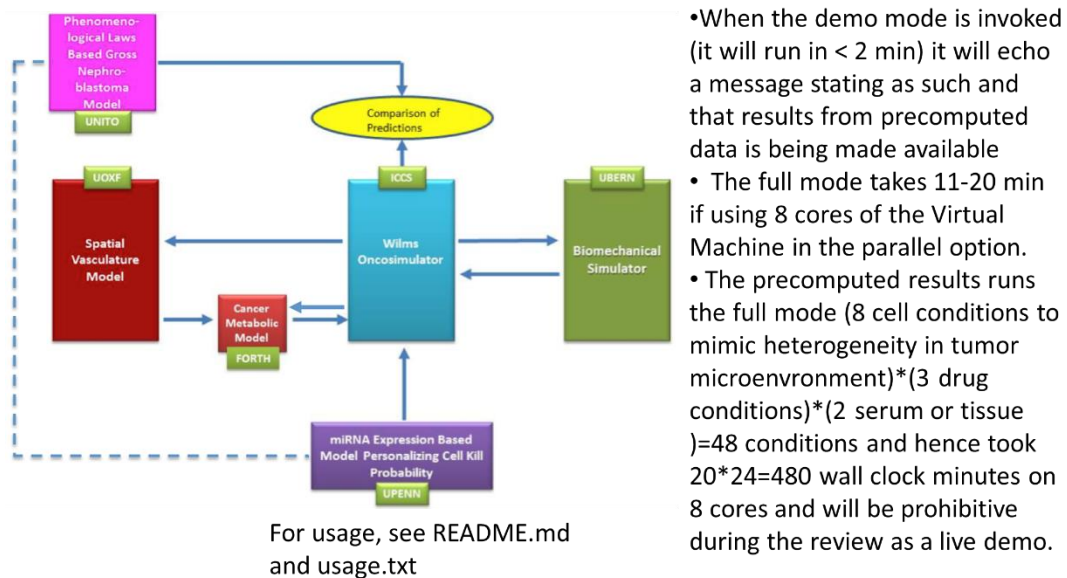


Fig. 11: Flowchart showing the passing of information between the hypermodels including the molecular hypermodel.

References

1. Chen, W. W., Schoeberl, B., Jasper, P. J., Niepel, M., Nielsen, U. B., Lauffenburger, D. a, & Sorger, P. K. (2009). Input-output behaviour of ErbB signaling pathways as revealed by a mass action model trained against dynamic data. *Molecular Systems Biology*, 5(239), 239.
2. Choi, M., Shi, J., Jung, S. H., Chen, X., & Cho, K.-H. (2012). Attractor landscape analysis reveals feedback loops in the p53 network that control the cellular response to DNA damage. *Science Signaling*, 5(251), ra83.
3. Cuadrado, A., & Nebreda, A. R. (2010). Mechanisms and functions of p38 MAPK signalling. *The Biochemical Journal*, 429(3), 403–417
4. Gottlieb, T. M., Leal, J. F. M., Seger, R., Taya, Y., & Oren, M. (2002). Cross-talk between Akt, p53 and Mdm2: possible implications for the regulation of apoptosis. *Oncogene*, 21(8), 1299–1303.
5. Chou, C. H., Chang, N. W., Shrestha, S., Hsu, S. D., Lin, Y. L., Lee, W. H., Tsai, T. R. (2016). miRTarBase 2016: updates to the experimentally validated miRNA-target interactions database. *Nucleic acids research*, 44(D1), D239-D247
6. Ludwig, N., Nourkami-Tutdibi, N., Backes, C., Lenhof, H.-P., Graf, N., Keller, A., ... Background. (1996). Circulating Serum miRNAs as Potential Biomarkers for Nephroblastoma. *Journal of Clinical Oncology*, 14(5), 1526–1531.
7. Brenner, D. J. (2008). The Linear-Quadratic Model Is an Appropriate Methodology for Determining Isoeffective Doses at Large Doses Per Fraction. *Seminars in Radiation Oncology*, 18(4), 234–239

Study 3: Adaptation of Oncosimulators (Wilms and Lung) and Biomechanical model coupling: Assessing Evolution of Tumour Shape and Position

Tumour Position and Shape

Evolution of position and shape of the growing tumour results from the interaction of multiple processes and are influenced by chemical gradients, due to local differences in the availability of nutrients [cite Non-linear model of cancer growth and metastasis: a limiting nutrient as a major determinant of tumour shape and diffusion [G. P. Pescarmona, M. Scalerandi, P. P. Delsanto, C. A. Condat, <https://www.ncbi.nlm.nih.gov/pubmed/10687891>], and physical constraints. Additionally, tumour position may be affected by morphological changes, such as weight loss or tissue scarring.

While the influence of chemical gradients and nutrients is not taken into account by the CHIC hypermodel, physical constraints and resulting forces are represented through the biomechanical component model (BMS). Evolution of tumour shape and location in the present hypermodel is governed by the interaction between the OncoSimulator (OS) and BMS hypomodels.

BMS computes a field of ‘least-pressure’ directions based on the stresses arising from local variations in tumour cell concentration. OS uses this information to inform the movement of tumour cells within the boundaries of the simulation domain. The communication between BMS and OS thus involves the exchange of scalar and vector fields that describe those parameters throughout the respective 3D domain of each simulator component.

Given the complexity of the problem, prediction of tumour shape and position is an explorational feature of the mechanistic CHIC hypermodels, with the primary goal to investigate mechanisms and feasibility of coupling tightly interacting models within the CHIC hypermodeling framework. Over the course of Task 6.4, the conceptual and practical challenges involved in coupling the Biomechanical and Onco-Simulator were investigated, their interaction improved and the ability of the entire hypermodel to predict tumour shape and position after therapy was evaluated. Accurate prediction of tumour shape and position, however, is not essential for answering the clinical questions pertinent to the Lung and Nephroblastoma scenarios.

Assessing Evolution of Tumour Shape and Position

Methods

A metric was defined for comparing tumour position between the available imaging time points and throughout the simulated tumour evolution, Fig. 1. First, medical images at both time points were registered using a rigid registration procedure in order to establish a common spatial reference frame. Then, the center-of-mass position was computed for both images (t_1 , t_2), as well as for the simulated tumour at every simulation timestep $t_{s,i}$ ($t_1 < t_{s,i} < t_2$). We used the distance between tumour center-of-mass positions at time points $t_{s,i}$ during the simulation and the final imaging time point t_2 as metric for the spatial agreement between simulation and reality.

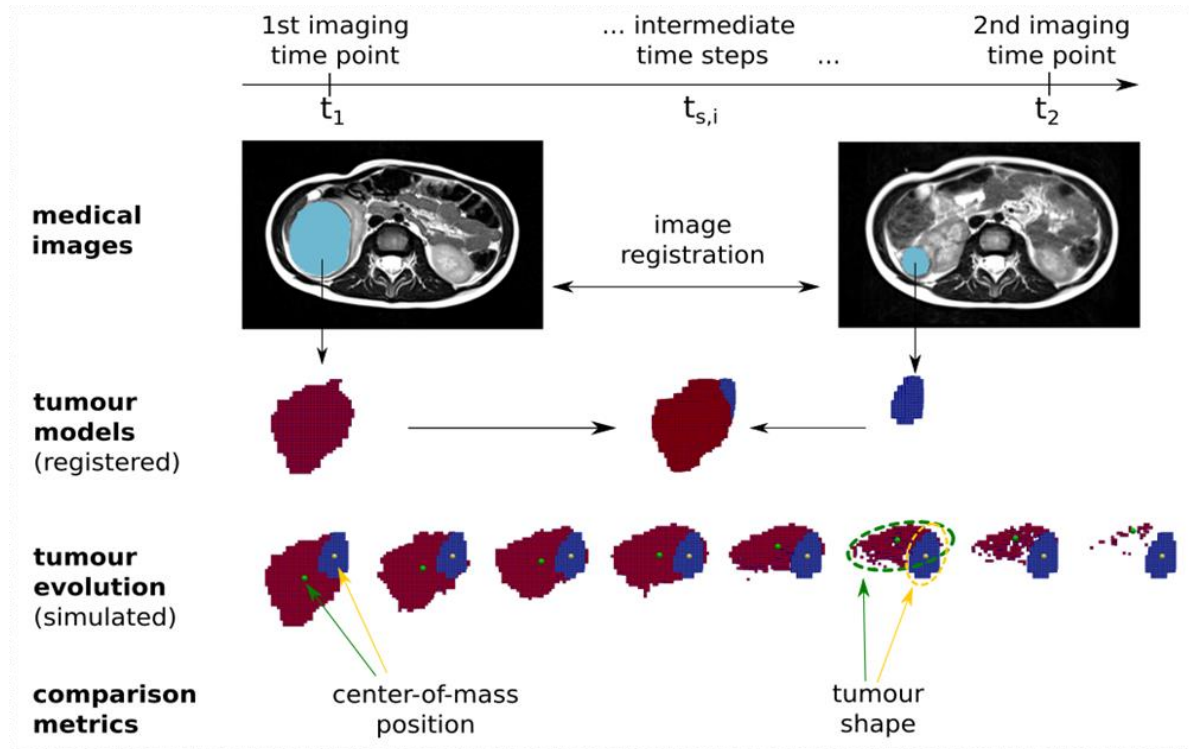


Figure 1: Assessment of simulated tumour shape and position.

Results

This assessment strategy was applied to results of the Nephroblastoma and Lung Cancer hypermodels. Fig. 2 illustrates 3D shape and position of the simulated tumour in comparison to the actually observed tumour. During the simulation period, tumour volume increases in the Lung scenario and decreases in the Nephroblastoma scenario.

Lung

The simulated growing tumour in the lung scenario maintains a compact shape, in agreement with observation. Its simulated and observed position at the second imaging time point are approximately 2 cm apart.

Nephroblastoma

Evolution of simulated tumour position with respect to the observed position differs between the two selected Nephroblastoma cases. While the COM distance remains in the range about 2cm for Wilms patient '5X', it increases to up to 4-5 cm for Wilms patient '6Z'. Visual comparison of tumour shape shows that the simulated tumour does not shrink isotropically to a compact bulk tumour with smaller radius as expected from the segmentations of the second imaging time points. Instead, the tumours appear to dissolve from one side, forming a porous and partially disconnected structure, compare Fig 2.

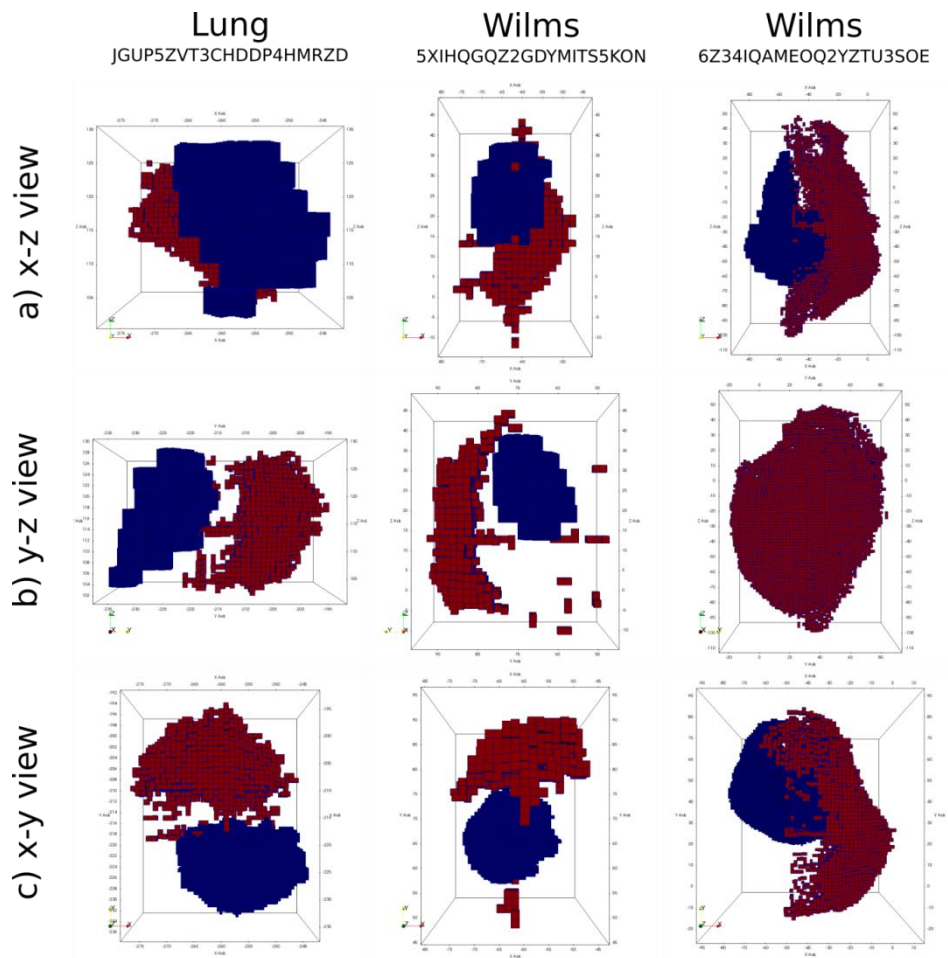


Figure 2: Visual comparison of shape and position between simulated (red) and observed (blue) tumours at the respective second imaging time point. During the simulation period, the tumour volume increases in the Lung scenario (day 1-98) and decreases in the Nephroblastoma scenario (patient 5X: day 1-35, patient 6Z: day 1-41).

Discussion & Conclusion

The hypermodel is found to reproduce realistic tumour shapes in growth scenarios, whereas shrinkage scenarios (Nephroblastoma) tend to result in tumour shapes that have a more 'diffuse' appearance than those observed. The hypermodel achieves a good prediction of tumour position in selected cases. However, systematic evaluation suggests that reliable prediction of tumour shape and position in Nephroblastoma and Lung cancer with the developed approach and the available information is not yet possible. This finding underlines the challenges involved in coupling the discrete OS and continuum-mechanics based BMS hypomodels.

The following paragraphs discuss the most important model and evaluation limitations that may explain the observed discrepancies. Addressing those challenges will be subject of future research.

Hypermodel

Clearly, any models' ability to approximate reality is limited by the information available for model building and configuration. Most critical for BMS is the uncertainty in mechanical tissue parameters (not patient-specific) and the lack of well-defined boundary conditions for mechanical computations that are particularly difficult to establish for the Nephroblastoma and Wilms scenarios.

In order to test the ability of a biomechanical model to reproduce tumour shape and position in a scenario with better defined mechanical boundary conditions, a mechanically-coupled tumour growth and normal tissue invasion model for brain cancer has been introduced in Deliverable 6.3. Initial studies with this model emphasized the importance of anisotropy in tissue properties and showed that consideration of bio-mechanical aspects alone may not be sufficient to reproduce the variety of observed tumour shapes, compare Fig. 3.

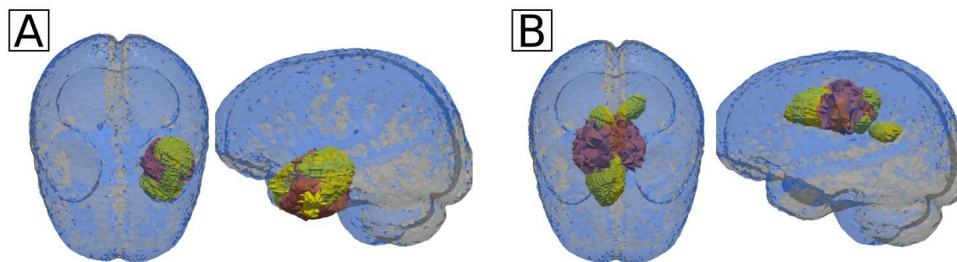


Figure 3: Comparison of simulated (red) to observed tumour shapes (yellow) for selected glioma cases based on the mechanically-coupled reaction diffusion model introduced in Deliverable 6.3. Good agreement is observed for regularly structured shapes (A), whereas highly irregular shapes are not reproduced in simulations (B). [cite "Evaluation of a mechanically-coupled reaction-diffusion model for macroscopic brain tumour growth" D. Abler, P. Büchler, In Book of Abstracts CMBBE 2016, due to be published in 'Lecture Notes in Bioengineering' ISSN: 2195-271X]

Morphological changes in the healthy tissue also influence tumour evolution. This aspect is not taken into account by the present hypermodel.

Evaluation Approach

The proposed evaluation approach relies on image registration techniques to compare simulation results to imaging data at a later time point. This process introduces an uncertainty in the relative positioning of the tumours. To reduce the importance of this uncertainty in future studies, the use of fixed anatomical markers as reference within the respective imaging frame could be investigated.

The center-of-mass position of simulated and observed tumour is used in the present analysis as reference for its average position in space. This approach works well to characterize the position of compact tumours, however, for dispersed tumour shapes, such as those simulated in shrinkage scenarios, the COM position may no longer be fully enclosed by the active tumour.

Hypomodels and Hypomodel-Coupling

The complexity of the coupling between OS and BMS may also provide partial explanation for the observed hypermodel behaviour. In particular, mapping of the pressure (direction of least-pressure) field computed by BMS into the discrete model of OS is challenging, as is the update of BMS with OS cell concentration values. Accuracy in both steps is affected by interpolation. Both simulators have been improved in close collaboration between ICCS and UNIBE to best reflect the underlying physical and biological processes. A remaining limitation of model interaction is linked to difficulties in synchronizing the spatial evolution of tumour cell distribution in both hypo-models. The focus of future work will be focused on this aspect of the coupling between biomechanical and biological simulation components.

Study 4: Adaptation and initial validation of the coupling of the molecular hypomodel with the nephroblastoma (Wilms) Oncosimulator

Three Nephroblastoma cases for which the segmentation of the tumour area on MRI imaging data as well as molecular and clinical data have been available, have been simulated with a coupled Wilms Oncosimulator and molecular hypermodel (fig. 1)

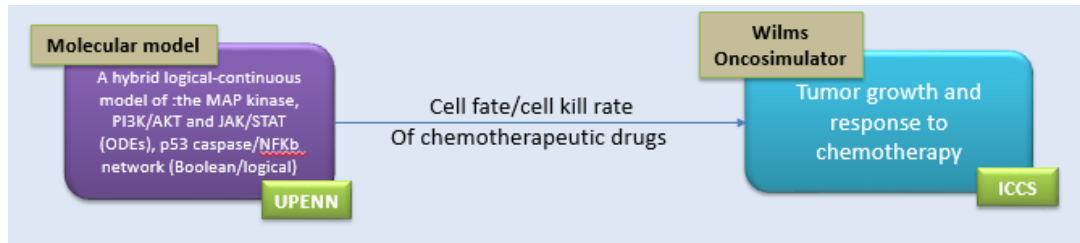


Fig 1. Wilms Oncosimulator and molecular hypermodel investigated in study 4.

All patients have received preoperative chemotherapy with a combination of actinomycin and vincristine according to the SIOP 2001/GPOH clinical trial for unilateral stage I-III nephroblastoma tumours.

The molecular hypomodel obtains the cell kill rate of the administered chemotherapy. The output of the molecular hypermodel is then used by the cell kinetic hypomodel. The input parameters of Wilms oncosimulator related to tumour cell kinetics are retrieved following adaptation of the model to the real clinical, histological and imaging data (table 1).

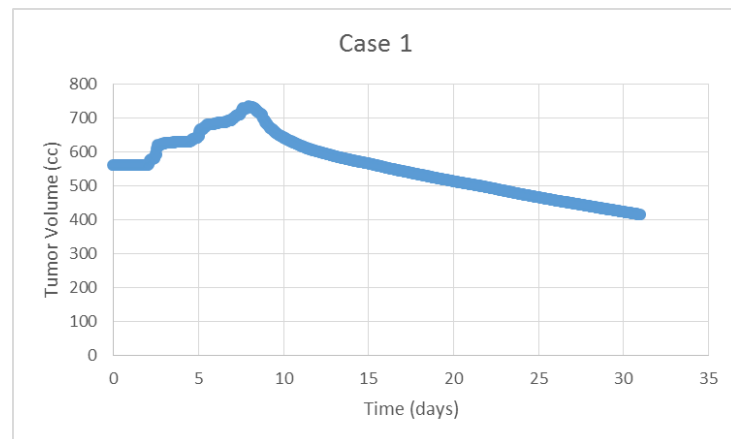
The relative dates (after pseudo-anonymization) of the two MRI acquisitions as well as the clinical tumour volumes as calculated based on the segmentation of the tumours on these imaging sets are depicted in table 2.

The simulated tumour volume reductions and the clinical are depicted in table 2. The simulated time evolution of the tumours is shown in figure 2 .

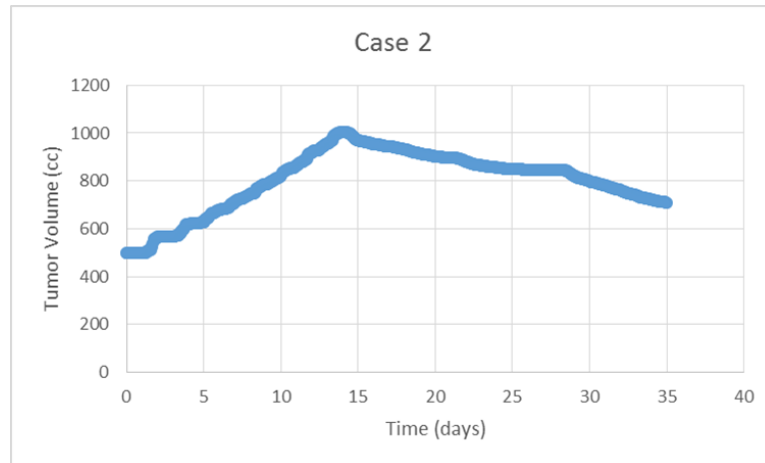
TABLE 2: Imaging data information of thee nephroblastoma patients simulated with molecular – oncosimulator hypermodel

	Imaging Date	V _{CT} (cc)	V _{VT} (cc)	DV _{CT} (%)	DV _{VT} (%)	Deviation (%)
Case 1	PRE: 18/6/1945	456	583	26.85	25.88	3.6
	POST: 18/7/1945	334	413			
Case 2	PRE: 10/8/1945	496	497	-43.98	-42.29	3.8
	POST: 14/9/1945	714	707			
Case 3	PRE: 28/1/1945	109	135.6	50.22	50.81	1.2
	POST: 25/2/1945	54	66.7			

A.



B.



C

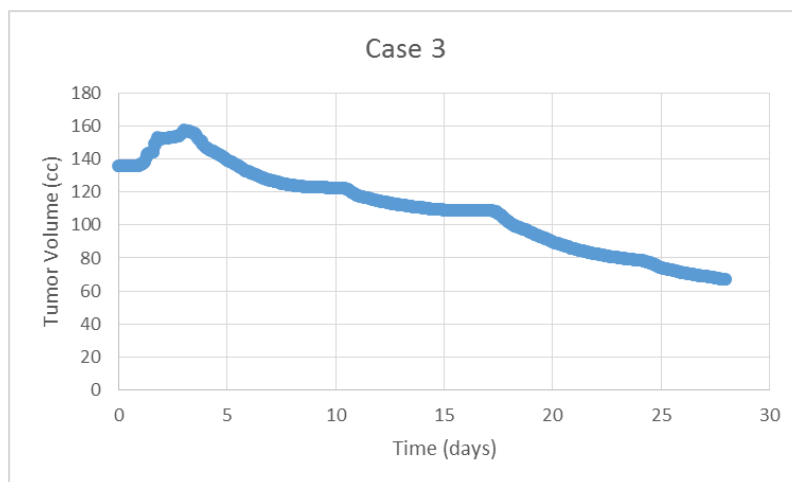


Figure 2: Time evolution of virtual simulated tumours of the first (A) the second (B) and the third (C) case of nephroblastoma patients.

TABLE I: Adaptation of parameter values related to tumour cell kinetics of the three simulated nephroblastoma patients

Parameter	Description	Value – Case 1	Value – Case 2	Value – Case 3
Tc	Cell cycle duration (h)	20	20	20
Psleep	Fraction of cells that enter G0 phase following mitosis	0.3	0.3	0.3
Psym	Fraction of stem cells that perform symmetric division	0.5	0.52	0.52
TN	Time needed for necrosis products to be removed	20	20	20
TA	Time needed for apoptosis products to be removed	6	6	6
NLIMP	Number of mitoses performed by LIMP cells before arrest	7	7	7
TG0	Duration of dormant phase	50	200	100
RA	Apoptosis rate of stem and LIMP cells	0.001	0.001	0.001
RADiff	Apoptosis rate of differentiated cells	0.0004	0.0007	0.0008
RNDiff	Necrosis rate of differentiated cells	0.0004	0.0005	0.002
PGotoG1	Fraction of G0 cells that re-enter cell cycle	0.001	0.001	0.01
CKP_Total (derived from molecular)	Fraction of cells lethally hit by vincristine and actinomycin following bolus drugs combined administration	0.975	0.67	0.67

Concluding, qualitatively an expected adaptation of the three cases analyzed has been achieved. The communication between the Wilms Oncosimulator and the molecular hypermodel has been checked and a reasonable behaviour has been demonstrated in the experiments.

Study 5: Adaptation and partial validation of the integrated Wilms Hypermodel

Two nephroblastoma patients for which imaging, clinical and molecular data are available have been simulated with the fully integrated Wilms multimodeler hypermodel (fig. 1) through the VPH-HF

infrastructure. Both patients have received preoperative chemotherapy with a combination of actinomycin and vincristine according to the SIOP 2001/GPOH clinical trial for unilateral stage I-III nephroblastoma tumours.

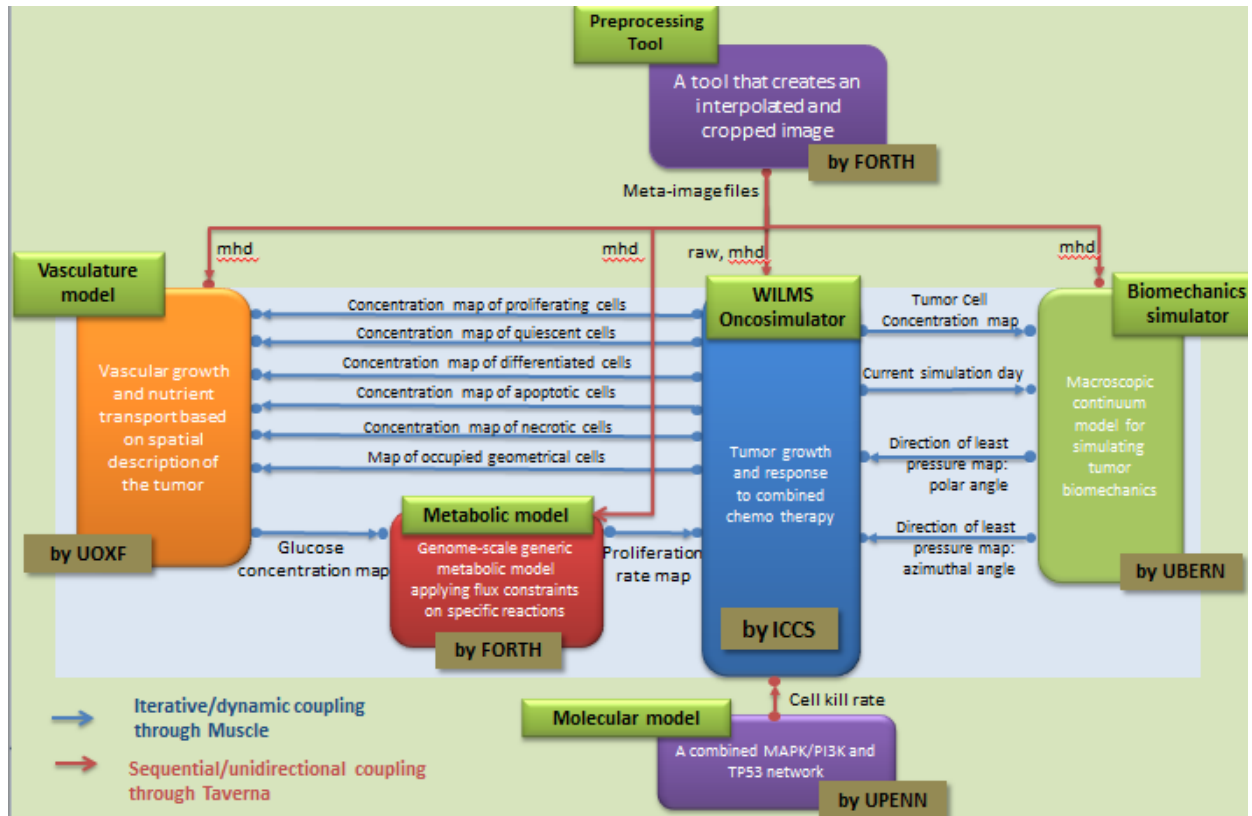


Figure 1: Wilms Multimodeler Hypermodel: integration scheme of Wilms oncosimulator, preprocessing tool, metabolic, molecular, vasculature and biomechanic hypomodels.

The MRI sets of patients acquired before the beginning of therapy are segmented and serve as input to the multimodeler hypermodel as well as the mi-RNA images of the patients. The real treatment schemes (fig. 2) administered are retrieved from the clinical data and are simulated for both patients. The initialization of the simulation is assumed the time point of the available MRI set pre-therapy and the end the time point of the second available MRI imaging set after the completion of therapy.

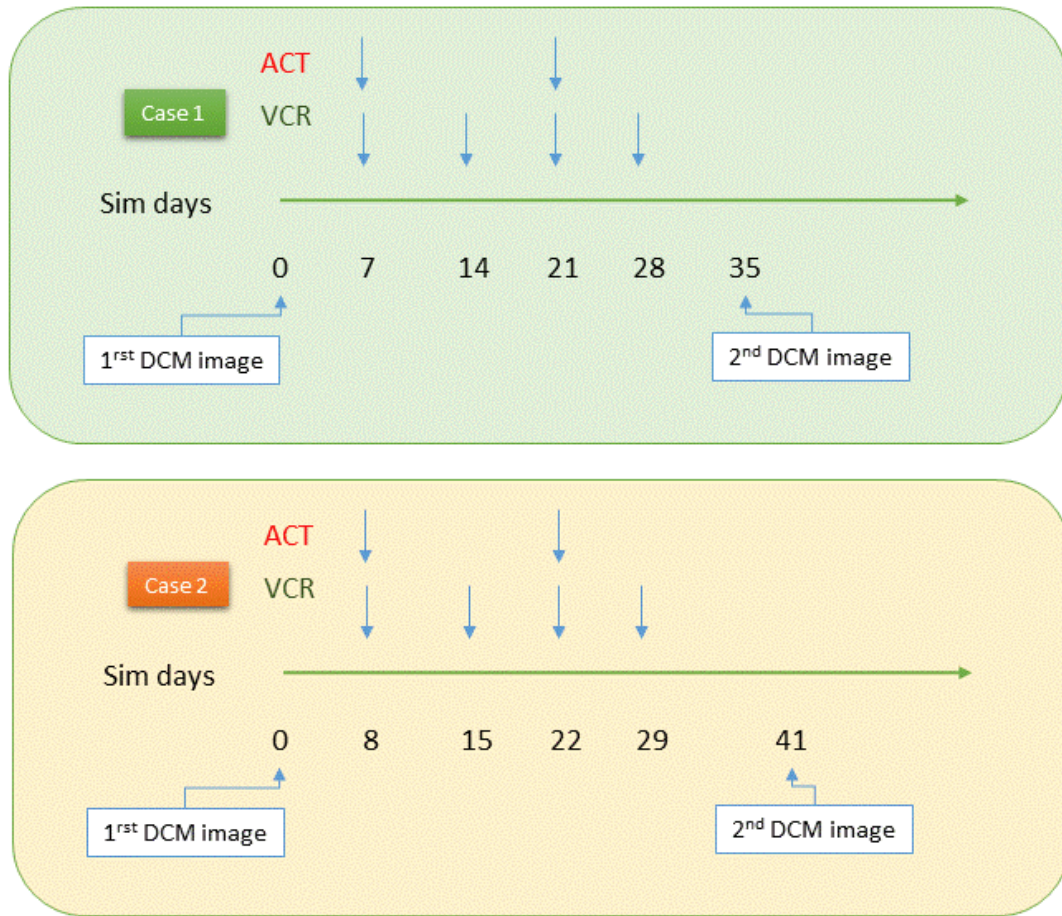


Fig 2: Pre-operative treatment schemes administered for the simulated patients

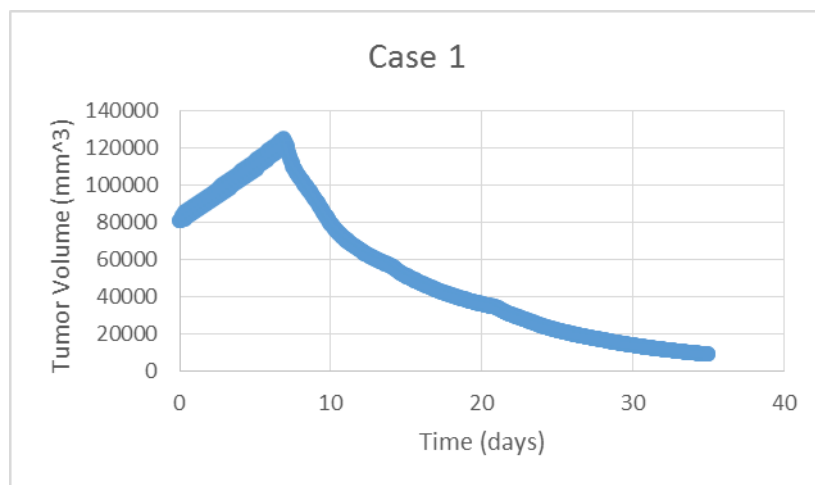
The relative dates (after pseudo-anonymization) of the two MRI acquisitions as well as the clinical tumour volumes as calculated based on the segmentation of the tumours on these imaging sets are depicted in table 1.

The input parameters of Wilms oncosimulator related to tumour cell kinetics are retrieved following adaptation of the model to the real clinical, histological and imaging data (table 2). The simulated tumour volume reductions and the clinical are depicted in table 1. The simulated time evolution of the tumours is shown in figure 2.

Table I: Imaging data information and volume reduction information of nephroblastoma patients simulated with the nephroblastoma multimodeller hypermodel

	Imaging Date	V_{CT} (cc)	V_{VT} (cc)	DV_{CT} (%)	DV_{VT} (%)	Deviation (%)
Case 1	PRE: 1950/11/17	78.54	80.99	90.68	90.39	0.32
	POST: 1950/12/22	7.32	11.34			
Case 2	PRE: 1953/08/26	754	785	80.5	80.25	0.31
	POST: 1953/10/06	147	155			

A.



B.

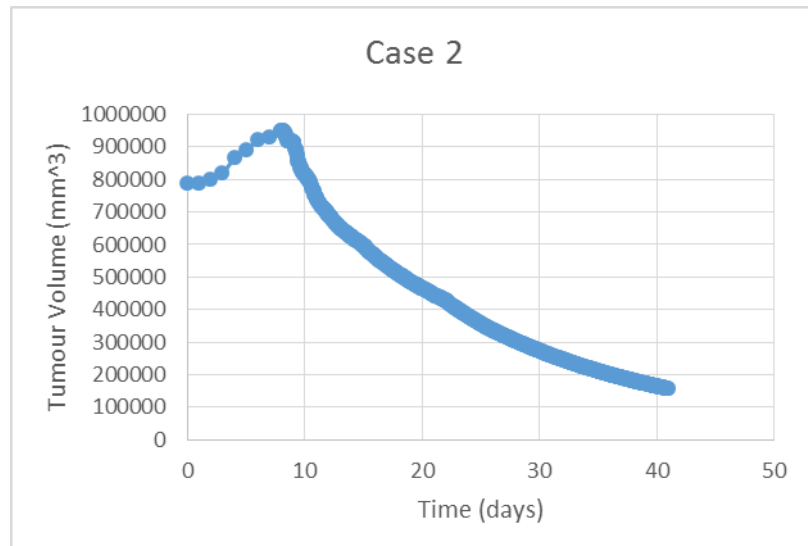


Figure 2: Time evolution of virtual simulated tumours of the first (A) and the second (B) case of nephroblastoma patients.

TABLE 2: Adaptation of parameter values related to tumour cell kinetics of the two simulated nephroblastoma patients

Parameter	Description	Value – Case 1	Value – Case 2
Tc	Cell cycle duration	6h	5
Psleep (derived from angiogenesis – metabolic)	Fraction of cells that enter G0 phase following mitosis	0.31	0.348
Psym	Fraction of stem cells that perform symmetric division	0.54	0.59
TN	Time needed for necrosis products to be removed	20	20
TA	Time needed for apoptosis products to be removed	6	6
NLIMP	Number of mitoses performed by LIMP cells before arrest	7	7
TG0	Duration of dormant phase	96	100
RA	Apoptosis rate of stem and LIMP cells	0.0055	0.006
RADiff	Apoptosis rate of differentiated cells	0.003	0.001
RNDiff	Necrosis rate of differentiated cells	0.005	0.0012
PGotoG1	Fraction of G0 cells that re-enter cell cycle	0.01	0.001
CKP_Total (derived from molecular)	Fraction of cells lethally hit by vincristine and actinomycin following bolus drugs combined administration	0.9159	0.897

The simulated time evolution of the tumours is shown in figure 2.

As the available information regarding a particular tumour's characteristics increases, a narrowing of the window of possible virtual scenarios is to be expected. Contrarily, after adequate "tuning" the simulation results could give valuable hints concerning tumour characteristics for which actual estimations might be missing in each case considered.

The conventional therapeutic developments in clinics still relies on a series of randomized clinical trials aimed at searching for favorable yet averaged treatment outcome. However, patient responses to a particular drug or therapy are known to fall into a range that deviates from this averaged behaviour. Multiscale cancer modeling may eventually help to explain not only why some therapies fail while others prove to be effective in controlling tumour progression but also why a particular treatment works only in a fraction of patients. Training the model on a patient's data will give a more accurate description of the specific kinetics of disease progression. Hence, this approach should provide a higher predictive power than that achieved with pooled data only. Introducing multiscale cancer modeling to medicine has the potential to facilitate the breakthrough of personalized medicine, and eventually maximize advances in science and technology for the benefit of cancer patients by helping select or optimize preventative and therapeutic patient care.

CHAPTER LC: THE NON SMALL CELL LUNG CANCER HYPERMODEL: CLINICAL ADAPTATION AND PARTIAL VALIDATION

(Please note that the numbering of sections, subsections, equations, figures and references within this chapter refers exclusively to the latter or even a section of it and is not applicable to other chapters of the document. If any of the above entities of another chapter is to be referred to, the chapter under consideration should also be mentioned through its two capital letter code)

I. The Angiogenesis Hypomodel for Nephroblastoma and Non Small Cell Lung Cancer

The development of the Angiogenesis hypomodel for Nephroblastoma and Non Small Cell Lung Cancer has been led by UOXF. ICCS has ensured the compatibility of the hypomodel with the rest of the interacting hypomodels as well as with the overarching topology of the corresponding hypermodels.

I.1 Overview

The Angiogenesis hypomodel describes the transport of nutrients in tumours at the tissue-scale. It uses the finite difference method to predict nutrient concentrations as a function of the three-dimensional spatial distribution of vessel volume fraction and tumour tissue, the latter being provided by other hypomodels. The Angiogenesis hypomodel returns a three-dimensional nutrient field, which can be used as input to other hypomodels.

For the Nephroblastoma and Non Small Cell Lung hypermodels the Angiogenesis component describes the transport of glucose and uses a vessel volume fraction that is fixed in time. This simple model was chosen to aid hypermodel integration and validation, as it has a favourably low number of input parameters. Open source software allowing the composition of a wide range of more detailed angiogenesis and tissue transport models for use with the VPH-HF has also been developed. This software will be of use as new clinical data becomes available in the future, or for the purpose of scientific research.

I.2 The Mathematical Model

The Angiogenesis hypomodel rationale and mathematical background has been described in detail in Deliverable 6.3 and is only briefly summarized here.

In general, the vasculature plays a vital role in the transport of nutrients and therapeutics to tumours, with tumour size limited by its ability to co-opt and maintain a vessel network. The Angiogenesis hypomodel is motivated by the well-known model of vascularized tumour growth by Hahnfeldt et al. [ANI]. This model describes the rate of change of tumour volume T as a function of carrying capacity K , assuming a spherical tumour:

$$T' = -\alpha T \log\left(\frac{T}{K}\right) \quad (1)$$

where α is a growth rate parameter. The adopted rate of change of the carrying capacity term is

$$K' = -\alpha_2 K + bT - dKT^{\frac{2}{3}} \quad (2)$$

where α_2 , b and d are constants. Implicit in this form is a balance between a rate of increase in carrying capacity due to tumour stimulation of new vasculature, and a rate of decrease in carrying capacity due to increasing diffusion length scales as the tumour grows. Since 3D imaging data and other hypomodels can give a more general tumour shape as inputs to the hypomodel, it is useful to relax the spherical tumour assumption.

The Angiogenesis hypomodel assumes steady-state, diffusion-limited transport of nutrient with concentration c , which is supplied by the vasculature at a rate dependent on vessel volume fraction V , and is consumed by tumour tissue at a rate proportional to the number of viable cells P . The tissue is assumed to comprise a tumour region and a non-tumour region, as shown in Fig. 1.

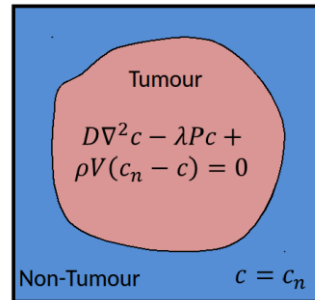


Fig. 1. The simulation domain for the transport problem. Distinct tumour and non-tumour regions are assumed.

In the non-tumour region it is assumed that the tissue is well vascularized and nutrient concentrations are set to a reference value c_n . In the tumour region nutrient transport is described by:

$$D\nabla^2 c - \lambda P c + \rho V(c_n - c) = 0 \quad (3)$$

where D is the effective nutrient diffusion coefficient in the tumour tissue, λ is the rate of nutrient consumption and ρ is rate of nutrient delivery by vessels.

Although the model has a physical basis, determination and physical interpretation of parameter values (D , λ , ρ , V , c_n) is challenging. In practice, these parameters should be treated in a phenomenological manner and used to fit model predictions to observed clinical tumour growth (or shrinkage) data. In the context of the Nephroblastoma and Non Small Cell Lung hypermodels the nutrient of interest is glucose, for which some literature-based, parameters values are adopted as initial approximations. These are shown in Table I.

Table I. Assumed parameter values for the vasculature hypomodel for nephroblastoma and lung.

Description	Symbol	Unit	Value	Source
Glucose Diffusivity	D	mm ² .hr ⁻¹	0.396	[AN2]
Glucose Consumption Rate	λ	(Num cells) ⁻¹ .hr ⁻¹	7.6e-10	Modified from [AN2]
Glucose Concentration in Non Tumour Regions	c_n	Kg.m ³	0.9	Value used in metabolic hypomodel
Vascular Delivery Efficiency	ρV	hr ⁻¹	0.25	User chosen/fit to data

The nutrient transport problem is solved on a regular finite difference grid in 3D. This method was chosen for computational efficiency and to avoid interpolation when used with the grid-based descriptions of cell growth used in other hypomodels.

1.3 Hypermodel Integration

Model integration with other hypomodels for use in the Nephroblastoma and Non Small Cell Lung hypermodels was described in detail in Deliverable 6.3. In brief, a cell population P is received from the ICCS tumour growth hypomodel at each grid point and each time point. The reaction diffusion equation for glucose transport is solved at each point, based on the current tumour geometry. The hypomodel outputs a normalized glucose field ($\frac{c}{c_n}$) at each point on the grid, and at each time point, for use by the FORTH metabolic component.

I.4 Hypomodel Testing and Parameter Identification

An advantage of the simple nature of the adopted hypomodel is that it allows for testing and a clear path for model comparison with clinical datasets. This section overviews verification and testing of the final hypomodel implementation.

For testing it is useful to assume a spherical tumour of radius R . Non-dimensionalising Eqn. (3) with spatial coordinate $\bar{x} = xR$ and concentration $\bar{c} = c/c_n$ gives:

$$\nabla^2 \bar{c} - \phi_1^2 \bar{c} + \phi_2^2 = 0 \quad (4)$$

where $\phi_2 = \sqrt{\frac{R^2}{D} \rho V}$ is a Thiele modulus related to vessel delivery efficiency and $\phi_1 = \sqrt{\frac{R^2}{D} (\lambda P + \rho V)}$ is a Thiele modulus related to tumour consumption efficiency. Assuming a 100.0 mm radius tumour, the parameter values in Table I, a typical cell number of $1.e9$ in a region of interest and a vessel volume fraction of 1.0 gives $\phi_1 = 160$ and $\phi_2 = 80$, suggesting a reasonably high rate of glucose consumption versus delivery and very high reaction versus diffusion timescales. Converting Eqn. 4 to spherical coordinates and dropping accents gives:

$$\frac{1}{r^2} \frac{d}{dr} \left(r^2 \frac{d^2 c}{dr^2} \right) - \phi_1^2 c + \phi_2^2 = 0 \quad (5)$$

with $\frac{dc}{dr} = 0$ at $r = 0$ and $c = 1$ at $r = 1$. This can be solved explicitly, giving

$$c(r) = \left(1 - \frac{\phi_2^2}{\phi_1^2} \right) \frac{\sinh(\phi_1 r)}{r \sinh(\phi_1)} + \frac{\phi_2^2}{\phi_1^2} \quad (6)$$

Solution values for a range of values of ϕ_1 and ϕ_2 are shown in Fig. 2, along with hypomodel predictions. This serves as both hypomodel verification and a means for identifying suitable parameter values when attempting to describe clinical observations.

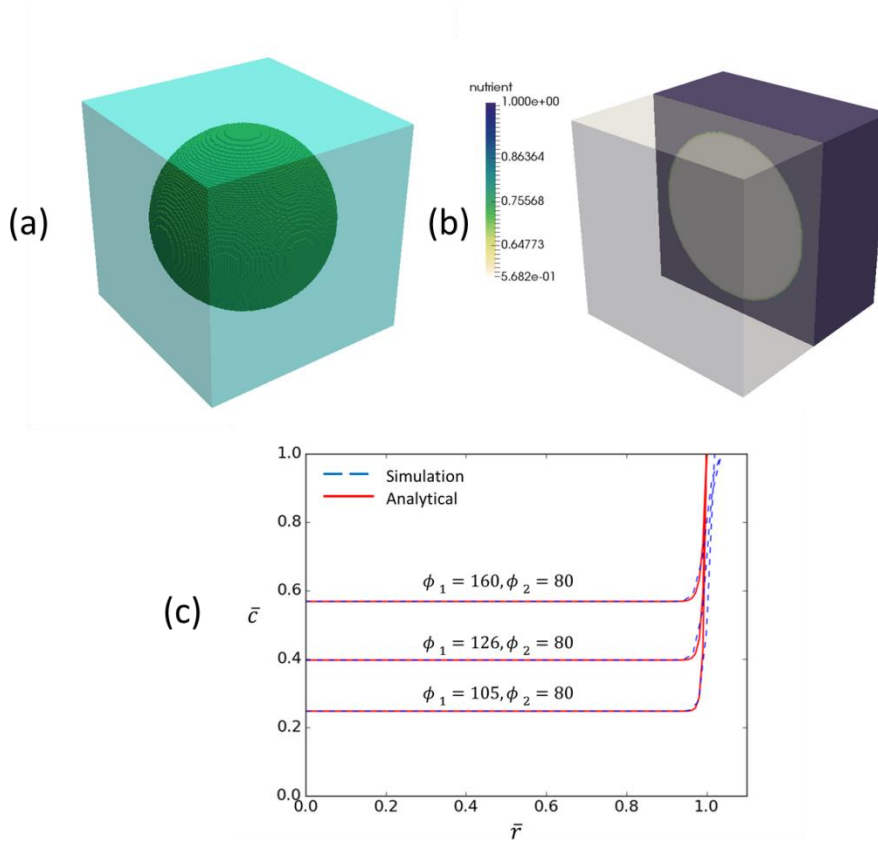


Fig. 2. (a) The test geometry for the hypomodel, a 100 mm radius spherical tumour. (b) The predicted dimensionless nutrient field for $\phi_1 = 160$ and $\phi_2 = 80$. (c) A comparison of the hypomodel predictions versus Eqn. 6. There is good agreement, within deviations at $\bar{r} = 1$ due to the use of a regular grid to discretize the spherical tumour.

The following model serves as a simple method for relating the hypomodel inputs to tumour growth rate predictions using the dimensional form of Eqn. (6), based on a more detailed treatment in Greenspan [AN3]:

$$R^2 \frac{dR}{dt} = \int_0^{R(t)} s c r^2 dr \quad (7)$$

where s is the tumour cell proliferation rate per unit nutrient concentration. Solution of Eqn. (7) following the steps in Greenspan [AN3] allows for the estimation of hypomodel parameter values

from clinical data by fitting of clinically observed tumour growth rates. In the case of the demonstrator hypermodels and CHIC clinical data, more detailed, integrated, fitting is required.

I.5 Future Exploitation

The model is implemented in the Chaste [AN4] open-source C++ framework for soft tissue modelling. As part of developments in this work package (WP6) a custom Chaste build was developed to allow the incorporation of MUSCLE libraries for run-time coupling of hypomodels and also packaging as a standalone executable. The latter was important for uploading software to the CHIC model repository and deploying to sandboxes on remote systems. A consequence is that many features of the Chaste library, including discrete cell based modelling, soft tissue mechanics and coupled PDE system solvers [AN4] can be used to rapidly build hypomodels for use with the CHIC based TAVERNA and MUSCLE execution workflows. Instructions for building CHIC compatible hypomodels with Chaste, and example source code, are available here: <https://github.com/jmsgrogan/Chic>.

I.6 High Resolution Models

Although the simple tissue scale models adopted here are best suited for hypermodel integration and clinical validation a range of alternative, high resolution models has also been developed and is available open-source here: <https://jmsgrogan.github.io/MicrovesselChaste/>. These models, an example of which is shown in Fig. 3, are useful for scientific research and informing coarse-grained tissue-scale hypomodels. They can be included in the hypermodelling framework following the mentioned examples here: <https://github.com/jmsgrogan/Chic>.

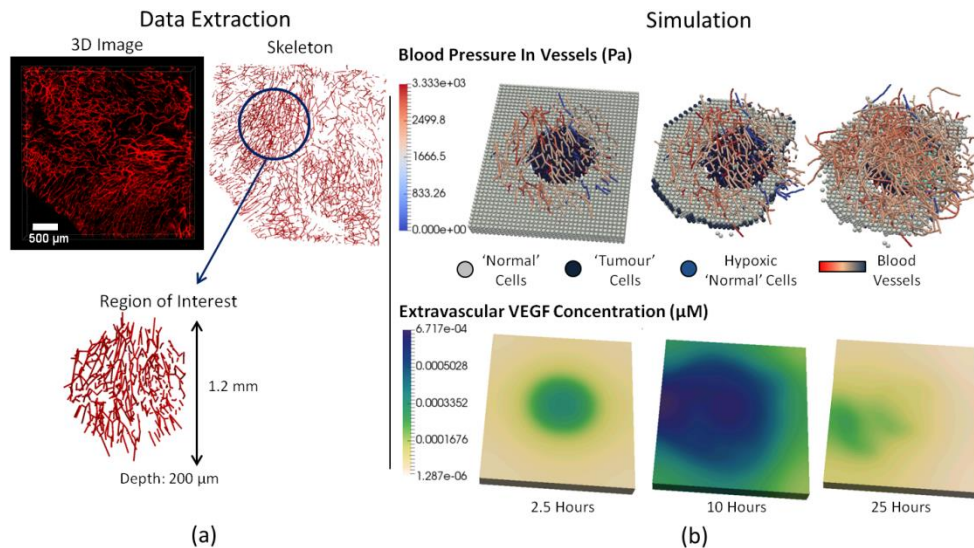


Fig. 3. High resolution angiogenesis and nutrient transport models built using Chaste. (a) Shows integration with high resolution intravital imaging data and (b) shows predicted tumour growth and angiogenesis.

I.7 References

[AN1] P. Hahnfeldt, D Panigraphy, J. Folkman, L. Hatky, "Tumour Development under Angiogenic Signalling: A Dynamical Theory of Tumour Growth, Treatment Response and Postvascular Dormancy", *Cancer Research* 59, pp4470-4775, 1999.

[AN2] H.P. Greenspan, "Models for the Growth of a Solid Tumour by Diffusion", *Studies in Applied Mathematics*, LI(4), pp317-340, 1972.

[AN3] G.R. Mirams et al., "Chaste: An Open Source C++ Library for Computational Physiology and Biology," *PLoS Computational Biology*, vol. 9, no.3, p. e1002970, 2013.

2. The Lung Cancer Molecular Model

2.1 Introduction

The lung cancer hypomodel has been developed by UPENN. The ErbB family of receptor tyrosine kinases and the signaling networks they influence have been implicated in a wide variety of cancers. The wild type and mutant forms of this receptor have critical role in determining tumour cell fates (death and proliferation) and resistance to various forms of targeted and systemic therapies. The ErbB family of receptors form multiple homo and hetero dimers and are activated by various ligands like epidermal growth factor (EGF), neuregulins (NRG). The activated dimers can turn on multiple signaling pathways downstream like mitogenic Ras-MAPK cascade and PI3K/AKT pathway. These pathways and their interaction with ErbB receptors have been extensively studied and modeled in literature using various computational paradigms like mechanistic compartmental/spatial models as well as statistical machine learning based models. These models can be of great clinical value in determining drug effectiveness, dosage and duration as well as investigating development of resistance to drugs and effect of intra and inter-tumoural heterogeneity.

The ErbB receptor mediated signaling pathways, important as they are, are however one of many other important determinant of tumour cell fate and drug resistance. Of these, tumour suppressor TP53 mediated signaling pathways are particularly important and they interact in important ways with the ErbB receptor mediated signaling pathways to determine ultimate cell fates. The p53 mediated signaling pathways are particularly important in determining tumour cell response to DNA damage as induced by chemotherapeutic drugs like doxorubicin and vincristine as well as radiation therapy. Due to its importance this signaling pathway has also been studied in detail. However due to its complexity and incomplete knowledge of the network, detailed mechanistic models are very few and not as predictive. These pathways have mainly been modeled using discrete two or multi-state network models. Although these models are simplistic, a variety of useful information regarding cell fate in response to DNA damage can be extracted from them and these predictions can be easily verified with experiments leading to further refinement of the models.

Among the important signaling modules mentioned above – ErbB receptor mediated Ras-MAPK and PI3K-AKT pathways and the TP53 mediated DNA damage response pathways have been modeled individually with different modeling paradigms to varying degree of success. However, there have been very few attempts to integrate these models into a combined cellular model. Such an integrated model will be of great clinical value due to its scope and its ability to test a great variety of situations to give results that can be directly useful to a clinician or can be used as an input to phenomenological models of tumour growth in response to chemo and radiation therapies. However, due to large differences in the relevant time and spatial scales of the two modules and due to the different nature of modeling paradigms which have been successfully applied to them, such an integration is a challenging task. In this work, we have successfully integrated these modules by identifying various interfaces from the literature and by developing a simple framework for

information exchange keeping in mind the disparate time scales involved. By modeling the TP53 mediated signaling modules using a discrete network model we refine its predictions by running a continuum ordinary differential equations (ODE) based model of the ErbB receptor mediated signaling and passing information across the identified interfaces in both directions. In order to consider the effect of molecular profiling data from clinical subjects, in this work, we have also incorporated the miRNA expression data for various patients to re-normalize the initial expression levels of corresponding mRNAs to a given patient. This makes our model predictions patient-specific. In doing so, however, we have also taken into account the heterogeneity of the microenvironment and have adopted an ensemble of models approach by averaging over multiple conditions of receptor expression, growth factor availability, and nature of the memory coupling signaling and transcriptional modules. This modeling framework has been successfully applied to lung cancer and nephroblastoma demonstrators where the model predictions in the form of a Cell Kill Rate (CKR) has been used as an input to phenomenological tumour growth models.

2.2 Model Description

A detailed description of model formulation can be found in D6.3. The model is composed of two main signaling modules – ErbB receptor mediated Ras-MAPK and PI3K/AKT signaling module and TP53 mediated DNA damage response module. The main features of model are summarized below:

Input

1. Patient microRNA from tissue or serum; oncogene mutation
2. Treatment conditions- Radiation: dose and regimen

Model

1. Tumour microenvironment- growth factor level, temporal growth factor availability, receptor expression, heterogeneity of the tumour microenvironment
2. Integration of cell cycle, DNA damage response, mitogenic and survival signals, drugs

Output

Patient-specific cell kill probability, cell growth probability, and cell senescence probability in the presence and absence of specific drug/combinations, radiation treatment

2.3 Results

A) Application of the model to lung cancer demonstration

We have completed the implementation of the molecular model for lung cancer. In addition to the example above, the molecular modelling of the EGFR mutants has yielded the construction of networks specific to mutants, which encode dynamics and logic that are different from the wildtype. These, results have been combined with the Boolean model to yield a comprehensive molecular model for lung cancer. The model takes input from a patient-specific miRNA profile and renormalizes the nodes of the network. In addition, the model incorporates the sequencing information by considering the mutational status of EGFR, KRAS, BRAF, and AML/ALK in order to produce a customized network to match the patient's molecular profiles. We have further implemented the effect of radiation dosage in the model through the linear-quadratic model (LQ) for radiation treatment. In brief, the linear-coefficient is used to constrain the node that regulates the p53 activation is a radiation dose and regimen dependent fashion. The cell kill probability output by the model is then a function of the radiation exposure as well as the miRNA-mediated signalling. This property is then returned to the multi-modeler (described later in Fig. 11) for further processing of the clinical outcome.

The above general framework was adapted to the lung cancer demonstrator. For this case the selected patient underwent a treatment regimen as described in Fig. 7. As indicated, only the radiation treatment was considered for the review.

Imaging and treatment data overview:			Observations
The radiation treatment (with 4 fractions in total) has been considered for the review	Dicom	1/5/1951	TUMOUR EVIDENT, SURGERY AND COMPLETE REMISSION
	Dicom	6/12/51	
	Dicom	5/2/53	
	Surgery	4/3/1953	FIRST RECURRENCE
	Dicom	30/10/1953	TUMOUR NOT EVIDENT
	Chemo 1 st session start	15/1/1954	
	Chemo 4 th session end	26/3/1954	
	Dicom	25/5/1956	TUMOUR EVIDENT
	Dicom	31/8/1956	TUMOUR PROGRESSION
	Radiation start	6/9/1956	
	Radiation end	15/9/1956	
	Dicom	17/9/1957	NO TUMOR, RADIATION NECROSIS

Fig. 7: Summary of treatment regimen for a lung cancer patient selected from the CHIC data repository.

Radiation dosage introduces DNA single and double strand breaks which activates the p53 mediated DNA repair and apoptotic pathways. The effect of radiation dosage on cell kill is modeled almost universally using the phenomenological Linear-Quadratic model [7] which gives the fraction of

surviving cell as a function of radiation dosage (Gy) as below where D is the radiation dosage in Gy and α , β are empirical constants which correspond to dose dependent and independent parts of radiation response. G is the generalized Lea-Catcheside time factor.

$$S = \exp(-\alpha D + \beta G D^2)$$

We chose to replace the empirical constants α and β by using information obtained from our detailed mechanistic model. However due to the discrete nature of our p53 mediated DNA damage model, we are only able to account for the dose independent part (the linear term involving α). Future version will aim to account for the dose dependent part as well which requires a more detailed model which takes into account the various double strand DNA repair mechanisms. We activate the ATM kinase levels according to a probability $\exp(-\alpha * D)$ to obtain the cell survival. This survival is modified by the quadratic term involving β which is obtained from the literature. The overall scheme is shown below in Fig. 8.

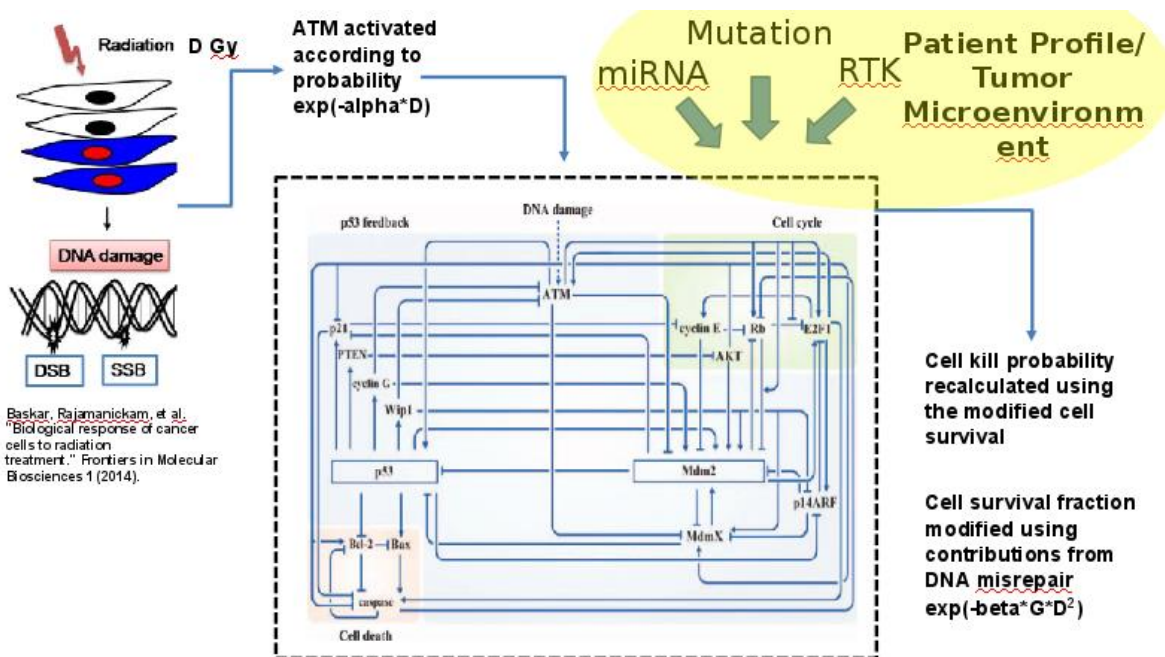


Fig 8: Overall scheme for the lung cancer hypomodel. The input to the model consists of the usual miRNA and mutation data for the specific patient. Also we activate the DNA damage by calculating a probability based on the radiation dosage D (Gy-1). The cell survival fraction obtained from the model is modified using the empirically calculated quadratic term of the LQ model.

The specific radiation dosage data and values of the empirical constants are as given below in Table 2:

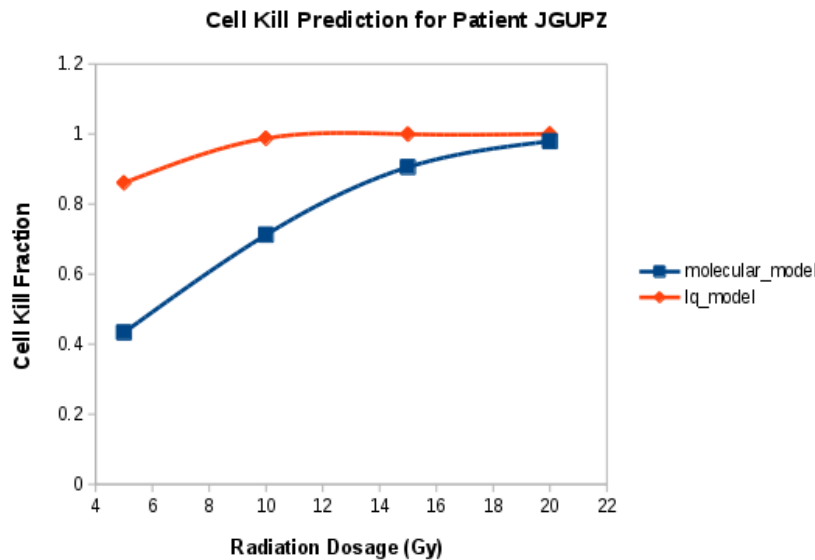
Table 2: LQ Model Parameters

LQ Model Parameters	
alpha (Gy ⁻¹)	0.35
beta (Gy ⁻²)	0.035
Pat JGUP5Z Radiation Dosage	
No. of fractions (n)	4
G (approx)	0.25
Total Dosage D (Gy)	20

B) Predicted Cell Kill Rate for demo patient for the lung cancer scenario

The model as adapted above was run using the available miRNA data and radiation dosage information to obtain cell kill fraction for different radiation dosages. The predicted cell kill rate from the molecular model was compared with that obtained from the empirical LQ model. We observe that the predicted cell kill rates converge at higher radiation dosages but molecular model prediction are lower compared to the LQ model at lower dosage fractions. The results obtained from the molecular model are averages over various growth factor and time scale considerations. The individual results and their distribution are also shown in Fig. 9.

A,



B.

Rad (Gy)	Mean Modified with DNA repair factor Modified Cell Kill Rate
5	0.433229728
10	0.712166676
15	0.905250224
20	0.979059557

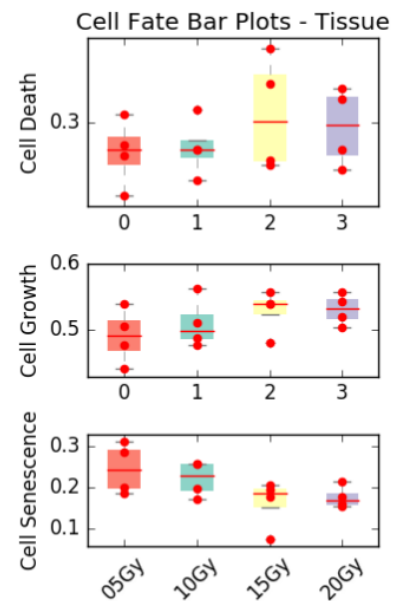


Fig 9: Main results of the lung cancer hypomodel. A – Cell kill fraction averaged over various growth factor concentration and cell cycle times as obtained from molecular model compared with the results obtained from the LQ model; B – Boxplots showing the distribution of the individual cases for different radiation dosages.

2.4 Conclusions and future work

The present work we describe an integrated cellular framework to model key cell signaling pathways operating at different time scales – a well-recognized challenge in the field. Here we model the ErbB receptor mediated Ras-MAPK and PI3K/AKT pathway and integrate it with p53 mediated DNA damage response pathway to obtain a cell kill rate under specific drug dosing and patient specific miRNA expression levels. The obtained cell kill rate was directly used as an input to phenomenological tumour growth models. The aim of such integrated molecular model is to provide a mechanistic foundation to the more empirical models used in the field to obtain cell kill and growth rates under particular dosage conditions. The integration of the models was accomplished by identifying model interfaces and passing information between runs of the two models. This framework has been tested for the lung cancer scenarios and the future work will be focused on performing a detailed sensitivity analysis to simulate the inherent tumour heterogeneity and also the effect of various mutations and subject the framework to clinical validation.

2.5 References

1. Chen, W. W., Schoeberl, B., Jasper, P. J., Niepel, M., Nielsen, U. B., Lauffenburger, D. a, & Sorger, P. K. (2009). Input-output behaviour of ErbB signaling pathways as revealed by a mass action model trained against dynamic data. *Molecular Systems Biology*, 5(239), 239.
2. Choi, M., Shi, J., Jung, S. H., Chen, X., & Cho, K.-H. (2012). Attractor landscape analysis reveals feedback loops in the p53 network that control the cellular response to DNA damage. *Science Signaling*, 5(251), ra83.
3. Cuadrado, A., & Nebreda, A. R. (2010). Mechanisms and functions of p38 MAPK signalling. *The Biochemical Journal*, 429(3), 403–417
4. Gottlieb, T. M., Leal, J. F. M., Seger, R., Taya, Y., & Oren, M. (2002). Cross-talk between Akt, p53 and Mdm2: possible implications for the regulation of apoptosis. *Oncogene*, 21(8), 1299–1303.
5. Chou, C. H., Chang, N. W., Shrestha, S., Hsu, S. D., Lin, Y. L., Lee, W. H., Tsai, T. R. (2016). miRTarBase 2016: updates to the experimentally validated miRNA-target interactions database. *Nucleic acids research*, 44(D1), D239–D247
6. Ludwig, N., Nourkami-Tutdibi, N., Backes, C., Lenhof, H.-P., Graf, N., Keller, A., ... Background. (1996). Circulating Serum miRNAs as Potential Biomarkers for Nephroblastoma. *Journal of Clinical Oncology*, 14(5), 1526–1531.
7. Brenner, D. J. (2008). The Linear-Quadratic Model Is an Appropriate Methodology for Determining Isoeffective Doses at Large Doses Per Fraction. *Seminars in Radiation Oncology*, 18(4), 234–239

3.The Metabolic Hypomodel for Lung Cancer

3.1 Non-Small Cell Lung Cancer (NSCLC)

The metabolic hypomodel for lung cancer has been developed by FORTH. NSCLC is a leading cause of cancer mortality worldwide (> 900000 deaths/year). NSCLC is a highly glycolytic lung cancer accounting for more than 85% of all lung cancers. Two major NSCLC subtypes have been reported: adenocarcinoma (LADC) and squamous cell carcinoma (LSCC). It has been shown that aerobic glycolysis in NSCLC is promoted through oncogenic mutations in two critical proteins, K-RAS and EGFR [1, 2]. Ras-driven cancer cells display increased glucose uptake and aerobic glycolysis that support both nucleotide biosynthesis and protein glycosylation for growth signaling. However, it should be noted that high heterogeneity in metabolism proteome has been observed i) compared to normal lung tissue, ii) between lung subtypes and iii) between primary and metastatic lung cancer. Recently, an extensive omics analysis [1] integrating DNA, RNA and proteomics data from normal lung, patient primary tumours and primary tumour-derived xenograft tumours revealed sets of proteins that are consistently up- or downregulated across tumours, recapitulated in xenograft tumours and their associated genes map into regions of focal amplification or deletion respectively. This DNA->RNA->protein association indicates a response to selective pressure driving cancer phenotype. As shown in Table I, from the reported metabolism proteome clusters in [1], we used specific clusters of proteins consistently upregulated in LADC (cluster index: C15) and LSCC (cluster index: C10) to constrain the corresponding metabolic fluxes of the genome-scale metabolic network. It is also important to mention that individual proteome clusters have been correlated with overall survival in cancers other than NSCLC. Interestingly, for some clusters, the patient's outcome –better or worse- did not coincide among the different cancer types. For example, cluster C10 was associated with better outcome in lung SCC, but with worse outcome in head and neck SCC, indicating that the whole proteome signature associated with a specific cancer type and not individual clusters is important for predicting a patient's outcome.

Table I. Specific metabolism proteome clusters upregulated in lung cancer as reported in [1]

Cluster ID	Cluster proteins (gene names)	Excluded from model
C10	ADSS, ATP2A2, CTPS1, IMPDH2, PKM2, PTGES3, SGPL1	SGPL1
C15	NAT10, NME2, OAT, PPAT, SHMT2, GART, PAICS, SRM, UMPS, QARS, ABCE1, ABCF2, ACOT7	OAT, SHMT2

We extend the work of Shlomi et al. [3] and apply a metabolic strategy that allows near optimal growth solution, while maximizing lactate secretion in order to describe the high-flux mechanisms that lead to a substantial increase of lactate production in tumour cells [4]. Variability around optimal growth is expected in biological systems including cancer. The method allows i) the study of genotype-phenotype relations, ii) the investigation of the metabolic rerouting that takes place within

the cell and iii) the exploration of the metabolic capabilities of tumour cells under specific constraints and objectives.

Protein/Enzyme levels bound the fluxes of the corresponding metabolic reactions. In the absence of quantitative information, metabolic reactions catalyzed by up-regulated metabolic proteins/enzymes, are constrained to carry non-zero fluxes via a lower bound, which is set equal to 0.1 $\mu\text{mol}/\text{mgDW}/\text{h}$. Different bounds have also been tested. The two clusters of metabolic proteins thus constrain differently the metabolic network, producing phenotypes with different metabolic capabilities.

In consistence with the metabolic properties of the glycolytic phenotype, a decline in growth yield (growth rate divided by glucose flux) is observed (Fig. 1a) at high growth rates, while increased glucose uptake rates (Fig. 1b) result in steep increases in lactate production in both the generic and constrained metabolic models. Furthermore, the simulations show that in all the different phenotypes studied, small deviations around the optimal growth rate of the order of 90-99% were sufficient for adequate lactate production but can drop significantly when glucose is limited (Fig. 1c). It should be noted that the C15 phenotype is incapable of producing optimal metabolic capabilities at glucose uptake rates less than 0.2 $\mu\text{mol}/\text{mgDW}/\text{h}$ (Fig. 1c). By definition, the optimal growth rate of any model derived from the generic one through the application of additional constraints cannot be higher than that obtained from the generic model.

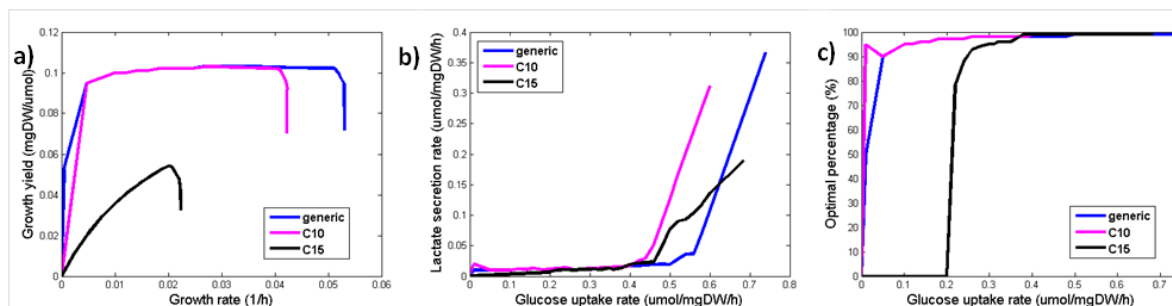


Figure 1. Predictions of the metabolic capabilities of the generic (blue), C10 (magenta) and C15 (black) cancer phenotypes under the lactate optimization strategy for specific flux bounds in the corresponding reactions.

3.2 Integration of cancer metabolic hypomodel with vasculature and tumour evolution components

As tumour grows well-vascularized regions providing sufficient nutrients to cancer cells can coexist with nutrient-limited regions within the tumour mass. In this work, glucose is assumed to be the only limiting resource, although oxygen can also be incorporated as well as glutamine. As described in many studies [5, 6], the dependence of glucose uptake on glucose concentration, C , can be modeled using Michaelis-Menten kinetics as can be seen in (1). In (1), C corresponds to the glucose concentration, V_{max} corresponds to the maximum rate of the process, which depends on many factors including the concentration of GLUT receptors and K_m is the saturation constant representing the concentration of glucose at which the uptake rate equals to $V_{max}/2$. In that manner, glucose availability places an upper bound in glucose uptake rate. Considering that Michaelis-Menten equation asymptotically approaches the maximum rate as glucose concentration increases, we also assume that V_{bound} reaches V_{max} when the glucose concentration C takes the maximum value C_{max} that is observed in tissues ($C_{max} = 0.9 \text{ kg m}^{-3}$).

$$v_{bound} = v_{max} \frac{C}{K_m + C} \quad (1)$$

A relatively slow varying environment is assumed where cancer cells can operate at optimal or near optimal growth rates constrained by the current nutrient availability. As illustrated in Figure 1, at each time interval, the glucose concentration is estimated at every position in the computational grid. The spatiotemporal-dependent inflow of glucose flux is constrained by the Michaelis-Menten kinetics model and an instantaneous optimization problem is solved for each cell position and time point. During that time interval, the fluxes of the metabolic model are assumed constant. The metabolic model provides information regarding the uptake fluxes (e.g. glucose), intake fluxes (e.g. lactate) and proliferation rate given the available glucose that is then used from the tumour evolution hypomodel to update its state. For computational efficacy, the cellular metabolic capabilities have been pre-calculated for the different glucose concentrations and a lookup table has been used instead of repeatedly solving the optimization problem at each position and time interval.

Given the current available glucose concentration, which is assumed constant within each time interval, the metabolic model provides information regarding the uptake flux of glucose, the intake flux of lactate as well as the proliferation time ($\ln(2)/\text{growth rate}$) to the components of the tumour growth model in order to implement their next iteration. Fig. 2 summarizes the predicted linking variables between the sub-cellular metabolic model and the supercellular tumour growth model. Although the glucose uptake rates (Fig. 2c) are very similar among the different phenotypes, their proliferation time (Fig. 2a) as well as the lactate production (Fig. 2b) are substantially different for the different concentrations of glucose.

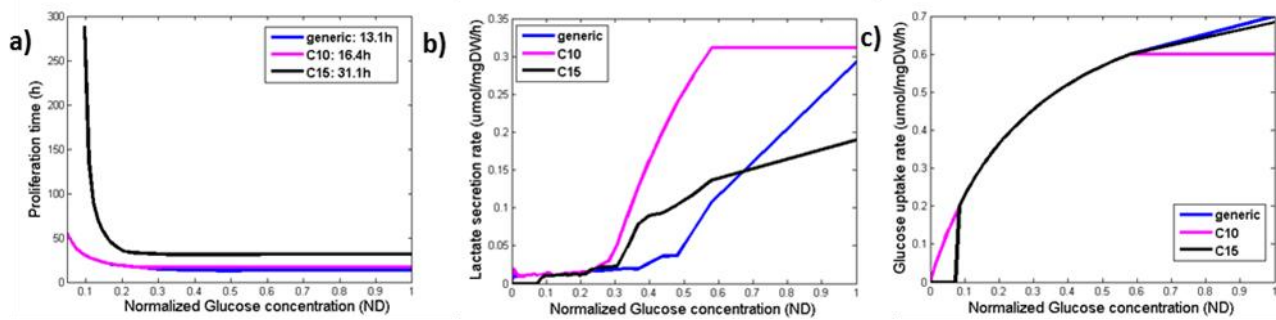


Figure 2. Predicted linking variables between the metabolic model and the HDC tumour growth model for specific flux bounds in the corresponding reactions.

3.3 References

1. Li, L., et al., Integrated omic analysis of lung cancer reveals metabolism proteome signatures with prognostic impact. *Nat Commun*, 2014. 5: p. 5469.
2. Davidson, S.M., et al., Environment Impacts the Metabolic Dependencies of Ras-Driven Non-Small Cell Lung Cancer. *Cell Metab*, 2016. 23(3): p. 517-28.
3. Shlomi, T., et al., Genome-scale metabolic modeling elucidates the role of proliferative adaptation in causing the warburg effect. *PLoS Comput Biol*, 2011. 7(3).
4. Tzamali, E., V. Sakalis, and K. Marias, The effects of near optimal growth solutions in genome-scale human cancer metabolic model, in *Bioinformatics & Bioengineering (BIBE), 2012 IEEE 12th International Conference 2012*: Larnaca, Cyprus.
5. Cheng, G., P. Markenscoff, and K. Zygorakis, A 3D hybrid model for tissue growth: the interplay between cell population and mass transport dynamics. *Biophys J*, 2009. 97(2): p. 401-14.
6. Chignola, R. and E. Milotti, A phenomenological approach to the simulation of metabolism and proliferation dynamics of large tumour cell populations. *Phys Biol*, 2005. 2(1): p. 8-22.

4. The Biomechanical Hypomodel for Nephroblastoma and Non Small Cell Lung Cancer

4.1 Tumour Position and Shape

The Biomechanical Hypomodel has been developed by UBERN. Evolution of position and shape of the growing tumour results from the interaction of multiple processes and are influenced by chemical gradients, due to local differences in the availability of nutrients [Pescarmona et al.], and physical constraints. Additionally, tumour position may be affected by morphological changes, such as weight loss or tissue scarring.

While the influence of chemical gradients and nutrients is not taken into account by the CHIC hypermodel, physical constraints and resulting forces are represented through the biomechanical component model (BMS). Evolution of tumour shape and location in the present hypermodel is governed by the interaction between the OncoSimulator (OS) and BMS hypomodels.

BMS computes a field of 'least-pressure' directions based on the stresses arising from local variations in tumour cell concentration. OS uses this information to inform the movement of tumour cells within the boundaries of the simulation domain. The communication between BMS and OS thus involves the exchange of scalar and vector fields that describe those parameters throughout the respective 3D domain of each simulator component.

Given the complexity of the problem, prediction of tumour shape and position is an explorational feature of the mechanistic CHIC hypermodels, with the primary goal to investigate mechanisms and feasibility of coupling tightly interacting models within the CHIC hypermodeling framework. Over the course of Task 6.4, the conceptual and practical challenges involved in coupling the Biomechanical and Onco-Simulator were investigated, their interaction improved and the ability of the entire hypermodel to predict tumour shape and position after therapy was evaluated. Accurate prediction of tumour shape and position, however, is not essential for answering the clinical questions pertinent to the Lung and Nephroblastoma scenarios.

4.2 Assessing Evolution of Tumour Shape and Position

4.2.1 Methods

A metric was defined for comparing tumour position between the available imaging time points and throughout the simulated tumour evolution, Fig. 1. First, medical images at both time points were registered using a rigid registration procedure in order to establish a common spatial reference frame. Then, the center-of-mass position was computed for both images (t_1 , t_2), as well as for the simulated tumour at every simulation timestep $t_{s,i}$ ($t_1 < t_{s,i} < t_2$). We used the distance between

tumour center-of-mass positions at time points $t_{s,i}$ during the simulation and the final imaging time point t_2 as metric for the spatial agreement between simulation and reality.

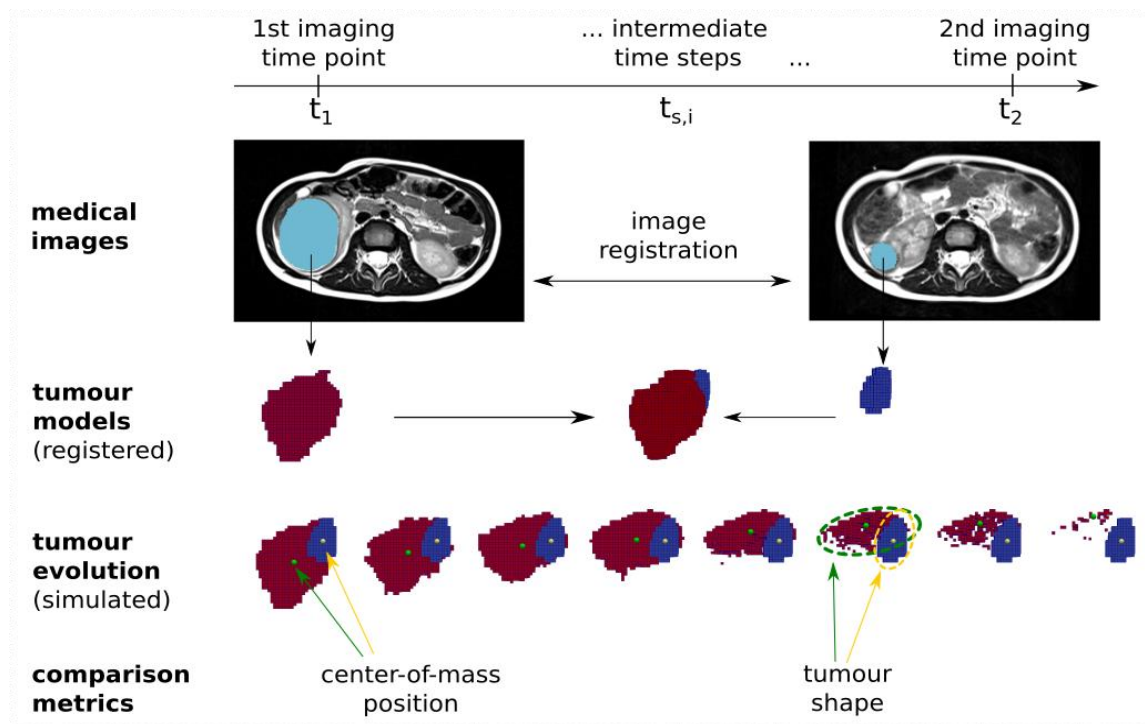


Figure 2: Assessment of simulated tumour shape and position.

4.2.2 Results

This assessment strategy was applied to results of the Nephroblastoma and Lung Cancer hypermodels. Fig. 2 illustrates 3D shape and position of the simulated tumour in comparison to the

actually observed tumour. During the simulation period, tumour volume increases in the Lung scenario and decreases in the Nephroblastoma scenario.

Lung

The simulated growing tumour in the lung scenario maintains a compact shape, in agreement with observation. Its simulated and observed position at the second imaging time point are approximately 2 cm apart.

Nephroblastoma

Evolution of simulated tumour position with respect to the observed position differs between the two selected Nephroblastoma cases. While the COM distance remains in the range about 2 cm for Wilms patient '5X', it increases to up to 4-5 cm for Wilms patient '6Z'. Visual comparison of tumour shape shows that the simulated tumour does not shrink isotropically to a compact bulk tumour with smaller radius as expected from the segmentations of the second imaging time points. Instead, the tumours appear to dissolve from one side, forming a porous and partially disconnected structure, compare Fig 2.

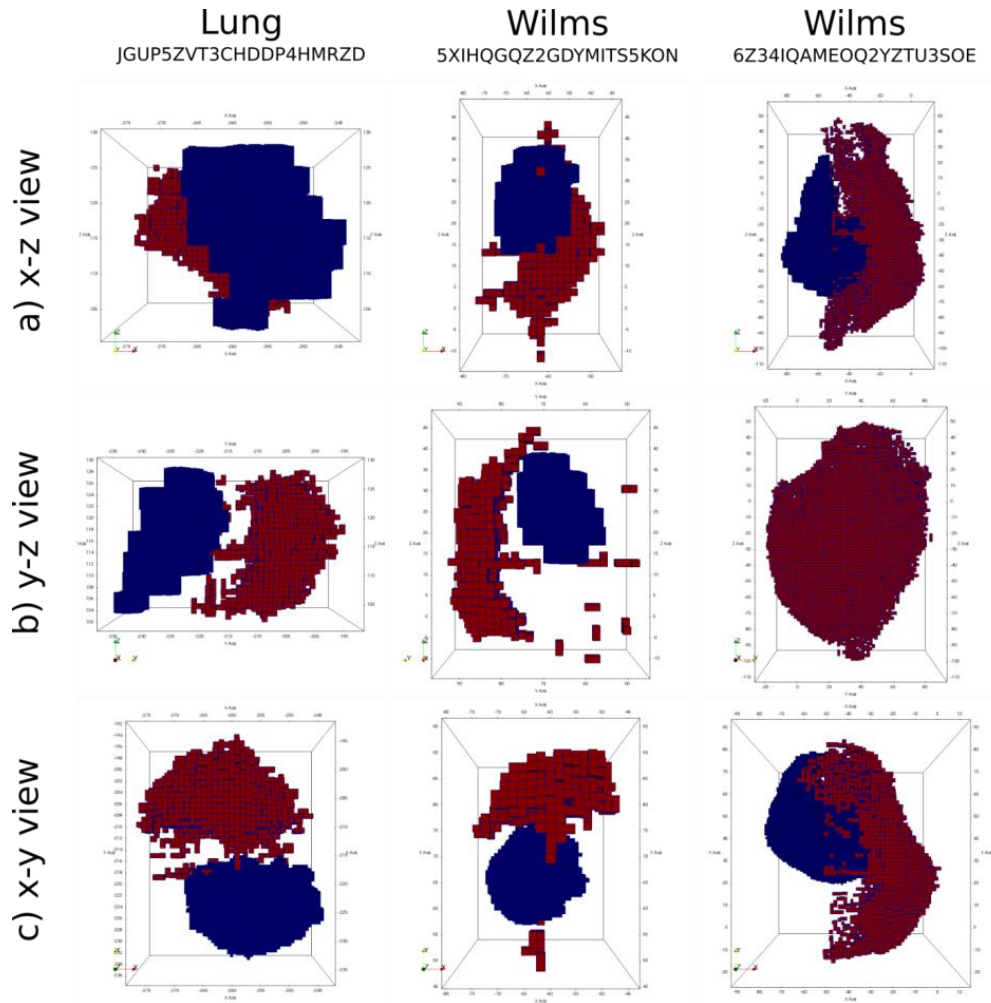


Figure 2: Visual comparison of shape and position between simulated (red) and observed (blue) tumours at the respective second imaging time point. During the simulation period, the tumour volume increases in the Lung scenario (day 1-98, before start of radiation) and decreases in the Nephroblastoma scenario (patient 5X: day 1-35, patient 6Z: day 1-41).

4.3 Discussion & Conclusion

The hypermodel is found to reproduce realistic tumour shapes in growth scenarios (Lung scenario-progression of recurrent NSCLC), whereas shrinkage scenarios (Nephroblastoma) tend to result in tumour shapes that have a more ‘diffuse’ appearance than those observed. The hypermodel achieves a good prediction of tumour position in selected cases. However, systematic evaluation suggests that reliable prediction of tumour shape and position in Nephroblastoma and Lung cancer with the developed approach and the available information is not yet possible. This finding underlines the challenges involved in coupling the discrete OS and continuum-mechanics based BMS hypomodels. The following paragraphs discuss the most important model and evaluation limitations that may explain the observed discrepancies. Addressing those challenges will be subject of future research.

Hypermodel

Clearly, any models’ ability to approximate reality is limited by the information available for model building and configuration. Most critical for BMS is the uncertainty in mechanical tissue parameters (not patient-specific) and the lack of well-defined boundary conditions for mechanical computations that are particularly difficult to establish for the Nephroblastoma and Wilms scenarios.

In order to test the ability of a biomechanical model to reproduce tumour shape and position in a scenario with better defined mechanical boundary conditions, a mechanically-coupled tumour growth and normal tissue invasion model for brain cancer has been introduced in Deliverable 6.3. Initial studies with this model emphasized the importance of anisotropy in tissue properties and showed that consideration of bio-mechanical aspects alone may not be sufficient to reproduce the variety of observed tumour shapes, compare Fig. 3.

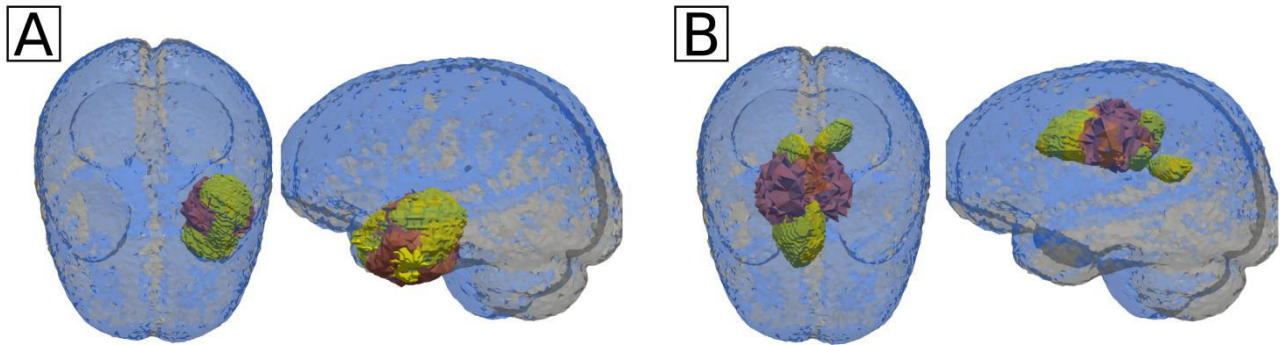


Figure 3: Comparison of simulated (red) to observed tumour shapes (yellow) for selected glioma cases based on the mechanically-coupled reaction diffusion model introduced in Deliverable 6.3. Good agreement is observed for regularly structured shapes (A), whereas highly irregular shapes are not reproduced in simulations (B). [Abler & P. Büchler, 2016]

Morphological changes in the healthy tissue also influence tumour evolution. This aspect is not taken into account by the present hypermodel.

Evaluation Approach

The proposed evaluation approach relies on image registration techniques to compare simulation results to imaging data at a later time point. This process introduces an uncertainty in the relative positioning of the tumours. To reduce the importance of this uncertainty in future studies, the use of fixed anatomical markers as reference within the respective imaging frame could be investigated.

The center-of-mass position of simulated and observed tumour is used in the present analysis as reference for its average position in space. This approach works well to characterize the position of compact tumours, however, for dispersed tumour shapes, such as those simulated in shrinkage scenarios, the COM position may no longer be fully enclosed by the active tumour.

Hypomodels and Hypomodel-Coupling

The complexity of the coupling between OS and BMS may also provide partial explanation for the observed hypermodel behaviour. In particular, mapping of the pressure (direction of least-pressure) field computed by BMS into the discrete model of OS is challenging, as is the update of BMS with OS cell concentration values. Accuracy in both steps is affected by interpolation. Both simulators have been improved in close collaboration between ICCS and UNIBE to best reflect the underlying physical and biological processes. A remaining limitation of model interaction is linked to difficulties in synchronizing the spatial evolution of tumour cell distribution in both hypo-models. The focus of

future work will be focused on this aspect of the coupling between biomechanical and biological simulation components.

4.2 References

G. P. Pescarmona, M. Scalerandi, P. P. Delsanto, C. A. Condat, Non-linear model of cancer growth and metastasis: a limiting nutrient as a major determinant of tumour shape and diffusion, <https://www.ncbi.nlm.nih.gov/pubmed/10687891>

D. Abler, P. Büchler, Evaluation of a mechanically-coupled reaction-diffusion model for macroscopic brain tumour growth, In Book of Abstracts CMBBE 2016, due to be published in 'Lecture Notes in Bioengineering' ISSN: 2195-271X

5. The Lung Cancer Oncosimulator Hypomodel and the Lung Cancer Hypermodel: Adaptation and Partial validation

5.1 Introduction

The Lung Cancer Oncosimulator, developed by ICCS-NTUA, that explicitly models cancer cell multiplication, cellular response to treatment and spatial expansion based on the notion of cellular automaton lies in the heart of the Lung multimodeller hypermodel. The Lung Oncosimulator, stemming from the *In Silico* Oncology and *In Silico* Medicine Group (ICCS- National Technical University of Athens) [Stamatakis et al. 2010, Kolokotroni et al. 2011], considers both radiotherapy and cisplatin-based doublet therapy. The Oncosimulator addresses clinical tumours, well beyond their initiation phase, and has been designed to incorporate patient specific data such as imaging-based, histopathological, molecular and treatment data.

The Oncosimulator is available as a standalone application or as a MUSCLE-enabled hypomodel. The MUSCLE-enabled version of the Oncosimulator explicitly addresses radiotherapy and cisplatin–vinorelbine doublet therapy. However, it can be easily adapted to other types of cisplatin-based doublet therapy.

A detailed presentation of Oncosimulator' s basic notions and algorithmic design, as well as a parametric investigation of its behaviour and an initial adaptation to Lung Cancer case are presented in deliverables D6.2 and D6.3. From the basic science perspective, the last year of the project was devoted to the resolution of new issues that have emerged, mainly related to the coupling of the Oncosimulator and the Biomechanics simulator. More specifically, Reconstruction algorithms, responsible for the spatial expansion and shrinkage of the tumour have been critically revised so that:

- tumour expansion and shrinkage is complaint to the overall pressure field of the surrounding tissues
- geometrical cells with artificially low number of biological cells are not created within the tumour. Such cells would create non-realistic pressure fields within the tumour and would affect the computations of BMS

Furthermore, cell kinetic model and the functions responsible for the movement of biological cells between geometrical cells have been critically revised so as to eliminate time synchronization of geometrical cells that leads to artificial periodic oscillations of tumour's cells populations and volume. Such oscillations appeared for specific value combinations of model parameters with the old reconstruction algorithms and were considerably magnified, in some cases, with the new algorithms. Finally, an extensive adaptation and partial validation work has been performed considering the following three clinical scenarios:

- Clinical Scenario A: Neoadjuvant Chemotherapy for Resectable Non–Small-Cell Lung Cancer
- Clinical Scenario B: Recurrence of Non–Small-Cell Lung Cancer
- Case scenario C: Progression and response to treatment of recurrent Non–Small-Cell Lung Cancer

The adaptation work addresses both the Lung Oncosimulator as a stand-alone application and as part of the Lung Hypermodel, depending on available data and clinical scenario.

5.2 Modified reconstruction algorithms

Adequately shaped morphological rules have been introduced (Stamtakos *et al.* 2010, D6.2) which may lead to tumour expansion, as is the case in free tumour growth, no change in tumour volume or tumour shrinkage as is usually the case after treatment administration. The adopted morphological rules [Dionysiou *et al.*, 2006] aim at simulating tumour expansion or shrinkage, while preserving a roughly uniform cell density throughout the tumour volume.

More specifically, let Number of Biological Cells (NBC) be the mean number of biological cells residing at a geometrical cell (GC) (i.e. voxel) of the mesh. At any given time point the total cell population that can be accommodated in each GC is allowed to fluctuate 10% around this mean value NBC.

Case A: If the total population exceeds the maximum value of $1.1 \cdot NBC$ then a procedure is initiated that attempts to unload the total GC population minus NBC to neighboring GCs (26 GC

neighborhood is considered) possessing empty space i.e. GCs with total cell population less than NBC. The procedure starts from the neighboring GC possessing the maximum free space. If two or more neighboring GCs possess the same free space then a random number generator is used so as to select the visiting order of the GCs. The procedure is repeated until all the excess cells have been transferred, provided this is possible. If the procedure fails to reduce the total population of the GC under consideration below the upper limit (maximum value) then an adjacent GC is freed from its contents which are moved outwards. The latter push the contents of a chain of geometrical cells outwards too. The excess contents of the GC under consideration are placed into the newly freed adjacent GC. The previous process leads to differential tumour expansion. The position of the GC to be freed from its contents relative to the GC with the excess contents is determined using a random number generator in the stand alone application or based on biomechanics simulator (BMS) input in the case of Lung Hypermodel. The shifting of the chain of GCs mentioned above can take place along the previously specified direction.

Case B: On the other hand if the GC's total cell population is below the minimum value then a similar procedure attempts to unload all cells to neighboring GCs possessing free space. If the GC becomes empty then a chain of GC contents is shifted towards the GC under consideration so as to fill the vacuum generated. The latter leads to differential tumour shrinkage. Shifting of the GC content chain takes place as follows. In the case of the standalone version of the OS, six lines of random direction are chosen based on a random number generator. The outermost non-empty GC along each one of these directions is detected and its "6-Neighbor" GCs belonging to the Tumour (NGCT) are counted. The direction corresponding to the maximum NGCT is selected. In the case of Lung Hypermodel the direction of GC 'shifting' is determined by the Biomechanics hypomodel.

The above procedures, however, may give rise to the following "side effects":

- **Case A:** If the total available space of the neighboring GCs is not adequate, the GC under consideration will not become empty and will be left partially filled with a low number of biological cells.
- **Case B:** A new GC emerges next to the GC under consideration which is filled with the excess contents of the GC under consideration. The excess content is always well below NBC and the new GC will be partially filled.

Summarizing, both previously described procedures result in the appearance of GCs with artificially low number of biological cells, and hence, areas with artificially low cell density within the tumour appear (Fig 1). In order to avoid the above occurrence, the reconstruction algorithms have been modified as following:

- **Case A:** An 'inward' shift of biological cells, along a chain of GCs occurs. As a result the GC under consideration is filled and a partially-filled GC appears

now at the boundary of the tumour. The direction along which the shift of biological cells occurs is determined as previously described.

- **Case B:** An 'outward' shift of the excess content occurs along a chain of GCs. As a result the new GC appears at the boundary of the tumour. The direction along which the shift of biological cells occurs is determined as previously described.

As illustrated in Fig I, a more uniform density is preserved throughout tumour bulk, with the modified reconstruction algorithms. The partially filled GCs appear at the boundary of the tumour. These GCs are occupied by both the tumour and the surrounding normal tissue.

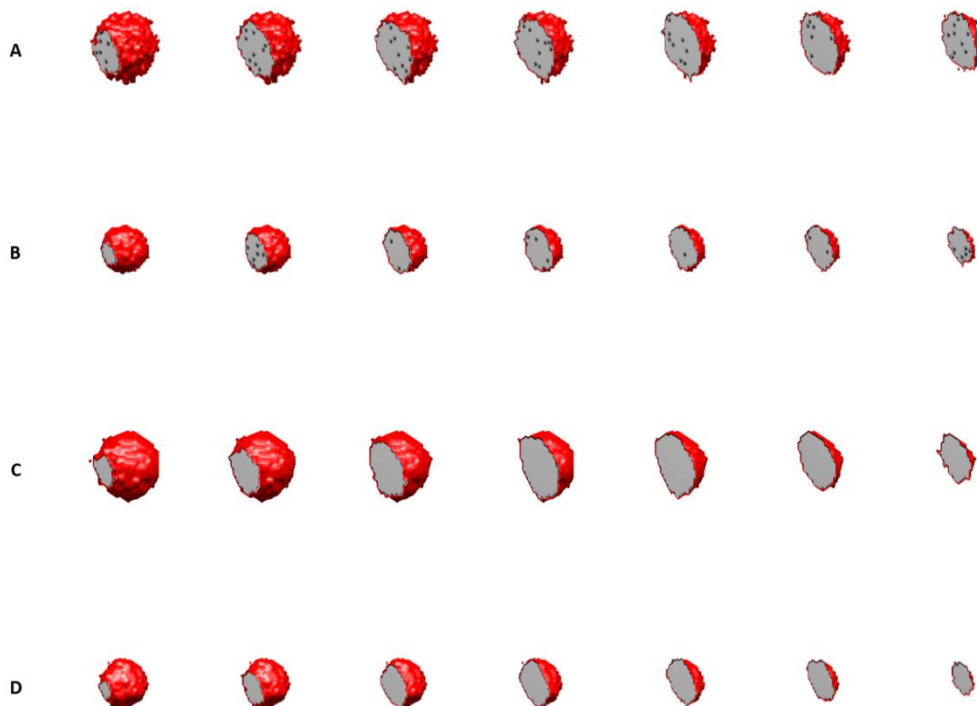


Fig I. Successive cutting planes of the virtual tumour at simulation day 30. Light gray denotes the GCs with population $\pm 10\%$ around the literature-based mean cell population. Dark gray denotes the GCs with population

below 90% of the literature-based mean cell population. A. Initial reconstruction algorithms - Free tumour growth simulation B. Initial reconstruction algorithms - Treatment response simulation C. New reconstruction algorithms - Free tumour growth simulation D. New reconstruction algorithms - Treatment response simulation. A homogeneous spherical tumour of 20mm diameter is considered. In the case of treatment response simulation, a cell cycle specific drug is administered on days 7, 14 and 28.

5.3 Elimination of GC synchronization

The proliferating cells (either stem or LIMP) residing within each GC are distributed into four subclasses corresponding to the four phases of cell cycle, i.e. G1, S, G2, M. For any given instant the biological cells belonging to the same cell cycle phase within a given GC are assumed synchronized. However, biological cells belonging to different GCs or to different categories and cell cycle phases within the same GC are not assumed synchronized. From the computational standpoint this is achieved by the use of a sufficient number of registers that are used to describe the state of proliferating cells in each GC occupied by the tumour. They include the number of biological cells residing in each phase and the time spent at each phase. A periodic oscillating pattern may be observed in the time course of the various tumour cell populations when the time registers of different GCs become similar, i.e. the different GCs tend to get synchronized. This characteristic pattern is significant for specific value combinations of model parameters with the initial reconstruction algorithms and may get considerably magnified with the new ones (Fig 2). The synchronization of different GCs is caused mainly by the movement of biological cells between GCs and secondary by the movement of biological cells between the various phases within a GC. More specifically:

- **Movement between GCs:** When an occupied GC receives a population of cells from a neighbor GC then its state, in each proliferating cell class/phase, is updated based on the population average time of the 'old' and 'new' populations.
- **Movement within a GC:** If the time that the biological cells have spent in the corresponding phase has become equal to the phase duration, then the cells enter the next phase. The time register of the 'next' phase is updated based on the population average time of the newly-arrived and the already residing populations.

Taking into consideration that the above movements take place thousands of times during a simulation, the continuous update of the time registers in each GC with mean values eventually lead to the synchronization of the different GCs.

In order to avoid time synchronization of the different GCs, the cell kinetic model and the functions responsible for the movement of biological cells between geometrical cells have been critically revised as described below:

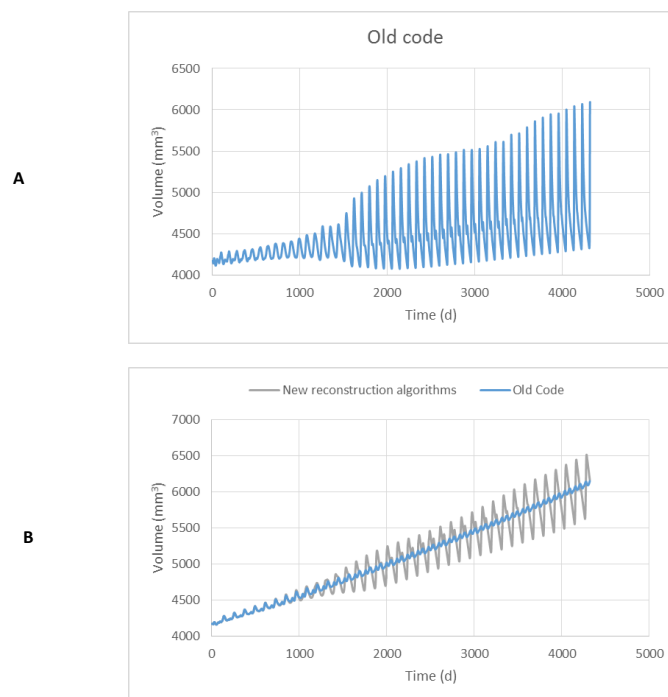
Cell kinetic model

Active cell cycle phase is not divided into four subclasses corresponding to each cell cycle phase (G1, S, G2, M), but is considered as one class, denoted in Fig 3 as the proliferating class. The user can define the number n of proliferation and G0 classes in each GC. Parametric investigation has revealed the same ‘quality’ of results with increasing n . A value $n=1$ is adopted for the needs of CHIC to minimize computational costs.

Movement of biological cells between GCs

When an occupied GC receives a population of cells from a neighbor GC then, in each proliferating cell class/phase, the time that the cells have spent takes the time of either the ‘old’ or ‘new’ population by using a random number generator. The probability of each time to be chosen is analogous to the size of the corresponding population.

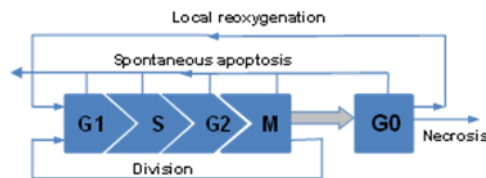
With the above modifications the computation of average times when cells enter the next phase are now avoided. A comparison of the initial and new algorithms is depicted in Fig 4 for a slow and moderate growing tumour. The periodic oscillation pattern is absent from the results given by the new algorithms.



ADAPTATION OF PARAMETER VALUES AND RESULTING CANCER CHARACTERISTICS		
Parameter	A	B
Cell cycle duration	90 h	120 h
Duration of dormant phase	311 h	769 h
Time needed for necrosis products to disappear	79 h	140 h
Time needed for apoptosis products to be removed	7 h	6 h
Number of mitoses performed by LIMP cells before differentiation	18	7
Apoptosis rate of stem and LIMP cells	0.0003 h^{-1}	0.001 h^{-1}
Apoptosis rate of differentiated cells	0.1 h^{-1}	0.001 h^{-1}
Necrosis rate of differentiated cells	0.001 h^{-1}	0.0013 h^{-1}
Fraction of G0 cells that re-enter cell cycle	0.01	0.4
Fraction of cells that enter G0 phase following mitosis	0.25	0.37
Fraction of stem cells that perform symmetric division	0.37	0.6

Fig 2. Indicative oscillation pattern in Oncosimulator results. A. Simulated time course of tumour volume with the initial reconstruction algorithms. A value combination of input parameters that results in oscillations of significant magnitude has been chosen here. B. Simulated time course of tumour volume with the initial and new reconstruction algorithms. A value combination of input parameters that results in insignificant oscillations with the initial reconstruction algorithms has been chosen here. The new reconstruction algorithm magnify considerably the oscillations.

A.



B.

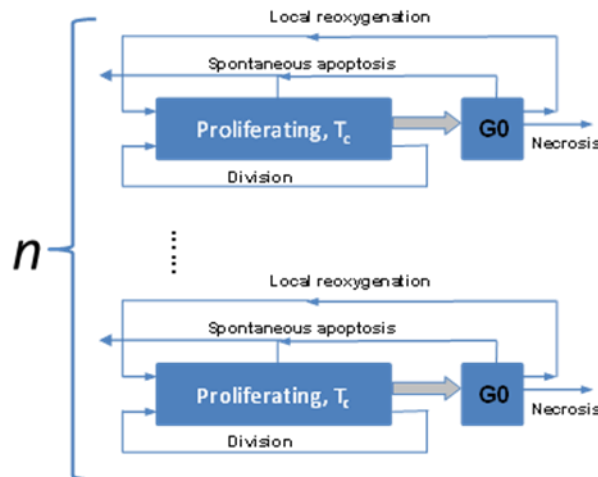
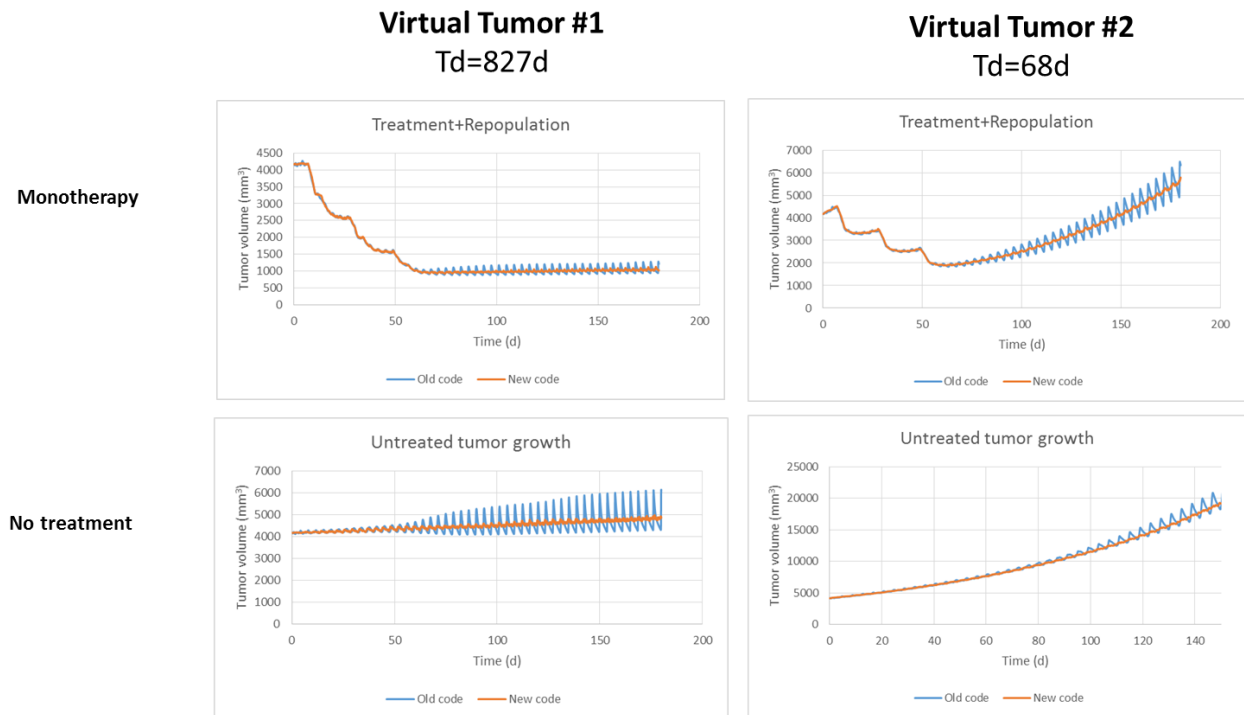


Fig 3. Initial (A) and modified (B) cell kinetic model cells (stem or LIMP) with proliferating capacity. Abbreviations: LIMP: Limited Mitotic Potential tumour cell. G1: Gap 1 cell cycle phase. S: DNA synthesis phase. G2: Gap 2 phase. M: Mitosis phase. G0: dormant, resting phase.



ADAPTATION OF PARAMETER VALUES AND RESULTING CANCER CHARACTERISTICS		
Parameter	#1	#2
Cell cycle duration	90 h	96 h
Duration of dormant phase	311 h	96 h
Time needed for necrosis products to disappear	79 h	120 h
Time needed for apoptosis products to be removed	7 h	6 h
Number of mitoses performed by LIMP cells before differentiation	18	18
Apoptosis rate of stem and LIMP cells	0.0003 h^{-1}	0.001 h^{-1}
Apoptosis rate of differentiated cells	0.1 h^{-1}	0.001 h^{-1}
Necrosis rate of differentiated cells	0.001 h^{-1}	0.001 h^{-1}
Fraction of G0 cells that re-enter cell cycle	0.01	0.01
Fraction of cells that enter G0 phase following mitosis	0.25	0.4
Fraction of stem cells that perform symmetric division	0.37	0.9

Fig 4. Comparison of initial and modified algorithms in the case of free tumour growth and treatment response. A homogeneous spherical tumour of 20mm diameter is considered. In the case of treatment response simulation, a cell cycle non - specific drug is administered on days 7, 28 and 49.

5.4 Integration - Hypermodel communication scheme

Oncosimulator – Preprocessing tool

The tumour morphology needs to be defined at a preprocessing step and provided to the Oncosimulator in the form of a raw/mhd metaimage. In this file, different subregions of interest should be noted with distinct colour numbers (e.g. white-255 for tumour area, black -0 for normal tissue) and the voxels should be cubic. Voxels of 1 or 2 mm (resolution) are commonly used. Furthermore, in order to reduce computational resources, the requested three-dimensional representation should not correspond to the entire image scan, but to a ‘region of interest’ centered on the tumour, with available space around it to permit growth simulations. The amount of this extra space can be defined based on the maximum dimension of the tumour.

The transformation of the segmented metaimages to a raw file format compatible to the Oncosimulator input specifications, is implemented by the preprocessing tool. Since, voxels in the initial imaging data sets are usually non-isotropic, i.e. their dimensions differ in the x-, y- and z-direction, the segmented metaimages need resampling. The tool also performs cropping to reduce the size of the initial image at a smaller region of interest centered on the tumour.

The communication between the oncosimulator and the preprocessing tool is sequential. The cropped and interpolated metaimages of the tumour domain (in the form of mhd and raw files) produced by the preprocessing tool are passed as a static input to the Oncosimulator via VPH-HF platform.

Oncosimulator – Molecular model

Cellular intrinsic sensitivity or resistance to treatment is a determinant of treatment outcome. The cell kill probability of a tumour cell is explicitly computed by the molecular model based on the molecular profile (e.g. EGFR mutations, miRNA expression data etc.) of the patient.

The communication between the Oncosimulator and the molecular model is sequential. The probability of a tumour cell to be lethally hit by a given therapy regimen is passed as a static input to the Oncosimulator via VPH-HF platform. In the case of chemotherapy the value is exploited directly by the Oncosimulator. In the case of radiotherapy the value is translated to the α (alpha) (Gy^{-1}) and β (beta) (Gy^{-2}) radiosensitivity parameters of the LQ model by applying the formula:

$$a = - \frac{\ln(1 - CKR)}{D + \frac{D^2}{\alpha/\beta}}$$

$$\beta = \frac{\alpha}{\alpha/\beta}$$

where α/β the alpha to beta ratio, CKR the cell kill rate provided by the molecular model and D (Gy) the radiation dose.

Oncosimulator – Vasculature – Metabolic models

The hyper-modelling scenario dictates an iterative communication scheme between the three hypomodels. This dynamic coupling is implemented via MUSCLE [Borgdorff et al. 2014]. The Oncosimulator computes the updated tumour domain geometry and the number of proliferating, quiescent, differentiated, apoptotic and necrotic tumour cells at each geometrical cell/voxel of the grid and send them to the vasculature model. Based on tumour cell concentration, the vasculature model passes the normalized concentration of glucose in each geometrical cell to the metabolic model. The metabolic model, which describes the aberrant metabolism of cancer cells at the genome scale based on the current glucose concentration, returns to the Oncosimulator the local proliferation rate of the tumour cells that reside within each geometrical cell. The local conditions of nutrient supply, such as glucose concentration, primarily regulate the withdrawal of tumour cells in a quiescent state, in an attempt by the tumour to sustain viability under conditions of reduced nutrient supply. Hence, a reasonable first approximation, is to translate the proliferation rate, a , to the fraction of newborn cells entering quiescent state, P_{sleep} , using the following formula:

$$P_{sleep} = \frac{1 - e^{aT_c/2}}{1 - (P_{G0toG1}/T_{G0})/(a + 1/T_{G0})}, \quad \text{derived from Eq. (7) in Kolokotroni et al. 2011}$$

where T_c the cell cycle duration, T_{G0} the residence time of tumour cells in quiescent state and P_{G0toG1} the fraction of quiescent cells re-entering cell cycle.

Oncosimulator – Biomechanics simulator

The hyper-modelling scenario dictates an iterative communication scheme between the two simulators. This dynamic coupling is implemented via MUSCLE [Borgdorff et al. 2014]. The Oncosimulator computes cell proliferation in the case of free growth or cell loss in the case of treatment and sends the updated cell concentration information to the biomechanical solver. Based on this information the Biomechanics simulator calculates the stress distribution and passes the preferred direction of cell movement and, hence, of tumour growth/shrinkage, to the Oncosimulator. This direction corresponds to the direction against which the cells sense a minimum pressure.

5.5 Adaptation and Partial Validation

5.5.1 Clinical Scenario A: Neoadjuvant Chemotherapy for Resectable Non-Small-Cell Lung Cancer

The use of cisplatin in combination with another agent remains the standard of care in NSCLC [Goffin *et al.* 2010]. For patients with resectable tumours, neoadjuvant chemotherapy can be proven particularly beneficial in terms of operability, event-free survival, time to distant recurrence and overall survival [NSCLC Meta-analysis Collaborative Group, 2014]. However, if treatment fails, a considerable time will have passed during which the tumour may have advanced or even become inoperable [NSCLC Meta-analysis Collaborative Group, 2014].

Prediction of treatment failure and selection of the optimal therapeutic strategy can be greatly potentiated by the use of mechanistic models that summarize our knowledge on cancer progression and response to treatment. However, up to now, the adaptation, validation and establishment of mechanistic models in predictive medicine has been hindered by the limited availability of data directly linked to the input parameters. Needless to say, in several occasions, no established method exists for the direct measurement of model parameters.

Determinant for the personalized prediction of cancer response is the resistance/sensitivity profile of tumour cells to the specific anti-tumour regimen [Georgiadi *et al.* 2012, komarova 2011]. In-vitro experiments for the evaluation of drug cytotoxicity on cancer cell lines have been proven only indicative, as they cannot reproduce the conditions of tumour microenvironment [Lee *et al.* 2013]. On the other hand, mechanistic models may provide means to estimate in vivo drug efficacy.

In the present study, a range of plausible values of the cell killing efficacy of chemotherapy has been estimated for NSCLC treated with various cisplatin-based doublet regimens by using Lung Oncosimulator, a mechanistic model of cancer response to treatment. The cell killing efficacy of chemotherapy is expressed as the sum of cell kill rates, CKR_{sum} , of the two drugs considered. Our modelling methodology takes into account cell re-population between drug administrations. Parameterization has been driven by principal mechanisms characterizing cancer biology, namely uncontrolled cell proliferation, reversible dormancy, clonal heterogeneity, hypoxia and attenuated apoptosis. A detailed description of the model's formulation can be found in deliverables D6.2 and D6.3.

5.5.1.1 Patient data

Thirteen patients with newly diagnosed NSCLC are included in the following study. The patients were treated at the Institute of Pathology of the University Hospital of Saarland between 2006 and 2010. The patients were between 45 and 67 years of age. Nine of the patients were diagnosed with squamous cell carcinoma (SCC) and the rest four with adenocarcinoma (ADC). None of the patients had previous cancer occurrence. All patients had stage III or IV disease according to TNM Classification of Malignant Tumours, 7th ed. There were two patients with distant metastases at the time of diagnosis. All patients received primary systemic chemotherapy prior to surgery. Pseudonomized data from the patients were used according to the approval of the ethical committee Ethik-Kommission, Ärztekammer des Saarlandes.

All patients were treated preoperatively with a cisplatin-based doublet regimen (Table I): one patient received a combination therapy with cisplatin (75 mg/m²) plus docetaxel (75 mg/m²), three patients received cisplatin (80 mg/m²) plus gemcitabine (1250 mg/m²), and nine patients were given cisplatin (80 mg/m²) plus vinorelbine (30 mg/m²). The cisplatin/gemcitabine and cisplatin/vinorelbine doublet regimens were given as a three-week cycle, administered two or three times. On day 1 of each cycle the patients received a short IV infusion (10-30min) of gemcitabine (or vinorelbine), followed by a 1-2 h IV infusion of cisplatin, whereas on day 8 only gemcitabine (or vinorelbine) was administered. In the case of cisplatin/docetaxel doublet regimen, both chemotherapeutic agents (1h IV infusion of docetaxel followed by 1h IV infusion of cisplatin) were given on day 1 of a 21-day cycle, repeated three times. After systemic chemotherapy, the patients underwent surgical resection of the primary tumour and/or the regional lymph nodes.

The patient specific data that have been used to clinically adapt the Lung Oncosimulator are the applied chemotherapeutic scheme (drugs, administration instants) and the 3D image of the tumour as segmented from CT imaging data (Table I). Interactive segmentation was performed at soft tissue window in the present study. The sets of imaging data refer to the primary tumour and were provided for two time instances before, and during or after the completion of the systemic treatment (prior to surgery). The reconstructed images contain information only about the external boundary of the tumour, whereas information concerning any distinct internal metabolic region is absent. Accordingly, the virtual tumour implemented is assumed homogeneous with a shape compliant to the segmented tumour shape.

Table I. Summary of clinical data.

Case #	Histo logic type*	Tumour volume (mm ³) at initial CT acquisition	Tumour volume (mm ³) at second CT acquisition	Relative volume reduction (% of initial volume)	Interval (days) between CT acquisitions	Interval (days) between initial CT and treatment onset	Drug administrations (day) [‡]
Cisplatin (80 mg/m²) & Gemcitabine (1250 mg/m²)							
1	SCC	100264	46776	53.35	47	5	GEM: 1 st , 8 th , 22 nd , 29 th , CIS: 1 st , 22 nd
2	SCC	568264	168048	70.43	46	4	GEM: 1 st , 8 th , 22 nd , 29 th , CIS: 1 st , 22 nd
3	SCC	101216	26336	73.98	45	4	GEM: 1 st , 8 th , 22 nd , 30 th , CIS: 1 st , 22 nd
Cisplatin (75 mg/m²) & Docetaxel (75 mg/m²)							

4	SCC	41376	18352	55.65	67	27	DOC: 1 st , 22 nd , CIS: 1 st , 22 nd
Cisplatin (80 mg/m²) & Vinorelbine (30 mg/m²)							
5	SCC	20760	5824	71.95	90	47	VIN: 1 st , 8 th , 22 nd , 29 th , CIS: 1 st , 22 nd
6	SCC	41056	23416	42.97	63	14	VIN: 1 st , 8 th , 22 nd , 29 th , 43 rd , CIS: 1 st , 22 nd , 43 rd
7	SCC	39776	15840	60.18	42	1	VIN: 1 st , 22 nd , 29 th , CIS: 1 st , 22 nd
8	SCC	133864	29816	77.73	47	5	VIN: 1 st , 8 th , 22 nd , 29 th , CIS: 1 st , 22 nd
9	SCC	123016	131160	-6.62	83	27	VIN: 1 st , 8 th , 29 th , 36 th , CIS: 1 st , 29 th
10	ADC	45160	8544	81.08	69	27	VIN: 1 st , 8 th , 22 nd , 29 th , CIS: 1 st , 22 nd
11	ADC	63136	20632	67.32	46	0	VIN: 1 st , 8 th , 26 th , 33 rd , CIS: 1 st , 26 th
12	ADC	99872	51752	48.18	60	18	VIN: 1 st , 8 th , 22 nd , 29 th , CIS: 1 st , 22 nd
13	ADC	111744	29264	73.81	104	21	VIN: 1 st , 8 th , 36 th , 43 rd , 64 th , 71 st , CIS: 1 st , 36 th , 64 th

*SCC: Squamous cell carcinoma, ADC: Adenocarcinoma

‡ Day 1 is treatment onset. Only the drug administration time points in the interim between the two CT acquisitions are recorded. Only these time points have been considered for the quantification of treatment efficacy.

5.5.1.2 Pattern of Virtual Tumour Growth and Response to Treatment

The model supports the division of tumour volume into regions of distinct metabolic activity (i.e. necrotic, quiescent and proliferative). However, due to the lack of relevant info in the segmented

tumour images, only a single metabolic region is considered. This implies that all model parameters affecting tumour cell kinetics have the same value throughout a tumour's volume. Furthermore, the kinetics of tumour cell proliferation (i.e. phase durations and transition rates or fractions) are assumed constant throughout simulation, reflecting the mean values over the simulation time window. Such an approximation is considered applicable for a relatively short time interval compared to the tumour's lifetime. Finally, the model aims at simulating fully developed, clinical tumours, well beyond their initiation phase. For such a biological system it is rational to assume that a state of population equilibrium and of balanced growth has been achieved. The methodology developed for the initialization of tumour cell populations [Stamatakis *et al.* 2010, Kolokotroni *et al.* 2011] ensures conditions of balanced growth at the beginning of the simulation.

A tumour characterized by space and time invariant growth kinetics parameters and population equilibrium would demonstrate a grossly exponential growth pattern [Kolokotroni *et al.* 2011]. Even though it is generally accepted [Steel 2002] that tumours grow in a Gompertzian manner during their lifetime, i.e. growth progressively slows down as the tumour enlarges, tumours that follow exponential law have been reported frequently in literature. Indeed, several lung cancer cases reported in literature exhibit fairly constant growth rates on the logarithmic scale [Friberg & Mattson 1997, Mackintosh *et al.* 2014, Quint *et al.* 2008] over prolonged periods of time, ranging from months to years. It has been argued that these tumours were probably still in the exponential phase of Gompertzian curve at the time of diagnosis and clinical surveillance [Quint *et al.* 2008].

Figs 5A and 5B show the simulated time course of a macroscopically homogeneous tumour under free growth or treatment conditions respectively. In the case of treatment a typical scheme for NSCLC has been assumed that is based on the combination of two chemotherapy drugs i.e. cisplatin and gemcitabine. The doublet regimen is administered three times as a three-weeks cycle. On the first day of treatment cycle the patient is given both gemcitabine and cisplatin. On the same day of the following week (day eight) only gemcitabine is administered. Qualitatively a fairly expected and reasonable tumour dynamics behaviour can be easily noticed. An exponential pattern of growth in the absence of treatment and tumour regression followed by repopulation after each chemotherapeutic session in the case of treatment are successfully demonstrated.

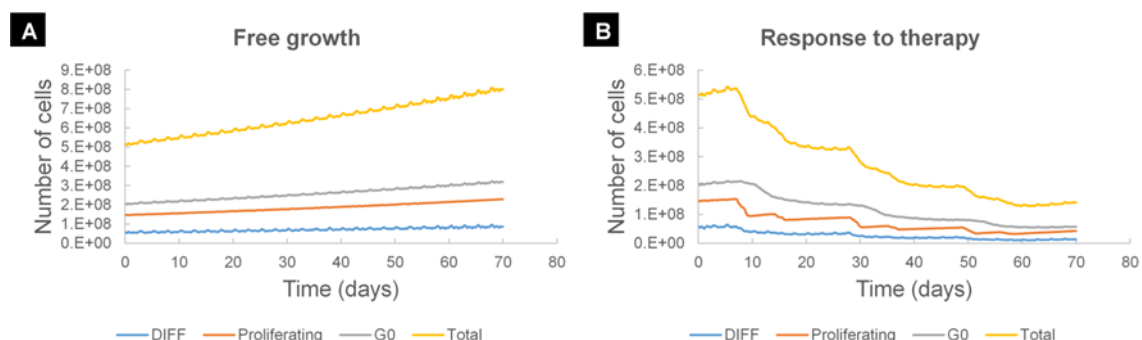


Fig 5. Simulated time course of selected cancer cell populations. (A) Various tumour cell populations as a function of time in the case of free tumour growth. A homogeneous spherical tumour of 10mm diameter is considered. (B) Various tumour cell populations as a function of time in the case of treatment response. A homogeneous spherical tumour of 10mm diameter is considered. A cell cycle specific (gemcitabine) and a cell cycle non-specific (cisplatin) drug are administered as a three-week cycle. Gemcitabine is given on days 7, 14, 28, 35, 49, 56. Cisplatin is administered on days 7, 28 and 49. After each chemotherapeutic session a drop in the various tumour cell populations is observed, followed by tumour repopulation.

Table 2 presents the input parameters of the simulation model and their range of values according to the conducted literature survey (the results of the survey can be found in D6.2) or based on logical assumptions supported by basic science or clinical experience.

Table 2. Model parameters related to tumour free growth and therapy.

Parameter symbol	Description	Units	Value range	References
CELL PHASE DURATIONS				
$T_C[\text{class}^*]$	Cell cycle duration	hours	18-134	Lieber et al., 1976; Kimura et al. 1979; Loh et al. 1984; Olsson et al. 1984; Brower et al. 1986; Masuda et al. 1991; Campling et al. 1992; Liu & Tsao, 1993; Giaccone et al. 1992; Li et al. 2012
$T_{G0}[\text{class}^*]$	G0 (dormant phase) duration i.e. time interval before a dormant cell re-enters cell cycle or dies through necrosis	hours	90-1200	extension of Durand & Sham 1998
$T_A[\text{region}^\ddagger]$	Time needed for both apoptosis to be completed and its products to be removed from the tumour	hours	1-25	Kerr et al. 1972, Gavrieli et al., 1992; Bursch et al. 1990
$T_N[\text{region}^\ddagger]$	Time needed for both necrosis to be completed and its lysis products to be removed from the tumour	hours	1-200	Ginsberg T., 1996, estimation based on fraction of necrotic cells
CELL CATEGORY/PHASE TRANSITION RATES AND FRACTIONS[†]				
R_A	Apoptosis rate of living stem and limp tumour cells, i.e. fraction of cells dying through apoptosis per unit time	hours ⁻¹	0-0.001	estimation
R_{ADiff}	Apoptosis rate of differentiated tumour cells	hours ⁻¹	0.0001-0.02	extension of Rawlins & Hogan, 2006, 2008; Lippmann 2000; Flindt 2006;
R_{NDiff}	Necrosis rate of differentiated tumour cells	hours ⁻¹	0-0.02	estimated to achieve the given GF
$P_{sym}[\text{region}^\ddagger]$	Fraction of stem cells that perform symmetric division	-	0-0.4	estimation based on Pine et al. 2010; Morrison et al. 2012
$P_{sleep}[\text{region}^\ddagger]$	Fraction of cells entering the G0 phase following mitosis	-	0-1	Estimated to achieve the given T_d
$P_{G0toG1}[\text{class}^*][\text{region}^\ddagger]$	Fraction of dormant (stem and LIMP) cells that re-enter cell cycle	-	0-1	-
MISCELLANEOUS PARAMETERS				
N_{LIMP}	Number of mitoses performed by LIMP cells before becoming differentiated	-	8-24	Estimation based on fraction of stem cells
CHEMOTHERAPY PARAMETERS				
$T_{\text{chemo, adm}}$	Time point of nth drug	days	-	clinical data

[n][drug [†]]	administration, n=1,...			
Cell kill rate[drug [†]]	The numbers of biological cells lethally hit by the drug at each administration	-	0-1	-
CKF [class [*]]	Cell kill factor i.e. factor adapting cell killing probability to stem or LIMP cells	-	0-1 for stem, 1 for LIMP	-

^{*}Defined separately for **stem** and **LIMP** cells (class: {stem, limp})

[‡]Defined separately for **proliferating** and **necrotic** region (region: {proliferating, necrotic})

[†]Defined separately for each drug administered

ⁱThe parameters included under this term express fractions and, therefore, can theoretically take any value between zero and unity. Whenever possible this range has been narrowed based on logical assumptions supported by literature or basic science.

5.5.1.3 Clinical Adaptation

5.5.1.3.1 Methodology

A. Generation of a NSCLC subtype-specific LHS sample of parameter values used for CKR estimation

The Latin Hypercube Sampling method is used to generate a plausible collection of model parameter values that corresponds to virtual tumours having a common proliferation pattern in terms of volume doubling time, T_d , growth fraction (GF), apoptotic cell fraction (AF), expressed as the apoptotic cell population out of total cells, necrotic cell fraction (NF), expressed as the necrotic cell population out of total cells. We consider the fraction of newborn cells that enter the G0 phase, P_{sleep} , the necrosis rate of differentiated cells, R_{NDiff} , the duration of apoptosis, T_A , and the duration of necrosis, T_N , as the dependent parameters of this multi-constrained problem. The independent variables comprise the rest of the model parameters that regulate tumour proliferation pattern, i.e. cell cycle time, T_C , the duration of G0 phase, T_{G0} , the apoptosis rate of stem and LIMP cells, R_A , the apoptosis rate of differentiated cells, R_{ADiff} , the symmetric division fraction, P_{sym} , the fraction of stem cells that re-enter cell cycle from a quiescent state, P_{G0toG1} , the number of mitoses performed by LIMP cells before becoming terminally differentiated N_{LIMP} , and resistance of stem cells to chemotherapy, CKF , and the above mentioned tumour proliferation features: GF, T_d , AF and NF.

The analysis has been performed using the Matlab toolbox. The built-in function 'lhsdesign' is run to produce N combinations of the independent model parameters: T_C , T_{G0} , R_A , R_{ADiff} , P_{G0toG1} , P_{sym} , N_{LIMP} , and CKF of stem cells. LHS output is modified in the case of parameters with value range other than $[0, 1]$ and parameters of integer type. For input parameters bounded in any range $[a_p, b_p]$ other than $[0, 1]$, the 'lhsdesign' output has been rescaled by applying the formula:

$$a_p + (b_p - a_p) * x_p \quad (4)$$

where x_p the vector of the N returned values for parameter p . For integer input parameters the rescaled values are rounded to the nearest integer.

For each combination of parameter values, parameters P_{sleep} , R_{NDiff} , T_A and T_N , are derived from the following formulas, so as to achieve the given T_d , GF, AF and NF.

Initially, the P_{sleep} value is computed so as to achieve the given T_d :

$$P_{sleep} = \frac{1 - e^{(a+R_A)T_C} / (1 + P_{sym})}{1 - \frac{P_{G0toG1}}{T_{G0}} / \left(a + R_A + \frac{1}{T_{G0}} \right)} \quad (\text{derived from Eq (7) in of Kolokotroni et al., 2011}) \quad (5)$$

R_{NDiff} , is calculated in order to achieve the given GF

$$R_{NDiff} = \frac{1 - P_{sym}}{\frac{1}{A} \left(\frac{1}{GF} - 1 \right) - B} - a - R_{ADiff} \quad (\text{derived from Eq (47) in S2 Text in Kolokotroni et al., 2016}) \quad (6)$$

where

$$A = \frac{a + R_A}{e^{(a+R_A)T_C} - 1} \quad (7)$$

$$B = \frac{1 - P_{sym}}{a + R_A + \frac{1}{T_{G0}}} P_{sleep} \quad (8)$$

By taking into account that the ratio of apoptotic, N_A , to proliferating, N_p , population is given by

$$\frac{N_A}{N_P} = \frac{AF}{GF} \frac{1}{Living/Total} = \frac{AF}{GF} \frac{1}{1 - AF - NF} \quad (9)$$

T_A , can be calculated based on Eq (13) in S2 Text in Kolokotroni *et al.*, 2016:

$$T_A = \left(\frac{\frac{R_A}{N_A} + \frac{R_A}{N_P} (1 + P_{sym}) P_{sleep} \frac{A}{a + R_A + \frac{1}{T_{G0}}} + \frac{R_{ADiff}}{N_A} (1 - P_{sym}) \frac{A}{a + R_{ADiff} + R_{NDiff}} - a}{\frac{N_A}{N_P}} \right)^{-1} \quad (10)$$

Finally, T_N has been determined for the given NF based on Eq (17) in S2 Text in Kolokotroni *et al.*, 2016

$$\frac{N_N}{N_P} = \frac{NF}{GF} \frac{1}{1 - AF - NF} \quad (11)$$

$$T_N = \left(\frac{\frac{(1 - P_{G0toG1})}{\frac{T_{G0}}{N_N}} (1 + P_{sym}) P_{sleep} \frac{A}{a + R_A + \frac{1}{T_{G0}}} + \frac{R_{NDiff}}{N_N} (1 - P_{sym}) \frac{A}{a + R_{ADiff} + R_{NDiff}} - a}{\frac{N_N}{N_P}} \right)^{-1} \quad (12)$$

The above methodology is applied for each NSCLC subtype considered, i.e. ADC and SCC. The derived two LHS samples of parameter values are used for the estimation of the cell killing ability of the various cisplatin-based doublet regimens.

B. CKR estimation

The cell kill rate of cisplatin, $CKR_{cis-DDP}$, is adapted to the observed tumour size reduction. The adaptation of $CKR_{cis-DDP}$ has been performed automatically using an optimization procedure (the built-in function 'fzero' of Matlab), that returns the value of the $CKR_{cis-DDP}$ for which the difference between the observed or given volume reduction and the simulation outcome is zero. During this optimization procedure the rest of the model parameters, including the CKR of the second drug, are kept constant.

5.5.1.3.2 Results

The histology, treatment and response data of 13 lung cancer clinical cases have been retrospectively analyzed in order to evaluate the *in vivo* efficacy of three different cisplatin-based doublet regimens: cisplatin plus gemcitabine, cisplatin plus docetaxel and cisplatin plus vinorelbine. The following tumour proliferation features have been also considered here. For the clinical cases classified as ADC the assumptions are as follows: (a) $T_d=225d$, (b) $GF=0.18$, (c) $AF=0.01$, (d) $NF=0.02$ and (e) $SF<0.001$. For the clinical cases classified as SCC we have considered: (a) $T_d=109d$, (b) $GF=0.36$, (c) $AF=0.01$, (d) $NF=0.20$ and (e) $SF<0.001$. Furthermore, the ranges of the model parameters are given in Table 2. LHS has been run to generate 2000 combinations of parameter values that fulfill the above requirements, as described previously. After excluding combinations that result in biologically non-relevant tumours, i.e. negative cell class transition rates P_{sleep} and R_{NDiff} , or in tumours with non-relevant proliferation dynamics, i.e. T_d beyond $\pm 10\%$ of T_d and/or stem cell fractions higher than 1‰ (based on SoA results) and/or $T_A>24h$ and/or $T_N>200h$ and/or $R_{NDiff}>0.02h^{-1}$, a subset of $N=146$ and 175 combinations has been finally considered for the SCC and ADC cases respectively.

For each clinical case and for each of the N sets, the $CKR_{cis-DDP}$, and therefore CKR_{sum} , that results in the observed volume reduction is estimated. The cell kill rate of the second drug, CKR_B , has been assumed equal to 0.2 with the exception of clinical case 9 for which a value equal to 0.1 has been assumed. This selection of CKR_B value has been made with the criterion to have a solution for $CKR_{cis-DDP}$ for all the N LHS combinations considered. Fig 6 shows the median (dot), 10th and 90th percentile (lower and upper boundary of solid line) and minimum and maximum (lower and upper boundary of dashed line) of the N CKR_{sum} estimates for each clinical case. Even though the estimated values of CKR_{sum} vary considerably for all clinical cases, the vast majority of the values (80%) is confined in a much smaller range, not exceeding, with the exception of one case, an average of 0.1 units around the median value. We observe that the treatment efficacy is very low in 2 cases (15.4% of the total cases) with a median CKR_{sum} below 0.3, low in 2 cases (15.4% of the total cases) with a median CKR_{sum} approximately 0.38, moderate in 6 cases (46.1% of the total cases) with a median CKR_{sum} between 0.47 and 0.57, high in 2 cases (15.4% of the total cases) with a median CKR_{sum} approximately 0.61 and very high in 1 case (7.7% of the total cases) with a median CKR_{sum} approximately 0.71. The efficacy of the three cisplatin-doublet regimens seems comparable; however, the sample size is too small, especially for cisplatin/docetaxel and cisplatin/gemcitabine regimens, to draw statistically significant conclusions.

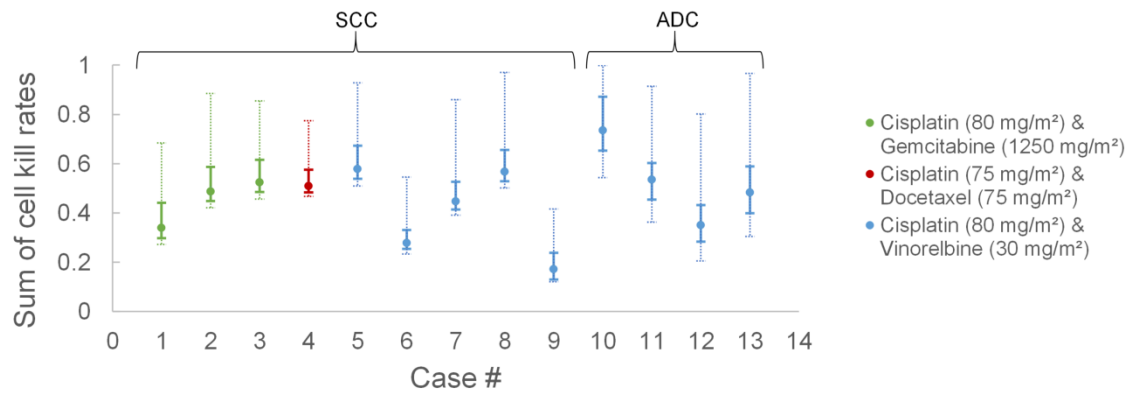


Fig 6. Drug cytotoxicity results for the clinical cases. The estimated sum of cell kill rates, CKR_{sum} for the cisplatin-based doublet regimen given to each clinical case (denoted by its ID number) is displayed. Latin Hypercube Sampling (LHS) has been run to produce two sets of value combinations of model parameters, one for the Adenocarcinoma (ADC) and one for the Squamous Cell Carcinoma (SCC) clinical cases. For each value combination the CKR_{sum} that results in the clinically observed volume reduction is determined. At any given case the dot denotes the median (50th percentile) of the N estimated values, the lower and upper boundaries of the solid line denote the 10th and 90th percentile, whereas the dashed line extends to the two extreme values of the estimated CKR_{sum} .

In Fig 7 the scatterplots of the N CKR_{sum} values for one SCC and one ADC clinical case are shown versus indicative model parameters and the proportion of dormant and terminally differentiated cells. We observe that for both ADC and SCC cases, the highest values of CKR_{sum} are associated with short cell cycle durations (Figs 7A and 7J), shortly lived terminal differentiated cells (or equivalent removal rate of DIFF cells above 0.01h⁻¹) (Figs 7B and 7K) and resistant stem cells by a factor of 2 or above (or equivalent CKF of stem cells < 0.5) (Figs 7G and 7P). For the SCC case the highest values of CKR_{sum} are found for low P_{sym} (Fig 7C) and low P_{sleep} (Fig 7D). Furthermore, tumours with higher fractions of dormant cells, at the expense of terminally differentiated cells (GF is constant), tend to require a higher CKR_{sum} to achieve the same volume reduction (Figs 7H, 7I, 7Q and 7R).

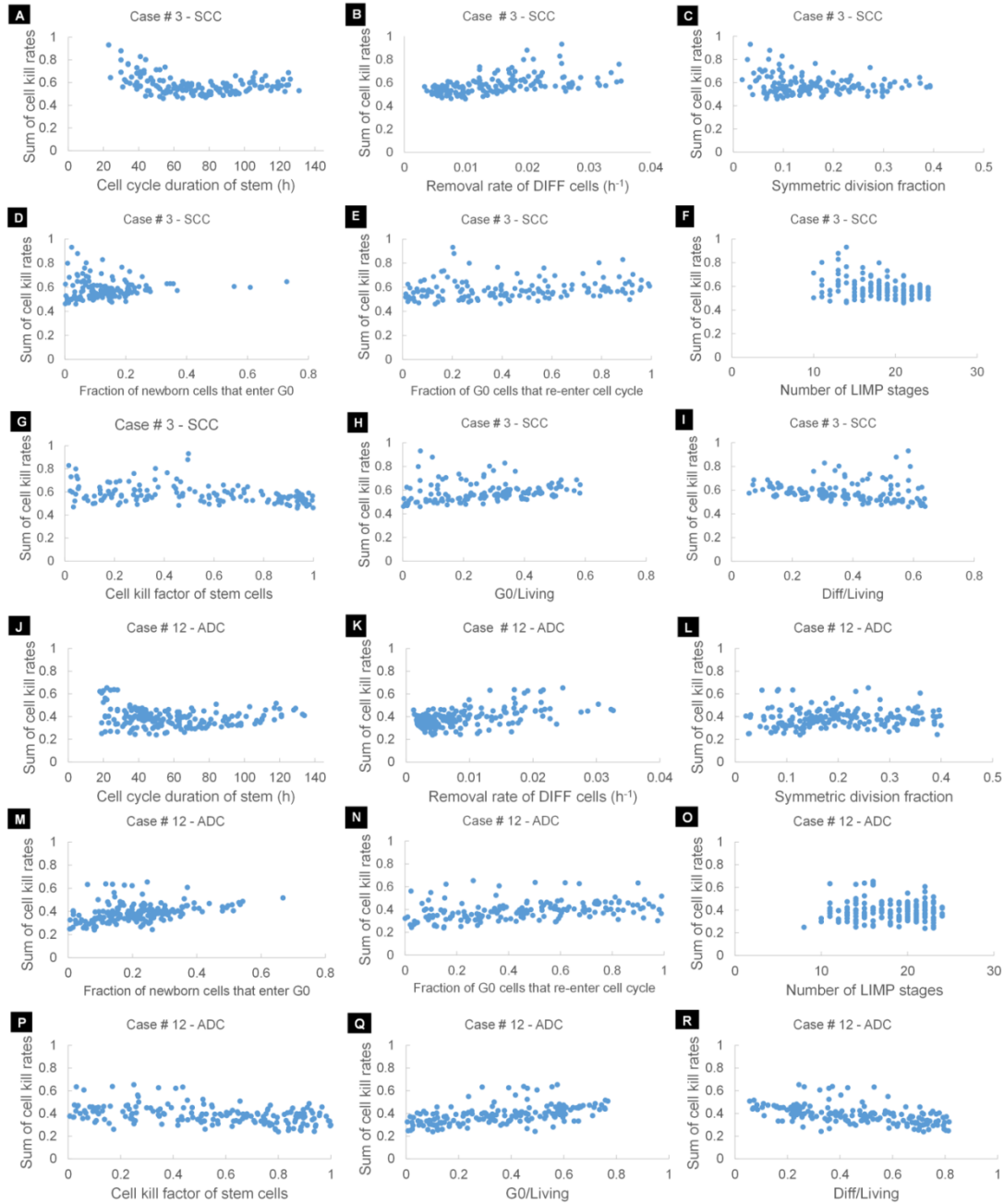


Fig 7. Scatterplots of the Cell Kill Rate (CKR) estimates vs. indicative model parameters and tumour proliferation features for the clinical cases 3 (Squamous Cell Carcinoma - SCC) and 12 (Adenocarcinoma - ADC). All model parameters are varied simultaneously. The ordinate represents the sum of cisplatin and gemcitabine cell kill rates for case #3 and cisplatin and vinorelbine for case #12. The samples have a size of 146 and 175 for the SCC (#3) and ADC (#12) cases, respectively. They originate from two Latin Hypercube Sampling (LHS) runs of 2000 combinations of parameter values after excluding the ones with negative cell proliferation kinetics or cell proliferation kinetics that fall beyond the reference values for NSCLC in general and SCC and ADC representative cases specifically (see Results section). The ‘removal rate of DIFF cells’ is the sum of apoptosis rate, R_{ADiff} , and necrosis rate, R_{NDiff} , of terminally differentiated cells.

5.5.1.4 Clinical validation

5.5.1.4.1 Methodology

The three mutually perpendicular dimensions of the surgically resected tumour has been provided for the 12 out of the 13 patients (Table 3). An early validation is attempted here, by comparing the post-surgical excision measurements with the simulated tumour size at the time of surgery. It should be noted that the size of the resected tumour has not been considered for the estimation of $CKR_{cis-DDP}$ in the previous section; however, it is exploited here for validation purposes. In particular, for each clinical case and for each of the N parameter sets with corresponding $CKR_{cis-DDP}$ derived in the previous section, an extended simulation has been performed starting from the first CT acquisition until the date of surgery. The extra time interval simulated for each clinical case is reported in Table 3. For three clinical cases, additional drug administrations have taken place during this interval and have been modelled assuming the estimated values of $CKR_{cis-DDP}$.

Table 3. Clinical data for model validation.

Case #	Interval (days) between second CT and surgery	Tumour maximum diameter a(cm)	Tumour maximum diameter b(cm)	Tumour maximum diameter c(cm)	Volume (ml)	Equivalent tumour diameter (cm)	Additional drug administrations (day) [‡]
1	20	6	4.5	3	42.4115	4.326749	none
2	21	6	5.5	4	69.11504	5.091643	GEM: 43 rd , 50 th , CIS: 43 rd
3	18	2.5	1.6	1.6	3.351032	1.856636	none
4	36	3	2	1.5	4.712389	2.080084	DOC: 44 th , CIS: 44 th
5	5	2.5	1.8	1.5	3.534292	1.889882	none
6	39	4	3.7	3	23.24779	3.541014	VIN: 50 th
7	7	3.5	3.3	2.5	15.11891	3.067896	none
8	3	3.5	3.5	3.3	21.16648	3.432022	none
9	28	8	7.5	5.5	172.7876	6.910423	none
10	20	2.1	1.9	1.3	2.715907	1.731033	none
11	6	4	3.5	2	14.66077	3.036589	none
13	22	4.7	4	3.1	30.51534	3.877096	none

[‡] Day 1 is treatment onset. Only the drug administration time points in the interim between the second CT and the surgery are recorded.

5.5.1.4.2 Results

Fig 8A depicts the boxplots of the N predicted tumour sizes for each clinical case in comparison with the real ones. Since it is customary in clinical practice to assess the size of a solid tumour by measuring its maximum dimension(s), tumour size is expressed by means of an equivalent diameter. The predicted tumour volume, V, is translated to the equivalent diameter, d, assuming that the tumour is approximated by a sphere of the same volume

$$d = 2 \times \sqrt[3]{\frac{3V}{4\pi}} \quad (16)$$

The equivalent diameter of the surgically resected tumour is calculated as before. The volume of the resected specimen is determined by its three mutually perpendicular dimensions, after assuming that its shape is approximated by a triaxial ellipsoid [Protocol-SIOP-2001] (Table 3). In Fig 8B the predicted volume reduction is compared with the real one. Despite the large deviation observed between the minimum and the maximum values in both equivalent diameter and volume reduction graphs, the majority of the predictions are in fact confined around the median value. To that respect, the first, second (median) and third quartiles are considered for the validation of our predictions.

A good agreement between the prediction and the actual data is observed for the six out of twelve cases. In particular, the equivalent diameter of the resected tumour and, hence, the observed volume reduction, falls between the first and third quartiles of the predicted ones in three cases (# 2, 9, 13). Moreover, a deviation less than 10% (corresponding to less than 4mm difference) between the predicted median diameter and the one of the resected tumour is observed for three cases (# 1, 6 and 7). However, due to the small size of the initial tumour, a somewhat larger deviation is observed in the case of volume reduction for cases # 1 and 6. It is noteworthy that the cases # 2 and 6 received additional therapy during the extra simulation period.

A slightly higher deviation (12% to 20%) between the equivalent diameters of the median of the predicted values and the resected specimen is observed for the cases 5, 8 and 11. An even lower deviation that does not exceed 14% exists for volume reduction in the same cases. It is worth mentioning that for these cases the surgery takes place shortly after the second CT acquisition (Table 3), corresponding to a limited (after the second CT acquisition) simulated period; therefore, it is possible that any uncertainties in estimating the true tumour volume by both the imaging techniques and the post-surgical excision measurements may be comparable to the change in tumour sizes and play a role in the observed deviations. For example, volume estimation errors of 10 to 20% are typically expected (more prominent for small lesions) [Kuhnigk *et al.* 2006], whereas based on our simulation results the volumetric change in a period of only a few days is less than 10%.

The less agreement is observed for cases # 3, 4 and 10. The model seems to underestimate the cell killing efficacy of treatment and predicts a tumour at surgery that deviates from the resected tumour around 1cm for # 4 and #10 and 2cm for #3. However, for #10 the median volume reduction differs only 15% from the real one. The tumour proliferation profile considered may be a possible source of the observed discrepancies. Our literature study (S3 Text) has revealed a considerable intra-patient variability in the macroscopic characteristics of NSCLC. It is therefore expected our assumptions to deviate from reality for some of the cases. For more accurate results, the clinical data should contain information about the proliferation profile per patient as well.

By taking into account the existence of uncertainties in estimating the true tumour volume as described above, the limited number of data sets available for the estimation of CKR and the consideration of a single proliferation profile differentiated only on the grounds of the two histological subtypes of the available clinical cases, the gross agreement between the predicted

tumour values and the prost-surgery measured ones indicate that the proposed methodology/ model has a clear clinical potential.

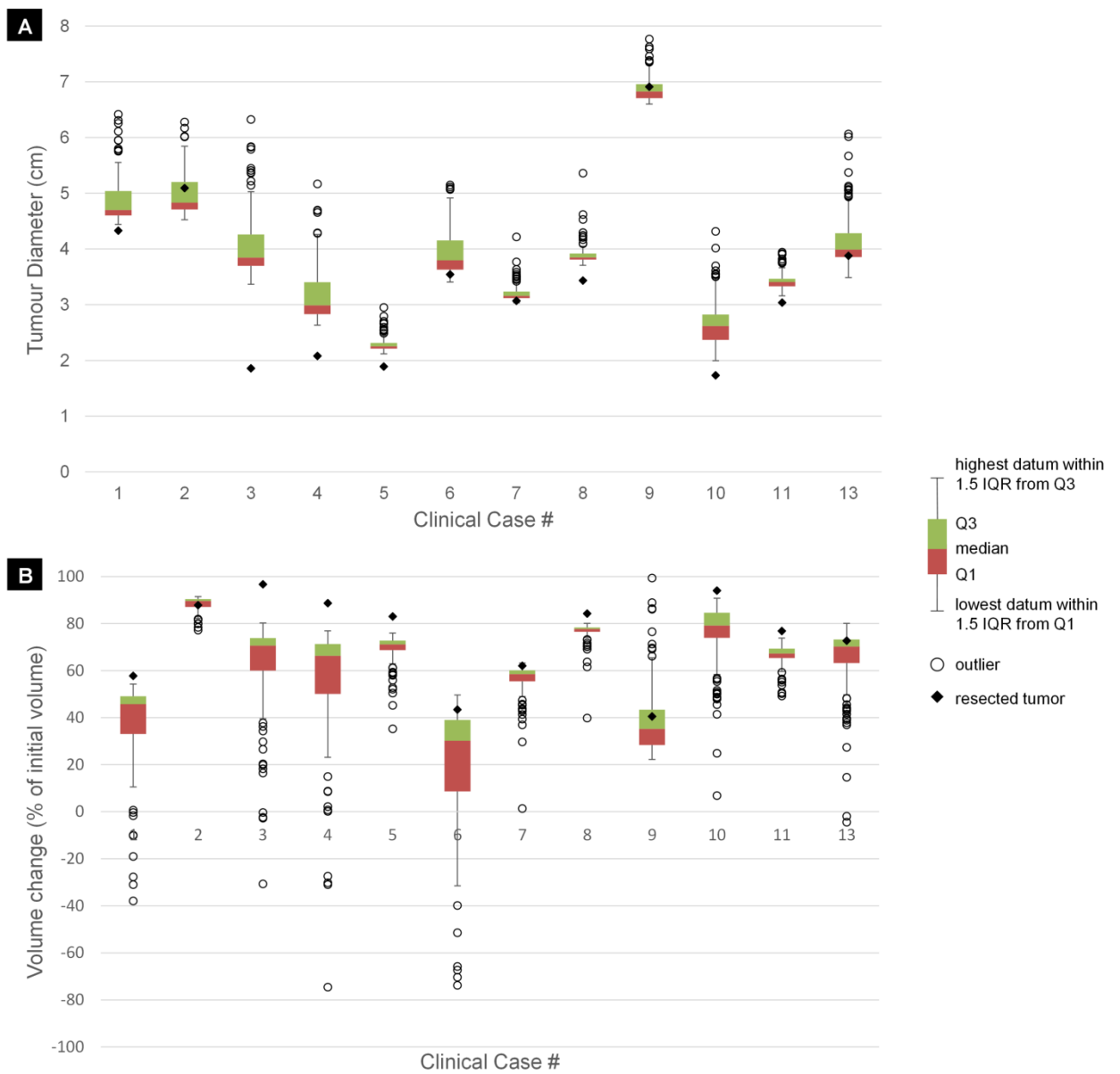


Fig 8. Box-and-whisker plots of model predictions at the time of surgery for the clinical cases. Each box and whisker plot corresponds to N (146 and 175 for the SCC and ADC cases respectively) independent predictions. Each prediction results from an extended model simulation starting from the first CT examination till the time of surgery. The simulations have assumed the estimated sum of cell kill rates, CKR_{sum} of Fig 6. At any given case the horizontal line between the green and the red boxes denotes the median (50th percentile) of the N predictions, the lower boundary of the red box and the upper boundary of the green box denote the first (Q1) and third (Q3) quartiles, whereas the predictions more than 1.5 interquartile (IQR) distance from the end of the boxes are denoted as outliers (depicted as circles). The whiskers extend from the lowest to the highest prediction that falls within 1.5 IQR from the outer edge of the boxes. The predictions correspond to (A) the equivalent diameter of the tumour at the time of surgery, defined as the diameter of a sphere with the same tumour volume as the predicted one and (B) the absolute value of the volume change of the tumour, expressed as a percentage of the initial volume. For the clinical case # 9 the volume change corresponds to an increase, whereas for rest cases to a reduction. The corresponding values derived by the measurements of the surgical resected tumour are denoted as a filled rhomb.

5.5.2 Clinical Scenario B: Recurrence of Non-Small-Cell Lung Cancer

Surgery remains the first line treatment of non-small cell lung cancer (NSCLC) patients. However, a proportion of lung cancer patients will recur, even after curative resection. For early-stage NSCLC the overall incidence of recurrence can be 30% to 55% [al-Kattan et al. 1997, Hoffman et al. 2000, Carnio et al. 2013, Uramoto et al. 2014]. The relapse rates are even higher for locally advanced or metastatic patients [Lou et al. 2014].

In the present study, we consider the initial phase in the life course of a recurrent tumour, when the microscopic seeds of cancer cells that have remained after surgery re-establishes the tumour. The study is performed by using Lung Oncosimulator as a stand-alone application, because no visible initial tumour exists for the application of the whole hypermodel.

The aim of the present study is to derive a group of virtual tumours that constitute solutions to the examined clinical case and efficiently cover the parameter space. These virtual tumours have common predefined proliferation characteristics, i.e. growth fraction and/or doubling time when they reach population equilibrium, and tumour volume at the date of the available imaging data, but, in general, will differ in their growth behaviour till the above date.

5.5.2.1 Patient data

Seven patients with relapsed NSCLC are included in the following study (Table 4). The patients were treated and followed up at the Institute of Pathology of the University Hospital of Saarland. The patients were between 60 and 71 years of age. All patients were diagnosed with adenocarcinoma (ADC) and had stage IA to IIIA disease according to TNM Classification of Malignant Tumours. All patients underwent surgical resection of primary tumour as a first-line treatment, without pre-operative chemotherapy. Available patient data correspond to a post-operative follow-up period that

extends until 2014. All available data were pseudonomized and their use for research purposes was according to the approval of the ethical committee Ethik-Kommission, Ärztekammer des Saarlandes. The patient specific data that have been used to clinically adapt the Lung Oncosimulator are the volume of the recurrent tumour, the date of image acquisition and the applied chemotherapeutic scheme (drugs, administration instants) before recurrence (if any) (Table 4). The volume has been computed by using CCGVis, from the 3D segmented images of the tumour. The segmentation was performed either on CT or PET imaging data using DrEye.

Table 4. Clinical data

Case #	Interval (days) between surgery and first CT/PET	Volume of recurrent tumour (ml)	Proliferation index (Ki-67) (%)	MVD (%)	Stage	Chemo before recurrence (day) [‡]
1	1584	6.85349	-	56.8	IA	no
2	362	0.945513	25	19	IB	unclear
3	1321	4.6778	-	37.2	IIB	unclear
4	699	2.03382	5	24	IIIA	unclear
5	883	22.5166	-		IIIA	no
6	1232	6.41383	36	13.8	IIA	unclear
7	455	8.59726	-	9.8	IIA	no

[‡] Days from surgery.

5.5.2.2 Clinical Adaptation

5.5.2.2.1 Methodology

A. Generation of a LHS sample of parameter values

The Latin Hypercube Sampling method is used to generate a plausible collection of model parameter values that corresponds to virtual tumours having a common proliferation pattern in terms of volume doubling time, T_d , growth fraction (GF). We consider the fraction of newborn cells that enter the G0 phase, P_{sleep} , and the necrosis rate of differentiated cells, R_{NDiff} , as the dependent parameters of this multi-constrained problem. The independent variables comprise the rest of the model parameters that regulate tumour proliferation pattern, i.e. cell cycle time, T_C , the duration of G0 phase, T_{G0} , the duration of apoptosis, T_A , and the duration of necrosis, T_N , the apoptosis rate of stem and LIMP cells, R_A , the apoptosis rate of differentiated cells, R_{ADiff} , the symmetric division fraction, P_{sym} , the fraction of stem cells that re-enter cell cycle from a quiescent state, P_{G0toG1} , the number of mitoses performed by LIMP cells before becoming terminally differentiated N_{LIMP} , and resistance of stem cells to chemotherapy, CKF , and the above mentioned tumour proliferation features: GF and T_d .

The analysis has been performed using the Matlab toolbox. The built-in function 'lhsdesign' is run to produce N combinations of the independent model parameters: T_C , T_{G0} , R_A , R_{ADiff} , P_{G0toG1} , P_{sym} , N_{LIMP} . LHS output is modified in the case of parameters with value range other than $[0, 1]$ and parameters of integer type. For input parameters bounded in any range $[a_p, b_p]$ other than $[0, 1]$, the 'lhsdesign' output has been rescaled by applying the formula:

$$a_p + (b_p - a_p) * x_p \quad (4)$$

where x_p the vector of the N returned values for parameter p . For integer input parameters the rescaled values are rounded to the nearest integer.

For each combination of parameter values, parameters P_{sleep} and R_{NDiff} , are derived from the following formulas, so as to achieve the given T_d and GF.

Initially, the P_{sleep} value is computed so as to achieve the given T_d :

$$P_{sleep} = \frac{1 - e^{(a+R_A)T_C} / (1 + P_{sym})}{1 - \frac{P_{G0toG1}}{T_{G0}} / \left(a + R_A + \frac{1}{T_{G0}} \right)} \quad (\text{derived from Eq (7) in of Kolokotroni et al., 2011}) \quad (5)$$

R_{NDiff} , is calculated in order to achieve the given GF

$$R_{NDiff} = \frac{1 - P_{sym}}{\frac{1}{A} \left(\frac{1}{GF} - 1 \right) - B} - a - R_{ADiff} \quad (\text{derived from Eq (47) in S2 Text in Kolokotroni et al., 2016}) \quad (6)$$

where

$$A = \frac{a + R_A}{e^{(a+R_A)T_C} - 1} \quad (7)$$

$$B = \frac{1 - P_{sym}}{a + R_A + \frac{1}{T_{G0}}} P_{sleep} \quad (8)$$

B. Initial stem cell estimation

The initial stem cell population, is adapted to the observed size of the recurrent tumour. The adaptation has been performed automatically using an optimization procedure (the built-in function 'fzero' of Matlab), that returns the value of the stem cell population for which the difference between the observed tumour size and the simulation outcome is zero. During this optimization procedure the rest of the model parameters are kept constant.

5.5.2.2. Results

The following tumour proliferation features have been considered in the present analysis: a. $T_d=60d$, 100d and 225d, b. GF equal to the patient's proliferation index (PI) or equal to 0.18 if PI is absent. The latter value corresponds to the average of median values reported in the reviewed literature for adenocarcinoma (D6.2). The ranges of the model parameters are given in Table 5. LHS has been run to generate 30 combinations of parameter values that fulfill the above requirements, as described previously. Combinations that result in negative cell class transition rates, namely negative P_{sleep} and R_{NDiff} , are excluded.

For each clinical case and for each of the finally considered value sets, the initial stem population that results in the observed tumour volume is estimated. Since, local tumour spread takes place by the collective migration of cancer cells or by migrating individual tumour cells [Höckel and Dornhöfer, 2005], as a starting hypothesis, solution is searched in the range between 1 and 1000 stem cells. A collection of more than 1000 stem cells would most probably associated with the existence of visible lesions after surgery and are, therefore, not considered in the present analysis.³ The following figures show the results of the adaptation for each clinical case.

Recurrence is due to the stem cells that have remained after surgery. However, as expected, since stem cell consists a small minority, the cell population that re-populates the tumour are the progenitor (LIMP) cells [Moore and Lyle, 2011]. Furthermore, we observe that the initial stem cell population is highly correlated with the fraction of stem cells that perform symmetric division, P_{sym} , and the growth rate of stem cells. Higher P_{sym} values and slower growth rates (higher doubling time) are associated with a lower population of initial stem cells that needs to have escaped therapy in order to re-establish the tumour. Finally, slowly growing stem cells seem to be associated with solutions that give visible tumours within the first few months after surgery. In the present analysis

³ A group of more than 1000 stem cells is more likely to be accompanied by the rest of the cell types that constitute a tumour, i.e. progenitor and terminally differentiated cells, at population equilibrium. According to Ishizawa et al. (2010) stem cell frequency in NSCLC adenocarcinoma can be as low as 0.00005. Based on this value 1000 stems cells corresponds to $20 \cdot 10^6$ living tumour cells and a tumour volume of 20 mm^3 (typical cell density $10^6/\text{mm}^3$ [Begg and Steel, 2002]) that can be visible by imaging modalities [Chiles, 2014].

the dynamics of stem and LIMP are considered the same. Further adaptation studies need to be performed assuming different dynamics between these populations.

Table 5. Value range of input parameters

Parameter symbol	Description	Units	Value range	References
CELL PHASE DURATIONS				
T_c	Cell cycle duration of stem and LIMP cells	hours	20-120	Lieber et al., 1976; Kimura et al. 1979; Loh et al. 1984; Olsson et al. 1984; Brower et al. 1986; Masuda et al. 1991; Campling et al. 1992 Liu & Tsao, 1993; Giaccone et al. 1992; Li et al. 2012
T_{G0}	G0 (dormant phase) duration of stem and LIMP cells	hours	90-500	extension of Durand & Sham 1998
T_{AL}	Time needed for both apoptosis to be completed and its products to be removed from the tumour	hours	1-25	Kerr et al. 1972, Gavrieli et al., 1992; Bursch et al. 1990
T_N	Time needed for both necrosis to be completed and its products to be removed from the tumour	hours	1-200	Ginsberg T., 1996
CELL CATEGORY/PHASE TRANSITION RATES AND FRACTIONS¹				
R_A	Apoptosis rate of living stem and LIMP cells	hours ⁻¹	0-0.001	estimation
R_{ADiff}	Apoptosis rate of differentiated tumour cells	hours ⁻¹	0.0001-0.02	extension of Rawlins & Hogan, 2006, 2008; Lippmann 2000; Flindt 2006;
R_{NDiff}	Necrosis rate of differentiated tumour cells	hours ⁻¹		Estimated to achieve the given GF
P_{sym}	Fraction of stem cells that perform symmetric division	-	0-0.4	estimation based on Pine et al. 2010; Morrison et al. 2012
P_{sleep}	Fraction of cells entering the G0 phase following mitosis	-		Estimated to achieve the given T_d
P_{G0toG1}	Fraction of dormant (stem and LIMP) cells that re-enter cell cycle	-	0-0.1	-
¹ The parameters included under this term express fractions and, therefore, can theoretically take any value between zero and unity. Whenever possible this range has been narrowed based on logical assumptions supported by literature or basic science.				

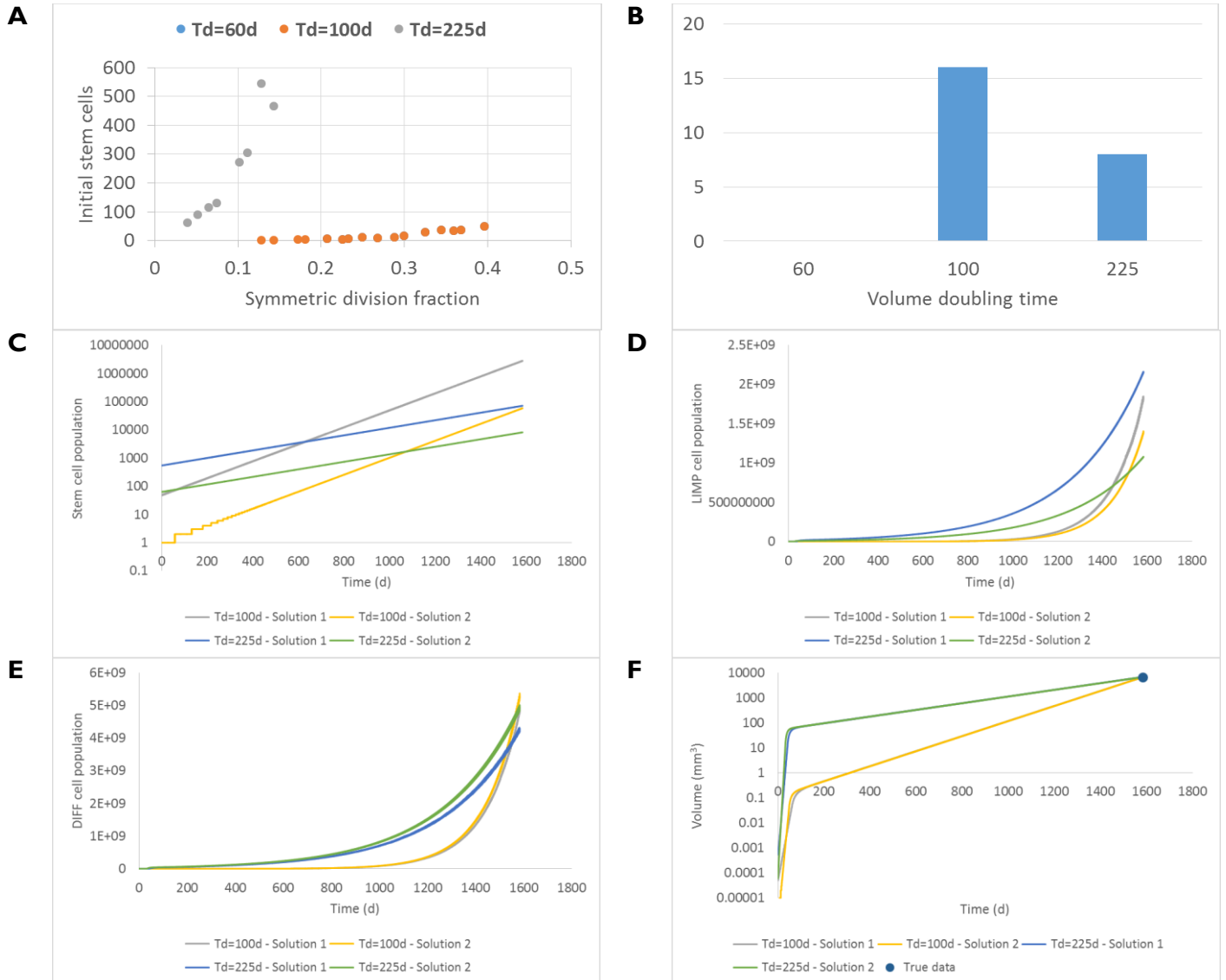


Fig 9. Adaptation results for clinical case #1. Latin Hypercube Sampling (LHS) has run to produce two sets of 30 combinations of model parameters. Combinations with negative cell phase transition rates and solutions with more than 1000 initial stem cells have been excluded. A. Scatterplot of the initial stem population vs. the fraction of stem cells that perform symmetric division. B. Number of solutions found per volume doubling time value. C. Time course of stem cell population for two indicative solutions per T_d value. D. Time course of LIMP cell population for two indicative solutions per T_d value. E. Time course of terminally differentiated cell population for two indicative solutions per T_d value. F. Time course of tumour volume for two indicative solutions per T_d value.

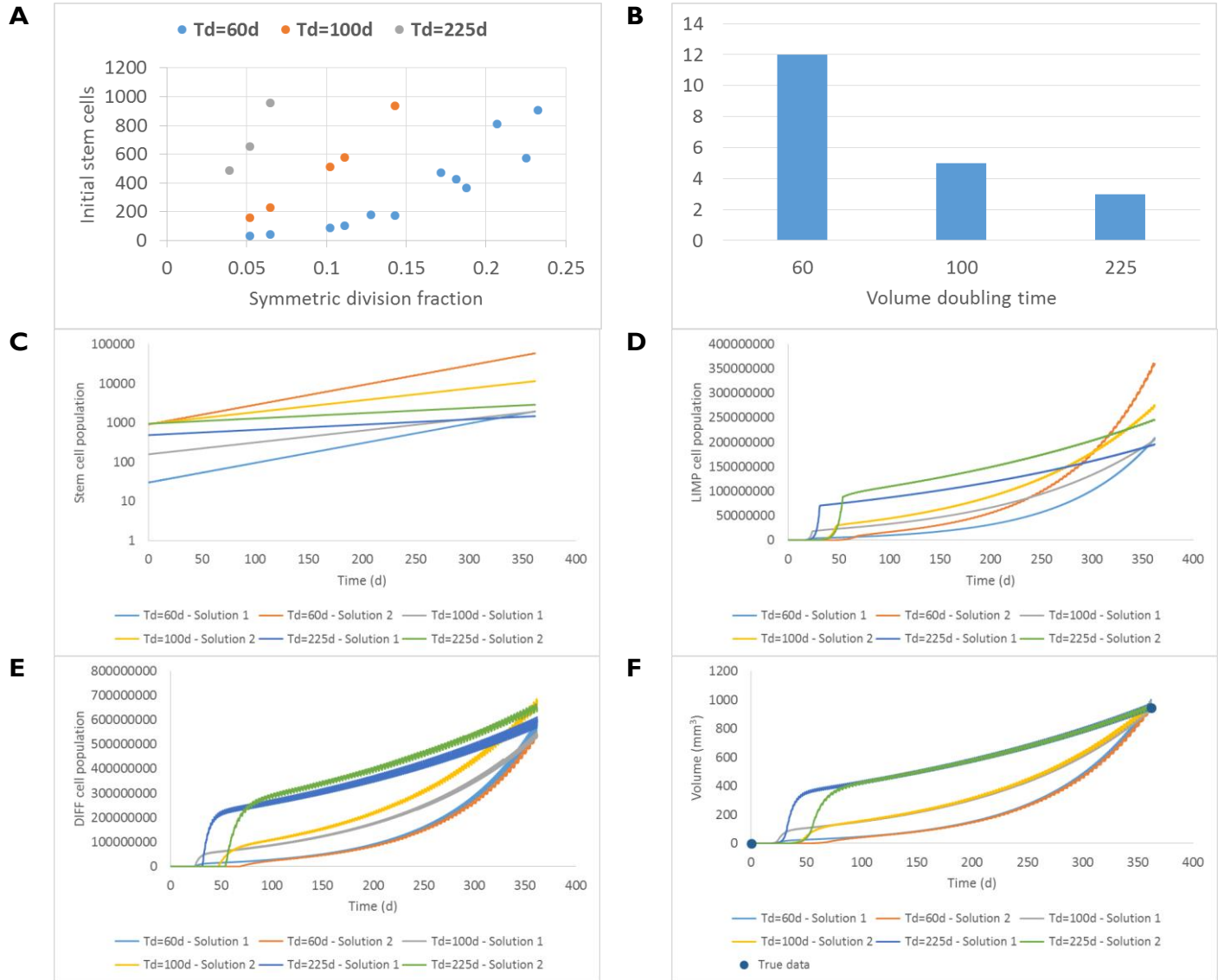


Fig 10. Adaptation results for clinical case #2. Latin Hypercube Sampling (LHS) has run to produce two sets of 30 combinations of model parameters. Combinations with negative cell phase transition rates and solutions with more than 1000 initial stem cells have been excluded. A. Scatterplot of the initial stem population vs. the fraction of stem cells that perform symmetric division. B. Number of solutions found per volume doubling time value. C. Time course of stem cell population for two indicative solutions per T_d value. D. Time course of LIMP cell population for two indicative solutions per T_d value. E. Time course of terminally differentiated cell population for two indicative solutions per T_d value. F. Time course of tumour volume for two indicative solutions per T_d value.

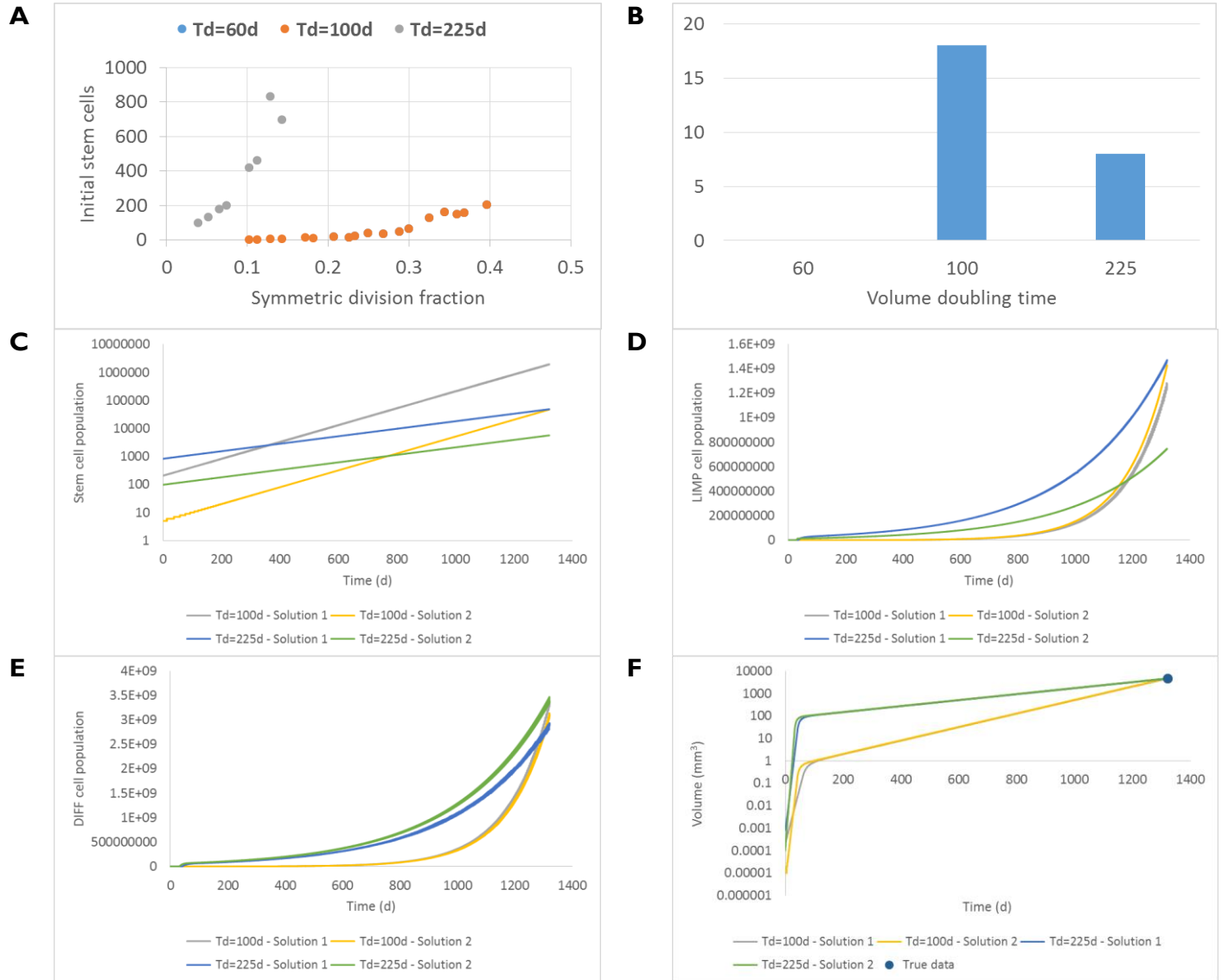


Fig 11. Adaptation results for clinical case #3. Latin Hypercube Sampling (LHS) has run to produce two sets of 30 combinations of model parameters. Combinations with negative cell phase transition rates and solutions with more than 1000 initial stem cells have been excluded. A. Scatterplot of the initial stem population vs. the fraction of stem cells that perform symmetric division. B. Number of solutions found per volume doubling time value. C. Time course of stem cell population for two indicative solutions per T_d value. D. Time course of LIMP cell population for two indicative solutions per T_d value. E. Time course of terminally differentiated cell population for two indicative solutions per T_d value. F. Time course of tumour volume for two indicative solutions per T_d value.

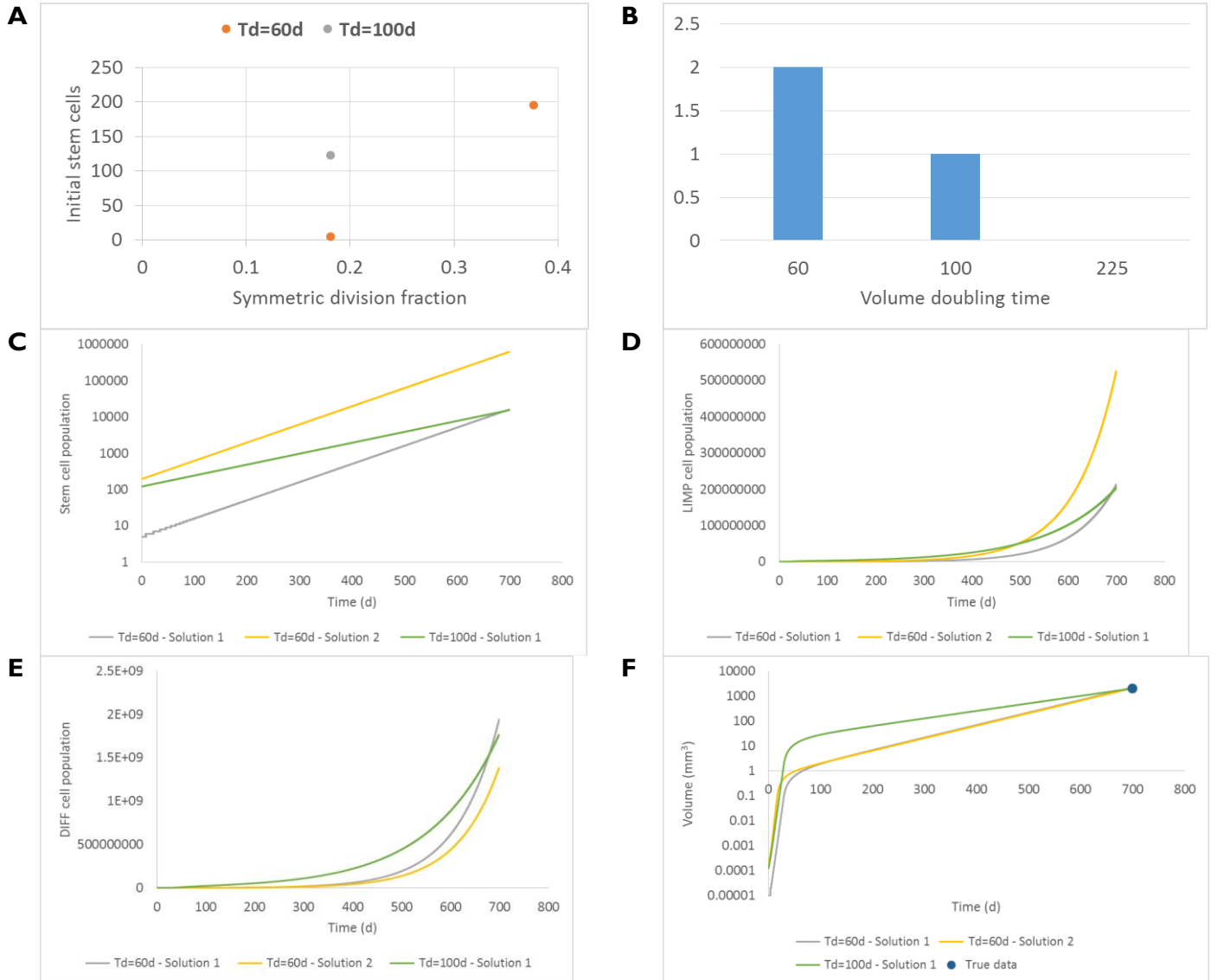


Fig 12. Adaptation results for clinical case #4. Latin Hypercube Sampling (LHS) has run to produce two sets of 30 combinations of model parameters. Combinations with negative cell phase transition rates and solutions with more than 1000 initial stem cells have been excluded. A. Scatterplot of the initial stem population vs. the fraction of stem cells that perform symmetric division. B. Number of solutions found per volume doubling time value. C. Time course of stem cell population for two indicative solutions per T_d value. D. Time course of LIMP cell population for two indicative solutions per T_d value. E. Time course of terminally differentiated cell population for two indicative solutions per T_d value. F. Time course of tumour volume for two indicative solutions per T_d value.

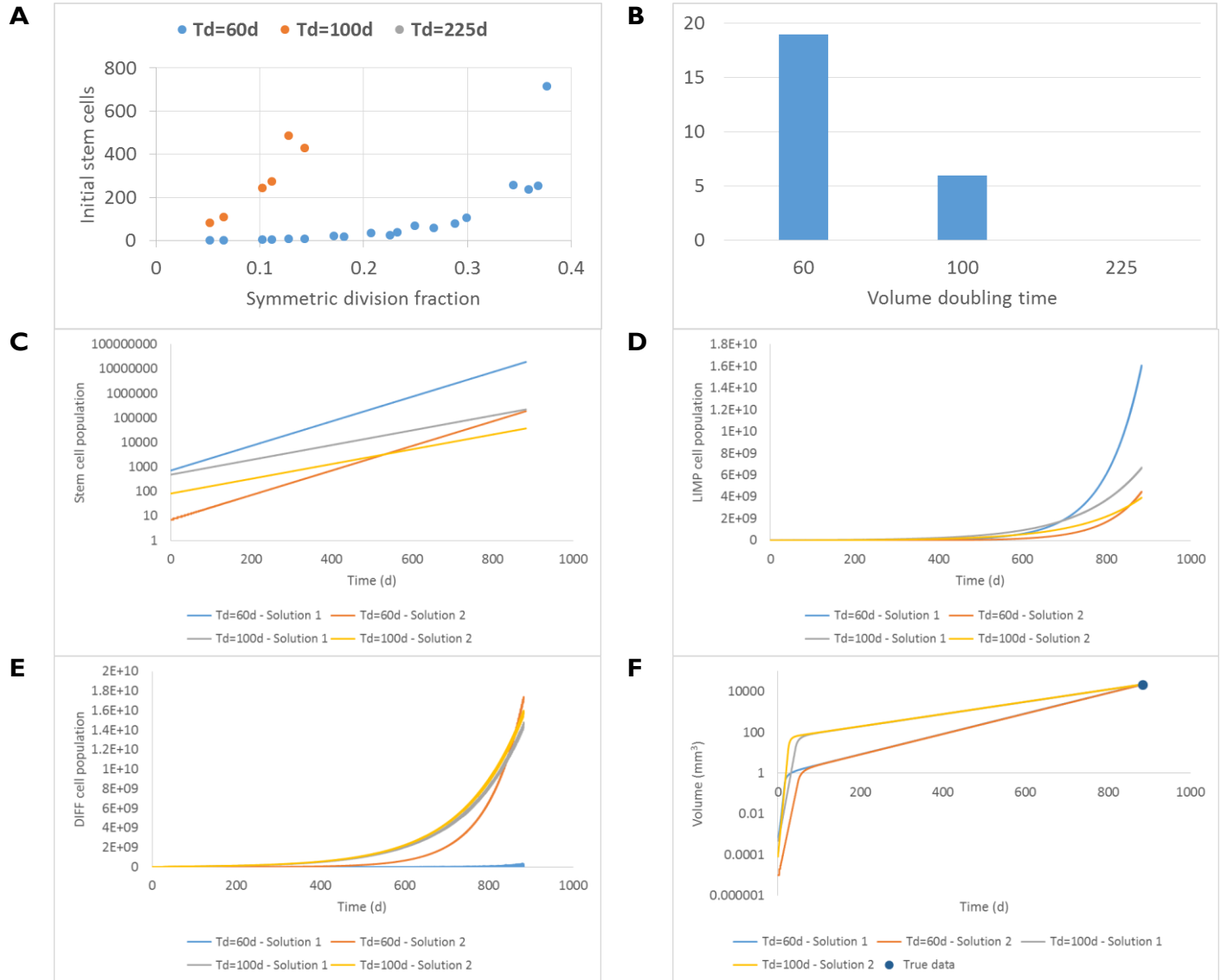


Fig 13. Adaptation results for clinical case #5. Latin Hypercube Sampling (LHS) has run to produce two sets of 30 combinations of model parameters. Combinations with negative cell phase transition rates and solutions with more than 1000 initial stem cells have been excluded. A. Scatterplot of the initial stem population vs. the fraction of stem cells that perform symmetric division. B. Number of solutions found per volume doubling time value. C. Time course of stem cell population for two indicative solutions per T_d value. D. Time course of LIMP cell population for two indicative solutions per T_d value. E. Time course of terminally differentiated cell population for two indicative solutions per T_d value. F. Time course of tumour volume for two indicative solutions per T_d value.

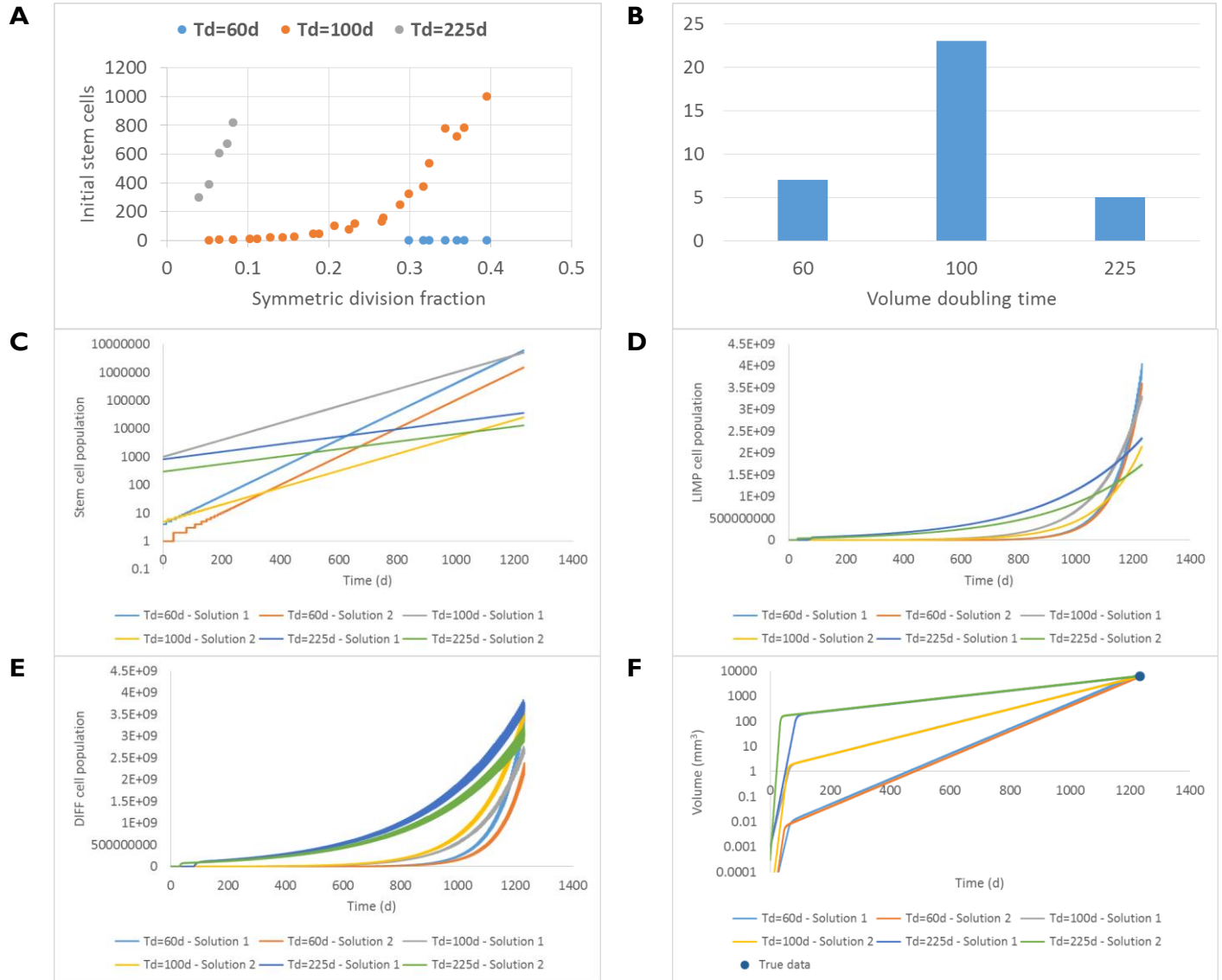


Fig 14. Adaptation results for clinical case #6. Latin Hypercube Sampling (LHS) has run to produce two sets of 30 combinations of model parameters. Combinations with negative cell phase transition rates and solutions with more than 1000 initial stem cells have been excluded. A. Scatterplot of the initial stem population vs. the fraction of stem cells that perform symmetric division. B. Number of solutions found per volume doubling time value. C. Time course of stem cell population for two indicative solutions per T_d value. D. Time course of LIMP cell population for two indicative solutions per T_d value. E. Time course of terminally differentiated cell population for two indicative solutions per T_d value. F. Time course of tumour volume for two indicative solutions per T_d value.

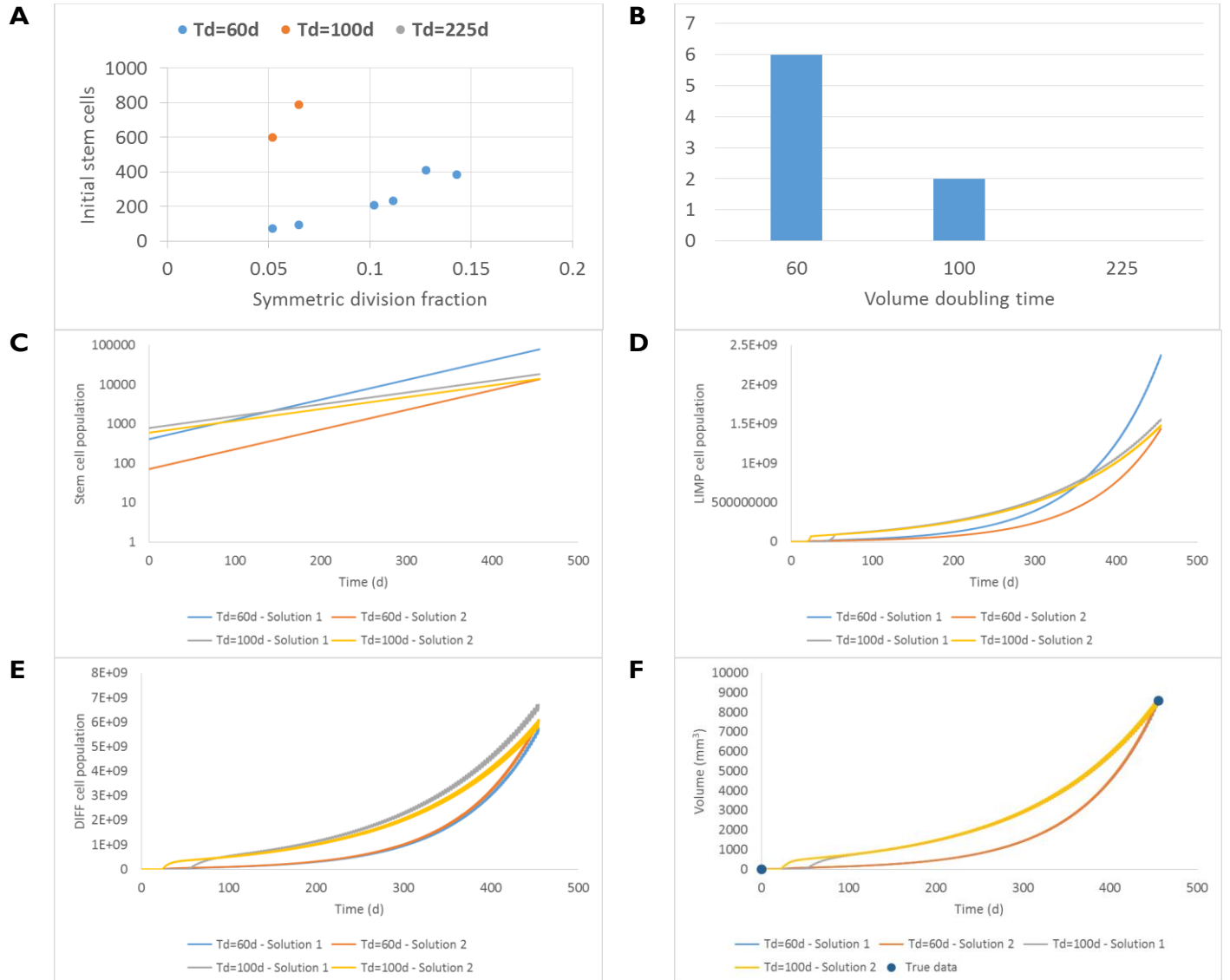


Fig 15. Adaptation results for clinical case #7. Latin Hypercube Sampling (LHS) has run to produce two sets of 30 combinations of model parameters. Combinations with negative cell phase transition rates and solutions with more than 1000 initial stem cells have been excluded. A. Scatterplot of the initial stem population vs. the fraction of stem cells that perform symmetric division. B. Number of solutions found per volume doubling time value. C. Time course of stem cell population for two indicative solutions per T_d value. D. Time course of LIMP cell population for two indicative solutions per T_d value. E. Time course of terminally differentiated cell population for two indicative solutions per T_d value. F. Time course of tumour volume for two indicative solutions per T_d value

5.5.3 Case scenario C: Progression and response to treatment of recurrent Non-Small-Cell Lung Cancer

Randomized clinical trials with advanced NSCLC, have shown that second-line chemotherapy in NSCLC patients who failed or relapsed first-line therapy, can offer modest and marginal survival benefits at the cost of considerable toxicity [Froudarakis & Briasoulis, 2010]. It is apparent that the optimal medical management of relapsed patients is a necessity and appropriate tools need to be developed to safe-guide therapeutic decisions. Treatment options include cisplatin or carboplatin combined with vinorelbine, docetaxel, gemcitabine, pemetrexed, etc., epidermal growth factor receptor inhibitors (erlotinib and gefitinib) and radiotherapy.

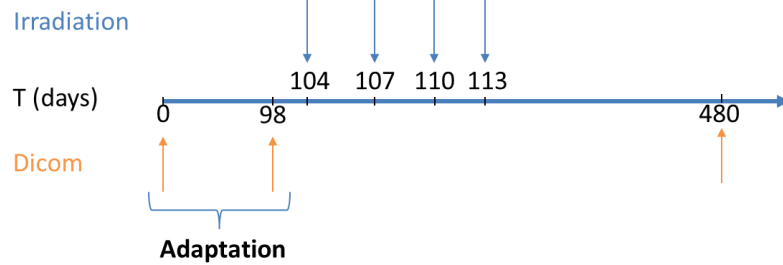
In the present study, we adapt and validate the Lung Hypermodel with a recurrent NSCLC adenocarcinoma case treated with irradiation. The clinical question addressed by the Hypermodel concerns the prediction of volume reduction of the tumour one year following the completion of tumour irradiation. The progression ‘phase’ of the recurrent tumour before irradiation is used to adapt the Lung Oncosimulator. More specifically, a group of virtual tumours that constitute solutions to the same adaptation problem and efficiently cover the parameter space are derived. These virtual tumours have common predefined proliferation characteristics i.e. growth fraction and doubling time, but, in general, will differ in their response to treatment. At a second step the Hypermodel is run to simulate tumour progression and treatment response and predict tumour volume after irradiation.

5.5.3.1 Patient data

One patient is considered in the present study. The patient received four fractions of 15 Gy. The radiation schedule is depicted in Fig 16. The patient specific data that have been exploited by the Lung Hypermodel are his/her mutation and miRNA data, proliferation index, the applied radiotherapeutic scheme (dose, radiation instants) and the 3D image of the tumour as reconstructed from CT imaging data. The sets of imaging data were provided for three time instants before and after treatment (Fig 16). There is no visible tumour approximately one year after treatment. Due to the non-availability of data related to any distinct internal metabolic regions, the virtual tumour implemented is homogeneous with a shape compliant to the reconstructed tumour image.

Irradiation schedule

- ☐ Total: 60Gy
- ☐ Dose: 15Gy/day



- ☐ Volume on day 0 based on the DICOM data: ~ 4.5 ml
- ☐ Volume on day 98 based on the DICOM data : ~ 5.5 ml
- ☐ Volume on day 480 based on the DICOM data : **no visible tumor**

Fig 16. Treatment schedule and volumetric measurements.

5.5.3.2 Hypermodel Adaptation and Validation

At the adaptation step, the following constrains/assumptions have been exploited

- The virtual tumour implementation must have a growth fraction (GF) equal to the proliferation index (Ki67) of the patient (=0.23).
- The volume doubling time must be around 370 days. The doubling time has been estimated based on the observed volume increase between the two available volumetric data before the radiation therapy.
- The value range of the input parameters are depicted in Table 6.

LHS has been run to generate 100 combinations of parameter values that fulfill the above requirements, following the methodology described in section 'Clinical Scenario B'. Combinations that result in negative cell class transition rates, namely negative P_{sleep} and R_{NDiff} , are excluded.

Table 7 lists the input parameter related to tumour cell kinetics, following adaptation of the hypermodel to the clinical case consider. The resulting tumour cell composition for each value

combination of input parameters are given in Table 8. The hypermodel predicts a lesion of 1mm^3 (Table 7) for all value combinations considered at the time point of the final CT acquisition. The predicted volume size is below the detection limit.

Table 6. Value Range of input parameters

Parameter	Range
Cell cycle duration (h)	20-70
Duration of dormant phase (h)	90-500
Time needed for necrosis products to disappear (h)	1-200
Time needed for apoptosis products to be removed (h)	1-25
Number of mitoses performed by LIMP cells before differentiation	18
Apoptosis rate of stem and LIMP cells (h^{-1})	0-0.001
Apoptosis rate of differentiated cells (h^{-1})	0.0002-0.003
Necrosis rate of differentiated cells (h^{-1})	Estimated to achieve the given GF
Fraction of G0 cells that re-enter cell cycle	0-1
Fraction of cells that enter G0 phase following mitosis	Estimated to achieve the given T_d
Fraction of stem cells that perform symmetric division	0-0.4

Table 7. Adaptation of parameter values and predicted tumour size

#	T_c (h)	T_G (h)	T_N (h)	T_A (h)	R_A (h ⁻¹)	R_{ADIF} (h ⁻¹)	R_{NDIF} (h ⁻¹)	P_{G0toG}	P_{sym}	P_{sleep}	N_{LIM}	Final Volume (mm ³)	Final Diameter (mm)
1	33	148	135	12	0.0002	0.0009	0.0237	0.9195	0.0727	0.4840	18	1.0921	1.2777
2	48	191	113	11	0.0010	0.0026	0.0049	0.8980	0.1335	0.2776	18	0.9272	1.2098
3	39	230	184	18	0.0010	0.0014	0.0122	0.7371	0.2080	0.3367	18	1.0701	1.2690
4	34	336	111	13	0.0009	0.0030	0.1164	0.3009	0.3749	0.3196	18	0.9961	1.2391
5	37	102	47	15	0.0007	0.0009	0.0070	0.3297	0.3344	0.3300	18	0.9885	1.2359
6	55	234	181	4	0.0009	0.0004	0.0052	0.7212	0.1322	0.1701	18	0.9539	1.2213
7	53	212	163	10	0.0009	0.0005	0.0050	0.4222	0.1840	0.1741	18	1.0120	1.2456
8	41	255	118	23	0.0010	0.0026	0.0077	0.3827	0.2919	0.2764	18	0.9880	1.2357
9	51	465	116	22	0.0010	0.0018	0.0058	0.6477	0.1818	0.1890	18	0.9724	1.2292
10	45	141	162	18	0.0006	0.0002	0.0067	0.4407	0.2228	0.2642	18	0.9881	1.2358
11	49	182	4	11	0.0006	0.0028	0.0034	0.3520	0.2049	0.2101	18	0.9474	1.2186
12	58	500	128	14	0.0009	0.0021	0.0034	0.6578	0.1387	0.1202	18	0.9549	1.2218
13	53	199	60	23	0.0007	0.0008	0.0050	0.5361	0.1531	0.1834	18	1.0158	1.2472
14	46	268	121	10	0.0007	0.0017	0.0064	0.3337	0.2421	0.2287	18	0.9885	1.2359
15	42	281	94	21	0.0006	0.0027	0.0083	0.2767	0.2830	0.2577	18	0.9465	1.2182
16	36	344	192	19	0.0006	0.0003	0.0805	0.6836	0.2062	0.3349	18	0.9643	1.2258
17	43	453	86	3	0.0008	0.0027	0.0161	0.8881	0.1587	0.2756	18	1.0314	1.2536
18	64	388	87	20	0.0005	0.0006	0.0041	0.8491	0.0540	0.0627	18	1.1582	1.3030
19	52	253	167	1	0.0005	0.0015	0.0050	0.5520	0.1451	0.1885	18	1.0085	1.2442
20	57	17	17	15	0.000	0.001	0.003	0.6267	0.105	0.150	18	0.9018	1.1987

#	T_c (h)	T_G (h)	T_N (h)	T_A (h)	R_A (h ⁻¹)	R_{ADIF} (h ⁻¹)	R_{NDIF} (h ⁻¹)	P_{G0toG}	P_{sym}	P_{sleep}	N_{LIM}	Final Volume (mm ³)	Final Diameter (mm)
0		4	9		5	4	9		0	2			
21	51	214	91	13	0.0006	0.0003	0.0067	0.8251	0.1020	0.2270	18	1.1553	1.3019
22	46	143	120	17	0.0004	0.0004	0.0059	0.2088	0.2515	0.2275	18	0.9627	1.2251
23	63	240	77	6	0.0001	0.0012	0.0036	0.2329	0.0623	0.0657	18	0.9010	1.1983
24	49	371	189	15	0.0004	0.0030	0.0058	0.3427	0.1909	0.1983	18	0.8963	1.1962
25	59	353	80	14	0.0004	0.0023	0.0032	0.5959	0.0862	0.1128	18	0.8891	1.1930
26	62	127	153	8	0.0005	0.0005	0.0042	0.7404	0.0683	0.1047	18	0.8669	1.1830
27	44	424	35	21	0.0004	0.0013	0.0163	0.4736	0.2015	0.2459	18	0.9068	1.2009
28	61	165	141	20	0.0001	0.0007	0.0042	0.6375	0.0553	0.1051	18	0.9906	1.2368
29	50	94	146	19	0.0002	0.0007	0.0049	0.3705	0.1775	0.2171	18	0.9003	1.1980
30	42	322	126	23	0.0007	0.0019	0.0097	0.1633	0.3177	0.2486	18	0.9185	1.2060
31	47	91	30	22	0.0001	0.0007	0.0053	0.3613	0.2020	0.2467	18	0.8983	1.1971
32	37	367	107	6	0.0006	0.0029	0.0609	0.1733	0.3602	0.2868	18	0.9241	1.2085
33	39	361	32	10	0.0008	0.0015	0.0180	0.1521	0.3620	0.2704	18	0.9151	1.2045
34	60	411	22	3	0.0003	0.0012	0.0039	0.0923	0.1191	0.0906	18	0.7248	1.1145
35	54	390	38	2	0.0009	0.0027	0.0032	0.2417	0.2007	0.1494	18	0.9238	1.2084
36	68	203	105	11	0.0007	0.0012	0.0028	0.1281	0.0658	0.0136	18	0.7807	1.1424
37	44	227	187	20	0.0003	0.0004	0.0082	0.2156	0.2578	0.2394	18	0.9374	1.2143
38	35	160	71	24	0.0008	0.0014	0.0079	0.0524	0.4387	0.2964	18	0.9171	1.2054
39	58	207	21	8	0.0000	0.0019	0.0035	0.4188	0.0861	0.1239	18	1.2262	1.3280
40	41	121	158	9	0.0002	0.0002	0.0064	0.0344	0.3357	0.2505	18	0.8905	1.1937
41	55	137	98	16	0.0002	0.0004	0.0046	0.1122	0.1629	0.1400	18	0.9380	1.2145
42	56	113	84	12	0.0001	0.0028	0.0025	0.5471	0.0933	0.1677	18	1.1777	1.3102
43	65	404	17	18	0.0008	0.0025	0.0019	0.7064	0.0842	0.0491	18	1.2811	1.3475
44	59	492	42	17	0.0007	0.0010	0.0042	0.1038	0.1542	0.0998	18	0.8968	1.1965

#	T_c (h)	T_G (h)	T_N (h)	T_A (h)	R_A (h ⁻¹)	R_{ADIF} (h ⁻¹)	R_{NDIF} (h ⁻¹)	P_{G0toG}	P_{sym}	P_{sleep}	N_{LIM} _P	Final Volume (mm ³)	Final Diameter (mm)
45	60	135	133	24	0.0004	0.0021	0.0024	0.0791	0.1276	0.0920	18	0.7665	1.1354
46	48	196	95	12	0.0006	0.0013	0.0046	0.0102	0.2786	0.1926	18	0.8782	1.1881
47	56	297	145	11	0.0005	0.0010	0.0053	0.9335	0.0660	0.1630	18	0.8359	1.1687
48	47	186	160	10	0.0008	0.0029	0.0029	0.0039	0.3047	0.2003	18	0.9163	1.2051
49	59	402	26	7	0.0002	0.0025	0.0034	0.6094	0.0698	0.1115	18	0.9869	1.2353
50	31	104	16	25	0.0007	0.0016	0.0116	0.5142	0.3213	0.4256	18	1.0724	1.2699
51	61	108	140	5	0.0001	0.0023	0.0024	0.5092	0.0684	0.1056	18	0.7529	1.1287
52	66	127	76	19	0.0004	0.0024	0.0017	0.0218	0.0685	0.0329	18	0.6991	1.1012
53	40	219	165	6	0.0000	0.0015	0.0119	0.3964	0.2191	0.2901	18	0.9201	1.2067
54	54	301	66	7	0.0001	0.0024	0.0044	0.5861	0.0935	0.1663	18	1.1918	1.3154
55	63	325	172	4	0.0004	0.0017	0.0030	0.4990	0.0714	0.0693	18	0.8841	1.1908
56	68	351	23	5	0.0006	0.0020	0.0020	0.8722	0.0515	0.0162	18	0.8029	1.1531
57	67	478	55	15	0.0007	0.0020	0.0022	0.6199	0.0703	0.0256	18	0.9331	1.2124
58	68	274	5	21	0.0004	0.0008	0.0033	0.3118	0.0406	0.0142	18	0.9877	1.2356
59	43	158	58	9	0.0003	0.0008	0.0090	0.7941	0.1112	0.3342	18	1.0408	1.2574
60	66	430	44	17	0.0003	0.0014	0.0031	0.2587	0.0499	0.0343	18	0.8994	1.1976
61	40	292	123	19	0.0006	0.0022	0.0170	0.9541	0.1087	0.3358	18	0.9541	1.2214
62	45	311	55	22	0.0005	0.0021	0.0103	0.9243	0.0939	0.2785	18	1.1196	1.2883
63	51	284	52	3	0.0005	0.0017	0.0062	0.9073	0.0828	0.2191	18	1.0011	1.2411
64	38	263	197	7	0.0004	0.0017	0.0219	0.8138	0.1242	0.3465	18	1.1372	1.2950
65	37	278	89	5	0.0003	0.0025	0.0312	0.7853	0.1279	0.3485	18	0.9505	1.2199
66	22	117	8	6	0.0003	0.0027	0.9095	0.4342	0.3939	0.4712	18	0.9503	1.2198

Table 8. Resulting cancer characteristics for each value combination of input parameters

#	Stem/Living	LIMP/Living	Prolif/Living	G0/Living	DIFF/Living	Apoptotic/Total	Necrotic/Total
1	0.00001	0.7359	0.2202	0.5157	0.2641	0.0024	0.4626
2	0.00002	0.4597	0.2260	0.2338	0.5403	0.0140	0.2307
3	0.00008	0.6629	0.2258	0.4371	0.3371	0.0103	0.4490
4	0.00114	0.9636	0.2275	0.7372	0.0353	0.0073	0.3768
5	0.00033	0.4836	0.2277	0.2563	0.5161	0.0087	0.1943
6	0.00001	0.3794	0.2286	0.1508	0.6206	0.0011	0.3759
7	0.00003	0.3831	0.2283	0.1548	0.6169	0.0036	0.3593
8	0.00024	0.6248	0.2282	0.3969	0.3749	0.0235	0.3010
9	0.00004	0.5345	0.2285	0.3061	0.4654	0.0210	0.2464
10	0.00006	0.4387	0.2282	0.2106	0.5612	0.0037	0.4204
11	0.00005	0.4194	0.2283	0.1912	0.5805	0.0182	0.0085
12	0.00002	0.4028	0.2287	0.1741	0.5972	0.0165	0.2083
13	0.00002	0.3841	0.2279	0.1562	0.6159	0.0135	0.1656
14	0.0001	0.5376	0.2280	0.3097	0.4623	0.0071	0.3035
15	0.00022	0.6496	0.2282	0.4216	0.3502	0.0190	0.2651
16	0.0001	0.9379	0.2258	0.7122	0.0620	0.0051	0.5137
17	0.00004	0.7657	0.2264	0.5393	0.2343	0.0019	0.2476
18	$<10^{-5}$	0.3049	0.2298	0.0751	0.6951	0.0083	0.1970
19	0.00002	0.4337	0.2277	0.2060	0.5663	0.0000	0.3419
20	0.00001	0.3327	0.2283	0.1044	0.6673	0.0103	0.3255
21	0.00001	0.4364	0.2267	0.2098	0.5636	0.0036	0.2606
22	0.00009	0.4179	0.2294	0.1886	0.5821	0.0039	0.3452
23	$<10^{-5}$	0.2888	0.2298	0.0590	0.7112	0.0035	0.1695
24	0.00005	0.5741	0.2282	0.3459	0.4259	0.0132	0.3580
25	0.00001	0.3728	0.2288	0.1440	0.6272	0.0171	0.1448
26	$<10^{-5}$	0.2773	0.2287	0.0487	0.7227	0.0022	0.3181
27	0.00008	0.7647	0.2277	0.5371	0.2352	0.0107	0.1310
28	$<10^{-5}$	0.2946	0.2282	0.0664	0.7055	0.0072	0.3001
29	0.00002	0.3354	0.2282	0.1072	0.6646	0.0060	0.3612
30	0.00038	0.6846	0.2299	0.4552	0.3150	0.0151	0.3395
31	0.00004	0.3570	0.2279	0.1291	0.6429	0.0087	0.1111
32	0.00091	0.9374	0.2304	0.7079	0.0617	0.0023	0.3592
33	0.00081	0.8098	0.2301	0.5805	0.1894	0.0074	0.1285

#	Stem/Living	LIMP/Living	Prolif/Living	G0/Living	DIFF/Living	Apoptotic/Total	Necrotic/Total
34	0.00001	0.3641	0.2299	0.1342	0.6359	0.0017	0.0556
35	0.00005	0.4412	0.2299	0.2114	0.5587	0.0018	0.0743
36	<10 ⁻⁵	0.2384	0.2299	0.0084	0.7616	0.0087	0.1794
37	0.00013	0.5567	0.2300	0.3268	0.4432	0.0034	0.4647
38	0.00164	0.6144	0.2299	0.3862	0.3839	0.0173	0.2671
39	0.00001	0.3359	0.2282	0.1077	0.6641	0.0085	0.0491
40	0.00031	0.4476	0.2300	0.2179	0.5521	0.0010	0.4495
41	0.00002	0.3185	0.2299	0.0886	0.6815	0.0037	0.2637
42	0.00001	0.3115	0.2280	0.0835	0.6885	0.0182	0.1418
43	<10 ⁻⁵	0.2844	0.2298	0.0546	0.7156	0.0319	0.0209
44	0.00002	0.3852	0.2300	0.1552	0.6148	0.0125	0.1031
45	0.00001	0.2792	0.2298	0.0494	0.7208	0.0293	0.2037
46	0.00014	0.4295	0.2299	0.1997	0.5704	0.0082	0.2511
47	<10 ⁻⁵	0.4080	0.2283	0.1796	0.5920	0.0055	0.3094
48	0.0002	0.4283	0.2299	0.1986	0.5716	0.0126	0.2937
49	0.00001	0.3963	0.2288	0.1676	0.6037	0.0090	0.0514
50	0.00036	0.6221	0.2251	0.3974	0.3775	0.0226	0.0849
51	<10 ⁻⁵	0.2729	0.2281	0.0448	0.7271	0.0054	0.2111
52	<10 ⁻⁵	0.2443	0.2299	0.0144	0.7557	0.0302	0.0935
53	0.00009	0.6653	0.2272	0.4383	0.3346	0.0014	0.4552
54	0.00001	0.4457	0.2277	0.2179	0.5543	0.0071	0.1503
55	<10 ⁻⁵	0.3053	0.2297	0.0756	0.6947	0.0029	0.2709
56	<10 ⁻⁵	0.2459	0.2299	0.0160	0.7541	0.0065	0.0324
57	<10 ⁻⁵	0.2615	0.2299	0.0317	0.7385	0.0207	0.0785
58	<10 ⁻⁵	0.2421	0.2300	0.0121	0.7580	0.0140	0.0099
59	0.00001	0.5191	0.2241	0.2950	0.4809	0.0033	0.2111
60	<10 ⁻⁵	0.2766	0.2299	0.0466	0.7234	0.0150	0.0890
61	0.00002	0.7360	0.2246	0.5114	0.2640	0.0122	0.3505
62	0.00001	0.6307	0.2254	0.4053	0.3693	0.0185	0.1700
63	0.00001	0.4845	0.2267	0.2578	0.5155	0.0019	0.1418
64	0.00002	0.7774	0.2255	0.5520	0.2226	0.0020	0.5031
65	0.00003	0.8392	0.2249	0.6143	0.1608	0.0018	0.3234
66	0.00149	0.9917	0.2263	0.7669	0.0068	0.0016	0.0684

5.6 References

Begg, A.C., Steel, G.G., 2002. Cell proliferation and growth rate of tumours. In: Steel, G.G. (Ed.), *Basic Clinical Radiobiology*, third ed. Arnold, London, UK.

J. Borgdorff, M. Mamonski, B. Bosak, K. Kurowski, M. Ben Belgacem, B. Chopard, D. Groen, P. V. Coveney, and A. G. Hoekstra, "Distributed multiscale computing with MUSCLE 2, the Multiscale Coupling Library and Environment," *Journal of Computational Science*, vol. 5, no. 5, pp. 719–731, Sep. 2014.

Bourgarel-Rey V, Savry A, Hua G, Carré M, Bressin C, Chacon C, Imbert J, Braguer D, Barra Y. Transcriptional down-regulation of Bcl-2 by vinorelbine: identification of a novel binding site of p53 on Bcl-2 promoter. *Biochem Pharmacol.* 2009 Nov 1;78(9):1148-56. doi: 10.1016/j.bcp.2009.06.025. Epub 2009 Jun 23.

Brouckaert G, Kalai M, Krysko DV, Saelens X, Vercammen D, Ndlovu MN, et al. Phagocytosis of necrotic cells by macrophages is phosphatidylserine dependent and does not induce inflammatory cytokine production. *Mol Biol Cell.* 2004 Mar;15(3):1089-100.

Brower M, Carney DN, Oie HK, Gazdar AF, Minna JD. Growth of cell lines and clinical specimens of human non-small cell lung cancer in a serum-free defined medium. *Cancer Res.* 1986 Feb;46(2):798-806.

Bursch W, Paffe S, Putz B, Barthel G, Schulte-Hermann R. Determination of the length of the histological stages of apoptosis in normal liver and in altered hepatic foci of rats. *Carcinogenesis.* 1990 May;11(5):847-53.

Campling BG, Haworth AC, Baker HM, Greer DL, Holden JJ, Bradley EC, et al. Establishment and characterization of a panel of human lung cancer cell lines. *Cancer.* 1992 Apr 15;69(8):2064-74.

Carnio S, Novello S, Papotti M, et al. Prognostic and predictive biomarkers in early stage non small-cell lung cancer: tumour based approaches including gene signatures. *Transl Lung Cancer Res* 2013;2:372-81.

Chiles Caroline, Lung Cancer Screening with Low Dose CT, *Radiol Clin North Am.* 2014 Jan; 52(1): 27–46. doi: 10.1016/j.rcl.2013.08.006

Chiu WH, Luo SJ, Chen CL, Cheng JH, Hsieh CY, Wang CY, Huang WC, Su WC, Lin CF. Vinca alkaloids cause aberrant ROS-mediated JNK activation, Mcl-1 downregulation, DNA damage, mitochondrial dysfunction, and apoptosis in lung adenocarcinoma cells. *Biochem Pharmacol.* 2012 May 1;83(9):1159-71. doi: 10.1016/j.bcp.2012.01.016. Epub 2012 Jan 20.

Durand RE, Sham E. The lifetime of hypoxic human tumour cells. *Int J Radiat Oncol Biol Phys.* 1998;42(4):711–5.

Emely Lindblom, Alexandru Dasu & Iuliana Toma-Dasu (2015) Optimal fractionation in radiotherapy for non-small cell lung cancer – a modelling approach, *Acta Oncologica*, 54:9, 1592-1598, DOI: 10.3109/0284186X.2015.1061207

Estève M-A, Carré M, Braguer D. Microtubules in apoptosis induction: are they necessary? *Curr Cancer Drug Targets.* 2007;7:713–729

Flindt, R. *Amazing Numbers in Biology*. Berlin: Springer -Verlag; 2006.

Friberg S, Mattson S. On the Growth Rates of Human Malignant Tumours: Implications for Medical Decision Making. *J Surg Oncol*. 1997;65:284–97.

Froudarakis ME, Briasoulis E. Advanced non-small cell lung cancer: on relapse rechallenge the tumour, not the patient. *BMC Res Notes*. 2010 Jul 14;3:195. doi: 10.1186/1756-0500-3-195.

Gavrieli Y, Sherman Y, Ben-Sasson SA. Identification of programmed cell death in situ via specific labeling of nuclear DNA fragmentation. *J Cell Biol*. 1992 Nov;119(3):493–501.

Georgiadi ECh, Dionysiou DD, Graf N, Stamatakis GS. Towards in silico oncology: adapting a four dimensional nephroblastoma treatment model to a clinical trial case based on multi-method sensitivity analysis. *Comput Biol Med*. 2012 Nov;42(11):1064–78. doi: 10.1016/j.combiomed.2012.08.008

Giaccone G, Gazdar AF, Beck H, Zunino F, Capranico G. Multidrug sensitivity phenotype of human lung cancer cells associated with topoisomerase II expression. *Cancer Res*. 1992 Apr 1;52(7):1666–74.

Ginsberg, T., 1996. Modellierung und Simulation der Proliferationsregulation und Strahlentherapie normaler und maligner Gewebe, Fortschritt-Berichte, VDI Verlag: Duesseldorf, Reihe 17: Biotechnik, Nr 140, 103–107.

Goffin J, Lacchetti C, Ellis PM, Ung YC, Evans WK; Lung Cancer Disease Site Group of Cancer Care Ontario's Program in Evidence-Based Care. First-line systemic chemotherapy in the treatment of advanced non-small cell lung cancer: a systematic review. *J Thorac Oncol*. 2010;5(2): 260–74. doi: 10.1097/JTO.0b013e3181c6f035

Guyon I. and A. Elisseeff, An Introduction to Variable and Feature Selection *Journal of Machine Learning Research* 3, 1157–1182 2003

Höckel M, Dornhöfer N. The hydra phenomenon of cancer: why tumours recur locally after microscopically complete resection. *Cancer Res*. 2005 Apr 15;65(8):2997–3002.

Hoffman PC, Mauer AM, Vokes EE. Lung cancer. *Lancet* 2000;355:479–85.

Ishizawa K, Rasheed ZA, Karisch R, Wang Q, Kowalski J, Susky E, Pereira K, Karamboulas C, Moghal N, Rajeshkumar NV, Hidalgo M, Tsao M, Ailles L, Waddell TK, Maitra A, Neel BG, Matsui W. Tumour-initiating cells are rare in many human tumours. *Cell Stem Cell*. 2010 Sep 3;7(3):279–82. doi: 10.1016/j.stem.2010.08.009.

Jin JY, Kong FM, Chetty IJ, Ajlouni M, Ryu S, Ten Haken R, Movsas B. Impact of fraction size on lung radiation toxicity: hypofractionation may be beneficial in dose escalation of radiotherapy for lung cancers. *Int J Radiat Oncol Biol Phys*. 2010 Mar 1;76(3):782–8. doi: 10.1016/j.ijrobp.2009.02.079.

Jordan P, Carmo-Fonseca M. Molecular mechanisms involved in cisplatin cytotoxicity. *Cell Mol Life Sci*. 2000;57(8–9):1229–35.

M.A. Jordan, L. Wilson Microtubules as a target for anticancer drugs *Nat. Rev. Cancer*, 4 (2004), pp. 253–265

al-Kattan K, Sepsas E, Fountain SW, et al. Disease recurrence after resection for stage I lung cancer. *Eur J Cardiothorac Surg* 1997;12:380-4.

Katzung BG, editor. *Basic and Clinical Pharmacology*. 8th ed. United States of America: McGraw-Hill; 2001.

Kerr JF, Wyllie AH, Currie AR. Apoptosis: a basic biological phenomenon with wide-ranging implications in tissue kinetics. *Br J Cancer*. 1972;26(4):239-57.

Kimura N, Shibuya T, Niho Y, Nakamura H, Matsuo S, Imamura T, et al. Human lung cancer cell line (KSNY) producing colony-stimulating activity which affects both human and mouse marrow cells. *Gan*. 1979 Dec;70(6):807-10.

Kuhnigk JM, Dicken V, Bornemann L, bakai A, Wormanns D, Krass S, Peitgen HO. Morphological segmentation and partial volume analysis for volumetry of solid pulmonary lesions in thoracic CT scans. *IEEE Transactions on Medical Imaging*. 2006; 25: 417-34.

Kolokotroni EA, Dionysiou DD, Uzunoglu NK, Stamatakis GS. Studying the growth kinetics of untreated clinical tumours by using an advanced discrete simulation model. *Math Comput Model*. 2011;54:1989-2006. doi:10.1016/j.mcm.2011.05.007

Kolokotroni E, Dionysiou D, Veith C, Kim Y-J, Sabczynski J, Franz A, et al. (2016) *In Silico Oncology: Quantification of the In Vivo Antitumour Efficacy of Cisplatin-Based Doublet Therapy in Non-Small Cell Lung Cancer (NSCLC) through a Multiscale Mechanistic Model*. *PLoS Comput Biol* 12(9): e1005093. doi:10.1371/journal.pcbi.1005093

Komarova NL. Building Stochastic Models for Cancer Growth and Treatment. In: Deisboeck TS, Stamatakis GS, editors. *Multiscale cancer modeling*. Boca Raton: CRC Press; 2011. pp. 339-58.

N. Laperriere, L. Zuraw, G. Cairncross. "The cancer Care Ontario Practice Guidelines Initiative Neuro-oncology Disease Site Group "Radiotherapy for newly diagnosed malignant glioma in adults: a systematic review"." *Rad Oncol.*, vol. 64, pp. 259-273, 2002.

Lee JJ, Huang J, England CG, McNally LR, Frieboes HB. Predictive Modeling of In Vivo Response to Gemcitabine in Pancreatic Cancer. *PLoS Comput Biol*. 2013;9(9):e1003231. doi: 10.1371/journal.pcbi.1003231

Li J, Yang H, Chen L, Li Y, Zhu Y, Dai Y, et al. Establishment and characterization of human non-small cell lung cancer cell lines. *Mol Med Rep*. 2012 Jan;5(1):114-7. doi: 10.3892/mmr.2011.613

Lieber M, Smith B, Szakal A, Nelson-Rees W, Todaro G. A continuous tumour-cell line from a human lung carcinoma Lieber with properties of type II alveolar epithelial cells. *Int J Cancer*. 1976 Jan 15;17(1):62-70.

Liu C, Tsao MS. Proto-oncogene and growth factor/receptor expression in the establishment of primary human non-small cell lung carcinoma cell lines. *Am J Pathol*. 1993 Feb;142(2):413-23.

Loh PM, Clamon GH, Robinson RA, White ML, Hukku B, Rossi NP, et al. Establishment and characterization of four new human non-small cell lung cancer cell lines. *Cancer Res*. 1984 Aug;44(8):3561-9.

Lou F, Sima CS, Rusch VW, Jones DR, Huang J. Differences in patterns of recurrence in early-stage versus locally advanced non-small cell lung cancer. *Ann Thorac Surg*. 2014 Nov;98(5):1755-60; discussion 1760-1. doi: 10.1016/j.athoracsur.2014.05.070. Epub 2014 Aug 7.

Mackintosh JA, Marshall HM, Yang IA, Bowman RV, Fong KM. A retrospective study of volume doubling time in surgically resected non-small cell lung cancer. *Respirology*. 2014 Jul;19(5):755-62. doi: 10.1111/resp.12311

Masuda N, Fukuoka M, Takada M, Kudoh S, Kusunoki Y. Establishment and characterization of 20 human non-small cell lung cancer cell lines in a serum-free defined medium (ACL-4). *Chest*. 1991 Aug;100(2):429-38.

Moore N, Lyle S. Quiescent, slow-cycling stem cell populations in cancer: a review of the evidence and discussion of significance. *J Oncol*. 2011;2011. pii: 396076. doi: 10.1155/2011/396076. Epub 2010 Sep 29.

Morrison BJ, Steel JC, Morris JC. Sphere Culture of Murine Lung Cancer Cell Lines Are Enriched with Cancer Initiating Cells. *PLoS One*. 2012;7(11):e49752. doi:10.1371/journal.pone.0049752

Morton Lippmann. *Environmental Toxicants: Human Exposures and Their Health Effects*. 3rd ed. New York: John Wiley & Sons, Inc.; 2000.

Murray, R. Mirzayans, A.L. Scott, J.M. Allalunis-Turner. "Influence of oxygen on the radiosensitivity of human glioma cell lines." *Am J Clin Oncol.*, vol. 26: e169-e170, 2003.

NSCLC Meta-analysis Collaborative Group. Preoperative chemotherapy for non-small cell lung cancer: a systematic review and meta-analysis of individual participant data. *Lancet* 2014;383:1561-71

Olsson L, Sorensen HR, Behnke O. Intratumoural phenotypic diversity of cloned human lung tumour cell lines and consequences for analyses with monoclonal antibodies. *Cancer*. 1984 Nov 1;54(9):1757-65.

Ormerod MG, Orr RM, Peacock JH. The role of apoptosis in cell killing by cisplatin: a flow cytometric study. *Br J Cancer*. 1994 Jan;69(1):93-100.

C. Perez, L. Brady L. *Principles and Practice of Radiation Oncology*. Philadelphia: Lippincott-Raven, 1998.

Pigott TD. A Review of Methods for Missing Data. *Educational Research and Evaluation* 2001, Vol. 7, No. 4, pp. 353±383

Pine SR, Ryan BM, Varticovski L, Robles AI, Harris CC. Microenvironmental modulation of asymmetric cell division in human lung cancer cells. *Proc Natl Acad Sci U S A*. 2010 Feb 2;107(5):2195-200. doi: 10.1073/pnas.0909390107

Protocol-SIOP-2001.pdf available in <https://www.skion.nl/workspace/uploads/Protocol-SIOP-2001.pdf> (last visited on 1 July 2016)

Quint LE, Cheng J, Schipper M, Chang AC, Kalemkerian G. Lung lesion doubling times: values and variability based on method of volume determination. *Clin Radiol*. 2008;63(1):41-8.

Rawlins EL, Hogan BL. Ciliated epithelial cell lifespan in the mouse trachea and lung. *Am J Physiol Lung Cell Mol Physiol*. 2008 Jul;295(1):L231-4. doi: 10.1152/ajplung.90209.2008

Rawlins EL, Hogan BL. Epithelial stem cells of the lung: privileged few or opportunities for many? *Development*. 2006 Jul;133(13):2455-65.

Saeys Y, Inza I, Larrañaga P. A review of feature selection techniques in bioinformatics. *Bioinformatics*. 2007 Oct 1;23(19):2507-17.

Siddik, Zahid H. Cisplatin: mode of cytotoxic action and molecular basis of resistance. *Oncogene*. 2003;22(47):7265–79.

Sorenson CM, Barry MA and Eastman A. Analysis of Events Associated With Cell Cycle Arrest at G2 Phase and Cell Death Induced by Cisplatin. *J Natl Cancer Inst*. 1990 May 2;82(9):749-55

de Souto MC, Jaskowiak PA, Costa IG. Impact of missing data imputation methods on gene expression clustering and classification. *BMC Bioinformatics*. 2015 Feb 26;16:64. doi: 10.1186/s12859-015-0494-3.

Stamatakis GS, Kolokotroni EA, Dionysiou DD, Georgiadi ECh, Desmedt C. An advanced discrete state – discrete event multiscale simulation model of the response of a solid tumour to chemotherapy. Mimicking a clinical study. *J Theor Biol*. 2010;266(1): 124-39. doi: 10.1016/j.jtbi.2010.05.019

G. Steel. *Basic Clinical Radiobiology*. London: Arnold, 2002.

Uramoto H, Tanaka F. Recurrence after surgery in patients with NSCLC. *Transl Lung Cancer Res*. 2014 Aug;3(4):242-9. doi: 10.3978/j.issn.2218-6751.2013.12.05.

Wang G, Reed E, Li QQ. Molecular basis of cellular response to cisplatin chemotherapy in non-small cell lung cancer (Review). *Oncol Rep*. 2004 Nov;12(5):955-65.

6. Lung Cancer Modelling: Statistical Approach

6.1 Introduction

Regarding NSCLC adenocarcinoma, a machine learning approach was investigated. The aim is to identify group of patients with high risk of recurrence based on their miRNA data and/or EGFR/BRAF/ALK mutation and clinical profile. Two classifiers trained with miRNA and/or clinical data have been developed. Standalone applications utilizing the above classifiers, compliant to the CHIC specifications in respect to model deployment and packaging, has been released and successfully tested and uploaded on CHIC platform.

6.2 Data sets

The set of clinical data is available for about 100 patients. They around 70 variables which are related to personal information, pathological studies, molecular data, treatment and response of a patient to treatment and radio imaging investigations:

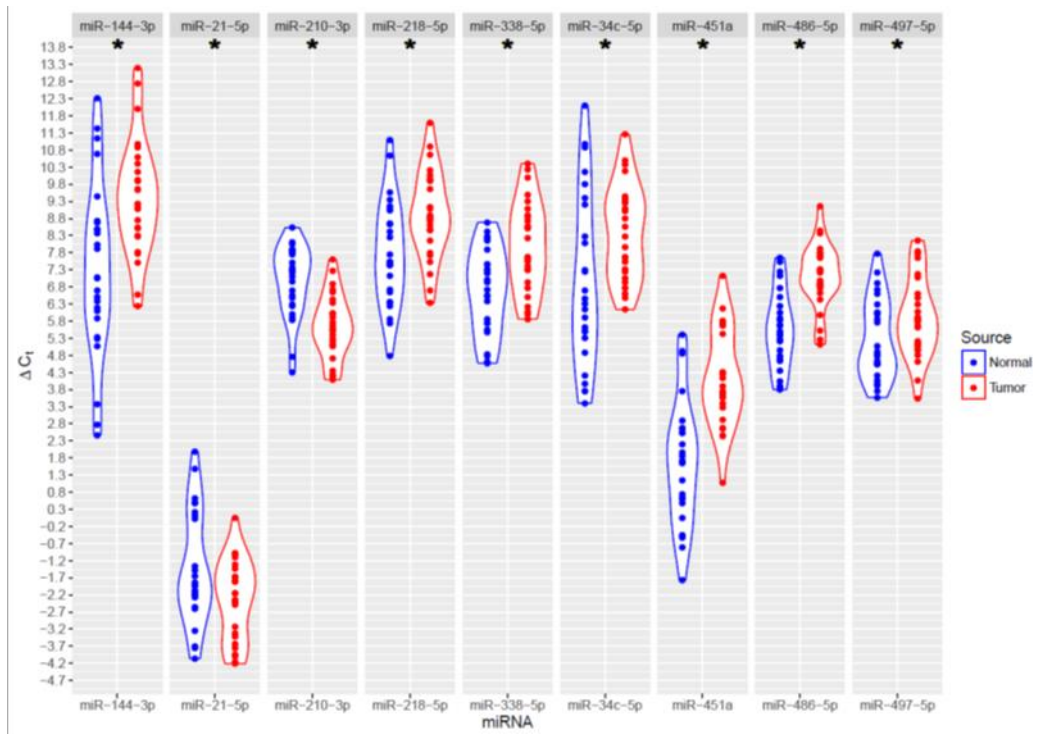
- **Personal information:** pseudonym, gender, birth date, vital status, date of death, survival period
- **Pathological studies:** specimen, frozen tissue availability, tumour size, primary or recurrent, surgery modality, surgery site, diagnosis, variants of adenocarcinoma, tumour grade, stage grouping off the tumour, performed ICH, proliferating index, microvascular density
- **Mutation data:** EGFR sequencing, exon 18, 19, 20, 21, Kras sequencing, exon 12/13, 61, 117/146, EML4_ALK, BRAF 11, 15
- **Chemotherapy/ Radiotherapy data:** number of cycles, start and finish date of each given cycles
- **Radio imaging investigations:** dates

Two sets of miRNA data are available:

- **20 patients:** Expression data for 2549 miRNAs, i.e the unnormalized and normalized expression values in tumour and normal tissue, the detection flag for tumour and normal tissue, and the fold-change of the normalized expression values between tumour and normal tissue. From this data set, recurrence after surgery is known for 10 patients.

- **50 patients:** From microarray analysis 9 miRNAs were selected which are over or under expressed in tumour compared with normal tissue (Figs 1, 2). Fold changes of the normalized expression values between tumour and normal tissue for these miRNAs were provided for the needs of CHIC. From this data set, recurrence after surgery is known for 17 patients. The results of the qPCR analysis from these miRNAs in 30 FFPE samples (15 G2 and 15 G3 graded) and 20 Kryo samples (10 G2 and 10 G3 graded) are depicted in Figs 1, 2. A statistical analysis that includes paired t Tests (normal vs tumour tissue) and correlation between miRNA and grading or overall survival is given in Tables 1-4.

A.



B.

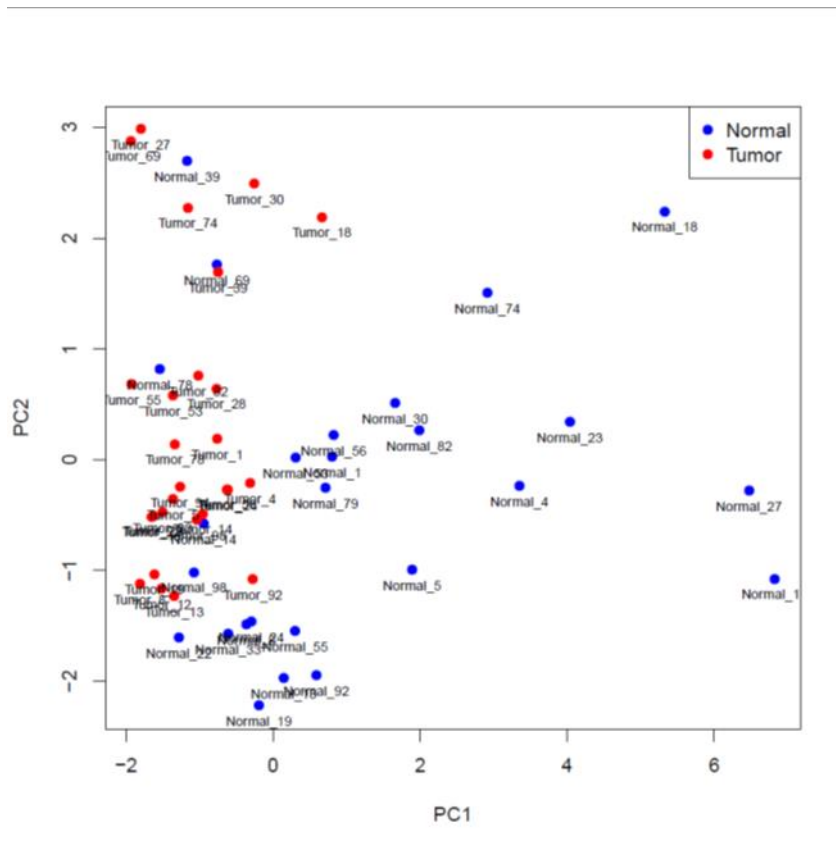


Fig 1. Analysis of FFPE Samples. A. Box-dot plots for mRNA expression (ΔC_t values) in tumour and normal tissue B. Principal Component Analysis of all samples represented by a scatter plot of the first versus second principal component.

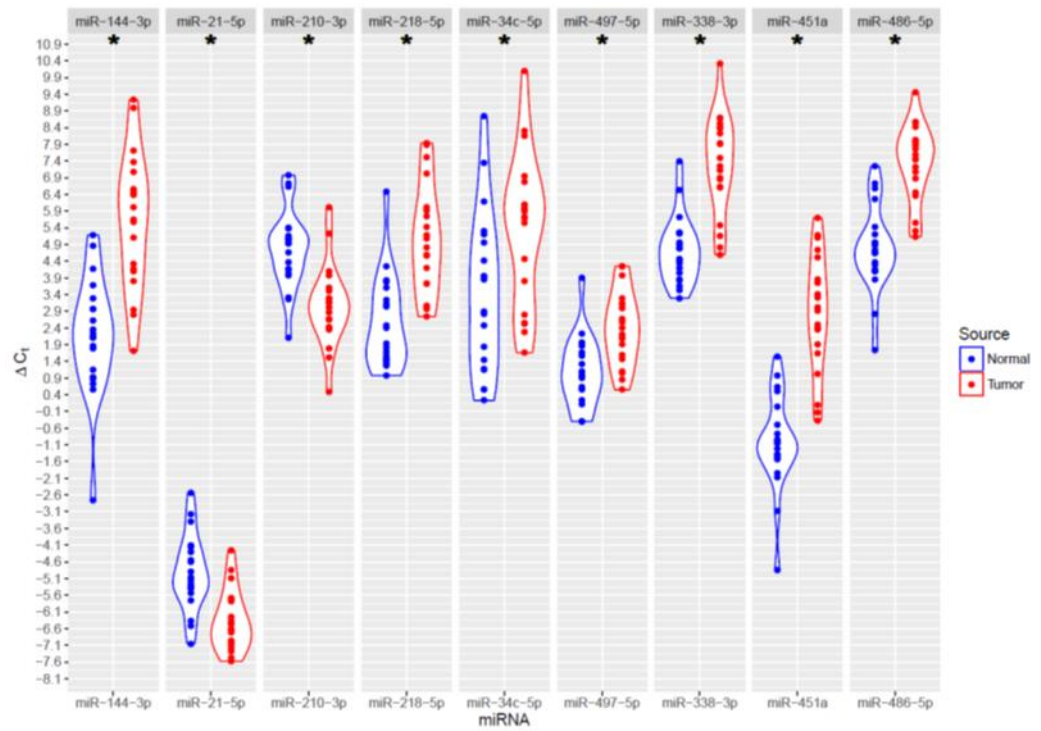
Table 1. Correlation between miRNA expression (C_i) and overall survival in FFPE samples

miRNA	Pearson correlation coefficients	
	Overall survival	Grading
miR-144-3p	-0.2125	0
miR-21-5p	0.164255	-0.10659
miR-210-3p	0.005662	-0.03198
miR-218-5p	-0.17445	-0.02931
miR-338-5p	-0.15773	0.007994
miR-34c-5p	-0.17196	0.149223
miR-451a	-0.21721	-0.00533
miR-486-5p	-0.08779	0.119911
miR-497-5p	-0.29965	0.029312

Table 2. Differences in miRNA expression Normal_vs_Tumour tissue in FFPE samples

miRNA	limma-test paired		t-test paired		AUC	Mean Normal	Mean Tumour
	raw values	p-values	raw t-test p-values	adjusted p-values			
miR-144-3p	0.040225	0.040225	0.042128	0.042128	0.2512	0.020977	0.00266
miR-21-5p	0.008485	0.009545	0.009157	0.010302	0.6288	4.5555	7.073564
miR-210-3p	9.72E-05	0.000607	0.000107	0.000652	0.8208	0.010891	0.023674
miR-218-5p	0.00562	0.007226	0.005092	0.006547	0.304	0.007068	0.003087
miR-338-5p	0.002271	0.004026	0.00234	0.004212	0.2352	0.013107	0.005451
miR-34c-5p	0.002032	0.004026	0.002223	0.004212	0.2992	0.02251	0.004104
miR-451a	0.002684	0.004026	0.002957	0.004436	0.1408	0.586383	0.087753
miR-486-5p	0.000145	0.000607	0.000165	0.000652	0.152	0.028284	0.009076
miR-497-5p	0.000202	0.000607	0.000217	0.000652	0.3488	0.033078	0.022007

A,



B.

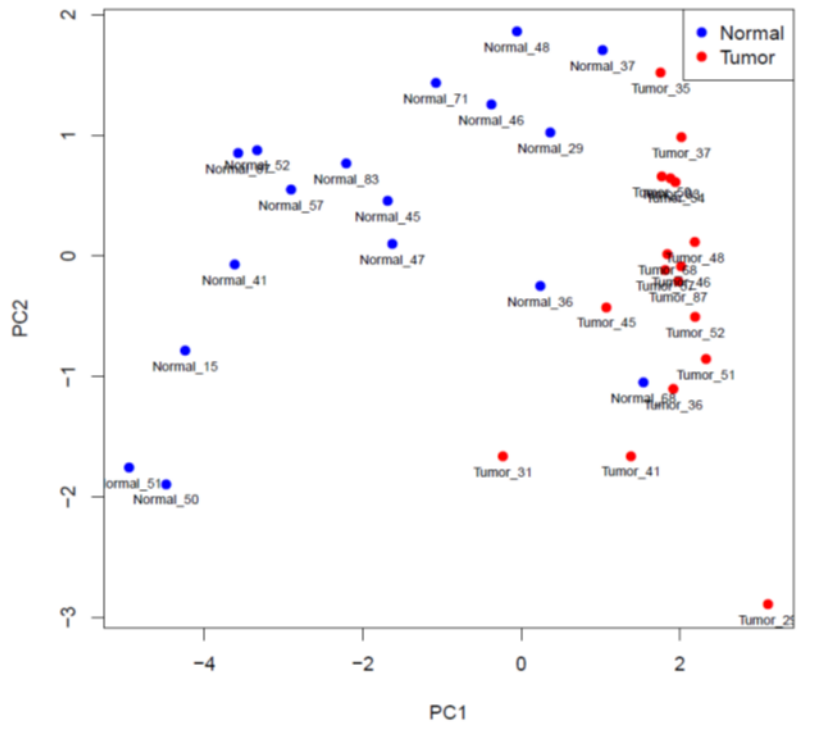


Fig 2. Analysis of Kryo Samples. A. Box-dot plots for mRNA expression (ΔC_t values) in tumour and normal tissue B. Principal Component Analysis of all samples represented by a scatter plot of the first versus second principal component.

Table 3. Correlation between miRNA expression (C_t) and overall survival in Kryo samples

miRNA	Pearson correlation coefficients	
	Overall survival	Grading
miR-144-3p	-0.115233274	0.112618501
miR-21-5p	0.01129738	0.216574041
miR-210-3p	0.072114941	0.142938867
miR-218-5p	-0.117869329	0.229568483
miR-338-5p	-0.122199991	0.294540696
miR-34c-5p	-0.148183965	0.3161981

miR-451a	-0.016004621	-0.155933309
miR-486-5p	-0.035021877	0.030320366
miR-497-5p	-0.031444374	-0.004331481

Table 4. Differences in *miRNA* expression Normal_vs_Tumour tissue in Kryo samples

miRNA	limma-test paired		t-test paired		AUC	Mean Normal	Mean Tumour
	raw values	p-values	adjusted p-values	raw t-test p-values	adjusted p-values		
miR-144-3p	0.001479		0.002219	0.001761	0.002642	0.056122	0.232316
miR-21-5p	0.000721		0.001298	0.000888	0.001598	0.892857	42.547540
miR-210-3p	0.006714		0.007554	0.007627	0.008581	0.933673	0.053222
miR-218-5p	0.000263		0.000595	0.000327	0.000736	0.117347	0.236809
miR-338-5p	0.029717		0.029717	0.032512	0.032512	0.198980	0.211952
miR-34c-5p	0.002432		0.003127	0.002874	0.003695	0.163265	0.598605
miR-451a	0.000116		0.000524	0.000055	0.000303	0.040816	0.039890
miR-486-5p	0.000061		0.000524	0.000082	0.000303	0.005102	1.771549
miR-497-5p	0.000265		0.000595	0.000101	0.000303	0.045918	0.033754

6.3 Developed Classifiers

6.3.1 Classifier #1

The classifier aims to predict the clinical evolution of a surgical treated patient with NSCLC adenocarcinoma. The classifier was trained based on the 1st set of miRNA data. Only miRNA expression data and particularly the fold-change of the normalized expression values between tumour and normal tissue was considered. Patients with unknown recurrence after surgery were excluded. The final size of training set was 10. Two classes were considered: progression or complete remission. There were no missing values.

The workflow for the development and validation of the classifier consists of the following steps:

- *Feature selection:* A t-test statistic was chosen due to the small size of the sample (10) compared to the considerable large size of the feature space (2549). The 10 most significant features based on t statistics (i.e. the ones with the lowest p-value) were selected.
- *Training* a Naïve Bayes classifier with the selected features.
- *Cross-Validation:* Due to the small size of the sample, the classifier was validated by applying the leave-one-out method.

The accuracy of the Naïve Bayes classifier estimated based on the leave-one-out cross-validation method is 100% in the sample considered (Table 5). Even though the results are promising, no definite conclusions can be drawn, due to the small size of the sample.

Table 5. Confusion matrix of Naïve Bayes performance

		Predicted class		
		complete remission	recurrence	Recognition
Actual class	complete remission	4	0	100%
	recurrence	0	6	100%
	Precision	100%	100%	

6.3.2 Classifier #2

The classifier aims to predict the clinical evolution of a surgical treated patient with NSCLC adenocarcinoma. The classifier was built based on the 2nd set of miRNA data (9 miRNAs). The following clinical data were also considered: Age, Gender, Grade, Stage, Tumour microvascular density (MVD). Patients with unknown recurrence after surgery as well as metastatic patients were excluded. The final size of training set was 14. Two classes were considered: yes (recurrence), no (recurrence). There were no missing values.

The workflow for the development and validation of the classifier consists of the following steps:

- *Feature selection*: Forward selection and Backward elimination methods were applied to select the most relevant subset of features for use in model construction.
- *Training of various classifiers*: Naïve Bayes, Random Forest, Neural
- *Cross-Validation*: Due to the small size of the sample, the classifiers were validated by applying the leave-one-out method

- *Validation* with a test set of 5 patients that have not clear recurrence but Dicoms with visible tumours at some point after surgery. Recurrence is considered positive.

The Neural Network classifier performed better than Naïve Bayes and Random Forest. It was build based on Age, Stage, 6 miRNA expression data. The accuracy of the Neural Network classifier estimated based on the leave-one-out cross-validation method is 71.43% in the training set considered (Table 6). Furthermore, it predicted with an accuracy of 80% the recurrence in the test set (Table 7). Even though the results are promising, no definite conclusions can be drawn, due to the small size of the sample.

Table 6. Confusion matrix of Neural Network performance

		Predicted class		
		complete remission	recurrence	Recognition
Actual class	complete remission	5	3	62.50%
	recurrence	1	5	83.33%
	Precision	83.33%	62.50%	

Table 7. Neural Network results on the test set

Patient #	Prediction	Confidence (no)	Confidence (yes)	Actual class
1	no	0.7834	0.2163	yes
2	yes	0.00564	0.99436	yes
3	yes	0.3807	0.6193	yes
4	yes	0.0951	0.9049	yes
5	yes	0.0003	0.9997	yes

CHAPTER GB: THE GLIOBLASTOMA HYPERMODEL: CLINICAL ADAPTATION AND PARTIAL VALIDATION

(Please note that the numbering of sections, subsections, equations, figures and references within this chapter refers exclusively to the latter and is not applicable to other chapters of the document. If any of the above entities of another chapter is to be referred to, the chapter under consideration should also be mentioned through its two capital letter code)

The Glioblastoma Multiforme Statistical Model

I. Background

As depicted in figure I, both the adaptive and the innate immune system interact with GBM, through a variety of cell types and molecular mechanisms. Most commonly, the immune system of a patient suffering from GBM is found to be completely paralyzed. Concerted action of immunosuppressive cells like regulatory T cells, myeloid derived suppressor cells and microglia suppress a variety of immune reactions against the tumour; Regulatory T cells impair the antigen-presenting functions and maturation of dendritic cells and thereby suppress the production of antigen-specific, activated cytotoxic T cells in the lymph nodes. Furthermore, the killing potential of cytotoxic T cells and natural killer (NK) cells is impaired by the immunosuppressive action of myeloid derived suppressor cells and microglia. These mechanisms contribute to the induction of tolerance against the tumour [refs 1-34, included in the diagram].

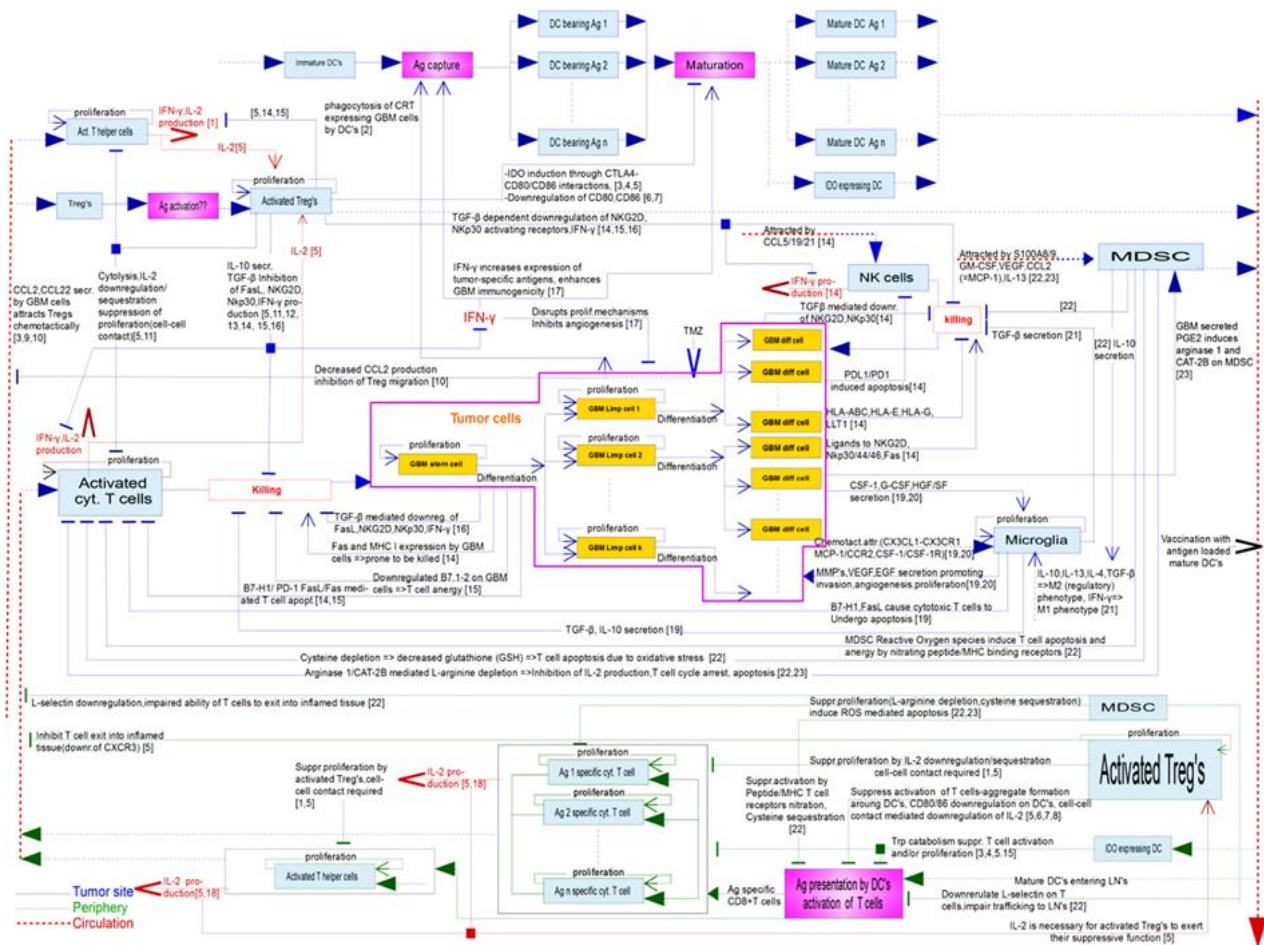


Figure 1. Cellular and molecular mechanisms involved in the interaction of GBM and the immune system (references on the diagram)

Dendritic cell vaccination is a method which aims at circumventing these immunosuppressive mechanisms and reshape the patient's immune system so that it reacts effectively against the tumour. White blood cells drawn from the patient's blood are differentiated to dendritic cells. These are furtherly cultivated with lysates from the resected tumour, aiming to produce antigen-loaded mature dendritic cells which are then injected into the patient's body in specific vaccination schedules (figure 2). The rational is that these in-vitro matured antigen-bearing dendritic cells have the capacity to present their antigens to naïve T cells in the lymph nodes, and induce their activation and proliferation. These activated cytotoxic T cells are expected to react against the tumour, by killing cancer cells. This process is further expected to induce immunological memory against GBM [35,36,37,38,39,40].

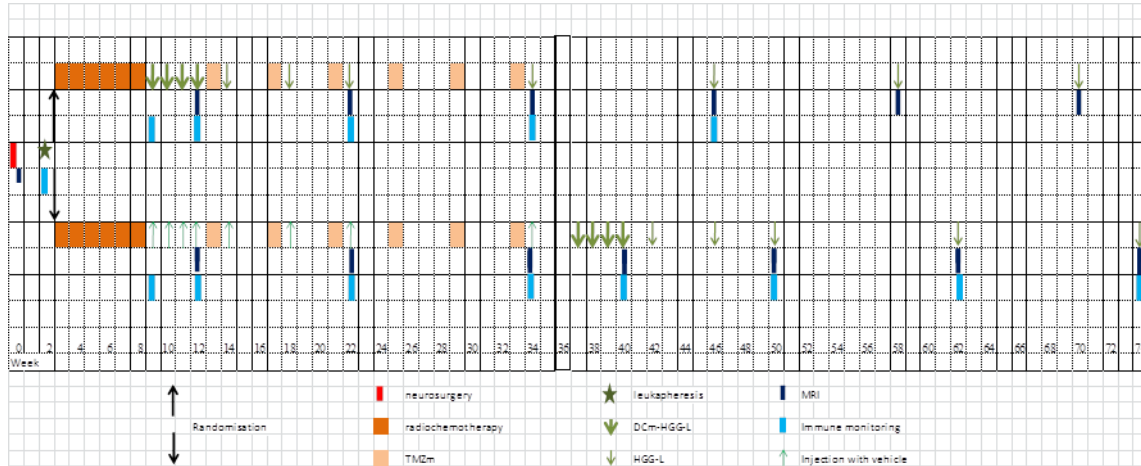


Figure 2. Dendritic cell vaccination and overall treatment schedule. There are two possible vaccination schedules; Just after radiochemotherapy or after 6 cycles of maintenance chemotherapy. Patients are randomly assigned to one of these schedules.

2. Objectives

The three main clinical questions the model seeks to answer are:

- 1) Will a specific GBM patient become a long term survivor (overall survival > 24 months) or suffer from early relapse and death (< 12 months)? → based on patient-, pathology- and immune profile
- 2) Will dendritic cell vaccination help to reach long term survival?
- 3) If yes, should vaccination be given early or late?

3. Clinical use of the statistical/machine learning model

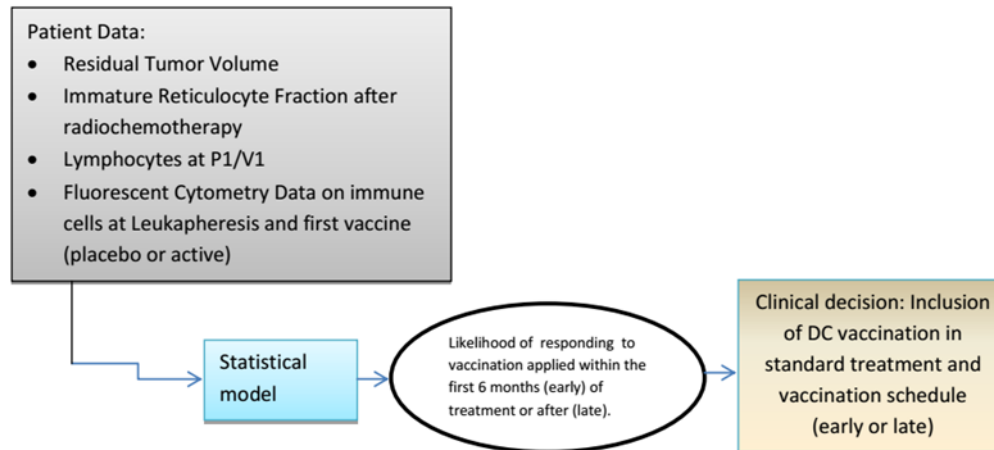


Figure 3: Master topology of the planned GBM hypermodel.

Figure 3 depicts the clinical use of the model. From the analysis presented in detail in the following sections, it turns out that the patient characteristics most relevant to provide answers to the aforementioned clinical questions are the following:

1. Residual Tumour Volume, that is, the tumour volume left in the patient after surgery. It has been already demonstrated by numerous studies (see references) that this variable is expected to have an impact in the patients outcome. In our model, this variable is categorical and takes only 2 values: RTV=0 and RTV>0.
2. Immature reticulocyte fraction. This variable consists essentially an index of bone marrow recovery after radiochemotherapy. In our case takes only 2 values: Low (when its value is up to 0.21) and Normal (when its value is above 0.21). To the best of our knowledge, there is no literature identifying this variable as a relevant prognostic factor. However, we will show in what follows that this variable in combination with vaccination schedule (early/late) stratify the total patient population in subgroups, within each of which strong correlations between fluorescent cytometry derived data and overall survival exist.

3. Lymphocytes at first vaccine, right after radiochemotherapy. To the best of our knowledge, there is no literature identifying this variable as a relevant prognostic factor. However it was observed that the majority (36/44) of patients reaching overall survival >24 months had low lymphocytes at PI/VI. Further analysis showed that this variable defines patient subgroups within which quite strong correlations between patient data and overall survival exist.
4. Fluorescent cytometry data, taken at the time points of leukapheresis and just after radiochemotherapy. It has already been suggested [35-40] that these quantities seem to play a role in the final outcome. Here we present a statistical analysis which demonstrates strong evidence supporting this suggestion.

4. Newly available data

Already provided data have been extensively described in the previous deliverables. Of note, these data alone seemed not to include the information needed for answering the aforementioned clinical questions.

Newly added data included cytokine measurements taken from patients blood (IFN-g, Gal-I, IL-12, IL-10, MCP-I, VEGF) at Leukapheresis, 1st, 7th and 8th vaccines. Several machine learning methodologies were employed [41-45], however, none of these measurements showed a significant predictive potential regarding overall or progression free survival.

The most important new addition to the available clinical data was Fluorescent Cytometry measurements i.e. relative quantities of immune system cells in a patients' blood. These data are thoroughly described in the next section.

4.1. Fluorescent Cytometry data

These data concern the following immune system cells and their relative quantities:

1. Natural Killer cells (NK)
2. Total T cells (CD45+CD3+ cells)
3. Cytotoxic T cells (CD45+CD3+CD8+CD4- cells or CTL)
4. T helper cells (CD45+CD3+CD4+CD8- cells or Th)

5. Regulatory T cells (CD45+CD3+CD4+CD25+CD127- cells or Tregs)

For each of the CTLs, Thelpers and Tregs percentages of CD69+ and PD1+ subpopulations are given. Each of the aforementioned cell populations is given as a percentage of a specific parent population as depicted in the following figure.

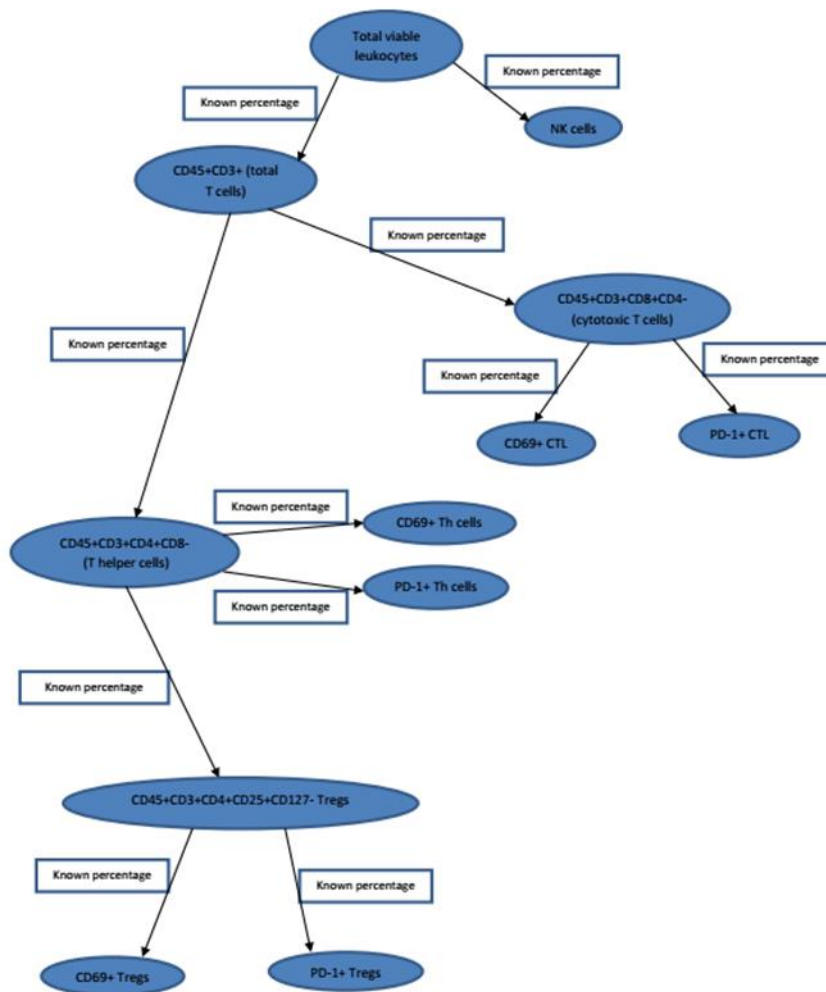


Figure 4: Fluorescent Cytometry Data

Blood for these measurements is taken at the time points leukapheresis (denoted also as V0), 1st, 7th and 8th vaccines. Thus, for each of these time points 11 numbers are known, each one corresponding to one of the percentages depicted in figure 4. Since PI/VI is the point of first intervention, pertinent clinical decisions (include or not vaccination in treatment, early or late vaccination) have to be taken by taking into account data available up to the specific time point. Thus, for the purposes of the specific study, only data from V0 (leukapheresis) and PI/VI (first vaccine, placebo or active) were used.

5. Model Development

A variety of commonly used machine/statistical learning methods were employed to discover if the available clinical data can predict and/or correlate with overall survival. These methods included decision trees [41,42], probabilistic graphical networks [43-45], support vector machines [46] and ensemble methods [41,42]. None of the above methods provided results. Thus, a custom method was developed, whose rational and steps are described below.

- 1) It has already been suggested that relative quantities of immune system cells and at leukapheresis and PI/VI, plus their evolvement during radiochemotherapy were expected to play a role in the outcome [35-40].
- 2) The structure implied in Figure 4 enables the calculation of a large variety of ratios between immune system cells, for example CTL/Tregs at leukapheresis, ThCD69+/NK at PI/VI etc.
- 3) Based suggestion 1 and observation 2, the available data set was enriched to include all meaningful ratios between immune cells at the same time point i.e. leukapheresis or PI/VI, as described in observation 2.
- 4) Last, additional features were introduced, attempting to quantify the evolvement of the aforementioned quantities during radiochemotherapy, i.e. all complex ratios of the form (CTL/Tregs at PI/VI) / (CTL/Tregs at leukapheresis).
- 5) The enriched data set consisted of 789 numerical features, all derived from the initial fluorescent cytometry data taken at leukapheresis and PI/VI.
- 6) The Pearson correlation coefficients of each of these features with overall survival were calculated. No strong correlations were detected.

- 7) For all possible combinations of these 789 features taken 2 at a time, canonical correlation analysis was performed between each such combination and overall survival. No strong correlations were detected. The same analysis was performed by considering all possible combinations of the 789 features taken 3 at a time. Again, no strong correlations were detected. Of note, the computational complexity of this analysis is factorial; to perform an exhaustive analysis considering combinations of 4 features was intractable, at least within the prescribed time limitations.
- 8) From steps 6 and 7 and the heterogeneity of the patient population as it is reflected in the categorical variables included in the data, it seemed apparent that there is no correlation between such fluorescent cytometry derived features and overall survival that holds for the entire patient population, or at least not one that can be discovered in a realistic computational time.
- 9) Thus, a different approach was taken. Evidently, the group of the 134 available patients is largely heterogeneous. Essentially, each value of any categorical variable (e.g. RTV=0 or Lymphocytes_at_V0=Low etc) specifies a specific subgroup of patients, which may behave completely different than the others. Taking into account these categorical variables, subgroups of the patient population were found within which strong correlations between fluorescent cytometry derived features and overall survival hold.
- 10) By the analysis performed so far, several such subgroups have been found which are defined as follows:
 - a. By the categorical variables Residual Tumour Volume (RTV=0, RTV>0) and Vaccination Schedule (=Early, Late). Four distinct subgroups are defined by these variables:
 - i. Patients with RTV=0 and Vaccination=Early.
 - ii. Patients with RTV=0 and Vaccination=Late.
 - iii. Patients with RTV>0 and Vaccination=Early.
 - iv. Patients with RTV>0 and Vaccination=Late.
 - b. By the categorical variables Immature_Reticulocyte_Fraction at PI/VI (= Low, Normal) and Vaccination Schedule (=Early, Late). Four distinct subgroups are defined by these variables:
 - i. Patients with Imm.Reticul.Fr at PI/VI=Low and Vaccination=Early.
 - ii. Patients with Imm.Reticul.Fr at PI/VI=Low and Vaccination=Late.
 - iii. Patients with Imm.Reticul.Fr at PI/VI=Normal and Vaccination=Early.
 - iv. Patients with Imm.Reticul.Fr at PI/VI=Normal and Vaccination=Late.

- c. By the categorical variables Lymphocytes at PI/VI (=Low, fixed) and Vaccination Schedule (=Early, Late). Two distinct subgroups are defined by these variables:
 - i. Patients with Lymphocytes=Low and Vaccination=Early.
 - ii. Patients with Lymphocytes=Low and Vaccination=Late.

II) Each of the previously defined 10 subgroups was analyzed as described in steps 6 and 7. Each subgroup was analyzed in two 'versions' a) as such and b) by first disregarding patients of the subgroup whose tumour was in more than location and patients which relapsed before PI/VI. Generally, this seemed to improve the strength of the discovered correlations.

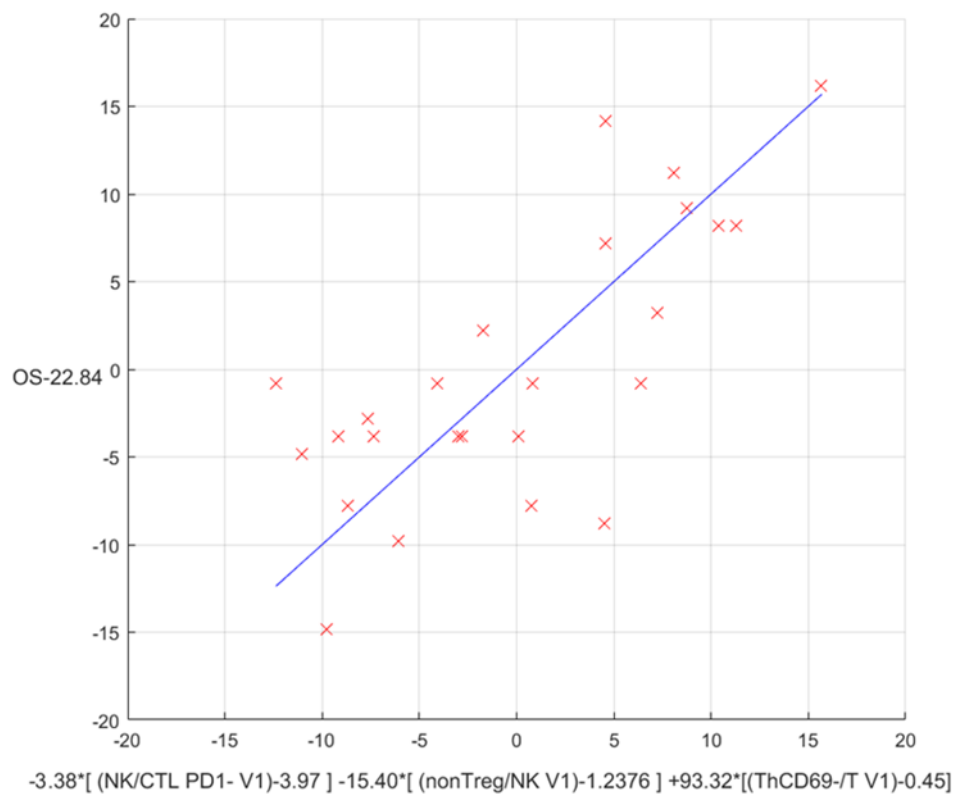
6.Results

Below we present the results of the previously described analysis. For each subgroup a table is given containing the most strong correlations discovered within the particular subgroup. Explanations on how to understand the tables are given below table I.

After each table, a chart visualizing the strongest correlation in the specific subgroup is given. In what follows, let OS denote overall survival. The vertical axis corresponds to the quantity (OS – average OS in the specific subgroup). The horizontal axis corresponds to the quantity found to correlate most strongly with the (OS – average OS in the specific subgroup) in the specific subgroup. Red x's denote the actual patient values. In all charts, the vast majority of patients lies in the 1st and 3rd quadrants, as was expected by the strong positive correlation coefficients. This visualizes the fact that if the quantity in the horizontal axis is above zero, then the OS can be expected to be above its average value in the specific subgroup. There are no major outliers, that is, x's in the upper left of the 2nd or lower right of the 4th quadrant. The blue line is essentially the quantity in the horizontal axis plotted against itself, and shows how this quantity can be used to estimate overall survival.

I) Patients with Imm.Reticul.Fr at PI/VI=Low, Vaccination=Early. Number of patients=25

Correlation	F1	avg1	C1	F2	avg2	C2	F3	avg3	C3	avg_O5	p-value
0.7486	'NK/CTL_PD1-V1'	3.9720	-3.3856	'nonTreg/NK V1'	1.2376	-15.4054	'ThCD69-/T V1'	0.4548	95.5216	22.8400	0.000611
0.7351	'NK/CTL_PD1-V1'	3.9720	-3.3872	'Th(CD4+)/NK V1'	1.4573	-12.8426	'ThCD69-/T V1'	0.4548	95.0476	22.8400	0.000309
0.7343	'CTL_PD1-/CTL_PD1-V1'	0.5621	18.0614	'ThPD1-/TregPD1-V1'	64.5591	-0.7590	'ThPD1-/TregPD1-V1/V0'	2.6802	19.7497	22.8400	0.000831
0.7336	'NK/CTL_PD1-V1'	3.9720	-3.3974	'Th(CD4+/CD69-/NK V1'	1.4087	-13.4488	'ThCD69-/T V1'	0.4548	94.0695	22.8400	0.000850
0.7308	'Th(CD4+)/V1'	0.4690	90.5251	'NK/CTL_PD1-V1'	3.9720	-3.3151	'nonTreg/NK V1'	1.2376	-15.5801	22.8400	0.000629
0.7256	'CTL_PD1-/CTL_PD1-V0'	1.3356	-4.1866	'Th(CD4+)/PD1-/NK V1/V0'	0.9576	27.1035	'Treg/NK V1/V0'	2.3516	-6.7096	22.8400	0.001096
0.7246	'Th(CD4+)/V1'	0.4690	90.5705	'NK/CTL_PD1-V1'	3.9720	-3.3273	'Th(CD4+)/NK V1'	1.4573	-13.0854	22.8400	0.001131
0.7244	'ThCD69-/TregPD1-V0'	31.4541	-0.6289	'TregCD69-/CTL_CD69-V1'	0.1931	-95.1713	'TregPD1-/CTL_PD1-V1'	0.1901	83.5204	22.8400	0.001137
0.7236	'NK/TregPD1-V1'	92.4202	-0.1211	'CTL_PD1-/CTL_PD1-V1'	0.5621	21.6694	'ThPD1-/TregCD69-V1/V0'	116.7313	0.1033	22.8400	0.001164
0.7228	'NK/TregPD1-V1'	92.4202	-0.0635	'CTL_PD1-/CTL_PD1-V1'	0.5621	17.2599	'ThPD1-/TregCD69-V1/V0'	1.0042	10.2503	22.8400	0.001195
0.7223	'ThPD1-/TregPD1-V0'	17.6151	-0.7714	'TregPD1-/CTL_CD69-V1'	0.0898	-291.3539	'TregPD1-/CTL_PD1-V1'	0.1268	189.8266	22.8400	0.001214
0.7220	'Th/TregPD1-V0'	32.1681	-0.6115	'TregCD69-/CTL_CD69-V1'	0.1931	-94.5235	'TregPD1-/CTL_PD1-V1'	0.1901	82.4571	22.8400	0.001224
0.7215	'ThCD69-/TregPD1-V0'	31.4541	-0.6232	'TregCD69-/CTL_CD69-V1'	0.1845	-105.5934	'TregPD1-/CTL_PD1-V1'	0.1901	90.2149	22.8400	0.001231
0.7205	'ThCD69-/TregPD1-V0'	31.4541	-0.6790	'Treg/CTL V1'	0.2086	-67.5816	'Th/CTL_CD69-V1'	46.5712	0.2281	22.8400	0.001261
0.7200	'Th/TregPD1-V0'	32.1681	-0.6065	'TregCD69-/CTL V1'	0.1845	-104.7818	'TregPD1-/CTL_PD1-V1'	0.1901	89.1954	22.8400	0.001302
0.7197	'nonTreg/TregPD1-V0'	29.8658	-0.6399	'TregCD69-/CTL_CD69-V1'	0.1931	-95.3518	'TregPD1-/CTL_PD1-V1'	0.1901	82.4295	22.8400	0.001311
0.7195	'CTL_PD1-/CTL_PD1-V1'	0.5621	18.2513	'ThPD1-/TregCD69-V1'	111.0290	-0.1123	'ThPD1-/TregCD69-V1/V0'	1.0042	16.3949	22.8400	0.001322
0.7188	'nonTreg/TregPD1-V0'	29.8658	-0.6374	'TregCD69-/CTL V1'	0.1845	-106.1820	'TregPD1-/CTL_PD1-V1'	0.1901	89.3974	22.8400	0.001348
0.7185	'ThCD69-/TregPD1-V0'	31.4541	-0.6814	'Treg/CTL V1'	0.2086	-67.0113	'ThCD69-/CTL_CD69-V1'	45.5444	0.2299	22.8400	0.001361
0.7177	'NK/TregPD1-V0'	31.9101	-0.1432	'Th(CD4+)/PD1-/NK V1/V0'	0.9576	25.7428	'Treg/NK V1/V0'	2.3516	-5.3578	22.8400	0.001395



How to understand the table:

- Each row essentially describes a correlation between the weighted sum of 3 features (F1,F2,F3) and the quantity (OS –average OS in the specific subgroup). The (Pearson) correlation coefficient is in the respective row of the first column.
- avg1,avg2,avg3 are the mean values of F1,F2,F3 respectively and avg_OS is the average value of OS, for the specific subgroup.
- C1,C2,C3 are the weights of F1,F2,F3 in the weighted sum.

Generally we read the following:

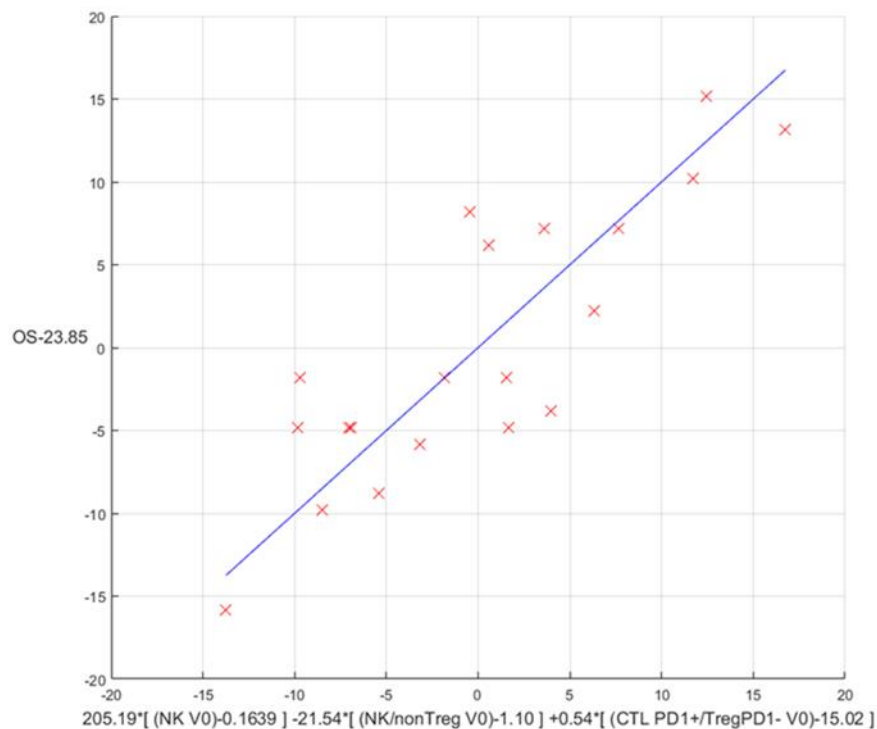
- The quantity $C1*(F1-avg1)+C2*(F2-avg2)+C3*(F3-avg3)$ correlates positively with the quantity OS-avg_OS, and the respective correlation coefficient is in the respective row of the first column. The corresponding p-value in the respective row of the last column.
- For example, in row 1:

The quantity $-3.38*(F1-3.972)-15.40*(F2-1,2376)+93.32*(F3-0.4548)$,
where F1= NK/CTL_PD1- at V1 , F2= nonTreg/NK at V1 , F3= ThCD69-/T at V1
correlates with the quantity OS-22.84 with correlation coefficient=0.7436 and $p<10^{-3}$.

A qualitative way to interpret this correlation is the following: If for a patient holds $-3.38*(F1-3.972)-15.40*(F2-1,2376)+93.32*(F3-0.4548)>0$ then we can expect that his OS will be >22.84 . The larger the quantity $-3.38*(F1-3.972)-15.40*(F2-1,2376)+93.32*(F3-0.4548)$ is, the larger we can expect OS to be. The larger the correlation coefficient, the more confident we can be for our prediction.

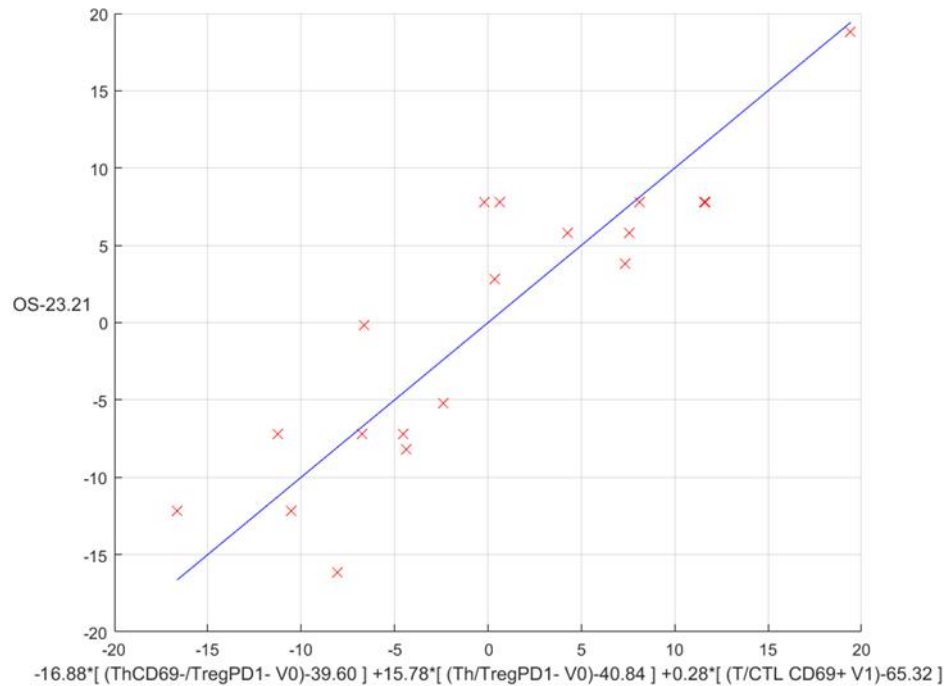
2) Patients with Imm.Reticul.Fr at PI/VI=Low, Vaccination=Early, Tumour in I location, No relapse before PI/VI Number of patients=20

Correlation	F1	avg1	C1	F2	avg2	C2	F3	avg3	C3	avg_OS	p-value
0.8480	NK VO	0.1639	205.1932	NK/nonTreg VO	1.1077	-21.5456	CTL PD1+/TregPD1- VO	15.0216	0.5487	23.8300	0.000108
0.8433	NK VO	0.1639	201.8126	NK/Th(CD4+) VO	1.0376	-22.8189	CTL PD1+/TregPD1- VO	15.0216	0.5646	23.8300	0.000134
0.8407	NK VO	0.1639	201.4176	NK/Th(CD4+)CD69+ VO	1.0537	-22.2184	CTL PD1+/TregPD1- VO	15.0216	0.5744	23.8300	0.000151
0.8313	NK VO	0.1639	218.0683	NK/Th(CD4+)CD69+ VO	47.3369	-0.4743	ThCD69+/T V1	0.0155	-411.0219	23.8300	0.000128
0.8249	NK/CTL PD1- V1	4.3279	-3.3978	nonTreg/NK V1	1.2160	-13.9831	ThCD69+/T V1	0.4761	102.8084	23.8300	0.000297
0.8228	NK/CTL PD1- V1	4.3279	-3.3992	Th(CD4+)/NK V1	1.4412	-11.2817	ThCD69+/T V1	0.4761	100.4881	23.8300	0.000324
0.8189	NK VO	0.1639	204.1941	NK/Th(CD4+)CD69+ VO	47.3369	-0.4351	Th(CD4+) CD69+ V1	0.0317	-187.6409	23.8300	0.000377
0.8189	NK VO	0.1639	204.1941	NK/Th(CD4+)CD69+ VO	47.3369	-0.4351	Th CD69+ V1	0.9988	197.6409	23.8300	0.000377
0.8181	NK/CTL PD1- V1	4.3279	-3.3790	Th(CD4+)CD69+/NK V1	1.3599	-11.8823	Th CD69+/T V1	0.4761	101.9461	23.8300	0.000380
0.8167	NK VO	0.1639	206.6646	NK/T(CD3) VO	0.4337	-48.9565	ThPD1+/Treg V1/VO	0.5820	13.7519	23.8300	0.000411
0.8160	NK VO	0.1639	200.4010	NK/T(CD3) VO	0.4337	-53.1833	ThPD1+/T V1/VO	0.9475	11.1014	23.8300	0.000422
0.8134	NK VO	0.1639	203.0485	NK/Th(CD4+)CD69+ VO	47.3369	-0.4321	ThCD69+/ThCD69+ V1	0.0334	-172.8203	23.8300	0.000482
0.8149	NK VO	0.1639	193.4340	NK/T(CD3) VO	0.4337	-51.2721	T/TThPD1- V1	3.0819	-1.5123	23.8300	0.000441
0.8135	NK VO	0.1639	201.6882	NK/Th(CD4+)CD69+ VO	47.3369	-0.4332	ThCD69+/nonTreg V1	0.0372	-160.3703	23.8300	0.000464
0.8120	NK VO	0.1639	201.4335	NK/nonTreg VO	1.1077	-20.2727	CTL PD1+/TregPD1- VO	28.3600	0.1365	23.8300	0.000480
0.8116	NK VO	0.1639	200.8736	NK/nonTreg VO	1.1077	-20.1871	CTL PD1+/TregPD1- VO	29.6610	0.1435	23.8300	0.000488
0.8097	NK VO	0.1639	198.9418	NK/Th(CD4+) VO	1.0376	-21.8823	CTL PD1+/TregPD1- VO	28.3600	0.1685	23.8300	0.000384
0.8097	NK/Th(CD4+)CD69+ V1	227.8363	-0.0143	Th(CD4+)CTL CD69+ V1	0.0937	-133.3439	T/ThCD69+ V1	2.8339	-11.4843	23.8300	0.000353
0.8094	NK VO	0.1639	198.4983	NK/Th(CD4+) VO	1.0376	-21.8554	CTL PD1+/TregPD1- VO	29.6610	0.1348	23.8300	0.000341
0.8090	NK VO	0.1639	200.4967	NK/T(CD3) VO	0.4337	-53.2483	T/ThPD1- V1/VO	1.1940	-7.0960	23.8300	0.000349



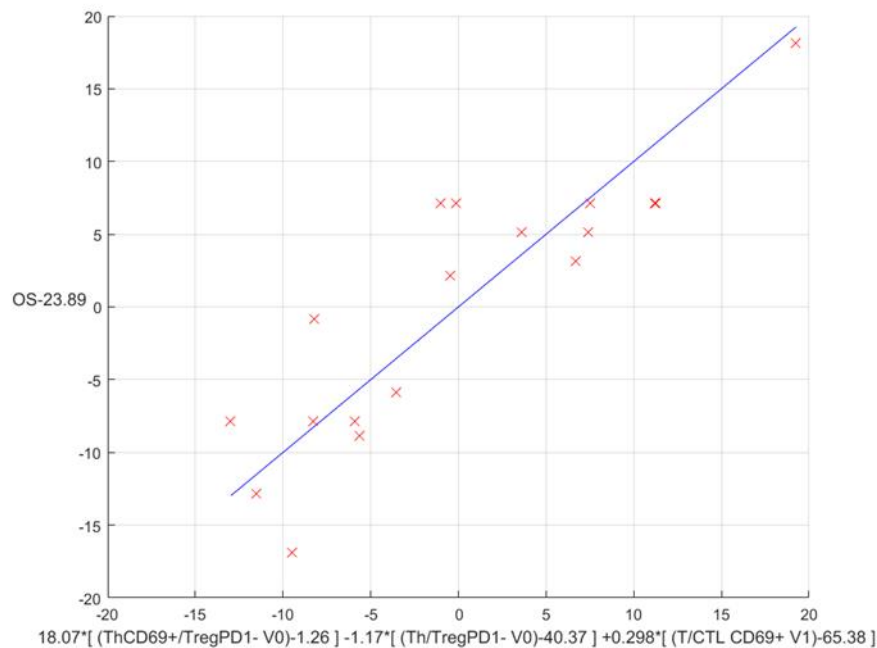
3) Patients with Imm.Reticul.Fr at PI/VI=Low, Vaccination=Late Number of patients=19

Correlation	F1	avg1	C1	F2	avg2	C2	F3	avg3	C3	avg_05	p-value
Q.8890	ThCD69+/TregPD1- V0	59.6014	-16.8892	Th/TregPD1- V0	40.8452	15.7857	T/CTL CD69+ V1	65.3228	0.1842	25.2105	0.000023
Q.8890	ThCD69+/TregPD1- V0	1.2418	16.8892	Th/TregPD1- V0	40.8452	-1.1035	T/CTL CD69+ V1	65.3228	0.1842	25.2105	0.000023
Q.8890	ThCD69+/TregPD1- V0	1.2418	15.7857	ThCD69+/TregPD1- V0	59.6014	-1.1035	T/CTL CD69+ V1	65.3228	0.1842	25.2105	0.000023
Q.8757	ThCD69+/TregPD1- V0	1.2418	15.9632	nonTreg+/TregPD1- V0	59.5094	-1.0658	T/CTL CD69+ V1	65.3228	0.1835	25.2105	0.000050
Q.8593	ThCD69+/TregPD1- V0	59.6014	-15.9181	Th/TregPD1- V0	40.8452	14.9105	CTL CD69+/CTL CD69+ V1	51.0600	0.4015	25.2105	0.000117
Q.8593	ThCD69+/TregPD1- V0	1.2418	15.9181	Th/TregPD1- V0	40.8452	-1.0078	CTL CD69+/CTL CD69+ V1	51.0600	0.4015	25.2105	0.000117
Q.8593	ThCD69+/TregPD1- V0	1.2418	14.9105	ThCD69+/TregPD1- V0	59.6014	-1.0078	CTL CD69+/CTL CD69+ V1	51.0600	0.4015	25.2105	0.000117
Q.8492	ThCD69+/TregPD1- V0	1.2418	15.1059	nonTreg+/TregPD1- V0	58.5094	-1.0010	CTL CD69+/CTL CD69+ V1	51.0600	0.4025	25.2105	0.000187
Q.8464	ThCD69+/TregPD1- V0	1.2418	13.2849	T/TregPD1- V0	98.6796	-0.2725	CTL CD69+/CTL CD69+ V1	51.0600	0.4085	25.2105	0.000212
Q.8449	ThCD69+/TregPD1- V0	1.2418	13.4644	T/TregPD1- V0	98.6796	-0.2916	T/CTL CD69+ V1	65.3228	0.3500	25.2105	0.000226
Q.8368	Th(CD4+) CD69+ V0	0.0238	571.8208	TregPD1-/CTL CD69+ V1	1.9564	7.8259	TregPD1-/CTL CD69+ V1/V0	2.3199	-6.5996	25.2105	0.000319
Q.8368	Th CD69+ V0	0.9762	-571.8208	TregPD1-/CTL CD69+ V1	1.9564	7.8259	TregPD1-/CTL CD69+ V1/V0	2.3199	-6.5996	25.2105	0.000319
Q.8365	T(CD8) V1	0.3482	-42.5648	CTL CD69+/ThCD69+ V1	71.2752	0.2407	ThCD69+/CTL PD1+ V1	0.0470	182.0124	25.2105	0.000524
Q.8365	T(CD8) V1	0.3482	-42.5850	CTL/ThCD69+ V1	73.6181	0.2385	ThCD69+/CTL PD1+ V1	0.0470	182.8512	25.2105	0.000526
Q.8333	ThCD69+/ThCD69+ V0	0.0246	53.23068	TregPD1-/CTL CD69+ V1	1.9564	7.7706	TregPD1-/CTL CD69+ V1/V0	2.3199	-6.5673	25.2105	0.000540
Q.8331	T(CD8) V1	0.3482	-52.4964	CTL/ThCD69+ V1	73.6181	0.2464	Th/CTL CD69+ V1	1.1000	11.5529	25.2105	0.000545
Q.8349	T(CD8) V1	0.3482	-52.2117	Th/CTL CD69+ V1	1.1000	11.4828	CTL CD69+/ThCD69+ V1	71.2752	0.1484	25.2105	0.000548
Q.8343	ThCD69+/Treg V0	0.4120	59.5651	ThPD1+/TregPD1- V0	22.5826	-1.2552	ThPD1+/CTL CD69+ V1	16.1545	1.0679	25.2105	0.000553
Q.8339	T(CD8) V1	0.3482	-52.9399	CTL/ThCD69+ V1	73.6181	0.2480	ThCD69+/CTL CD69+ V1	1.0723	12.0188	25.2105	0.000559
Q.8336	T(CD8) V1	0.3482	-52.6533	CTL CD69+/ThCD69+ V1	71.2752	0.2481	ThCD69+/CTL CD69+ V1	1.0723	11.9465	25.2105	0.000561



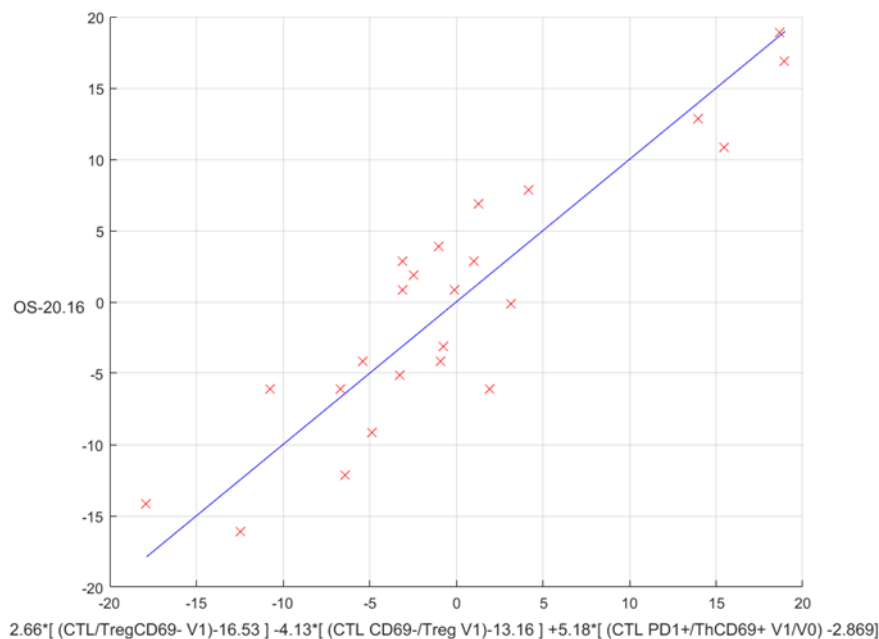
4) Patients with Imm.Reticul.Fr at PI/VI=Low, Vaccination=Late, Tumour in I location, No relapse before PI/VI. Number of patients=18

Correlation	F1	avg1	C1	F2	avg2	C2	F3	avg3	C3	avg_OS	p-value
0.8794	ThCD69+/TregPD1- V0'	1.2652	18.0715	Th/TregPD1- V0'	40.378291	-1.1736	T/CTL_CD69+ V1'	65.3896	0.2985	23.8889	0.000082
0.8794	ThCD69+/TregPD1- V0'	1.2652	18.0715	ThCD69+/TregPD1- V0'	39.113133	-1.1736	T/CTL_CD69+ V1'	65.3896	0.2985	23.8889	0.000082
0.8794	ThCD69+/TregPD1- V0'	39.1131	-18.0715	Th/TregPD1- V0'	40.378291	16.8979	T/CTL_CD69+ V1'	65.3896	0.2985	23.8889	0.000082
0.8670	ThPD1+/ThCD69+ V1'	9.2664	-0.5611	TregPD1+/NK V1/V0'	1.536534	-10.8236	TregCD69+/CTL_PD1- V1/V0'	3.0070	2.7325	23.8889	0.000154
0.8666	'CTL_CD69+ V0'	0.4417	-121.3390	ThCD69+/TregCD69+ V0'	4.170148	3.0493	'CTL_CD69+/ThCD69+ V1'	71.6915	0.2506	23.8889	0.000158
0.8628	ThCD69+/TregPD1- V0'	1.2652	16.9017	nonTregs/TregPD1- V0'	38.045209	-1.1526	T/CTL_CD69+ V1'	65.3896	0.2959	23.8889	0.000189
0.8622	'CTL_CD69+/Treg V0'	17.3514	-1.1657	ThCD69+/TregCD69+ V0'	4.170148	2.1734	'CTL_CD69+/CTL_CD69+ V1'	31.1926	0.4867	23.8889	0.000193
0.8621	'CTL/Treg V0'	18.0758	-1.1199	ThCD69+/TregCD69+ V0'	4.170148	2.2165	'CTL_CD69+/CTL_CD69+ V1'	31.1926	0.4771	23.8889	0.000194
0.8616	'CTL_PD1+/TregPD1- V0'	25.0124	-0.2373	TregPD1+/NK V1/V0'	1.536534	-9.3080	TregCD69+/CTL_CD69+ V1/V0'	2.3859	4.9458	23.8889	0.000199
0.8611	'NK/Th(CD4+/PD1- V1'	4.3948	-1.2793	TregPD1+/NK V1/V0'	1.536534	-13.4798	TregCD69+/CTL_PD1- V1/V0'	3.0070	3.1967	23.8889	0.000204
0.8606	ThPD1+/TregCD69+ V1'	5.1221	-1.2319	TregPD1+/NK V1/V0'	1.536534	-10.7794	TregCD69+/CTL_PD1- V1/V0'	3.0070	2.6202	23.8889	0.000209
0.8602	'CTL/CD69+ V0'	0.4417	-120.8790	ThCD69+/TregCD69+ V0'	4.170148	3.0502	'CTL/ThCD69+ V1'	74.0410	0.2468	23.8889	0.000212
0.8585	NK/TregPD1- V0'	87.8861	-0.0364	TregPD1+/NK V1'	0.043041	-194.7983	'ThCD69+/Treg V1/V0'	0.7466	-15.7656	23.8889	0.000229
0.8583	ThPD1+/CTL_CD69+ V1'	16.0529	0.3966	TregPD1+/NK V1/V0'	1.536534	-11.3711	TregCD69+/CTL_PD1- V1/V0'	3.0070	2.9283	23.8889	0.000232
0.8581	T/CTL_CD69+ V0'	2.5141	14.0012	ThCD69+/TregCD69+ V0'	4.170148	2.7151	'CTL_CD69+/ThCD69+ V1'	71.6915	0.2423	23.8889	0.000234
0.8567	'CTL_PD1+/ThCD69+ V1'	37.9595	0.2916	ThPD1+/CTL_PD1- V1'	1.251328	12.4571	Th(CD4+/PD1+/NK V1/V0'	1.0582	-8.1848	23.8889	0.000248
0.8560	TregPD1+/CTL_CD69+ V1'	1.9386	2.1878	TregPD1+/NK V1/V0'	1.536534	-11.2999	TregCD69+/CTL_PD1- V1/V0'	3.0070	2.8438	23.8889	0.000256
0.8555	'CTL_CD69+/TregPD1- V0'	2.1055	-2.6821	TregPD1+/NK V1/V0'	1.536534	-9.7097	TregCD69+/CTL_CD69+ V1/V0'	2.3859	5.2630	23.8889	0.000262
0.8548	'CTL_PD1+/ThCD69+ V1'	37.9595	0.1314	TregPD1+/NK V1/V0'	1.536534	-10.4543	TregCD69+/CTL_PD1- V1/V0'	3.0070	2.8052	23.8889	0.000271
0.8546	'CTL_CD69+/T V0'	0.4236	-119.0735	ThCD69+/TregCD69+ V0'	4.170148	2.8870	'CTL_CD69+/ThCD69+ V1'	71.6915	0.2539	23.8889	0.000279



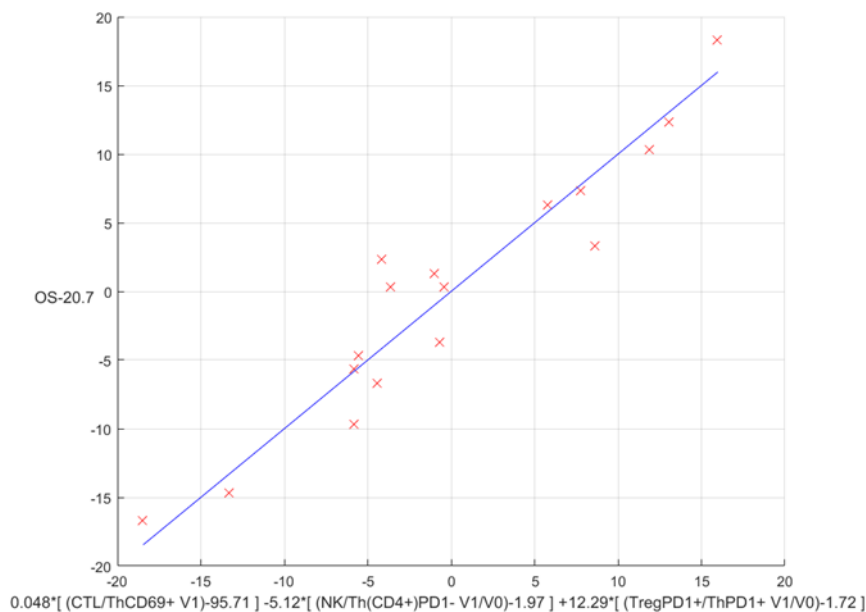
5) Patients with Imm.Reticul.Fr at PI/VI=Normal, Vaccination=Early. Number of patients=24

Correlation	F1	avg1	C1	F2	avg2	C2	F3	avg3	C3	avg_OS	p-value
0.9060	CTL/TregCD69+ V1	16.3833	2.6672	CTL_CD69+/Treg V1	13.163340	-4.1339	CTL_PD1+/ThCD69+ V1/V0	2.6693	3.1883	10.1667	0.00000011
0.8939	CTL_CD69+/Treg V1	13.3833	-4.1029	CTL_CD69+/TregCD69+ V1	15.690300	2.7433	CTL_PD1+/ThCD69+ V1/V0	2.6693	3.1270	10.1667	0.00000028
0.8922	CTL/Treg V1	13.7016	-3.9393	CTL/TregCD69+ V1	16.931504	2.6326	CTL_PD1+/ThCD69+ V1/V0	2.6693	3.1017	10.1667	0.00000039
0.8867	CTL_CD69+/TregCD69+ V1	141.4333	-0.0969	CTL_PD1+/TregCD69+ V1/V0	1.940003	9.7332	Treg/ThCD69+ V1/V0	1.8237	3.0792	10.1667	0.00000063
0.8809	CTL/TregCD69+ V1	147.1340	-0.0959	CTL_PD1+/TregCD69+ V1/V0	1.940003	9.9742	Treg/ThCD69+ V1/V0	1.8237	3.0596	10.1667	0.00000100
0.8771	NK/TregPD1+ V1	36.8796	-0.0850	CTL_CD69+/TregCD69+ V1	141.433405	-0.0741	CTL_PD1+/ThCD69+ V1/V0	2.6693	3.3828	10.1667	0.00000134
0.8766	NK/TregPD1+ V1	36.8796	-0.0863	CTL/TregCD69+ V1	147.133968	-0.0708	CTL_PD1+/ThCD69+ V1/V0	2.6693	3.3601	10.1667	0.00000138
0.8751	CTL_CD69+/TregCD69+ V1	141.4333	-0.0880	CTL_PD1+/ThCD69+ V1/V0	2.889308	3.7999	ThPD1+/Treg V1/V0	0.6866	-10.9181	10.1667	0.00000153
0.8745	T/CD8+/NK V1	2.8172	1.8963	CTL_CD69+/TregCD69+ V1	141.433401	-0.0870	CTL_PD1+/ThCD69+ V1/V0	2.6693	3.3701	10.1667	0.00000163
0.8733	CTL_CD69+/TregCD69+ V1	141.4333	-0.1001	CTL_CD69+/NK V1/V0	1.893331	2.1492	CTL_PD1+/ThCD69+ V1/V0	2.6693	3.0500	10.1667	0.00000177
0.8732	TregCD69+/NK V1	0.0236	121.2543	CTL_CD69+/TregCD69+ V1	141.433405	-0.0741	CTL_PD1+/ThCD69+ V1/V0	2.6693	3.3505	10.1667	0.00000178
0.8726	CTL_CD69+/TregCD69+ V1	141.4333	-0.0969	CTL_CD69+/NK V1/V0	1.933337	2.1071	CTL_PD1+/ThCD69+ V1/V0	2.6693	3.0590	10.1667	0.00000187
0.8711	T/CD8+/NK V1	2.8172	1.8385	CTL/TregCD69+ V1	147.133968	-0.0833	CTL_PD1+/ThCD69+ V1/V0	2.6693	3.3367	10.1667	0.00000208
0.8710	T/TregCD69+ V1	234.3764	-0.0479	CTL_CD69+/ThPD1+ V1/V0	2.310730	4.2430	Treg/ThCD69+ V1/V0	1.8237	3.1086	10.1667	0.00000209
0.8703	T/TregCD69+ V1	234.3764	-0.0482	CTL/ThPD1+ V1/V0	2.486660	4.1933	Treg/ThCD69+ V1/V0	1.8237	3.0867	10.1667	0.00000221
0.8695	CTL_CD69+/TregCD69+ V1	141.4333	-0.0964	CTL_PD1+/Treg V1/V0	1.822804	9.8150	Treg/ThCD69+ V1/V0	1.8237	3.0784	10.1667	0.00000232
0.8693	CTL/TregCD69+ V1	147.1340	-0.0963	CTL_CD69+/NK V1/V0	1.893331	2.1950	CTL_PD1+/ThCD69+ V1/V0	2.6693	3.0026	10.1667	0.00000236
0.8683	CTL/TregCD69+ V1	147.1340	-0.0961	CTL_CD69+/NK V1/V0	1.933337	2.1918	CTL_PD1+/ThCD69+ V1/V0	2.6693	3.0118	10.1667	0.00000230
0.8682	TregCD69+ V1	0.1385	87.7349	T/Treg V1	30.873297	-0.1071	CTL_PD1+/ThCD69+ V1/V0	2.6693	3.7743	10.1667	0.00000253
0.8682	TregCD69+ V1	0.8413	-97.7349	T/Treg V1	30.873297	-0.1071	CTL_PD1+/ThCD69+ V1/V0	2.6693	3.7743	10.1667	0.00000253



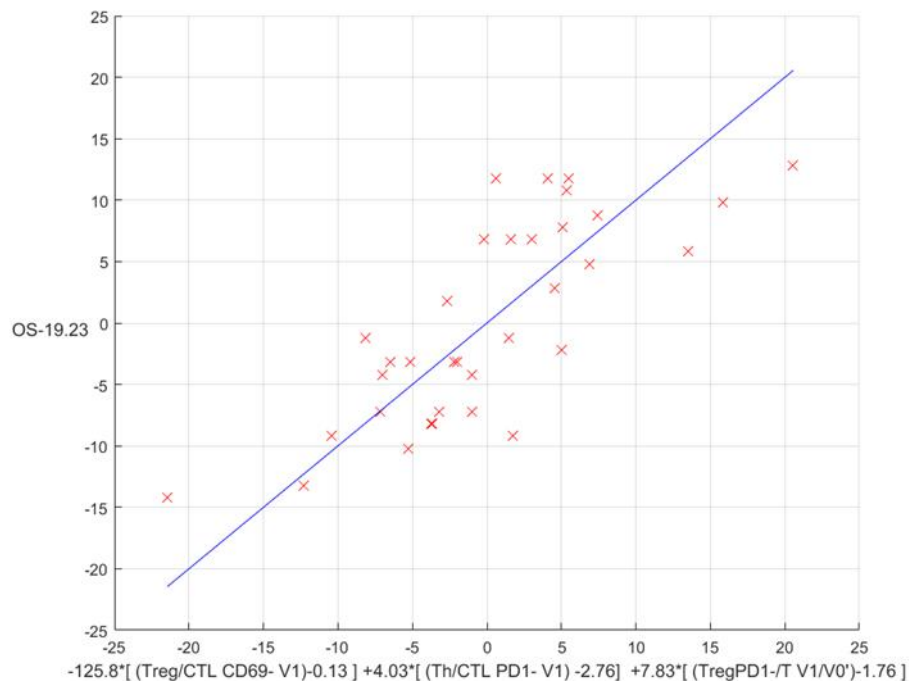
6) Patients with Imm.Reticul.Fr at PI/VI=Normal, Vaccination=Early, Tumour in I location, No relapse before PI/VI. Number of patients=17

Correlation	F1	avg1	C1	F2	avg2	C2	F3	avg3	C3	avg_O5	p-value
0.9516	'CTL/ThCD69+ V1'	92.7035	0.0486	'NK/Th(CD4+PD1+ V1/V0)	1.971116	-5.1239	'TregPD1+/ThPD1+ V1/V0'	1.7278	12.3982	20.7036	0.000001
0.9515	'CTL_CD69+/ThCD69+ V1'	92.2816	0.0500	'NK/Th(CD4+PD1+ V1/V0)	1.971116	-5.1445	'TregPD1+/ThPD1+ V1/V0'	1.7278	12.3232	20.7036	0.000001
0.9475	'T(CD8) V1/V0'	1.0787	13.7106	'Treg/ThPD1+ V1/V0'	1.046831	36.8130	'TregCD69+/ThPD1+ V1/V0'	1.9926	-26.5059	20.7036	0.000001
0.9440	'CTL_PD1+/ThCD69+ V1'	36.4780	0.1118	'NK/Th(CD4+PD1+ V1/V0)	1.971116	-5.1807	'TregPD1+/ThPD1+ V1/V0'	1.7278	13.0796	20.7036	0.000001
0.9434	'TregCD69+/ThCD69+ V1'	1.3982	4.4751	'T(CD8) V1/V0'	1.078680	12.4052	'ThPD1+/Treg V1/V0'	0.5304	-23.3731	20.7036	0.000002
0.9422	'CTL_PD1+/ThCD69+ V1'	36.4780	0.0831	'NK/Th(CD4+PD1+ V1/V0)	1.971116	-4.5572	'ThPD1+/TregPD1+ V1/V0'	0.6261	-44.0638	20.7036	0.000002
0.9416	'TregPD1+/CTL V0'	0.0714	-123.1271	'Th(CD4+) PD1+ V1/V0'	0.965472	-40.7923	'CTL_PD1+/T V1/V0'	1.1719	-13.0733	20.7036	0.000002
0.9402	'TregPD1+/CTL_CD69+ V0'	0.0769	-107.8834	'Th(CD4+) PD1+ V1/V0'	0.965472	-40.8624	'CTL_PD1+/T V1/V0'	1.1719	-13.2576	20.7036	0.000002
0.9400	'CTL_PD1+/ThPD1+ V0'	0.6312	20.2084	'CTL_CD69+/TregPD1+ V1/V0'	1.093267	-9.1407	'CTL_CD69+/ThPD1+ V1/V0'	2.6446	4.5691	20.7036	0.000002
0.9386	'NK V1/V0'	1.2768	6.2009	'NK/Th(CD4+PD1+ V1/V0)	1.971116	-5.2154	'ThPD1+/TregPD1+ V1/V0'	0.6261	-48.0213	20.7036	0.000002
0.9386	'TregPD1+/CTL_PD1+ V0'	0.1374	-58.4853	'Th(CD4+) PD1+ V1/V0'	0.965472	-40.4867	'CTL_PD1+/T V1/V0'	1.1719	-13.0510	20.7036	0.000002
0.9385	'ThPD1+/TregCD69+ V0'	9.0577	1.0247	'ThPD1+/TregCD69+ V1'	36.370448	-0.4863	'CTL_PD1+/T V1/V0'	1.6229	8.5360	20.7036	0.000002
0.9384	'TregCD69+/ThCD69+ V1'	1.3982	4.8328	'T(CD8) V1/V0'	1.078680	12.3438	'Treg/ThPD1+ V1/V0'	2.0468	6.4846	20.7036	0.000003
0.9381	'CTL_PD1+/ThPD1+ V0'	0.6312	20.0088	'CTL/ThPD1+ V1/V0'	2.612056	4.6365	'CTL_CD69+/TregPD1+ V1/V0'	1.0933	-9.2634	20.7036	0.000003
0.9374	'CTL_PD1+/T V1/V0'	1.1719	-14.5850	'ThPD1+/nonTreg V1/V0'	1.033487	-35.8077	'nonTreg/ThPD1+ V1/V0'	0.5319	-23.3732	20.7036	0.000003
0.9374	'T/ThCD69+ V1'	150.2318	0.0237	'NK/Th(CD4+PD1+ V1/V0)	1.9711	-4.3871	'ThPD1+/TregPD1+ V1/V0'	0.6261	-45.5174	20.7036	0.000003
0.9372	'ThPD1+/Treg V0'	7.7718	1.9383	'ThPD1+/TregCD69+ V1'	36.3704	-0.4576	'CTL_PD1+/T V1/V0'	1.6229	8.3609	20.7036	0.000003
0.9369	'CTL/ThCD69+ V1'	92.7035	0.0545	'NK/Th(CD4+PD1+ V1/V0)	1.9711	-4.3406	'ThPD1+/TregPD1+ V1/V0'	0.6261	-45.8063	20.7036	0.000003
0.9364	'CTL_CD69+/ThCD69+ V1'	92.2816	0.0554	'NK/Th(CD4+PD1+ V1/V0)	1.971116	-4.5551	'ThPD1+/TregPD1+ V1/V0'	0.6261	-45.8760	20.7036	0.000003
0.9363	'CTL_CD69+/PD1+ V1/V0'	1.4482	13.1183	'ThPD1+/ThPD1+ V1/V0'	1.001172	-34.3841	'ThPD1+/TregPD1+ V1/V0'	0.6261	-34.1382	20.7036	0.000003



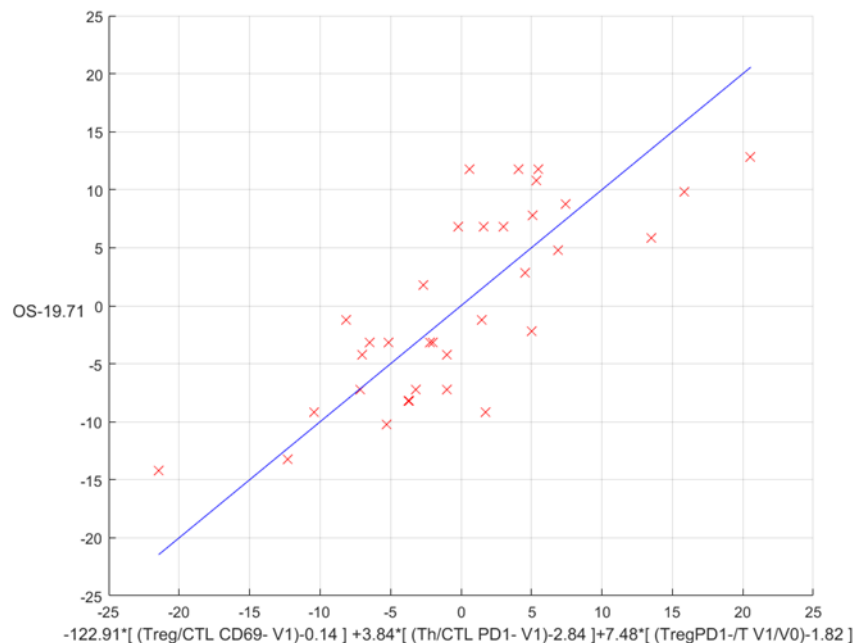
7) Patients with Imm.Reticul.Fr at PI/VI=Normal, Vaccination=Late. Number of patients=34

Correlation	F1	avg1	C1	F2	avg2	C2	F3	avg3	C3	avg_OS	p-value
0.7343	Treg/CTL_CD69-V1	0.1259	-125.8062	Th/CTL_PD1-V1	2.761523	4.0366	TregPD1/T V1/V0	1.7647	7.8327	19.2353	0.000004
0.7341	Treg/CTL_CD69-V1	0.1259	-126.6286	ThCD69/CTL_PD1-V1	2.699960	4.1450	TregPD1/T V1/V0	1.7647	7.8482	19.2353	0.000004
0.7339	TregCD69/CTL_CD69-V1	0.1198	-127.7883	ThCD69/CTL_PD1-V1	2.699960	3.4443	TregPD1/T V1/V0	1.7647	7.8341	19.2353	0.000005
0.7338	Treg/CTL V1	0.1293	-128.9419	Th/CTL_PD1-V1	2.761523	3.7614	TregPD1/T V1/V0	1.7647	7.8731	19.2353	0.000005
0.7336	Treg/CTL V1	0.1293	-128.8228	ThCD69/CTL_PD1-V1	2.699960	3.6640	TregPD1/T V1/V0	1.7647	7.7542	19.2353	0.000005
0.7337	TregCD69/CTL_CD69-V1	0.1198	-126.8028	Th/CTL_PD1-V1	2.761523	3.3486	TregPD1/T V1/V0	1.7647	7.5335	19.2353	0.000005
0.7327	Treg/CTL_CD69-V1	0.1359	-116.6785	nonTreg/CTL_PD1-V1	2.423350	4.0461	TregPD1/T V1/V0	1.7647	7.8443	19.2353	0.000006
0.7315	TregCD69/CTL V1	0.1141	-131.0215	ThCD69/CTL_PD1-V1	2.699960	3.2199	TregPD1/T V1/V0	1.7647	7.4780	19.2353	0.000008
0.7312	TregCD69/CTL_CD69-V1	0.1198	-118.8101	nonTreg/CTL_PD1-V1	2.423350	3.2704	TregPD1/T V1/V0	1.7647	7.6388	19.2353	0.000008
0.7311	TregCD69/CTL V1	0.1141	-130.1285	Th/CTL_PD1-V1	2.761523	3.1235	TregPD1/T V1/V0	1.7647	7.3835	19.2353	0.000008
0.7310	Treg/CTL V1	0.1293	-119.9480	nonTreg/CTL_PD1-V1	2.423350	3.7724	TregPD1/T V1/V0	1.7647	7.7840	19.2353	0.000008
0.7303	TregCD69/CTL_CD69-V1	0.1198	-99.1369	T/CTL_PD1-V1	6.068190	1.7347	TregPD1/T V1/V0	1.7647	6.7126	19.2353	0.000009
0.7276	TregCD69/CTL V1	0.1141	-104.0440	T/CTL_PD1-V1	6.068190	1.6935	TregPD1/T V1/V0	1.7647	6.6936	19.2353	0.000009
0.7351	TregCD69/CTL V1	0.1141	-121.2128	nonTreg/CTL_PD1-V1	2.423350	3.1530	TregPD1/T V1/V0	1.7647	7.4894	19.2353	0.000012
0.7351	Treg/CTL V1	0.1293	-95.4253	T/CTL_PD1-V1	6.068190	1.7664	TregPD1/T V1/V0	1.7647	6.6971	19.2353	0.000014
0.7345	Treg/CTL_CD69-V1	0.1359	-90.4826	T/CTL_PD1-V1	6.0682	1.8181	TregPD1/T V1/V0	1.7647	6.7367	19.2353	0.000010
0.7312	TregCD69/CTL_CD69-V1	0.1198	-112.3382	ThPD1/CTL_PD1-V1	1.6337	4.1830	TregPD1/T V1/V0	1.7647	7.8172	19.2353	0.000034
0.7284	Treg/CTL_CD69-V1	0.1359	-109.2465	ThPD1/CTL_PD1-V1	1.6337	5.0289	TregPD1/T V1/V0	1.7647	8.1377	19.2353	0.000037
0.7256	Treg/CTL V1	0.1293	-112.3316	ThPD1/CTL_PD1-V1	1.633684	4.6474	TregPD1/T V1/V0	1.7647	7.9593	19.2353	0.000044
0.7343	TregCD69/CTL V1	0.1141	-115.6014	ThPD1/CTL_PD1-V1	1.633684	3.8789	TregPD1/T V1/V0	1.7647	7.6534	19.2353	0.000047



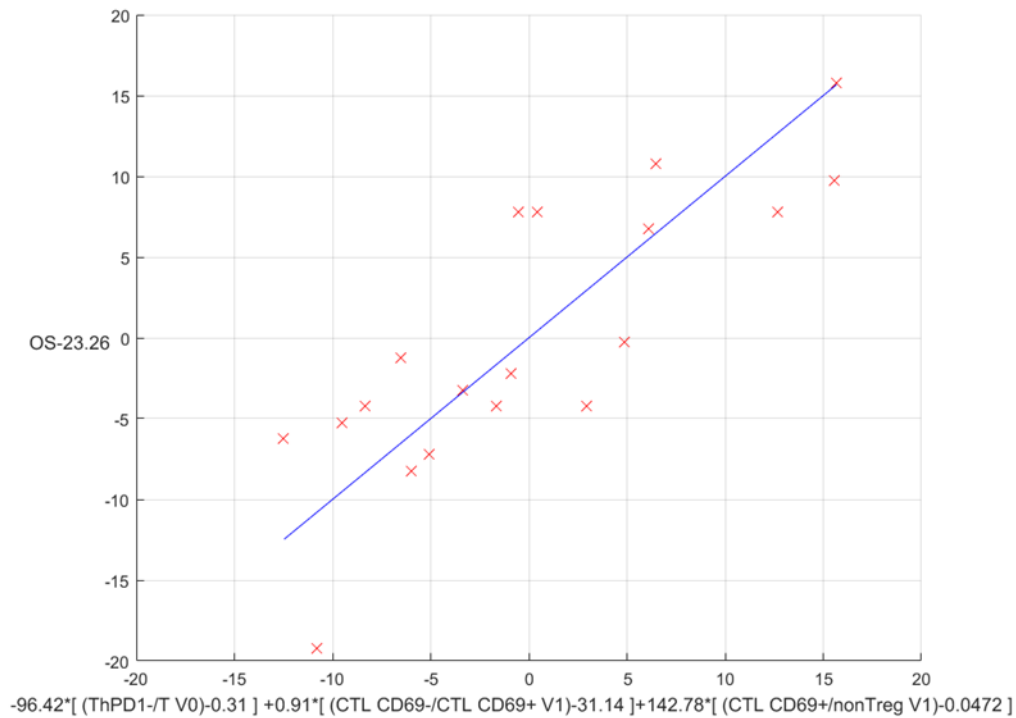
8) Patients with Imm.Reticul.Fr at PI/VI=Normal, Vaccination=Late, Tumour in I location, No relapse before PI/VI. Number of patients=32

Correlation	P1	avg1	C1	P2	avg2	C2	P3	avg3	C3	avg_OS	p-value
0.7833	Treg/CTL_CD69-V1	0.1410	-122.9100	Th/CTL_PD1-V1	2.945501	2.9455	TregPD1-T.V1/V0	1.8216	7.4852	19.7155	0.000006
0.7825	Treg/CTL_CD69-V1	0.1410	-122.6995	ThCD69-CTL_PD1-V1	2.751505	2.9455	TregPD1-T.V1/V0	1.8216	7.5952	19.7155	0.000006
0.7798	Treg/CTL-V1	0.1341	-125.9995	Th/CTL_PD1-V1	2.945501	2.9455	TregPD1-T.V1/V0	1.8216	7.5102	19.7155	0.000007
0.7795	Treg/CTL-V1	0.1341	-125.7927	ThCD69-CTL_PD1-V1	2.751505	2.9697	TregPD1-T.V1/V0	1.8216	7.4250	19.7155	0.000007
0.7787	TregCD69-CTL_CD69-V1	0.1343	-124.7024	ThCD69-CTL_PD1-V1	2.751505	2.9556	TregPD1-T.V1/V0	1.8216	7.5850	19.7155	0.000007
0.7764	TregCD69-CTL_CD69-V1	0.1343	-125.9995	Th/CTL_PD1-V1	2.945501	2.9824	TregPD1-T.V1/V0	1.8216	7.1985	19.7155	0.000007
0.7742	TregCD69-CTL_CD69-V1	0.1343	-97.8744	T/CTL_PD1-V1	6.182009	2.8818	TregPD1-T.V1/V0	1.8216	6.9700	19.7155	0.000008
0.7736	Treg/CTL_CD69-V1	0.1410	-124.1655	ImmTreg/CTL_PD1-V1	2.495001	2.9455	TregPD1-T.V1/V0	1.8216	7.5905	19.7155	0.000010
0.7734	TregCD69-CTL-V1	0.1354	-122.5672	T/CTL_PD1-V1	6.182009	2.8054	TregPD1-T.V1/V0	1.8216	6.9005	19.7155	0.000010
0.7731	TregCD69-CTL-V1	0.1354	-127.8810	ThCD69-CTL_PD1-V1	2.751505	2.9502	TregPD1-T.V1/V0	1.8216	7.1160	19.7155	0.000011
0.7706	TregCD69-CTL-V1	0.1354	-127.0552	Th/CTL_PD1-V1	2.945501	2.9454	TregPD1-T.V1/V0	1.8216	7.0355	19.7155	0.000011
0.7695	Treg/CTL-V1	0.1341	-117.5575	ImmTreg/CTL_PD1-V1	2.495001	2.9699	TregPD1-T.V1/V0	1.8216	7.4255	19.7155	0.000012
0.7692	TregCD69-CTL_CD69-V1	0.1343	-116.1829	ImmTreg/CTL_PD1-V1	2.495001	2.1724	TregPD1-T.V1/V0	1.8216	7.1855	19.7155	0.000012
0.7619	TregCD69-CTL-V1	0.1354	-119.4977	ImmTreg/CTL_PD1-V1	2.495001	2.9550	TregPD1-T.V1/V0	1.8216	7.1249	19.7155	0.000017
0.7555	Treg/CTL-V1	0.1341	-94.1947	T/CTL_PD1-V1	6.182009	1.6531	TregPD1-T.V1/V0	1.8216	6.5255	19.7155	0.000024
0.7500	Treg/CTL_CD69-V1	0.1410	-95.5055	T/CTL_PD1-V1	6.1521	1.7554	TregPD1-T.V1/V0	1.8216	6.5997	19.7155	0.000031
0.7445	TregCD69-CTL_CD69-V1	0.1343	-110.1650	ThPD1-CTL_PD1-V1	1.6555	2.9595	TregPD1-T.V1/V0	1.8216	7.4254	19.7155	0.000040
0.7435	Treg/CTL_CD69-V1	0.1410	-107.2755	ThPD1-CTL_PD1-V1	1.6555	4.8157	TregPD1-T.V1/V0	1.8216	7.7224	19.7155	0.000042
0.7414	CTL_PD1-CTL_CD69-V0	0.6212	34.4445	ThCD69-Th/PD1-V0	0.0971	-1.80.1556	TregPD1-CTL_PD1-V1	0.1102	-5.5.575	19.7155	0.000046
0.7407	TregPD1-Th/PD1-V0	0.0555	-125.5555	TregPD1-CTL_PD1-V1	0.1102	-5.5.7400	ThCD69-CTL_PD1-V1/V0	0.1675	6.7929	19.7155	0.000047



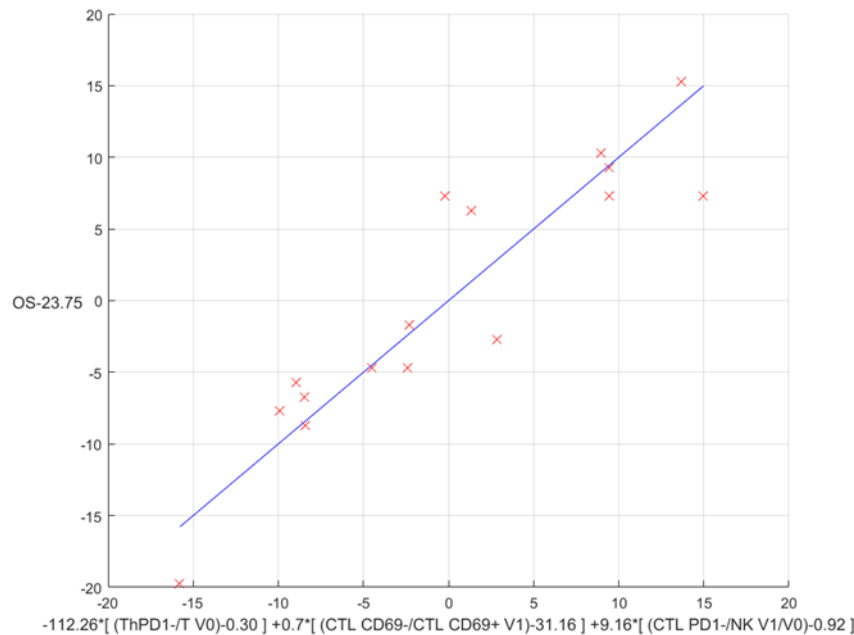
9) Patients with RTV=0, Vaccination=Early. Number of patients=19

Correlation	F1	avg1	C1	F2	avg2	C2	F3	avg3	C3	avg_OS	p-value
0.82146548	ThPD1-/TV0	0.815425053	-96.426859	CTL_CD69-/CTL_CD69+V1	81.14005703	0.912048008	CTL_CD69+/nonTregV1	0.047285554	142.783883	28.26815789	0.000581502
0.817401684	CTL_CD69+/TregCD69-V1	0.482044892	12.417801	NK/CTL_CD69+V1/V0	1.832086972	-4.960039524	CTL_CD69-/TV1/V0	1.814282384	-10.779378552	28.26815789	0.000674877
0.8183337	ThPD1-/TV0	0.815425053	-94.479241	CTL_CD69-/TV1	0.015370826	987.5629974	CTL_CD69-/CTL_CD69+V1	81.14005703	1.156410256	28.26815789	0.000700861
0.818298936	ThPD1-/TV0	0.815425053	-98.797026	CTL_CD69-/CTL_CD69+V1	81.14005703	0.88440398	CTL_CD69+/ThCD69-V1	0.042481457	150.879298	28.26815789	0.000702292
0.814891484	T/ThCD69+V1	2.255110384	6.5292666	NK/CTL_CD69+V1/V0	1.832086972	-5.20381498	CTL_CD69-/TV1/V0	1.814282384	-12.40035083	28.26815789	0.000738487
0.814548958	ThPD1-/TV0	0.815425053	-93.981118	CTL_CD69-/CTL_CD69+V1	81.14005703	0.884220914	CTL_CD69+/ThV1	0.04181222	155.4768473	28.26815789	0.000747527
0.811426191	CTL_TregCD69-V1	11.04156462	0.489754	NK/CTL_CD69+V1/V0	1.832086972	-4.848491445	CTL_CD69-/TV1/V0	1.814282384	-10.54435187	28.26815789	0.000834333
0.810792511	CTL_CD69-/TregCD69-V1	10.60951963	0.508353	NK/CTL_CD69+V1/V0	1.832086972	-4.846758824	CTL_CD69-/TV1/V0	1.814282384	-10.53121229	28.26815789	0.000832919
0.809685487	T/TregPD1-V1	38.1643368	0.1633402	NK/CTL_CD69+V1/V0	1.832086972	-4.868389081	CTL_CD69-/TV1/V0	1.814282384	-9.514273627	28.26815789	0.00088002
0.808073836	NK/CTL_CD69+V1/V0	1.832086972	-6.0685374	CTL_TregPD1-V1/V0	1.48834686	8.121181261	CTL_CD69+/ThPD1-V1/V0	2.221803417	-6.540682245	28.26815789	0.000936558
0.807757803	CTL_CD69+/TregV1	0.87393571	13.096529	NK/CTL_CD69+V1/V0	1.832086972	-5.169000696	CTL_CD69-/TV1/V0	1.814282384	-10.86491367	28.26815789	0.000946709
0.807329715	TregPD1-/ThPD1+V1	0.2362335	-17.544773	NK/CTL_CD69+V1/V0	1.832086972	-4.926357351	CTL_CD69+/CTL_CD69+V1/V0	1.026523654	-15.94236578	28.26815789	0.000960587
0.806858672	TregPD1-/ThPD1+V1	0.2362335	-17.693352	CTL_CD69+/CTL_CD69+V1/V0	1.022451719	-13.99268739	NK/CTL_CD69+V1/V0	1.832086972	-4.997330387	28.26815789	0.000976058
0.805757569	CTL_CD69+/TregPD1-V1	0.774784751	9.366489	NK/CTL_CD69+V1/V0	1.832086972	-4.888668915	CTL_CD69-/TV1/V0	1.814282384	-10.17146649	28.26815789	0.001013021
0.805405165	NK/CTL_CD69+V1/V0	1.832086972	-6.1154186	CTL_CD69+/ThPD1-V1/V0	2.221803417	-6.467092105	CTL_CD69-/TregPD1-V1/V0	1.157983688	7.96674639	28.26815789	0.001025089
0.803546752	NK/CTL_CD69+V1/V0	1.832086972	-5.7679927	CTL_TregCD69-V1/V0	1.217637484	7.923888098	CTL_CD69+/ThPD1-V1/V0	2.221803417	-6.412761169	28.26815789	0.001025704
0.803465026	TregCD69+/ThPD1+V1	0.332394108	-15.108021	NK/CTL_CD69+V1/V0	1.832086972	-4.720730025	CTL_CD69+/CTL_CD69+V1/V0	1.026523654	-15.08418684	28.26815789	0.001095512
0.803417328	CTL_TregPD1-V1	15.42725179	0.2081173	NK/CTL_CD69+V1/V0	1.832086972	-4.886923048	CTL_CD69-/TV1/V0	1.814282384	-10.09628181	28.26815789	0.001095398
0.803175445	CTL_CD69-/TregPD1-V1	16.69796704	0.2164497	NK/CTL_CD69+V1/V0	1.832086972	-4.888035676	CTL_CD69-/TV1/V0	1.814282384	-10.09202969	28.26815789	0.001104216
0.8030485706	CTL/ThV1	1.045003049	6.7391046	NK/CTL_CD69+V1/V0	1.832086972	-5.246095612	CTL_CD69-/TV1/V0	1.814282384	-12.1816473	28.26815789	0.00110897



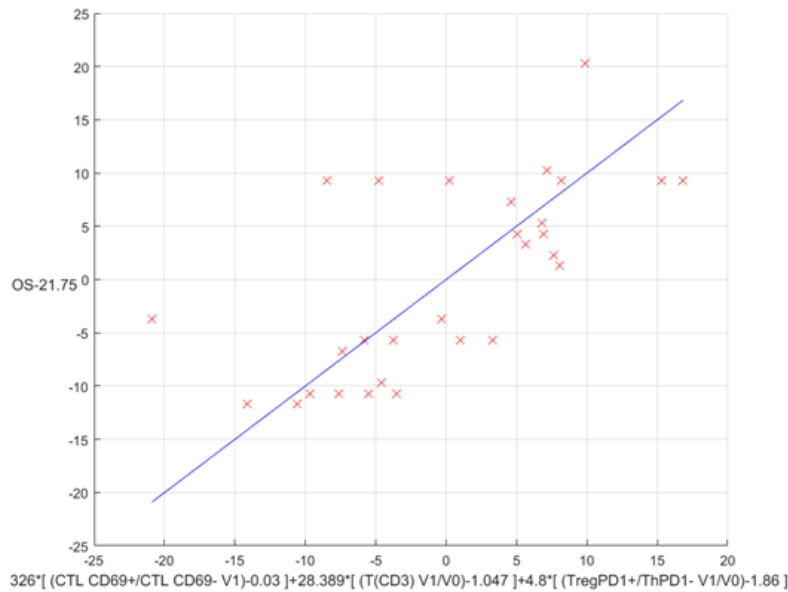
10) Patients with RTV=0, Vaccination=Early, Tumour in 1 location, No relapse before PI/VI. Number of patients=16

Correlation	F1	avg1	C1	F2	avg2	C2	F3	avg3	C3	avg_O5	p-value
0.914899103	ThPD1-/T V0	0.30399013	-112.126144	CTL_CD69+/CTL_CD69+ V1	31.16269982	0.70741987	CTL_PD1-/NK V1/V0	0.923723118	9.162394144	23.75	4.789-05
0.900902006	CTL_CD69-/NK V1/V0	1.804575928	5.6187388	ThPD1-/CTL_CD69+ V1/V0	1.524114409	-10.88771878	CTL_CD69+/ThPD1- V1/V0	1.9833322	-8.238648973	23.75	0.000112328
0.899674516	CTL_CD69-/NK V1/V0	1.790094952	5.6336961	ThPD1-/CTL_CD69+ V1/V0	1.524114409	-10.70239588	CTL_CD69+/ThPD1- V1/V0	1.9833322	-8.203439026	23.75	0.000120816
0.886161128	ThPD1-/CTL_CD69+ V0	3.084251035	1.3509997	ThCD69+/ThPD1- V1	16.82184966	1.421493688	NK/ThPD1- V1/V0	0.842987613	-17.4416344	23.75	0.002449993
0.883676363	ThPD1-/CTL_CD69+ V0	3.084251035	1.3509997	ThCD69+/ThPD1- V1	16.82184966	1.421493688	NK/ThPD1- V1/V0	0.842987613	-15.57183393	23.75	0.002390888
0.884780069	ThPD1-/T V0	0.30399013	-108.356624	CTL_CD69+/CTL_CD69+ V1	31.16269982	0.739627918	TCD8+/NK V1/V0	1.289160008	6.340696169	23.75	0.000261021
0.88285459	CTL_CD69+/V1/V0	2.103000643	20.39776	NK/CTL_CD69+ V1/V0	1.917886962	-9.411143681	CTL_CD69+/ThPD1- V1/V0	1.9833322	-7.96787087	23.75	0.000287069
0.882790772	ThPD1-/CTL_CD69+ V0	4.966335703	1.8235066	ThCD69+/ThPD1- V1	16.82184966	1.424398303	NK/ThPD1- V1/V0	0.842987613	-15.92664415	23.75	0.000288372
0.881979333	CTL_PD1-/NK V1/V0	2.425688475	3.637438	ThPD1-/CTL_CD69+ V1/V0	1.524114409	-10.35737021	CTL_CD69+/ThPD1- V1/V0	1.9833322	-8.263770076	23.75	0.000305862
0.880337393	ThPD1-/CTL_CD69+ V0	4.320018836	1.9304089	ThCD69+/ThPD1- V1	16.82184966	1.423686342	NK/ThPD1- V1/V0	0.842987613	-16.56630687	23.75	0.000313664
0.878448036	ThPD1-/CTL_CD69+ V0	3.084251035	2.4823263	nonThPD1-/ThPD1- V1	15.26556803	1.413612386	NK/ThPD1- V1/V0	0.842987613	-16.9990705	23.75	0.000323814
0.876946841	ThPD1-/CTL_CD69+ V0	3.084251035	2.5248264	Th/ThPD1- V1	17.23148974	1.373394477	NK/ThPD1- V1/V0	0.842987613	-17.05468899	23.75	0.000378148
0.87578415	ThPD1-/CTL_CD69+ V0	3.084251035	3.0189264	Th/ThPD1- V1	17.23148974	1.488244391	NK/ThPD1- V1/V0	0.842987613	-15.1911392	23.75	0.000398308
0.874778077	ThPD1-/CTL_CD69+ V0	4.966335703	1.7747403	nonThPD1-/ThPD1- V1	15.26556803	1.413686235	NK/ThPD1- V1/V0	0.842987613	-15.51908914	23.75	0.00041754
0.873877502	ThPD1-/CTL_CD69+ V0	4.966335703	1.8070264	Th/ThPD1- V1	17.23148974	1.376786009	NK/ThPD1- V1/V0	0.842987613	-15.33331142	23.75	0.00043721
0.871976313	ThPD1-/CTL_CD69+ V0	4.320018836	1.8748394	nonThPD1-/ThPD1- V1	15.26556803	1.413686235	NK/ThPD1- V1/V0	0.842987613	-16.13663269	23.75	0.000470069
0.870338106	ThPD1-/CTL_CD69+ V0	4.320018836	1.9068135	Th/ThPD1- V1	17.23148974	1.373394477	NK/ThPD1- V1/V0	0.842987613	-16.17834233	23.75	0.000504086
0.869648173	NK/CTL_CD69+ V1/V0	1.817886962	-5.6895475	CTL_CD69+/ThPD1- V1/V0	1.9833322	-7.578718936	CTL_CD69+/T V1/V0	1.180470837	23.68376383	23.75	0.000520169
0.869342777	ThPD1-/CTL_PD1- V1	0.383803113	-16.433948	CTL_CD69+/ThPD1- V1/V0	1.009629376	-16.80123891	ThPD1-/CTL_CD69+ V1/V0	1.829369635	-4.70290879	23.75	0.000526838
0.868976184	ThPD1-/CTL_CD69+ V0	3.084251035	2.9423362	nonThPD1-/ThPD1- V1	15.26556803	1.413686235	NK/ThPD1- V1/V0	0.842987613	-14.88834603	23.75	0.000534974



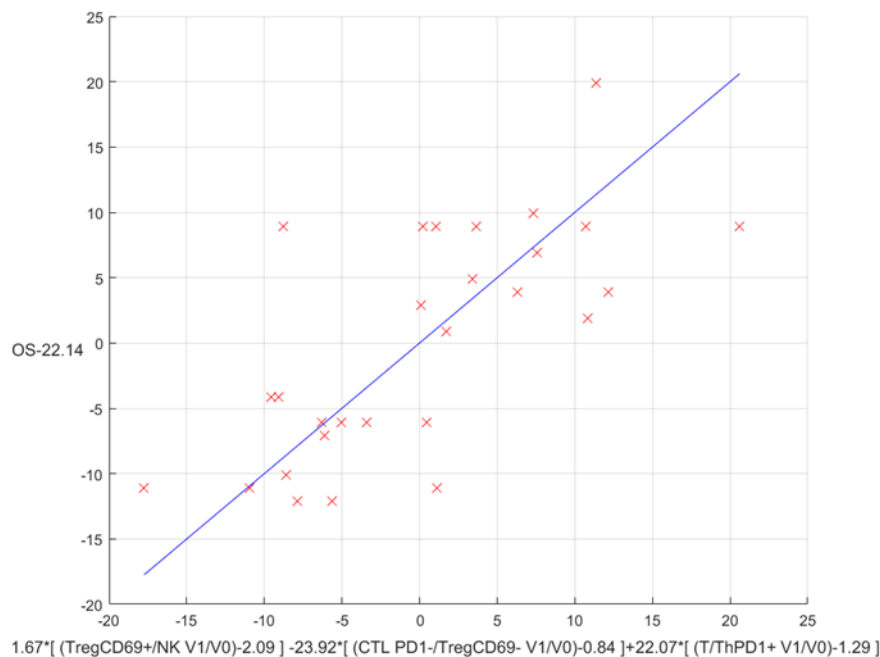
I I) Patients with RTV=0, Vaccination=Late. Number of patients=29

Correlation	F1	avg1	C1	F2	avg2	C2	F3	avg3	C3	avg_D5	p-value
0.867574546	CTL_CD69+/CTL_CD69-V1	0.03514112	526.00499	T (CD3) V1/V0	1.047351173	28.38969306	TregPD1+/ThPD1- V1/V0	1.86559203	4.80559285	21.75582069	0.001774107
0.66635294	CTL_PD1+/CTL_PD1-V0	1.039393383	-7.9554294	CTL_CD69+/T V1	0.015442745	889.9645722	T (CD3) V1/V0	1.047351173	25.25697916	21.75582069	0.001843011
0.665958968	T/CTL_CD69-V0	76.9555729	-0.1718757	T (CD3) V1/V0	1.047351173	21.54782195	ThPD1+/CTL_CD69+ V1/V0	1.119790915	-6.207359635	21.75582069	0.001858814
0.665175721	CTL_CD69+ V1	0.968006897	-356.63685	T (CD3) V1/V0	1.047351173	28.46131956	TregPD1+/ThPD1- V1/V0	1.86559203	4.785870849	21.75582069	0.001900853
0.665175721	CTL_CD8+/CD69+ V1	0.051993105	356.63685	T (CD3) V1/V0	1.047351173	28.46131956	TregPD1+/ThPD1- V1/V0	1.86559203	4.785870849	21.75582069	0.001900853
0.65473696	T (CD3) V1/V0	1.047351173	21.811137	Th PD1- V1/V0	0.995789166	-111.5245008	ThPD1+/ThPD1- V1/V0	1.051975462	32.26700483	21.75582069	0.002353669
0.652362016	T (CD3) V1/V0	1.047351173	22.558878	TregCD69+/ThPD1- V1/V0	1.956925744	9.764304591	nonTreg/ThPD1- V1/V0	0.971092339	58.50486701	21.75582069	0.002724622
0.652327775	CTL_PD1+/T V0	0.22042731	78.425529	ThCD69+/CTL_PD1- V1	0.049919545	146.0716603	T (CD3) V1/V0	1.047351173	21.187472	21.75582069	0.002727156
0.651798944	T (CD3) V1/V0	1.047351173	21.830555	TregCD69+/ThPD1- V1/V0	1.956925744	11.28955192	ThPD1+/nonTreg V1/V0	1.0586481	-56.68855562	21.75582069	0.002766551
0.65062278	CTL_CD69+ V1/V0	1.00890723	-947.97848	CTL_CD69+/T V1/V0	1.15240674	-29.2059419	CTL_PD1+/ThPD1+ V1/V0	2.296501075	4.800657595	21.75582069	0.002832386
0.650085525	CTL_CD69+/CTL_CD69- V1	0.03514112	260.0756	T (CD3) V1/V0	1.047351173	22.40623357	T/CTL_PD1- V1/V0	1.029267256	11.26201848	21.75582069	0.002997706
0.648234493	CTL_CD69+ V1	0.968006897	-284.08552	T (CD3) V1/V0	1.047351173	22.4774045	T/CTL_PD1- V1/V0	1.029267256	11.24559597	21.75582069	0.003042666
0.648234453	CTL_CD8+/CD69+ V1	0.051993105	294.08552	T (CD3) V1/V0	1.047351173	22.4774045	T/CTL_PD1- V1/V0	1.029267256	11.24559597	21.75582069	0.003042666
0.647871367	CTL_CD69+ PD1+ V0	0.468931034	-32.282709	T (CD3) V1/V0	1.047351173	19.9672327	T/CTL_PD1- V1/V0	1.029267256	11.09038155	21.75582069	0.003074575
0.647871367	CTL_PD1- V0	0.531068966	32.282709	T (CD3) V1/V0	1.047351173	19.9672327	T/CTL_PD1- V1/V0	1.029267256	11.09038155	21.75582069	0.003074575
0.64713114	CTL_CD8+/PD1+ V0	0.468931034	-38.80627	T (CD3) V1/V0	1.047351173	21.47089906	TregPD1+/CTL_PD1- V1/V0	1.66061154	2.415721232	21.75582069	0.003135772
0.64713114	CTL_PD1- V0	0.531068966	38.80627	T (CD3) V1/V0	1.047351173	21.47089906	TregPD1+/CTL_PD1- V1/V0	1.66061154	2.415721232	21.75582069	0.003135772
0.646955626	CTL_PD1+/CTL_PD1- V0	1.039393383	-5.5831619	T (CD3) V1/V0	1.047351173	18.96758751	T/CTL_PD1- V1/V0	1.029267256	10.43861135	21.75582069	0.003150433
0.646417168	CTL_CD8+/PD1+ V0	0.468931034	-43.259662	CTL_CD69+/T V1	0.015442745	867.5759953	T (CD3) V1/V0	1.047351173	26.71862919	21.75582069	0.003195777
0.646417168	CTL_PD1- V0	0.531068966	43.259662	CTL_CD69+/T V1	0.015442745	867.5759953	T (CD3) V1/V0	1.047351173	26.71862919	21.75582069	0.003195777



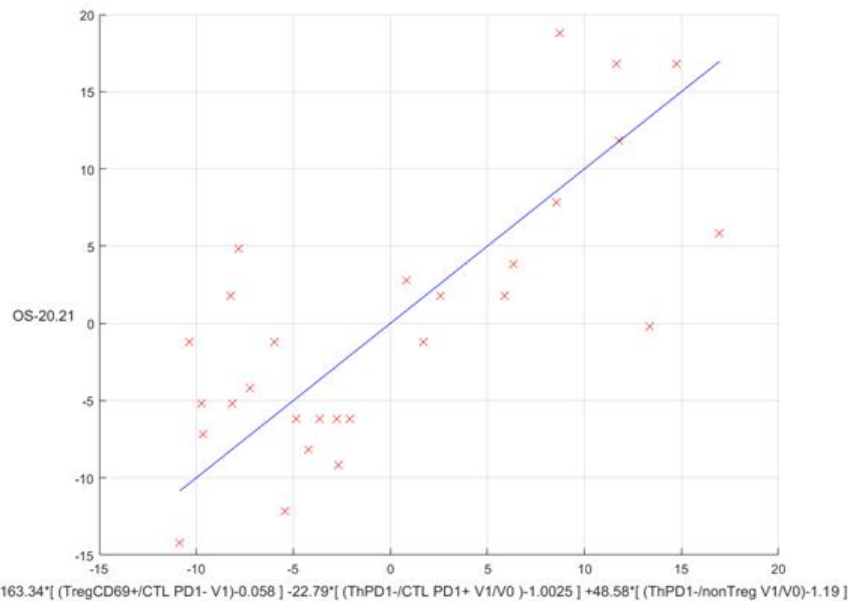
12) Patients with RTV=0, Vaccination=Late, Tumour in I location, No relapse before PI/VI. Number of patients=28

Correlation	P1	avg1	C1	P2	avg2	C2	P3	avg3	C3	avg_OS	p-value
0.706081371	TregCD69+V1/V0	0.090856016	1.6701553	CTLPD1+TregCD69-V1/V0	0.647815315	-25.92327648	T/ThPD1+V1/V0	1.038315586	22.07956493	2.14285714	0.000102291
0.701400791	CTLPD69+TregPD1-V0	1.748591078	-1.9462818	CTLPD1+TregCD69-V1/V0	0.647815315	-27.54905606	T/ThPD1+V1/V0	1.038315586	20.78970327	2.14285714	0.000587506
0.695801508	CTLPD1+TregCD69-V1/V0	0.847815315	-51.480102	T/ThPD1+V1/V0	1.038315586	20.53905906	ThPD1+nonTregV1/V0	1.048877946	-25.28556945	2.14285714	0.000911003
0.695841551	ThPD1+V1/V0	0.958570178	-39.282821	CTLPD1+TregCD69-V1/V0	0.647815315	-50.29085747	T/ThPD1+V1/V0	1.038315586	25.78978351	2.14285714	0.000956105
0.695825971	CTLPD1+TregCD69-V1/V0	0.847815315	-27.610104	nonTregThCD69+V1/V0	1.097875421	-4.981045939	T/ThPD1+V1/V0	1.038315586	25.50969587	2.14285714	0.000959581
0.69678251	ThPD1+TregPD1-V0	16.63870806	-0.1900788	CTLPD1+TregCD69-V1/V0	0.647815315	-27.08624178	T/ThPD1+V1/V0	1.038315586	21.11078185	2.14285714	0.000992574
0.695840822	TregPD1+CTLPD69+V1/V0	2.78700931	-1.1728121	CTLPD1+TregCD69-V1/V0	0.647815315	-25.64392771	T/ThPD1+V1/V0	1.038315586	20.75058007	2.14285714	0.001035665
0.695805954	TregCD69+ThPD1+V0	0.090856016	1.6701553	CTLPD1+TregV1/V0	0.671004644	-25.27875747	T/ThPD1+V1/V0	1.038315586	25.75155939	2.14285714	0.001039559
0.695820038	ThCD69+TregPD1-V0	1.090091796	-1.9218785	CTLPD1+TregCD69-V1/V0	0.647815315	-25.01056502	T/ThPD1+V1/V0	1.038315586	21.61157584	2.14285714	0.001039002
0.695819459	CTLPD1+TregCD69-V1/V0	0.847815315	-27.709717	ThCD69+ThCD69+V1/V0	1.194485194	-4.169886185	T/ThPD1+V1/V0	1.038315586	25.25476159	2.14285714	0.001039037
0.695820038	ThPD1+TregPD1-V0	16.63870806	-0.1900788	CTLPD1+TregCD69-V1/V0	0.647815315	-27.42185902	T/ThPD1+V1/V0	1.038315586	20.92700174	2.14285714	0.001042176
0.695841551	TregPD1+ThPD1+V0	1.948310281	2.8518279	CTLPD1+TregCD69-V1/V0	0.647815315	-24.03811109	T/ThPD1+V1/V0	1.038315586	22.16959587	2.14285714	0.001044585
0.695840515	CTLPD69+ThPD1-V0	0.043940652	-82.287817	CTLPD1+TregCD69-V1/V0	0.647815315	-25.49787801	T/ThPD1+V1/V0	1.038315586	21.13207776	2.14285714	0.001100559
0.695825569	ThPD1+TregCD69+V0	15.710756654	0.028779	CTLPD1+TregCD69-V1/V0	0.647815315	-27.40631778	T/ThPD1+V1/V0	1.038315586	22.05414464	2.14285714	0.001106559
0.691095107	CTLPD1+TregCD69-V1/V0	0.847815315	-25.687492	TregPD1+ThCD69+V1/V0	3.082467715	-1.054875905	T/ThPD1+V1/V0	1.038315586	25.68748587	2.14285714	0.001135772
0.695867801	TregPD1+TregPD1-V0	1.190655516	-1.6386555	CTLPD1+TregCD69-V1/V0	0.647815315	-27.14985676	T/ThPD1+V1/V0	1.038315586	21.78758519	2.14285714	0.001236715
0.694857589	ThPD1+TregPD1-V0	40.38775777	-0.0785551	CTLPD1+TregCD69-V1/V0	0.647815315	-24.67823865	T/ThPD1+V1/V0	1.038315586	19.28057942	2.14285714	0.001244455
0.695820071	TregPD1+ThPD1+V0	1.948310281	2.8518279	CTLPD1+TregV1/V0	0.671004644	-25.27875747	T/ThPD1+V1/V0	1.038315586	26.04859109	2.14285714	0.001254558
0.695820071	CTLPD69-V1/V0	1.008548827	-84.548501	CTLPD69+ThPD1+V0	1.125880164	-25.55857189	CTLPD1+ThPD1+V1/V0	2.068765558	4.658279109	2.14285714	0.001296496
0.687741892	ThPD1+CTLPD69+V1/V0	1.153494411	-5.5717551	CTLPD1+TregCD69-V1/V0	0.647815315	-27.55845752	T/ThPD1+V1/V0	1.038315586	20.55427375	2.14285714	0.001310589



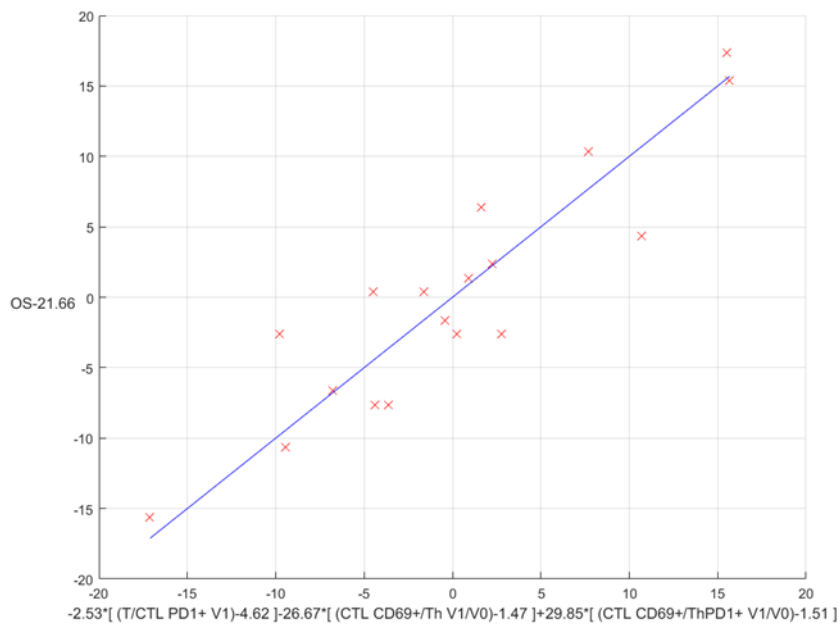
I3) Patients with RTV>0, Vaccination=Early. Number of patients=28

Correlation	F1	sig1	C1	F2	sig2	C2	F3	sig3	C3	sig_05	p-value
0.73805942	ThCD69+/CTL PD1- V1/V0	0.00847831	163.34745	ThPD1+/CTL PD1+ V1/V0	1.002024302	-22.7978944	ThPD1+/nonTreg V1/V0	1.19453347	48.5845657	20.1412571	0.000234702
0.731515967	CTL PD1- V1/V0	0.075452207	-8.875124	NK/Th(CD4H)CD69+ V1/V0	2.854197713	8.345471287	NK/Th(CD4H)PD1- V1/V0	2.656407572	-8.882262103	20.1412571	0.000283626
0.731801333	TregPD1+/NK V0	0.052082104	187.26848	CTL PD1+/T V1	0.314819179	81.43483336	T/ThPD1- V1/V0	1.426118983	-11.18330048	20.1412571	0.000304620
0.730301982	TregPD1+/ThCD69+ V1	3.076109407	2.7287209	CTL PD1+/ThPD1- V1/V0	2.937853587	-9.48993616	CTL PD1+/nonTreg V1/V0	2.811465715	10.35530932	20.1412571	0.000219427
0.729301862	TregPD1-/NK V0	0.052082104	132.02003	Th PD1- V1/V0	1.114803374	40.6127893	CTL PD1-/CTL PD1+ V1/V0	0.893257802	-21.09126353	20.1412571	0.000331304
0.728381875	NK/Th(CD4H)CD69+ V1/V0	2.854197713	8.2778819	NK/Th(CD4H)PD1- V1/V0	2.859407372	-8.76192708	CTL PD1-/CTL PD1+ V1/V0	0.893257802	-4.64899572	20.1412571	0.000385437
0.724800791	CTL/TregPD1- V1/V0	1.037070709	-10.08115	CTL PD1+/ThCD69+ V1/V0	2.869497129	-4.99581132	TregPD1+/ThPD1- V1/V0	2.691941229	-3.148725901	20.1412571	0.000292854
0.72186464	CTL CD69+/TregPD1- V1/V0	1.048183449	-9.8134329	CTL PD1+/ThCD69+ V1/V0	2.869497129	-4.99580904	TregPD1+/ThPD1- V1/V0	2.691941229	-3.148725901	20.1412571	0.000292854
0.721865976	ThCD69+/TregPD1- V0	0.75185044	8.188035	NK/TregPD1- V1	38.24433908	-0.054488907	TregPD1+/ThCD69+ V1	3.076109407	3.801190155	20.1412571	0.000429989
0.718940372	TregPD1-/NK V0	0.052082104	113.88971	CTL PD1-/CTL PD1+ V1/V0	0.893257802	-18.16168375	ThPD1-/nonTreg V1/V0	1.19453347	33.27423736	20.1412571	0.000468881
0.7178776	CTL PD1+/ThCD69+ V1/V0	2.869497129	4.7180044	TregPD1+/ThPD1- V1/V0	2.869497129	-4.761138986	T/ThPD1- V1/V0	0.746943724	-17.66127596	20.1412571	0.000486128
0.715024389	Th(CD4H) CD69+ V0	0.020039286	351.28001	NK/TregPD1- V1	38.24433908	-0.054488907	TregPD1+/ThCD69+ V1	3.076109407	3.64394725	20.1412571	0.000546566
0.715024389	Th CD69+ V0	0.878660714	-151.28001	NK/TregPD1- V1	38.24433908	-0.054488907	TregPD1+/ThCD69+ V1	3.076109407	3.64394725	20.1412571	0.000546566
0.714777763	ThCD69+/ThCD69+ V0	0.020070099	331.30568	NK/TregPD1- V1	38.24433908	-0.054488907	TregPD1+/ThCD69+ V1	3.076109407	3.940165527	20.1412571	0.000551729
0.713745869	NK/Th(CD4H)CD69+ V1/V0	2.854197713	7.7342448	NK/Th(CD4H)PD1- V1/V0	2.859407372	-8.063308738	CTL PD1-/T V1/V0	0.894489362	-9.630226517	20.1412571	0.000711928
0.713545874	Th(CD4H) CD69+ V0	0.020039286	408.36197	TregPD1+/ThCD69+ V1	3.076109407	3.71983343	TregPD1+/TregPD1- V1/V0	0.833276902	-6.338675724	20.1412571	0.000737102
0.713545874	Th CD69+ V0	0.878660714	-408.36197	TregPD1+/ThCD69+ V1	3.076109407	3.71983343	TregPD1+/TregPD1- V1/V0	0.833276902	-6.338675724	20.1412571	0.000737102
0.713303881	ThCD69+/nonTreg V0	0.021012893	317.808	NK/TregPD1- V1	38.24433908	-0.054488907	TregPD1+/ThCD69+ V1	3.076109407	3.613725613	20.1412571	0.000779534
0.713067384	ThCD69+/ThCD69+ V0	0.020070099	384.70586	TregPD1+/ThCD69+ V1	3.076109407	3.71983343	TregPD1+/TregPD1- V1/V0	0.833276902	-6.378380488	20.1412571	0.000845597
0.711807102	ThCD69+/nonTreg V0	0.021012893	389.62721	TregPD1+/ThCD69+ V1	3.076109407	3.68373443	TregPD1+/TregPD1- V1/V0	0.833276902	-6.374762376	20.1412571	0.000813988



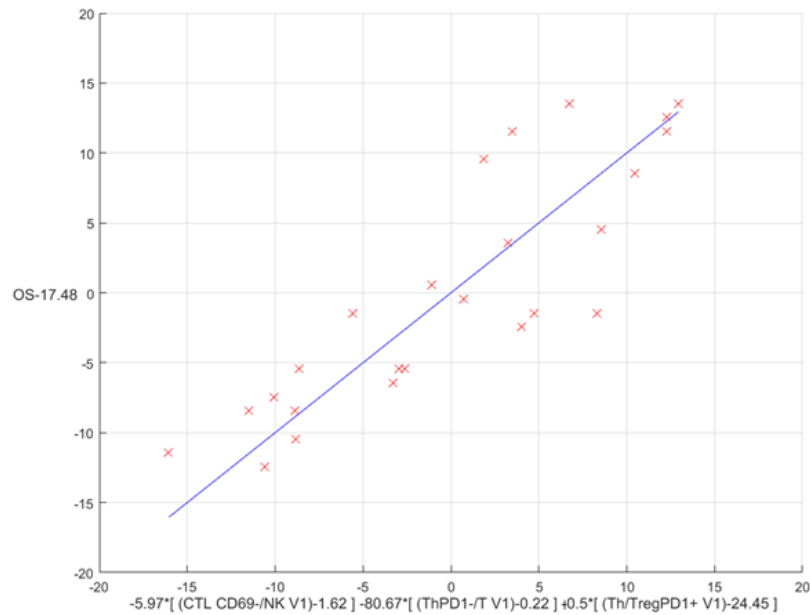
I4) Patients with RTV>0, Vaccination=Early, Tumour in I location, No relapse before PI/VI.Number of patients=18

Correlation	F1	avg1	C1	F2	avg2	C2	F3	avg3	C3	avg_OS	p-value
0.910089133	T/CTL PD1+ V1	4.632711937	-2.3326475	CTL CD69+Th V1/V0	1.478972738	-16.87077946	CTL CD69+Th PD1+ V1/V0	1.534789879	28.05233476	21.66666667	1.02E-05
0.909677916	CTL CD69+Th CD69+ V1/V0	1.577120048	5.5524131	CTL PD1+nonThag V1/V0	1.459238773	-9.930464051	Th PD1+nonThag V1/V0	1.042433433	-18.77699285	21.66666667	1.23E-05
0.904206082	CTL CD69+NK V0	0.038863787	-107.02617	Th PD1+CTL CD69+ V1	22.3309964	-0.54831468	Th CD4+ PD1+ V1/V0	0.962626101	-49.8061483	21.66666667	1.81E-05
0.903496021	Th CD4+CD69+ NK V0	1.681406675	-8.1481357	NK/Thag PD1+ V0	32.3212401	-0.487169807	Thag PD1+Th CD69+ V1/V0	1.617389462	5.126423157	21.66666667	1.93E-05
0.90297561	CTL CD69+CTL CD69+ V0	28.18204636	0.424985	T/CTL CD69+ V1	77.31088665	-0.28017472	Th CD4+ PD1+ V1/V0	0.962626101	-43.31076773	21.66666667	2.01E-05
0.901838309	T/CTL PD1+ V1	4.632711937	-2.4726554	CTL CD69+Th CD69+ V1/V0	1.478038616	-15.57787873	CTL CD69+Th PD1+ V1/V0	1.534789879	28.04050266	21.66666667	2.16E-05
0.900382111	Th CD4+ NK V0	1.722424351	-7.8275132	NK/Thag PD1+ V0	32.3212401	-0.486469724	Thag PD1+Th CD69+ V1/V0	1.617389462	5.187894629	21.66666667	2.33E-05
0.89838449	nonThag NK V0	1.597128491	-10.43346	NK/Thag PD1+ V0	32.3212401	-0.486473185	CTL CD69+Th CD69+ V1/V0	1.577120048	4.96747408	21.66666667	2.59E-05
0.897426111	Th PD1+ CTL V1	0.793366835	-10.273588	CTL CD69+Th V1/V0	1.478972738	-16.13176967	CTL CD69+Th PD1+ V1/V0	1.534789879	30.94689712	21.66666667	2.64E-05
0.89707331	nonThag NK V0	1.597128491	-8.328175	NK/Thag PD1+ V0	32.3212401	-0.486168861	Thag PD1+Th CD69+ V1/V0	1.617389462	5.11015733	21.66666667	2.81E-05
0.89495973	Th PD1+ CTL CD69+ V1	0.6348337	-9.7712754	CTL CD69+Th V1/V0	1.478972738	-17.8604762	CTL CD69+Th PD1+ V1/V0	1.534789879	30.7383687	21.66666667	3.02E-05
0.89447671	Th PD1+ CTL PD1+ V1	1.457389931	-4.8136961	CTL CD69+Th V1/V0	1.478972738	-17.86047624	CTL CD69+Th PD1+ V1/V0	1.534789879	30.87002111	21.66666667	3.02E-05
0.8940482	CTL CD69+Th CD69+ V1/V0	1.577120048	5.335869	CTL PD1+Th V1/V0	1.366653448	-8.67368197	Th PD1+nonThag V1/V0	1.042433433	-15.86043261	21.66666667	3.03E-05
0.89390118	Th CD4+CD69+ NK V0	1.681406675	-10.02815	NK/Thag PD1+ V0	32.3212401	-0.504171803	CTL CD69+Th CD69+ V1/V0	1.577120048	4.830765766	21.66666667	3.23E-05
0.894787983	CTL CD69+Th CD69+ V1/V0	1.577120048	5.1689315	CTL PD1+Th CD69+ V1/V0	1.367847741	-8.64842019	Th PD1+nonThag V1/V0	1.042433433	-18.71351101	21.66666667	3.37E-05
0.89367604	CTL Th CD69+ V1/V0	1.813486651	7.523309	CTL PD1+Thag PD1+ V1/V0	0.730904888	-17.54668985	Thag PD1+Th CD69+ V1/V0	2.11325135	-8.471993771	21.66666667	3.62E-05
0.89363339	CTL Th CD69+ V1/V0	1.813486651	7.7596904	CTL PD1+Thag PD1+ V1/V0	0.730904888	-17.7380481	Thag CD69+Th V1/V0	2.108991772	-8.57484036	21.66666667	3.62E-05
0.893018947	Thag V1/V0	2.096950778	-10.516151	CTL Th CD69+ V1/V0	1.813486651	7.80083734	CTL PD1+Thag PD1+ V1/V0	0.730904888	-18.38361369	21.66666667	3.73E-05
0.891761321	CTL CD69+Th CD69+ V1/V0	1.577120048	5.1074693	CTL PD1+nonThag V1/V0	1.459238773	-9.26311283	Th PD1+Th PD1+ V1/V0	0.988190359	-10.37138018	21.66666667	3.81E-05
0.891101578	CTL CD69+Th CD69+ V1/V0	1.814884136	7.7856123	CTL PD1+Thag PD1+ V1/V0	0.730904888	-17.96578383	Thag CD69+Th V1/V0	2.108991772	-8.638091611	21.66666667	3.89E-05



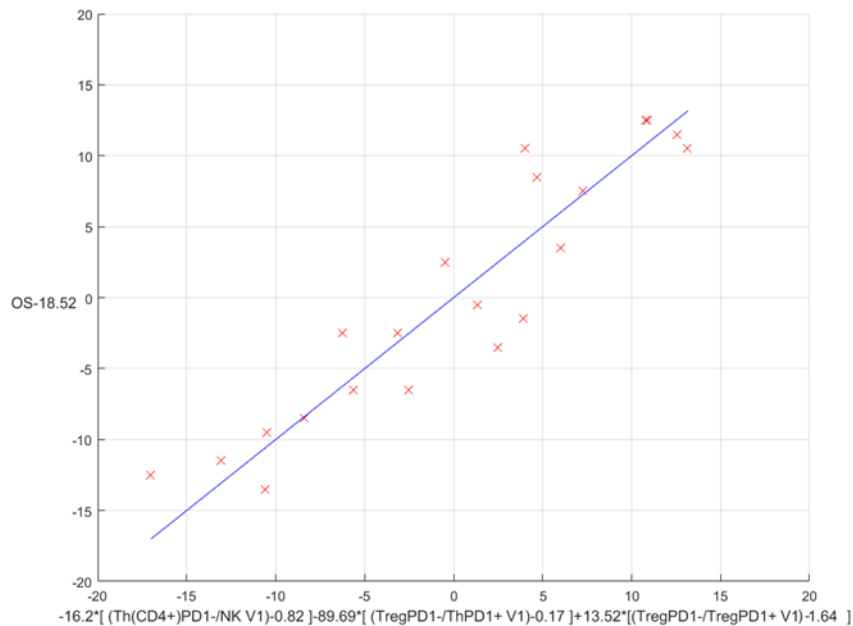
I5) Patients with RTV>0, Vaccination=Late. Number of patients=25

Correlation	P1	avg1	C1	P2	avg2	C2	P3	avg3	C3	avg_OS	p-value
0.662078769	CT _U CD69+/NK V1	1.621046245	-8.9702015	ThPD1+/T V1	0.22040446	-80.67058585	Th/TregPD1+ V1	24.48721667	0.52240303	17.45	1.62E-06
0.662078896	CT _U CD69+/NK V1	1.621046245	-8.9282857	ThCD69+/TregPD1+ V1	24.01583217	0.50815556	ThPD1+/T V1	0.22040446	-80.50462036	17.45	1.02E-06
0.662493275	CT _U CD69+/NK V1	1.66289139	-8.8129036	ThPD1+/T V1	0.22040446	-80.41823031	Th/TregPD1+ V1	24.48721667	0.5206467733	17.45	1.93E-06
0.66208939	CT _U CD69+/NK V1	1.66289139	-8.8649415	ThCD69+/TregPD1+ V1	24.01583217	0.512494261	ThPD1+/T V1	0.22040446	-80.29362736	17.45	2.89E-06
0.659591462	CT _U CD69+/NK V1	1.621046245	-8.7828037	ThPD1+/T V1	0.22040446	-79.70120332	Th/TregPD1+ V1	21.76813465	0.517487134	17.45	2.59E-06
0.659590654	CT _U CD69+/NK V1	1.621046245	-8.322719	TregPD1+/ThPD1+ V1	0.155927602	-88.78838586	ThPD1+/T V1	0.22040446	-80.22158645	17.45	2.42E-06
0.659591319	CT _U CD69+/NK V1	1.66289139	-8.1092519	TregPD1+/ThPD1+ V1	0.155927602	-88.58838587	ThPD1+/T V1	0.22040446	-80.39146762	17.45	2.95E-06
0.648302704	CT _U CD69+/NK V1	1.66289139	-8.8269742	ThPD1+/T V1	0.22040446	-79.44819686	Th/TregPD1+ V1	21.76813465	0.52155593	17.45	2.85E-06
0.648305665	ThCD4+/PD1+/NK V1	0.726916201	-14.575152	TregPD1+/ThPD1+ V1	0.155927602	-85.5285727	TregPD1+/ThPD1+ V1	1.66289139	10.58783347	17.45	5.43E-06
0.64566546	CT _U CD69+/NK V1	0.061643547	-11.010315	CT _U CD69+/ThPD1+ V1	1.492391232	7.022839515	ThPD1+/Th/Treg V1	0.658992719	-35.3336355	17.45	5.95E-06
0.644293956	ThCD4+/PD1+ V1	0.43638	-11.029615	CT _U CD69+/NK V1	0.061643547	-11.029615	CT _U CD69+/ThPD1+ V1	1.492391232	7.022839515	17.45	6.42E-06
0.644293956	ThPD1+ V1	0.9172	-11.029615	CT _U CD69+/NK V1	0.061643547	-11.029615	CT _U CD69+/ThPD1+ V1	1.492391232	7.022839515	17.45	6.42E-06
0.64328286	CT _U CD69+/NK V1	0.061643547	-10.466655	ThPD1+/CT _U CD69+ V1	1.515315165	-0.623453717	TregPD1+/ThPD1+ V1	0.155927602	-84.18323837	17.45	7.63E-06
0.643286004	T(CD5)/NK V1	5.458123822	-1.6527462	TregPD1+/ThPD1+ V1	0.155927602	-85.9421274	ThPD1+/T V1	0.22040446	-80.87642945	17.45	7.69E-06
0.643286004	ThCD4+/PD1+/NK V1	0.726916201	-11.029615	ThPD1+/TregPD1+ V1	0.597323276	2.241256782	ThPD1+/Th/Treg V1	0.670445855	-11.04312215	17.45	7.73E-06
0.639691095	CT _U CD69+/NK V1	1.66289139	-8.8695052	ThPD1+/CT _U CD69+ V1	1.515315165	-0.572844402	TregPD1+/ThPD1+ V1	0.155927602	-70.91168435	17.45	8.44E-06
0.639483145	CT _U CD69+/NK V1	1.66289139	-8.8851556	ThPD1+/CT _U CD69+ V1	1.515315165	-0.623453717	ThPD1+/TregPD1+ V1	0.597323276	0.910365543	17.45	8.56E-06
0.63765994	CT _U CD69+/NK V1	0.061643547	-12.492667	CT _U CD69+/ThPD1+ V1	1.492391232	6.992334465	ThPD1+/Th/Treg V1	0.496026091	35.3336355	17.45	9.58E-06
0.637614092	CT _U CD69+/NK V1	1.621046245	-8.6473751	ThPD1+/CT _U CD69+ V1	1.515315165	-0.572844402	TregPD1+/ThPD1+ V1	0.155927602	-70.91168435	17.45	9.61E-06
0.636934079	CT _U CD69+/NK V1	1.621046245	-8.7815456	ThPD1+/CT _U CD69+ V1	1.515315165	-0.623453717	ThPD1+/TregPD1+ V1	0.597323276	0.910365543	17.45	1.02E-06



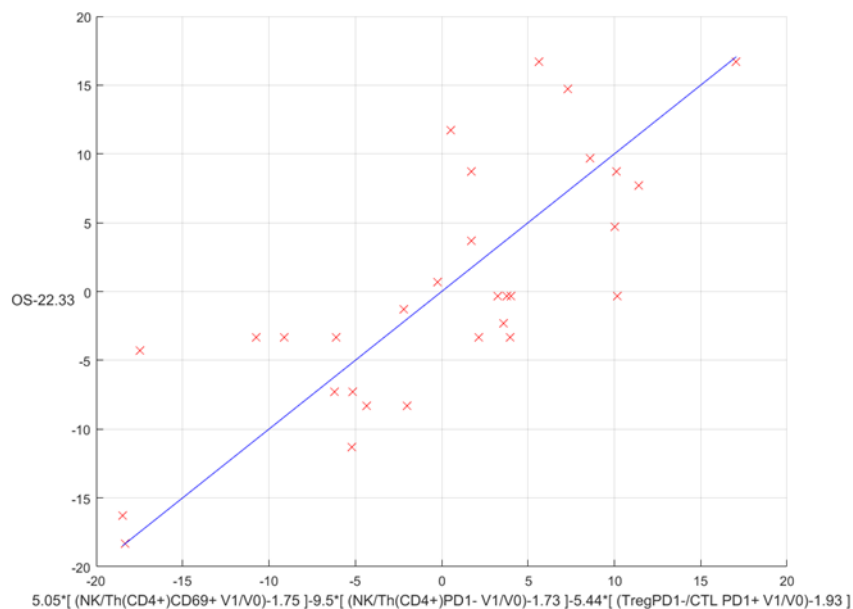
16) Patients with RTV>0, Vaccination=Late, Tumour in I location, No relapse before PI/VI. Number of patients=21

Correlation	P1	avg1	C1	P2	avg2	C2	P3	avg3	C3	avg_O5	p-value
0.93012672	Th(CD4+PD1-/NK V1)	0.82623237	-8.307946	TregPD1-/ThPD1+ V1	0.71714579	-9.90791378	TregPD1-/TregPD1+ V1	1.84278564	18.33088001	18.93300000	1.17E-07
0.93320948	Th(CD4+CD69-/NK V1)	1.568297489	-30.161818	Th(CD4+PD1-/NK V1)	0.766234284	-46.03958958	Th/TregPD1+ V1	24.44922934	0.53476176	18.93300000	2.38E-07
0.933309056	Th(CD4+CD69-/NK V1)	1.568297489	-30.161818	Th(CD4+PD1-/NK V1)	0.766234284	-46.04042787	Th(CD69-/TregPD1+ V1)	2.939393048	0.833110184	18.93300000	2.78E-07
0.934800178	Th(CD4+V1)	1.592857521	-29.563112	Th(CD4+PD1-/NK V1)	0.766234284	-44.95406018	Th/TregPD1+ V1	24.44922934	0.820585104	18.93300000	4.17E-07
0.934800178	Th(CD4+V1)	1.592857521	-29.563112	Th(CD4+PD1-/NK V1)	0.766234284	-44.95406018	Th/TregPD1+ V1	24.44922934	0.820585104	18.93300000	4.17E-07
0.934800178	Th(CD4+PD1-/NK V1)	0.766234284	-46.03958958	Th(CD4+PD1-/NK V1)	0.766234284	-46.03958958	Th/TregPD1+ V1	24.44922934	0.820585104	18.93300000	4.17E-07
0.937554811	Th(CD4+CD69-/NK V1)	1.568297489	-30.161818	Th(CD4+PD1-/NK V1)	0.766234284	-46.04042787	nonTreg/TregPD1+ V1	21.80941848	0.574484351	18.93300000	4.44E-07
0.91696451	Th(CD4+V1)	1.592857521	-29.563112	Th(CD4+PD1-/NK V1)	0.766234284	-46.03958958	Th(CD69-/TregPD1+ V1)	2.939393048	0.833110184	18.93300000	4.54E-07
0.91696451	Th(CD4+V1)	1.592857521	-29.563112	Th(CD4+PD1-/NK V1)	0.766234284	-46.03958958	Th(CD69-/TregPD1+ V1)	2.939393048	0.833110184	18.93300000	4.54E-07
0.91696451	Th(CD4+PD1-/NK V1)	0.766234284	-46.03958958	Th(CD4+PD1-/NK V1)	0.766234284	-46.03958958	Th(CD69-/TregPD1+ V1)	2.939393048	0.833110184	18.93300000	4.54E-07
0.91495871	Th(CD4+CD69-/NK V1)	1.568297489	-30.161818	Th(CD4+PD1-/NK V1)	0.766234284	-46.04042787	Th/TregPD1+ V1	24.44922934	0.81123388	18.93300000	5.89E-07
0.934737939	Th(CD4+PD1-/NK V1)	0.82623237	-8.307946	nonTreg/NK V1	1.87245411	-20.93827818	Th/TregPD1+ V1	24.44922934	0.754087999	18.93300000	6.01E-07
0.93500000	Th(CD4+V1)	1.592857521	-29.563112	Th(CD4+PD1-/NK V1)	0.766234284	-46.03958958	nonTreg/TregPD1+ V1	21.80941848	0.839948552	18.93300000	6.74E-07
0.93500000	Th(CD4+V1)	1.592857521	-29.563112	Th(CD4+PD1-/NK V1)	0.766234284	-46.03958958	nonTreg/TregPD1+ V1	21.80941848	0.839948552	18.93300000	6.74E-07
0.93500000	Th(CD4+PD1-/NK V1)	0.766234284	-46.03958958	Th(CD4+PD1-/NK V1)	0.766234284	-46.03958958	nonTreg/TregPD1+ V1	21.80941848	0.839948552	18.93300000	6.74E-07
0.934800178	Th(CD4+PD1-/NK V1)	0.82623237	-8.307946	nonTreg/NK V1	1.87245411	-20.94454794	Th(CD69-/TregPD1+ V1)	2.939393048	0.799344103	18.93300000	6.77E-07
0.933400000	Th(CD4+CD69-/NK V1)	1.568297489	-30.161818	Th(CD4+PD1-/NK V1)	0.766234284	-46.04042787	Th(CD69-/TregPD1+ V1)	2.939393048	0.799344103	18.93300000	7.04E-07
0.933400000	Th(CD4+CD69-/NK V1)	1.568297489	-30.161818	Th(CD4+PD1-/NK V1)	0.766234284	-46.04042787	nonTreg/TregPD1+ V1	21.80941848	0.830146941	18.93300000	9.28E-07
0.907480004	Th(CD4+PD1-/NK V1)	0.766234284	-46.03958958	nonTreg/NK V1	1.87245411	-20.94454794	Th/TregPD1+ V1	24.44922934	0.830146941	18.93300000	1.17E-06
0.906380006	Th(CD4+PD1-/NK V1)	0.766234284	-46.03958958	nonTreg/NK V1	1.87245411	-20.94454794	Th/TregPD1+ V1	24.44922934	0.830146941	18.93300000	1.28E-06



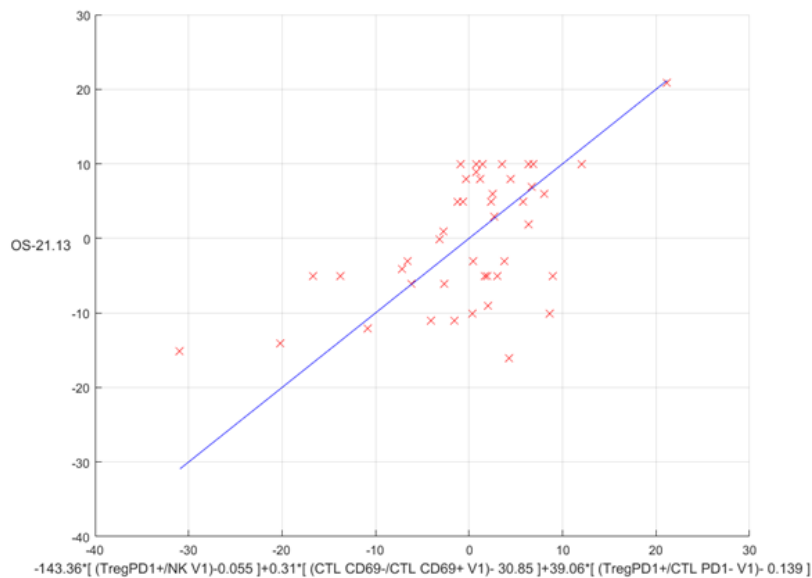
17) Patients with Low lymphocytes at PI/VI, Vaccination=Early, tumour in I location, No relapse before PI/VI. Number Of patients=30.

Correlation	P1	avg1	C1	P2	avg2	C2	P3	avg3	C3	avg_OS	p-value
0.773641655	NK/Th(CD4+ICD69+ V1/V0)	1.754676304	5.081765117	NK/Th(CD4+PD1+ V1/V0)	1.754676304	-5.803652277	TregPD1+CTLA4PD1+ V1/V0	1.924480959	-5.448245162	22.55555555	2.40E-05
0.763334164	NK/Th(CD4+PD1+ V1/V0)	1.754676304	-6.35650121	TregPD1+CTLA4PD1+ V1/V0	1.924480959	-5.344630305	nonTreg/Th(CD69+ V1/V0)	0.94586322	9.30330975	22.55555555	4.30E-05
0.755481534	NK/Th(CD4+PD1+ V1/V0)	1.754676304	-6.552755934	TregPD1+CTLA4PD1+ V1/V0	1.924480959	-4.127875509	TregPD1+Th(CD69+ V1/V0)	1.566111655	4.516565939	22.55555555	4.85E-05
0.747497164	TregPD1+Th(CD69+ V1/V0)	3.009410479	2.325452361	NK/Th(CD4+PD1+ V1/V0)	1.754676304	-6.553347935	TregPD1+CTLA4PD1+ V1/V0	1.924480959	-4.441565195	22.55555555	4.89E-05
0.733633539	NK/Th(CD4+PD1+ V1/V0)	1.754676304	-6.377921131	TregPD1+CTLA4PD1+ V1/V0	1.924480959	-4.324239775	nonTreg/Th(CD69+ V1/V0)	0.94586322	9.326767951	22.55555555	6.85E-05
0.73043126	NK/Th(CD4+PD1+ V1/V0)	1.754676304	-6.585577032	TregPD1+CTLA4PD1+ V1/V0	1.924480959	-5.423514631	TregPD1+Th(CD69+ V1/V0)	1.566111655	4.442761099	22.55555555	6.89E-05
0.730354126	NK/Th(CD4+PD1+ V1/V0)	1.754676304	-6.599445034	TregPD1+CTLA4PD1+ V1/V0	1.924480959	-5.462316306	TregPD1+Th(CD69+ V1/V0)	1.566111655	4.462225825	22.55555555	6.75E-05
0.730354126	NK/Th(CD4+PD1+ V1/V0)	1.754676304	-6.599445034	TregPD1+CTLA4PD1+ V1/V0	1.924480959	-5.462316306	Th(CD69+Th(CD69+ V1/V0)	1.023276217	6.331366995	22.55555555	7.37E-05
0.747497164	NK/Th(CD4+PD1+ V1/V0)	1.754676304	-6.552755934	TregPD1+CTLA4PD1+ V1/V0	1.924480959	-4.127875509	nonTreg/Th(CD69+ V1/V0)	0.94586322	9.326767951	22.55555555	7.85E-05
0.745440304	NK/Th(CD4+PD1+ V1/V0)	1.754676304	-6.625693704	TregPD1+CTLA4PD1+ V1/V0	1.924480959	-5.65931347	TregPD1+Th(CD69+ V1/V0)	1.566111655	5.415193071	22.55555555	8.35E-05
0.742377135	NK/Th(CD4+PD1+ V1/V0)	1.754676304	-6.442767822	TregPD1+CTLA4PD1+ V1/V0	1.924480959	-5.651162546	Th(CD69+Th(CD69+ V1/V0)	1.023276217	6.331366995	22.55555555	9.49E-05
0.755481534	NK/Th(CD4+PD1+ V1/V0)	1.754676304	-6.48742446	TregPD1+CTLA4PD1+ V1/V0	1.924480959	-4.424001636	Th(CD69+Th(CD69+ V1/V0)	1.023276217	6.756675055	22.55555555	0.00010862
0.756203921	NK/Th(CD4+PD1+ V1/V0)	1.754676304	-6.656063564	TregPD1+CTLA4PD1+ V1/V0	1.924480959	-4.478854215	TregPD1+Th(CD69+ V1/V0)	1.566111655	5.326552196	22.55555555	0.000121692
0.754277315	NK/Th(CD4+PD1+ V1/V0)	1.754676304	-6.595153306	TregPD1+CTLA4PD1+ V1/V0	1.924480959	-5.369551157	TregPD1+Th(CD69+ V1/V0)	1.566111655	5.34536406	22.55555555	0.000151602
0.755607034	NK/Th(CD4+PD1+ V1/V0)	1.754676304	-6.69505977	NK/Th(CD4+PD1+ V1/V0)	1.924480959	-11.61040496	TregPD1+CTLA4PD1+ V1/V0	1.924480959	-5.65931347	22.55555555	0.000164314
0.755607034	NK/Th(CD4+PD1+ V1/V0)	1.754676304	-6.69505977	TregPD1+CTLA4PD1+ V1/V0	1.924480959	-4.424001636	TregPD1+Th(CD69+ V1/V0)	1.566111655	5.326552196	22.55555555	0.00017006
0.75804217	NK/Th(CD4+PD1+ V1/V0)	1.754676304	-6.664165555	TregPD1+CTLA4PD1+ V1/V0	1.924480959	-4.606642066	TregPD1+Th(CD69+ V1/V0)	1.566111655	5.326552196	22.55555555	0.000185516
0.757193434	NK/Th(CD4+PD1+ V1/V0)	1.754676304	-6.69505977	NK/Th(CD4+PD1+ V1/V0)	1.924480959	-11.61040496	TregPD1+CTLA4PD1+ V1/V0	1.924480959	-5.65931347	22.55555555	0.000189593
0.757193434	NK/Th(CD4+PD1+ V1/V0)	1.754676304	-6.69505977	TregPD1+CTLA4PD1+ V1/V0	1.924480959	-4.424001636	TregPD1+Th(CD69+ V1/V0)	1.566111655	5.326552196	22.55555555	0.000189594
0.758597555	NK/Th(CD4+PD1+ V1/V0)	1.754676304	-7.303157131	TregPD1+CTLA4PD1+ V1/V0	1.924480959	-4.707082555	T/Th(CD69+ V1/V0)	1.173069067	5.350195455	22.55555555	0.000189757



I8) Patients with Low lymphocytes at PI/VI, Vaccination=Late, tumour in I location, No relapse before PI/VI. Number Of patients=44.

Coefficient	F1	avg1	C1	F2	avg2	C2	F3	avg3	C3	avg_C3	p-value
0.577490017	TragPD1+TNK V1	0.05576257	-142.36555	CTL_CD69+CTL_CD69+V1	20.65550141	0.016918555	TragPD1+CTL_PD1-V1	0.139779474	39.0553931	21.13656364	0.000610034
0.576495247	TragPD1+TNK V1	0.05576257	-120.8636434	TragCD69+CTL_PD1-V1	2.160465075	0.000000759	TTragCD69+V1/V1	0.695974514	5.993617574	21.13656364	0.000679699
0.575037663	TragPD1+TNK V1	0.05576257	-120.8636434	TragCTL_PD1-V1/V1	2.161617769	0.000000000	TTragCD69+V1/V1	0.695974514	7.571222029	21.13656364	0.000000000
0.571633264	TragPD1+TNK V1	0.05576257	-115.8607493	CTLTragCD69+V1/V1	1.161456875	0.000000000	CTL_PD1+TNK V1/V1	1.176596127	-6.414455576	21.13656364	0.001100204
0.571758826	TragPD1+TNK V1	0.05576257	-116.8187319	CTL_CD69+TragCD69+V1/V1	1.170117819	0.000000000	CTL_PD1+TNK V1/V1	1.176596127	-6.553427082	21.13656364	0.001168316
0.57157487	TTCDD+TNK V1	1.804665209	-1.805651011	CTL_CD69+TNK V1/V1	1.10691431	0.047600910	NK/CTL_PD1-V1/V1	1.1797307659	2.769492397	21.13656364	0.001113321
0.571580249	TragPD1+TNK V1	0.05576257	-116.1601769	CTLTragCD69+V1/V1	1.161456875	0.000000000	CTL_PD1+TNK V1/V1	1.1791845104	-6.958718605	21.13656364	0.001123749
0.571499216	TragPD1+TNK V1	0.05576257	-146.9411762	ThCD69+Trag V1/V1	0.03094115	24.12436981	TragCD69+nonTrag V1/V1	0.073851883	11.96732119	21.13656364	0.001126155
0.570945106	TragPD1+TNK V1	0.05576257	-137.1033351	CTL_CD69+TragCD69+V1/V1	1.170117819	0.000788187	CTL_PD1+TNK V1/V1	1.1791845104	-6.466446001	21.13656364	0.001146544
0.570776456	TTCDD+TNK V1	1.804665209	-1.805651011	CTL_CD69+TNK V1/V1	1.149004955	0.179103187	NK/CTL_PD1-V1/V1	1.1797307659	2.806440018	21.13656364	0.001150558
0.5688454	ThCD69+TragPD1-V1	25.95459219	-0.150468781	TragPD1+TNK V1	0.05576257	-138.7278747	TragCD69+TragCD69+V1/V1	1.1810597729	2.676929974	21.13656364	0.001128244
0.568547151	ThPD1+TragPD1-V1	14.844888015	-0.141540146	TragPD1+TNK V1	0.05576257	-140.5790492	TragCD69+TragCD69+V1/V1	1.1810597729	2.840203497	21.13656364	0.001128854
0.568721028	TTCDD+TNK V1	1.804665209	-1.805651011	NK/CTL_CD69+V1/V1	1.171787119	4.395065595	CTL_CD69+TNK V1/V1	1.18081451	5.013249799	21.13656364	0.001245478
0.568010146	ThTragPD1-V1	36.848496	-0.145448855	TragPD1+TNK V1	0.05576257	-138.9478469	TragCD69+TragCD69+V1/V1	1.1810597729	2.703010099	21.13656364	0.001146551
0.568044058	nonTrag+TragPD1-V1	24.70293201	-0.147501159	TragPD1+TNK V1	0.05576257	-139.0338477	TragCD69+TragCD69+V1/V1	1.1810597729	2.67741109	21.13656364	0.001158686
0.567879394	TragPD1+TNK V1	0.05576257	-114.1037861	CTL_CD69+TragCD69+V1/V1	1.170117819	0.180164669	CTL_PD1+nonTrag V1/V1	1.183474087	-7.915875416	21.13656364	0.001165945
0.567474922	CTL_PD1+TragCD69+V1	110.5168753	0.041403075	ThPD1+CTL V1	0.470319187	-30.13603008	ThCD69+CTL_PD1-V1	0.069308571	176.1848543	21.13656364	0.001165916
0.567413692	TTCDD+TNK V1	1.804665209	-1.805651011	CTL_CD69+TNK V1/V1	1.149004955	0.111310099	NK/CTL_CD69+V1/V1	1.1797307659	4.414448515	21.13656364	0.001168916
0.567369851	TragPD1+TNK V1	0.05576257	-113.1307851	CTLTragCD69+V1/V1	1.161456875	0.000000000	CTL_PD1+nonTrag V1/V1	1.183474087	-7.915875416	21.13656364	0.001168919
0.56683105	TragPD1+TNK V1	0.05576257	-144.62399	TragCD69+nonTrag V1/V1	2.073861882	11.61864028	nonTragTrag V1/V1	0.081382018	21.56074361	21.13656364	0.001207454



7. Remarks on validation aspects of the glioblastoma statistical model

It is noted that from a statistical point of view, a *strict* validation of the designed model is not feasible, for the following two reasons:

- 1) The available number of patients is rather small, and becomes even smaller by disregarding patients with missing values which are practically unusable.
- 2) The entire model building process requires a large amount of computational time, of the order of days. Any cross-validation scheme would require an unrealistic amount of computational time.

However, the stability and the meaningfulness of the results can be supported by the following arguments:

- 1) In all charts provided, the vast majority of patients lies in the 1st and 3rd quadrants, as was expected by the strong positive correlation coefficients. This visualizes the fact that if the quantity in the horizontal axis is above zero, then the overall survival (OS) can be expected to be above its average value in the specific subgroup. There are no major outliers, that is, x's in the upper left of the 2nd or lower right of the 4th quadrant.
- 2) All correlations are supported by strong corresponding p-values.
- 3) A geometric consideration of the results reveals the following. For any subgroup, say of n patients, there exists a corresponding n -dimensional space, where all quantities (OS, NK, Tregs, Th/Tregs) of the specific group lie as n -dimensional vectors. The number n , i.e. the dimension of these vectors is in the order of 20. Any of the discovered correlations is essentially a strong correlation (tending to collinearity) between a linear combination of 3 such vectors with the vector of OS. Given that this linear combination consists of exactly 3 vectors while the dimension of the space these vectors lie is in the order of 20, we can speculate that the model is not overfitted. Furthermore, we can also speculate that the discovered correlations are not accidental, and do not correspond to a spurious pattern. Finding 3 random n -dimensional vectors that correlate strongly with a specific given one (in our case OS) is an event with very low probability. To assume that our data do indeed tend to fit the discovered patterns is an assumption that has much higher probability of being true

than the assumption that there is no pattern, a fact that is also represented by the strong p-values.

7. References

- [1] O.Grauer,P.Wesseling G.Adema, Immunotherapy of diffuse gliomas: Biological Background,Current status and Future Developments ,Brain Pathology 2009.
- [2] Kim TG, Kim CH, Park JS, Park SD, Kim CK, Chung DS, Hong YK, Immunological factors Relating to the Antitumour Effect of Temozolomide Chemoimmunotherapy in a Murine Glioma Model. Clin Vaccine Immunol. 2010 Jan;17(1):143-53
- [3] Wainwright DA, Balyasnikova IV, Chang AL, Ahmed AU, Moon KS, Auffinger B, Tobias AL, Han Y, Lesniak MS. , IDO expression in brain tumours increases the recruitment of regulatory T cells and negatively impacts survival ,Clin Cancer Res. 2012 Nov 15;18(22):6110-21.
- [4] Choi BD, Fecci PE, Sampson JH,Regulatory T cells move in when gliomas say I-DO, Clin Cancer Res. 2012 Nov 15;18(22):6086-8
- [5] H.von Boehmer, Mechanisms of suppression by suppressor T cells, Nat Immunol. 2005 Apr;6(4):338-44
- [6] Onishi Y, Fehervari Z, Yamaguchi T, Sakaguchi S, Foxp3+ natural regulatory T cells preferentially form aggregates on dendritic cells in vitro and actively inhibit their maturation. Proc Natl Acad Sci U S A. 2008 Jul 22;105(29):10113-8
- [7] Sakaguchi S, Wing K, Onishi Y, Prieto-Martin P, Yamaguchi T.,Regulatory T cells: How do they suppress immune responses? Int Immunol. 2009 Oct;21(10):1105-11.
- [8] Tadokoro CE, Shakhar G, Shen S, Ding Y, Lino AC, Maraver A, Lafaille JJ, Dustin ML. Regulatory T cells inhibit stable contacts between CD4+ T cells and dendritic cells in vivo J Exp Med. 2006 Mar 20;203(3):505-11..
- [9] Sonabend AM, Rolle CE, Lesniak MS.,The role of regulatory T cells in malignant Glioma, Anticancer Res. 2008 Mar-Apr;28(2B):143-50.
- [10] Jordan JT, Sun W, Hussain SF, DeAngulo G, Prabhu SS, Heimberger AB. Preferential migration of regulatory T cells mediated by glioma secreted chemokines can be blocked by chemotherapy. Cancer Immunol Immunother. 2008 Jan;57(1):123-31.
- [11] Fecci PE, Mitchell DA, Whitesides JF, Xie W, Friedman AH, Archer GE, Herndon JE 2nd, Bigner DD, Dranoff G, Sampson JH.Increased regulatory T cell fraction amidst a diminished CD4 compartment explains cellular immune defects in Patients with malignant glioma. Cancer Res. 2006 Mar 15;66(6):3294-302.
- [12] Camara NO, Seville F, Lechler RI. Human CD4+CD25+ regulatory cells have marked and sustained effects on CD8+ T cell activation. Eur J Immunol 2003;33:3473–83
- [13] Piccirillo CA, Shevach EM. Cutting edge: control of CD8+ T cell activation by CD4+CD25+ immunoregulatory cells. J Immunol 2001;167:1137–40.
- [14] Ogbomo HI, Cinatl J Jr, Mody CH, Forsyth PA. Immunotherapy in gliomas: Limitations and potential of natural killer cell therapy. Trends Mol Med. 2011 Aug;17(8):433-41.

- [15] Albesiano E, Han JE, Lim M. Mechanisms of local immunoresistance in glioma. *Neurosurg Clin N Am*. 2010 Jan;21(1):17-29
- [16] Crane CA et al, TGF-beta downregulates the activating receptors NKp30 and NKG2D on NK and CD8+ T cells. *Neuro Oncol* 12, 7-13
- [17] Kane A., Yang I. Interferon-gamma in BrainTumour Immunotherapy *Neurosurg Clin N Am*. 2010 Jan;21(1):77-86
- [18] Alberts B. Molecular biology of the cell, chapters 24-25.
- [19] Yang I, Han SJ, Kaur G, Crane C, Parsa AT. The role of microglia in Central Nervous System immunity and Immunotherapy. *J Clin Neurosci*. 2010 Jan;17(1):6-10
- [20] da Fonseca AC, Badie B. Microglia and Macrophages in Malignant Gliomas: Recent Discoveries and Implications for Promising Therapies. *Clin Dev Immunol*. 2013;2013:264124.
- [21] W. Li and M. B. Graeber, The molecular profile of microglia under the influence of glioma, *Neuro-Oncology* 14(8):958–978, 2012
- [22] Ostrand-Rosenberg S. Myeloid-derived suppressor cells: more mechanisms for inhibiting anti-tumour immunity, *Cancer Immunol Immunother*. 2010 Oct;59(10):1593-600.
- [23] Kohanbash G, Okada H. Myeloid-derived Suppressor cells (MDSC's) in Gliomas and Glioma development. *Immunol Invest*. 2012;41(6-7):658-79.
- [24] D'Agostino PM, Gottfried-Blackmore A, Anandasabapathy N, Bulloch K. Brain dendritic cells: biology and pathology, *Acta Neuropathol*. 2012 Nov;124(5):599-614.
- [25] Banchereau JI, Briere F, Caux C, Davoust J, Lebecque S, Liu YJ, Pulendran B, Palucka K. Immunobiology of dendritic cells. *Annu Rev Immunol*. 2000;18:767-811.
- [27] Mempel TR, Henrickson SE, Von Andrian UH. T-Cell priming by dendritic cells in lymph nodes occurs in three distinct phases. *Nature*. 2004 Jan 8;427(6970):154-9.
- [28] Wainwright DA, Sengupta S, Han Y, Lesniak MS. Thymus derived rather than tumour induced regulatory T cells predominate in brain tumours. *Neuro Oncol*. 2011 Dec;13(12):1308-1317.
- [29] Hugues S. Dynamics of dendritic cell-T cell interactions: a role in T cell outcome. *Semin Immunopathol*. 2010 Sep;32(3):227-38.
- [30] Lämmermann T, Sixt M. The microanatomy of T-cell responses. *Immunol Rev*. 2008 Feb;221:26-43
- [31] Miller MJ, Safrina O, Parker I, Cahalan MD. Imaging the single cell dynamics of CD4+ T cell activation by dendritic cells in lymph nodes. *J Exp Med*. 2004 Oct 4;200(7):847-56.
- [32] Ma DY, Clark EA. The role of CD40 and CD154/CD40L in dendritic cells. *Semin Immunol*. 2009 Oct;21(5):265-72.

- [33] Clarke SR The critical role of CD40/CD40L in the CD4-dependent generation of CD8+ T cell immunity. *J Leukoc Biol.* 2000 May;67(5):607-14.
- [34] Heath WR, Carbone FR. Cross-presentation, dendritic cells, tolerance and immunity. *Annu Rev Immunol.* 2001;19:47-64.
- [35] Van Gool SW Brain Tumour Immunotherapy: What have We Learned so Far? *Front Oncol.* 2015 Jun 17;5:98.
- [36] Dejaegher J, Van Gool S, De Vleeschouwer S Dendritic cell vaccination for glioblastoma multiforme: review with focus on predictive factors for treatment response *ImmunoTargets and Therapy*, 13 March 2014 Volume 2014:3 Pages 55—66
- [37] Ardon H, Van Gool S, Lopes IS, Maes W, Sciort R, Wilms G, Demaerel P, Bijttebier P, Claes L, Goffin J, Van Calenbergh F, De Vleeschouwer S. Integration of autologous dendritic cell-based immunotherapy in the primary treatment for patients with newly diagnosed glioblastoma multiforme: a pilot study. *J Neurooncol.* 2010 Sep;99(2):261-72.
- [38] Van Gool S, Maes W, Ardon H, Verschuere T, Van Cauter S, De Vleeschouwer S. Dendritic cell therapy of high-grade gliomas. *Brain Pathol.* 2009 Oct;19(4):694-712
- [39] Ardon H, Van Gool SW, Verschuere T, Maes W, Fieuws S, Sciort R, Wilms G, Demaerel P, Goffin J, Van Calenbergh F, Menten J, Clement P, Debiec-Rychter M, De Vleeschouwer S. Integration of autologous dendritic cell-based immunotherapy in the standard of care treatment for patients with newly diagnosed glioblastoma: results of the HGG-2006 phase I/II trial. *Cancer Immunol Immunother.* 2012 Nov;61(11):2033-44
- [40] Garg A D, Vandenberg L, Koks C, Verschuere T, Boon L, Van Gool SW, Agostinis P. Dendritic cell vaccines based on immunogenic cell death elicit danger signals and T cell-driven rejection of high-grade glioma. *Science Translational Medicine* 02 Mar 2016: Vol. 8, Issue 328, pp. 328ra27
- [41] J. Han, M. Kamber, and J. Pei, *Data Mining: Concepts and Techniques*, 3rd edition, Morgan Kaufmann, 2011.
- [42] T. Hastie, R. Tibshirani, J. Friedman. *The Elements of Statistical Learning: Data Mining, Inference, and Prediction*, Second Edition (Springer Series in Statistics) 2009.
- [43] Koller D. and Friedman N. *Probabilistic Graphical Models Principles and Techniques*. The MIT Press, 2009
- [44] Friedman, N., Geiger, D., Goldszmidt, M. (1997) Bayesian network classifiers. *Machine Learning*, 29, 131–163
- [45] G. F. Cooper, E. Herskovits. A bayesian method for the induction of probabilistic networks from data. *Machine Learning*, October 1992, Volume 9, Issue 4, pp 309–347
- [46] John Shawe-Taylor, Nello Cristianini, *Kernel Methods for Pattern Analysis*, Cambridge University Press; 1 edition (June 28, 2004)

CHAPTER PC:THE PROSTATE CANCER HYPERMODEL: CLINICAL ADAPTATION AND PARTIAL VALIDATION

(Please note that the numbering of sections, subsections, equations, figures and references within this chapter refers exclusively to the latter and is not applicable to other chapters of the document, If any of the above entities of another chapter is to be referred to, the chapter under consideration should also be mentioned through its two capital letter code)

Modelling Hormonal Adjuvant Treatment in Prostate Cancer

Introduction

Radical prostatectomy (RP) is one of the most widespread curative treatments for localized Prostate Cancer (PCa), but tumour recurrence affect almost 20% of patients.

Since the gene coding for the Prostate Specific Antigen (PSA) is exclusively activated by the Androgen Receptors (AR) signalling in the prostatic epithelial cells [1], no PSA in the patient serum should be detected following RP, unless residual cells of the primary tumour or its metastasis reactivate. This is evidenced by the so called biochemical recurrence (BCR), defined as two consecutive PSA values of 0.2 ng/ml or greater.

In case of high-risk patients, with either advanced pathological stage, or positive surgical margins or regional lymph node metastasis or Gleason score ≤ 8 recurrence may occur quite early after RP, and adjuvant treatments (i.e. immediately subsequent RP) are delivered, mainly consisting in hormonal therapy.

The underlying rationale is based on the fact that, as recognized by Huggins and Hodges more than 70 years ago [2], PCa is an androgen-sensitive disease, and different approaches to reducing testosterone (bilateral orchiectomy, chronic administration of gonadotropin releasing hormone analogs, etc.) collectively indicated as androgen deprivation therapy (ADT), are nowadays considered as standard therapy at recurrence [3].

Both in normal prostate and in most PCa at early stages, AR bind dihydrotestosterone (DHT) concerted in the prostate from the testosterone produced by the testes. In normal prostate AR play a role in secreting proteins and stimulating/inhibiting normal prostate cells proliferation. AS tumour develops, stromal AR promote PCa cells growth and the tumour is purely androgen-dependent. Reduction or deletion of testosterone will therefore block tumour proliferation. This procedure is known as castration-analog ADT. Initially, ADT decreases cell proliferation and increases apoptosis, leading to an impressive response with suppression of prostate specific antigen (PSA) but, within around 24 months, despite maintenance of very low testosterone serum [4], tumour progression

towards castration-resistant prostate cancer (CRPC) occurs [5].

An alternative approach is the 'AR blockade' ADT, and finally the Combined Androgen Blockade (CAB). Details are given in Table I.

For adjuvant ADT in RP patients neither conclusive support for benefits [6] nor standard recommendations (www.nccn.org) exist.

Table I: ADT modalities

castration-analog ADT Luteinizing hormone(LH)-releasing hormone (LHRH) agonists (goserelin, histrelin, leuprolide, and triptorelin →drip in testosterone to castrate level after an initial 'flare'	AR blockade ADT An alternative approach to castration consists in inhibiting the activity of AR using non steroidal AR antagonists such as bicalutamide and flutamide.
combined approach (CAB) Since following LHRH agonists, an initial increase in testosterone synthesis is observed inducing an 'acute flare' in the PCa, AR blocking antiandrogens are sometimes co-administered for the first 7 days (see www.nccn.org). Such co-administration is called Combined Androgen Blockade (CAB)	

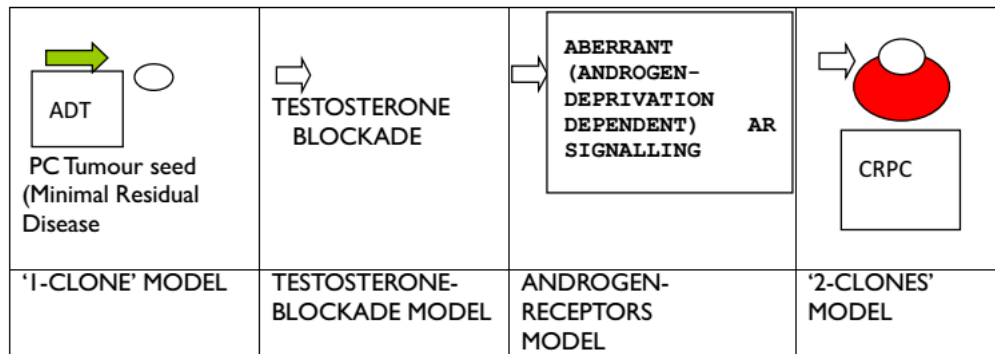


Figure 1: Schema of the 2-clones model construction

Many authors simulated ADT in prostatectomized patients, taking into account the appearance of Castration resistance: in particular, Kuang and Ideta (and their collaborators) [7] analyzed Intermittent Androgen Suppression, a type of ADT that consists of giving hormone therapy for 6 months, stopping it for 6 months and then beginning again. The common point in the cited models is the presence of two cells populations: one Androgen Sensitive and one Androgen Resistant. In some cases, the model specifies the complex dynamics of the androgen or of the testosterone [8][9].

The novelty of the present joint work is the implementation of the mathematical simulation of the different action of LHRH agonists (shortly: LHRH) and AR blocking drugs (shortly: anti-androgens) and of the genetic mechanisms accounting for the development of the CRPC, in addition to the description of the two tumour cells populations.

Another essential point is that theoretical results are compared with clinical data available by EUREKA1 study.

I. Simulation of testosterone blockade by LHRH agonists

The three key-hormones involved in testosterone regulation loop, i.e. Luteinizing Hormone - Releasing Hormone (LHRH), Luteinizing Hormone (LH) and testosterone (TE), interact via the following feedback and feed-forward relationships (see Figure 2). LHRH, which is secreted in hypothalamus, stimulates the secretion of LH in hypophysis (pituitary gland). The latter stimulates the secretion of TE in testes, which in its turn inhibits the secretion of LHRH and LH [10]. Experimental studies based on high-resolution time assay series reveal that concentrations of TE and LH in the adult male exhibit oscillative behaviour and their exact signal form depends on the individual [11][12]. Direct measurements of LHRH in human are difficult to implement due to ethical reasons but experiments on animals confirm that secretion of LHRH is also oscillative and pulsatile as well [12][13]. When the concentration of serum TE rises, LHRH pulses become sparser and their

amplitude diminishes [10].

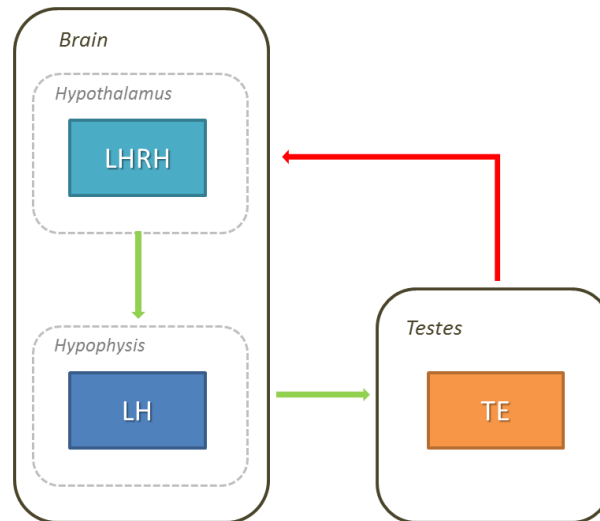


Figure 2: Feed-back (red arrow) and feed-forward (green arrow) relationships in LHRH-LH-TE axis

LHRH-agonists mechanism of action

For patients with advanced prostate cancer, LHRH agonists have provided ADT for more than three decades. As compared to native LHRH, LHRH agonists are more potent and have a longer half-life [14]. As the term “agonist” suggests, this kind of drug binds to LHRH receptors in the pituitary. Low doses of LHRH administered in a pulsatile manner similar to that found in the portal vessels, restore fertility in hypogonadal men and women [15]. High doses of native LHRH administered in a continuous way, produce a tentative stimulation of pituitary gonadotrophs that results in over-secretion of LH and an expected testosterone surge, termed as the flare effect. Following that, however, the LHRH receptor (LHRHR) is downregulated and desensitized, decreasing LH release and inhibiting testosterone production. The exact mechanism of receptors desensitization is not known [16]. Some of the widely used LHRH-agonists in clinical practise are leuprolide, goserelin, buserelin and nafarelin. For the needs of this work, we have included the pharmacokinetic properties of leuprolide.

Overview of the system

In order to simulate testosterone regulation by LHRH agonists and the flare effect, a two-component hypermodel has been built. The first component describes the pharmacokinetic properties of the 1-month depot formulation of leuprolide acetate while the second one monitors the dynamics of the hormones that regulate testosterone secretion. The two parts of the system communicate sequentially in the way that is outlined in Figure 3.

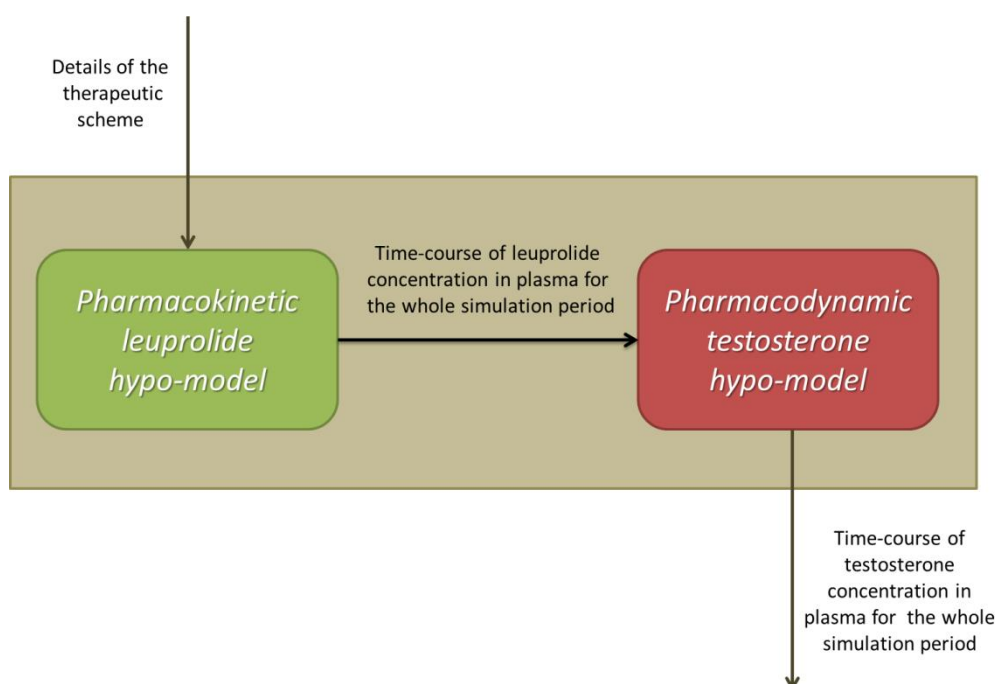


Figure 3: Information flow in the hyper-model for the response of testosterone levels (in plasma) to leuprolide mono-therapy.

Pharmacokinetic Leuprolide hypo-model

For the case of depot formulation of leuprolide acetate, a two-compartmental model with parallel first- and zero- order absorption processes as well as a delayed first- order process has been developed, based on [17]. The structure of the pharmacokinetic model is described in Figure 4.

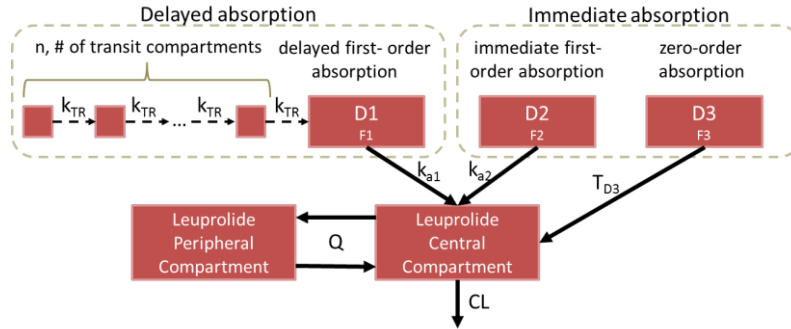


Figure 4: Two-compartmental pharmacokinetic hypo-model with parallel first- and zero- order absorption processes as well as a delayed first- order process for the case of depot formulation of leuprolide acetate.

The system consists of four ordinary differential equations (ODEs). Equation (1) monitors the drug amount in the delayed first-order absorption compartment while equation (2) computes the drug amount eliminating from the immediate first-order absorption. Equations (3) and (4) monitor leuprolide plasma concentration in the central and peripheral compartment respectively. Variables and parameters involved in the pharmacokinetic hypo-model are explained in Table 2.

$$\frac{dD_1}{dt} = F_1 \cdot BIO \cdot Dose \cdot k_{tr} \frac{(k_{tr} \cdot t)^n \cdot e^{-k_{tr} \cdot t}}{\sqrt{2\pi} \cdot n^{n+0.5} \cdot e^{-n}} - k_{a1} \cdot D_1 \quad (1)$$

$$\frac{dD_2}{dt} = -k_{a2} \cdot D_2 \quad (2)$$

$$\frac{dC}{dt} = \frac{k_{a1}}{V_C} \cdot D_1 + \frac{k_{a2}}{V_C} \cdot D_2 - \frac{CL}{V_C} \cdot C - \frac{Q}{V_C} \cdot C + \frac{Q}{V_P} \cdot P + \frac{k_{a3}}{V_C} \cdot Heaviside(t_{D_3} - t) \quad (3)$$

$$\frac{dP}{dt} = \frac{Q}{V_C} \cdot C - \frac{Q}{V_P} \cdot P \quad (4)$$

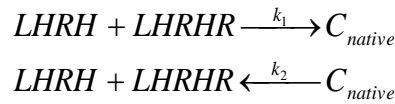
Table 2: Description and units of parameters and variables involved in the pharmacokinetic model

Variables/ parameters	Description	Estimated parameter values	Unit
C	Drug concentration in central compartment	n/a	ng/mL
P	Drug concentration in peripheral compartment	n/a	ng/mL
D_1	Drug amount in depot 1	n/a	mg
D_2	Drug amount in depot 2	n/a	mg
k_{a1}	Absorption rate constant for delayed process	0.2398	days ⁻¹
k_{a2}	Absorption rate constant for immediate process	0.9999	days ⁻¹
k_{a3}	Absorption rate constant for zero-order process	<i>Internally calculated</i>	mg*days ⁻¹
t_{D3}	Duration of zero-order absorption	0.0070	days
Dose	Drug dose	3.75	mg
$F1$	Fraction of dose absorbed via delayed first- order process	<i>Internally calculated</i>	-
$F2$	Fraction of dose absorbed via immediate first- order process	0.7527	-
$F3$	Fraction of dose absorbed via zero-order process	0.0561	-
MTT	Mean transit time	10.1286	days
k_{tr}	Transit rate constant	<i>Internally calculated</i>	days ⁻¹
n	Number of transit compartments	79.1360	-
BIO	Bioavailability	0.9540	
CL	Clearance	165.0918	L/day
V_c	Volume of distribution of central compartment	11.8350	L
Q	Inter-compartmental clearance	71.3195	L/day
V_p	Volume of distribution of peripheral compartment	9.9434	L

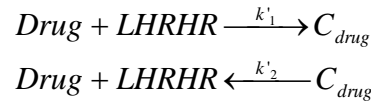
Pharmacodynamic testosterone hypo-model

For the simulation of the response of testosterone serum concentration to leuprolide mono-therapy schemes, a dynamical system consisting of six equations has been developed. The system monitors all the key players of the testosterone regulation loop and takes into account the following critical chemical reactions:

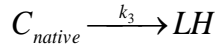
- LHRH binds via a reversible reaction to its free receptors (LHRHR) on the cell surface, forming LHRH-LHRHR complex C_{native} . k_1 , k_2 stand for production and degradation rate constants respectively.



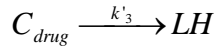
- LHRH agonist (leuprolide) binds via a reversible reaction to free receptors (LHRHR) on the cell surface, forming LHRH agonist-LHRHR complex C_{drug} . k'_1 , k'_2 stand for production and degradation rate constants respectively.



- C_{native} triggers LH synthesis and production. k_3 is the production rate constant.



- C_{drug} triggers LH synthesis and production. k'_3 is the production rate constant.



The pulsatile nature of LHRH secretion is addressed by considering the production rate as a cosine function of time with a dependence on testosterone levels through parameter α (see Equation (5)). For the term reflecting the production of LHRH receptors (LHRHR), a Hill function dependent on the concentration of LHRH has been selected (see Equation (6)). Leuprolide effect is incorporated in the model through the corresponding chemical reactions described above as well as through the drug-induced inhibition of LHRHR production, reflecting the down-regulation of receptors.

The dynamical system is formulated as following:

$$\frac{dx_1}{dt} = a \cdot \max(\cos(\omega t), 0) - k_1 \cdot x_1 \cdot x_2 + k_2 \cdot x_3 - c_1 \cdot x_1 \quad (5)$$

$$\frac{dx_2}{dt} = \frac{V_{\max}}{(x_1 + SF_1 \cdot Drug)^e + T^e} - k_1 \cdot x_1 \cdot x_2 + k_2 \cdot x_3 - k'_1 \cdot SF_1 \cdot Drug \cdot x_2 + k'_2 \cdot x_4 - c_2 \cdot x_2 \quad (6)$$

$$\frac{dx_3}{dt} = k_1 \cdot x_1 \cdot x_2 - k_2 \cdot x_3 - k_3 \cdot x_3 \quad (7)$$

$$\frac{dx_4}{dt} = k'_1 \cdot SF_1 \cdot Drug \cdot x_2 - k'_2 \cdot x_4 - k'_3 \cdot x_4 \quad (8)$$

$$\frac{dx_5}{dt} = l_3 \cdot x_3 + l'_3 \cdot x_4 - c_5 \cdot x_5 \quad (9)$$

$$\frac{dx_6}{dt} = s_6 \cdot x_5 - c_6 \cdot x_6 \quad (10)$$

Variables and parameters involved in the model are explained in Tables 3 and 4.

Table 3: Physical quantities monitored by the pharmacodynamic testosterone hypo-model along with their units and initial values used for fitting to clinical data.

physical quantity	description	variable	initial values	units
$LHRH$	Luteinizing Hormone-Releasing Hormone	x_1	0.001	nmol/L
$LHRHR$	Luteinizing Hormone-Releasing Hormone Receptors	x_2	0.03	nmol/L
C_{native}	Complex between Luteinizing Hormone-Releasing Hormone and Luteinizing Hormone-Releasing Hormone Receptors	x_3	0.000012	nmol/L
C_{drug}	Complex between LHRH agonist and Luteinizing Hormone-Releasing Hormone Receptors	x_4	0	nmol/L
LH	Luteinizing Hormone	x_5	4.68 [18]	mIU/mL
TE	Testosterone	x_6	4.12 [18]	ng/mL

Table 4: Parameters involved in the pharmacodynamic testosterone hypo-model

Parameters	Description	Estimated Parameter Values	Units
a	testosterone-dependent amplitude of pulsatile LHRH secretion (<i>internally computed</i>)	n/a	nmol/(L · day)
V_{\max}	maximal LHRHR production rate	1.7757	(nmol/L) ^{e+1} /day
T	LHRH concentration constant giving half-maximal LHRHR production rate	0.0308	(nmol/L) ^e
e	Hill coefficient	8.1458	-
f	frequency	12*	1/day
k_1	production rate constant of native complex (LHRH-LHRHR)	39.8667	L/(day · nmol)
k_2	degradation rate constant of drug complex (LHRH agonist – LHRHR)	7.2062	1/day
c_1	LHRH clearance rate	0.9003	1/day
k_1'	production rate constant of native complex	39.7755	L/(day · nmol)
k_2'	degradation rate constant of drug complex	7.3786	1/day
k_3	dissociation rate constant of native complex	8.7256	1/day
k_3'	dissociation rate constant of drug complex	12.0638	1/day

l_3	LH production rate constant due to native complex	397.5280	IU/(day nmol)
l_3''	LH production rate constant due to drug complex	401.4013	IU/(day nmol)
c_5	LH clearance rate constant	0.2916	l/day
s_6	TE secretion rate constant	0.5029	l/day
c_6	TE clearance rate constant	0.2169	ng/(day mL)
SFI	Scaling factor for unit conversion for leuprolide concentration: ng/mL → nmol/L	0.7877	-
Drug	Leuprolide concentration: linking point of the two hypo-models	<i>Calculated by the pharmacokinetic leuprolide model</i>	ng/mL

*Based on [12]

Fitting results

The pharmacokinetic and the pharmacodynamic testosterone hypomodel have been fitted to clinical data extracted from [18]. The objective of this study was to investigate the effectiveness, pharmacokinetics, and safety profile of a 1-month leuprolide acetate 3.75-mg depot formulation for suppressing testosterone concentrations in patients with prostate cancer.

For the pharmacokinetic leuprolide model, there has been use of Matlab built-in simulated annealing solver for finding global minima for nonlinear problems (Fig. 5).

The local fitting of the pharmacodynamic testosterone model to the available data, has been conducted with the use of Matlab built-in function for solving nonlinear least-squares (lsqnonlin), in conjunction with the trust region reflective algorithm (Fig. 6).

The result displayed in Fig. 5 was based on the mean (SD) plasma leuprolide concentration–time profile during the first 3 monthly intramuscular injections (days 0–84) of leuprolide acetate 3.75-mg depot in 12 patients with prostate cancer. For details see [18].

In order to quantify the clinical data, we have utilized PlotDigitizer software which allows data extraction (mean value \pm standard deviation) via its digitization.

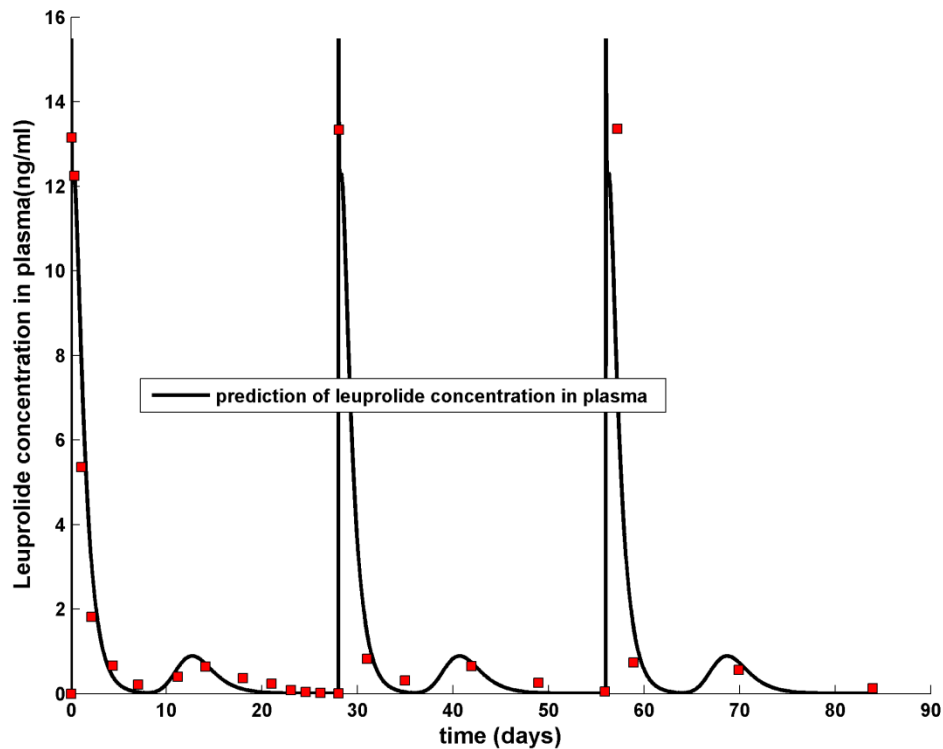


Figure 5: Fitting of the pharmacokinetic hypo-model to leuprolide concentration data in [18]. Parameter values and initial values are shown in Table 2 respectively. The normalized root mean square error, defined as the root mean square error divided by the range of values of the measured quantity (maximum value – minimum value), was calculated equal to 16.50%.

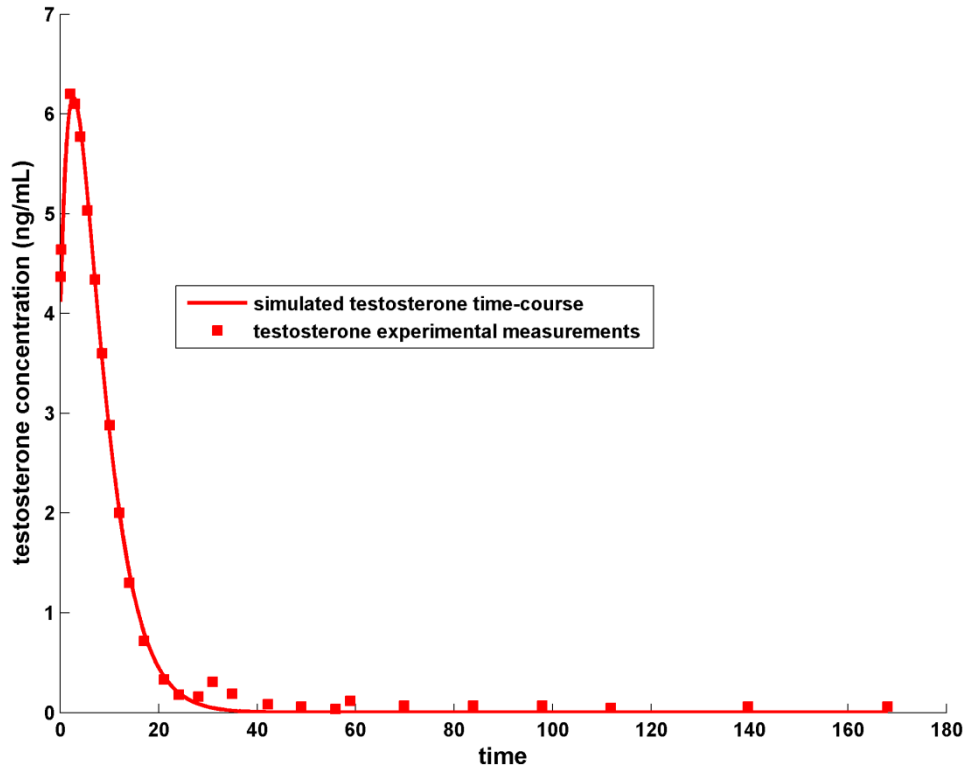


Figure 6: Fitting of the pharmacodynamic hypo-model to testosterone concentration data in [18]. Parameter values and initial values are shown in Tables 4 and 3 respectively. The normalized root mean square error, defined as the root mean square error divided by the range of values of the measured quantity (maximum value – minimum value), was calculated equal to 5.24%.

2. The Androgen Receptors and the genesis of castration-resistant cancer cells

Androgenic therapies have a temporary benefit of decreased cell proliferation and increased apoptosis due to the dependence of prostate cancer (PCa) cells on androgen, however aberrant AR signalling and genomic instabilities resistance develops by which PCa cells become independent of androgen [19].

One of the main mechanisms by which resistance develops is through cross-talk of AR pathway with other proliferative pathways like PI3K/AKT which do not explicitly depend on androgen. Three different pathways are investigated (see Table 5):

Table 5: Pathways under investigation for eventual cross-talks with AR- pathway

EGFR mediated Ras-MAPK	PI3K/AKT pathways	TP53 mediated DNA damage pathways
AR is found to be activated and stabilized by ErbB family of receptors in particular by EGFR and Her2 [20]. This enables the AR pathway to function even at very low concentrations of androgen leading to androgen independent prostate cancer	Is a key regulator of cell growth and suppression of apoptosis [21]. In many cell lines transformation to a malignant phenotype is often accompanied by a decrease in PTEN levels. PTEN deficient cells show a reciprocal feedback interaction between PI3K/AKT and AR pathways where inhibition of one can activate the other.	AR can upregulate transcription of cell cycle promoting genes like CDK4 and downregulate cell cycle inhibitors like p21. AR can also activate apoptosis inhibitors like Bax [21][22]. p53 has been found to inhibit synthesis of AR and so p53 inhibition can result in an increased expression of AR which can promote cell cycle progression [23].

This allows us to understand directly the effect of various treatments and how the patient-specific genetic profile determines the outcome of ADT and onset of resistance in prostate cancer. This cellular model is combined with a population level model to directly obtain the rate of tumour growth/decay for various treatments.

Core AR model description: The molecular model of AR signalling as implemented here is based on the well-known details about the AR pathway [19]. Here we have a three compartment model representing the cell extracellular medium, cytoplasm and the nucleus. A buffered level of testosterone is maintained at the extracellular medium. It can enter the cell at some fixed rate. Inside the cell (cytoplasm) it is converted to DHT by 5 α -reductase enzyme. Both testosterone and DHT can bind to the androgen receptor although the binding affinity for DHT is substantially higher. Upon ligand binding the receptor undergoes a conformational change and releases the bound HSPs (heat-shock proteins) to reveal the nuclear localization sequences. Then it dimerizes and can translocate to the nucleus where it can bind to the DNA and interacts with various transcriptional regulators to regulate expression of various target genes including PSA whose concentration is used as a marker for activity of androgen receptor. In the current model the synthesis of PSA is shown modeled as a catalytic reaction with the AR dimer acting as an activator. Separate reactions are included for synthesis of androgen receptors and degradation reactions for both AR and PSA; see Fig. 7. The complete list of reactions is given below in Table 6.

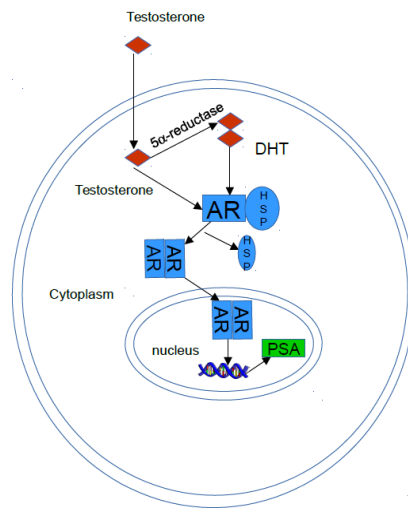


Fig 7: Schematic diagram of AR activation by testosterone/DHT and subsequent transcription of PSA [19]

Table 6: List of Reactions

No	Name	Reaction
1	AR dimerization testosterone	$AR(cyt) + AR(cyt) \rightarrow AR2;T$
2	AR dimerization DHT	$AR(cyt) + AR(cyt) \rightarrow AR2(cyt);D$
3	AR Transport	$AR2(cyt) \rightarrow AR2(nuc)$
4	AR synthesis	$\rightarrow AR(cyt)$
5	AR Degradation	$AR(cyt) \rightarrow$
6	PSA synthesis catalyzed	$AR2(nuc) \rightarrow AR2(nuc) + PSA$
7	PSA synthesis basal	$\rightarrow PSA$
8	PSA degradation	$PSA \rightarrow$
9	AR non-androgenic activation	$AR(cyt) + AR(cyt) \rightarrow AR2;N$
10	Testosterone reduction	$T \rightarrow D; 5\alpha\text{-reductase}$

AR signalling pathway and its interaction with other pathways: The core AR pathway as described above interacts with other signalling pathways which are important in regulating cellular fate. These interactions can affect AR activation and stability and hence can have important consequences in the

development and progression of prostate cancer and development of metastatic and castration resistant forms of prostate cancer.

Description of model interfaces: The above interactions are incorporated in individual modules in different ways depending on their mathematical structure.

A) Interactions with AR signalling module and EGFR mediated Ras/MAPK and PI3K/AKT signalling: both AR signalling and EGFR mediated Ras/MAPK and PI3K/AKT signalling are modeled as a set of continuous ordinary differential equations. It is assumed (verified to some extent from literature) that the average timescale of AR signalling events are much greater than the EGFR mediated Ras/MAPK and PI3K/AKT signalling. Thus from the perspective of AR signalling pathway the concentrations of the species participating in the other pathway is approximately constant. Hence we run the EGFR mediated Ras/MAPK and PI3K/AKT signalling module and pass the steady-state concentration of the species to the AR module.

B) Interactions with AR signalling module and P53 mediated DNA damage module: the p53 mediated DNA damage module is modeled as a discrete system where each species can have two states (0 or 1). Also this module is assumed to operate at time scale much greater than the AR signalling module. This affects both at what times information is passed and what information is passed. Since the p53 module can only interpret discrete signals the concentrations of the species obtained in AR module is converted to a discrete on/off signal using particular threshold. Similarly, the discrete states in p53 module can be converted to a continuous value assuming a bounded concentration of the species in the AR module.

Thus using the above setup, the net rate of AR production (as an example) will be described by equation (11):

$$\frac{d[AR]}{dt} = - \frac{k_{fT}[T][AR]}{1 + \frac{I}{K_I} + \frac{1 + \frac{[A]}{K_A}}{1 + \frac{[A]}{K_A}}} + k_{rT}[AR:T] - \frac{k_{fD}[DHT][AR]}{1 + \frac{I}{K_I} + \frac{1 + \frac{[A]}{K_A}}{1 + \frac{[A]}{K_A}}} + k_{rD}[AR:T] + \frac{k_{syn}}{1 + \frac{[TP53]}{K_{TP53}}}$$

In equation (11) the terms in brackets represents various species as below:

AR – Androgen Receptor; T – Testosterone; DHT – Dihydrotestosterone; I – Generic inhibitor to the AR testosterone binding reaction; A – Generic activator to AR testosterone binding reaction; AR:T – AR testosterone bound complex.

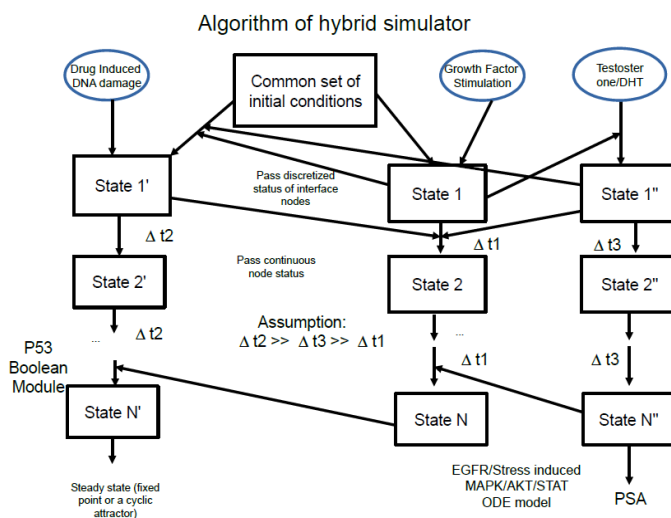
Here the net rate of AR production is a balance of net rates of production and consumption of AR through different reactions. These are:

1. AR binding to testosterone (reversible)
2. AR binding to DHT (reversible)
3. AR synthesis

The activator terms in the AR testosterone binding reaction represents species like HER2 and AKT which is obtained by running the other module. The AR synthesis term includes p53 as an inhibitor whose concentration is obtained by running the p53 module. The AR concentration is also discretized and passed to the p53 module where it appears in the state transition rules of species which are influenced by it (like CDK4, p21 and Bax).

The AR module described above is interfaced with the UPENN molecular model (described earlier for the lung cancer and neuroblastoma scenarios) in accordance with flowchart 1.

Flowchart:



Flowchart 1: AR module is integrated within the UPENN molecular model.

3. Patient-specific predictions of cell growth and death probabilities (rates) using the patient genomic profiles and the molecular model

Gene expression data for 20 patients were utilized using which the nodes of the molecular model were initialized individually for each subject. In Table 7, the genes that were differentially expressed compared to a control (healthy subject) are given for 4 out of the 20 patients. The remaining 16 patients did not show any differentially expressed genes relative to the control subject. For each patient, the gene names on the right column were obtained from gene expression data by comparing the gene expression with normal (healthy subject with no cancer) and picking the top 20 differentially expressed genes. These gene activities/concentrations were altered in our simulation.

PatientID	Differentially Expressed Genes WRT Control	DGEP (Y/N)?
CNT or Control	NA	N
AA65	CCNG1;CDKN1A;MDM4;CDK2	Y
Z59	CCNG1;CDKN1A;CDK2;CASP9	Y
AA69	CCNG1;CDKN1A;CDK2	Y
L12	CCNG1;CDKN1A;AR;CASP9	Y
B17	CCNG1;CDK2;AR;MDM4	Y
A3	CCNG1;CDK2;AR;MDM4	Y
W25	CCNG1;CDKN1A;CDK2;CASP9	Y
A5	CCNG1;CDKN1A;CDK2;CASP9	Y
B11	CCNG1;CDKN1A;MDM4;CDK2	Y
G70	None	N
C25	None	N
CC87	None	N
CC8	None	N

Table 7 Patient gene expression profiles showing top differentially expressed genes compared to a control (healthy) subject without cancer. The colours represent patients with similar patterns of differentially expressed genes. So patients shown is same colour can in principle be stratified into a cohort. For the purposes of this study, we pool all patients with differentially expressed genes into one cohort. These are indicated DGEP=Y in

the last column. Thus, two patient cohorts we consider here are represented by DGEP=Y and DEGP=N.

For each of these subjects and for the control subject, simulations were run using the molecular model for two different PTEN initial expression numbers and for five different testosterone concentrations (nM). The testosterone concentration variation simulated cell response to testosterone while low PTEN numbers (in relation to high numbers) represents onset of androgen resistance. These conditions are summarized in Table 8; in addition, the effect of intra tumour heterogeneity is factored by running each case in Table 8 for four conditions summarized in Table 9. That is, for each patient in Table 7, ten conditions in Table 8 are explored, and for each condition in Table 7, four cases in Table 9 are simulated, amounting to $10 \times 4 = 40$ simulations per patient. The results of cell growth rate, cell kill rate, and the net cell growth rate = cell growth minus cell kill rates for each patient as well as the control subject are depicted in Figure 8. The net “personalized” cell growth rates can be input into a larger population or multiscale model to track the tumour evolution. In figure 9, we report the ratio of net cell-growth rate at high testosterone levels to that of low testosterone levels for each patient. These calculations lead to estimation of parameters related to cell growth rate in population growth models of tumour customized to individualized patients or patient cohorts as described in the next section.

Table 8: Summary of testosterone and PTEN levels used in the model. The PTEN level represents protein numbers per cell.

Key	Condition
0	Testosterone (nM) = 1; PTEN (Num) = 5610
1	Testosterone (nM) = 5; PTEN (Num) = 5610
2	Testosterone (nM) = 10; PTEN (Num) = 5610
3	Testosterone (nM) = 15; PTEN (Num) = 5610
4	Testosterone (nM) = 20; PTEN (Num) = 5610
5	Testosterone (nM) = 1; PTEN (Num) = 56100
6	Testosterone (nM) = 5; PTEN (Num) = 56100
7	Testosterone (nM) = 10; PTEN (Num) = 56100
8	Testosterone (nM) = 15; PTEN (Num) = 56100
9	Testosterone (nM) = 20; PTEN (Num) = 56100

Table 9: Conditions for each case in Table 7 explored in the model in order to factor the effect of intra tumour heterogeneity. With (or without) memory refers to whether (or not) we reinitialize the continuous models after each time step or continue with current concentrations/activities of various species.

Condition	Value
EGF	0.1 nM
EGF	100 nM
Memory*	Yes
Memory	No

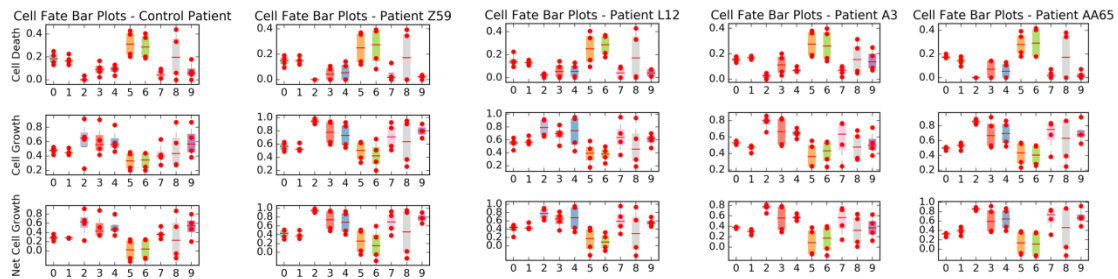


Figure 8: Model predictions of cell kill rate, growth rate, and net growth rate for control as well as four cancer patients summarized in Table 7. The remaining patients can be mapped to one of these five cases as implied by the colour codes in Table 7. The ten conditions (0 to 9) are the conditions summarized in Table 8. The four data points for each condition are the four states summarized in Table 9. The respective means over the four states are also depicted for each condition.

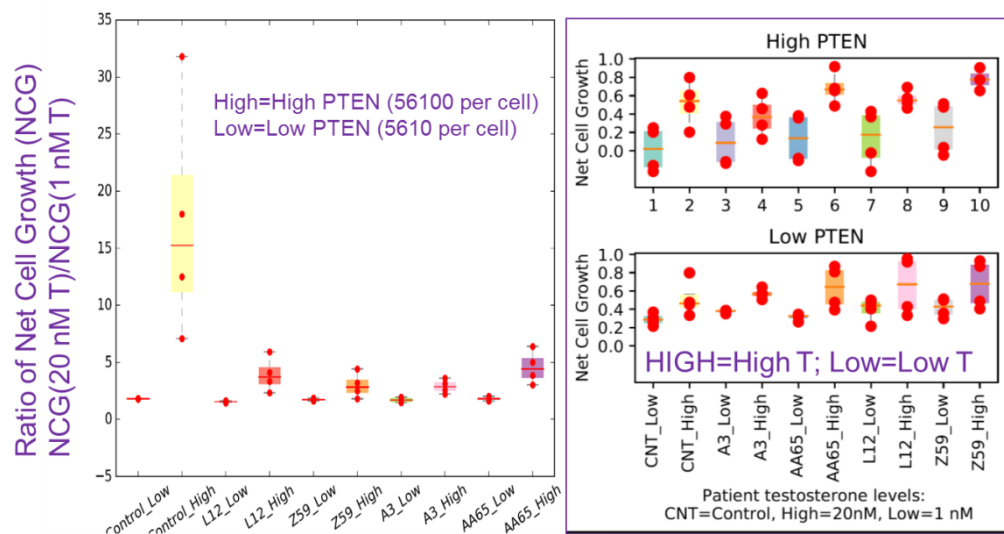


Figure 9: Ratio of net cell growth rate at high testosterone conditions to low testosterone conditions summarizing the predictions of response of an individual patient to ADT. The left panel depicts the ratio of net cell growth (NCG) in high T (testosterone) vs low T. High PTEN actually represents S cells and low PTEN represents PTEN down-regulated R cells. To make this clear, we have plotted on the right panels the actual data of the net cell growth rate (NCG) for S cells (top panel) and R cells (bottom panel). The legends in the respective panels further denote the definitions of High and Low.

4. The two cancer cell populations growth model

The starting hypothesis is that the tumour is in an initial phase (tumour seed or Minimal Residual Disease after surgery), i.e. it grows with an exponential law $dC_t(t)/dt = r_t \cdot C_t(t)$.

In case of a delayed treatment, the growth can be modelled with the Gompertzian or West's law, as shown in [24][25].

Following prostatectomy, if tumour seeds are still present, the ‘testosterone-sensitive’ population S grows with testosterone-dependent growth rate r :

$$r = r_0 + p T \quad (12)$$

In the absence of any therapy, a standard (and constant) T_0 value is assumed.

In case of ADT, we should consider two different scenarios. When a LHRH –agonist treatment is performed the Equation becomes:

$$1/S \, dS/dt = r(t) = r_0 + p T(t) \quad (13)$$

$T(t)$ being the testosterone concentration in plasma, given by the result of the ‘TESTOSTERONE-BLOCKADE’ model. This function, also addresses the ‘testosterone flare’ observed in the first week following LHRH therapy,

The effect of the AR-blocking anti-androgen therapy on both the PSA and testosterone production can be modelled in similar, but not identical, way.

In the case of LHRH and combined therapy a resistant clone of tumour cells is expected to develop. Its contribution, more than increasing the PSA production, is expected to enhance tumour progression. Its mathematical expression is given by:

$$dR/dt = (r_0 + a (K - S)/K) R \quad (14)$$

a being the additional tumour rate and K its carrying capacity.

The prostate cancer growth follows a Gompertzian law characterized by an initial exponential growth prior to its reaching a carrying capacity. We need to consider this type of behaviour if we are studying the entire period of life of the tumour. In this work, however, we consider only the first part of re-growth, so when the initial population is very small and the growth is exponential. The carrying capacity depends on the nutrients of the body and the available space. It still exists, but it is huge comparing to tumour size, so we can ignore it. If two populations are growing in the same site, however, we need to take into account that the two clones compete for the same nutrients and the same space. We can do it considering the carrying capacity.

The ‘additional’ rate, as well as carrying capacity, are due to the Castration Resistant cells.

The total PSA value is evaluated as:

$$PSA(t) = S_{coeff} * S(t) + R_{coeff} * R(t) \quad (15)$$

The parameter values are reported in Table 10 and Table 11.

Table 10: Parameter values definition and numerical simulations

Parameter	Values from the literature
r_0	$0.155 \pm 0.12 \text{ month}^{-1}$ (from UPENN model)
p	$0.01 \pm 0.008 \text{ cell}^{-1}$ (from UPENN model)
a	0.35 ± 0.02 (from UPENN model)
T_0	Between 0.09 and 0.21 g/month in [26]
$T(t)$	Function from the 'TESTOSTERONE-BLOCKADE' model
K	Local/metastatic values, in our simulations = 200 ng/mL
Scoeff	$0.145 \cdot 30 \text{ ag/mL/cell/month}$ (production rate of R: 0-0.29 ag/mL/cell/day in [27])
Rcoeff	$0.1825 \cdot 30 \text{ ag/mL/cell/month}$ (production rate of R: 0.015-0.35 ag/mL/cell/day in [27])

In the LHRH and combined models, the resistant population R always increases unless $R_0=0$. Based on the results of Figures 8 and 9, we can summarize the following:

- For S cells, the testosterone independent growth probability is 0.016 for control subject; we assume this maps to the $r_0=0.028 \text{ month}^{-1}$ for control subjects given in Table 10.
- For S cells, the mean value the testosterone independent growth probability for DGEP subjects is 0.155; hence, r_0 for DGEP subjects = 0.271 month^{-1} ($=0.155 \cdot 0.028/0.016$)
- For S cells, the testosterone-dependent growth probability calculated as delta NCG high T minus low T in Figure 9 for control subject= 0.505 ; this allows us to estimate p as follows. The testosterone-dependent rate in Equation 12 is pT which corresponds to the testosterone-dependent growth probability of 0.505; this equivalence yields $pT/r_0=0.505/0.016$ or $pT=(0.505/0.016) \cdot 0.028 \text{ month}^{-1}$. The testosterone concentration for this calculation was 20 nM (or 8 ng/ml) which yields the value for $p= (0.505/0.016) \cdot (0.028/8) = 0.11 \text{ month}^{-1} \text{ ng}^{-1} \text{ ml}$.
- For S cells, the mean testosterone-dependent growth probability calculated as mean delta NCG high T minus low T in Figure 9 over all DGEP subjects = 0.444 ; this results in $p=(0.444/0.155) \cdot (0.271/8) = 0.09 \text{ month}^{-1} \text{ ng}^{-1} \text{ ml}$ for DGEP subjects.

- For R cells under no competition, the growth rate (see Eq. 15) is $r_0 + a$ which we take to be proportional to the mean NCG for high and low T under low PTEN, see bottom right panel of Figure 9; (here, low PTEN is taken to be the marker of resistance). Based on this equivalence, we can estimate a for control and DGEP subjects, see below.
- For R cells, the mean value for NCG for control subject = 0.402 (obtained from averaging NCG for low and high T for control). Therefore, for control subjects $(r_0 + a)/(r_0) = \text{mean NCG for R cells} / \text{NCG for S cells under low T}$; hence, $1 + (a/r_0) = 0.402/0.016$, which yields $a = 24.125 * r_0 = 24.125 * 0.028 \text{ month}^{-1} = 0.6755 \text{ month}^{-1}$.
- For R cells, the mean value for NCG for DGEP subjects = 0.5055 (obtained from averaging NCG for low and high T for each DGEP subject and then taking the mean over the DGEP subjects). Therefore, for DGEP subjects $(r_0 + a)/(r_0) = \text{mean NCG for R cells} / \text{NCG for S cells under low T}$; hence, $1 + (a/r_0) = 0.5055/0.155$, which yields $a = 2.26 * r_0 = 2.26 * 0.271 \text{ month}^{-1} = 0.613 \text{ month}^{-1}$.
- The above estimates are summarized in Table 10.

In this section we show, by means of extensive numerical simulations, the behaviours of the tumour mass during the different treatments. We used ode45 of MATLAB (The Mathworks, Natick, MA, USA) to implement the simulations.

5. Model validation Vs EUREKAI database: PSA values prediction

The EUREKAI data collection contains a subset of prostatectomized patients who were considered as high-risk ones, based on their Gleason Score values ($GS \geq 8$) and the positive surgical margins. Those for which at least 4 PSA postoperative values were available, and info about the biochemical relapse were reported were selected for the present study.

Some of them underwent ADT adjuvant therapy either with LHRH or with AR-blocking drugs, in contrast to a control group of patients without any adjuvant therapy.

In order to check whether the parameter values cited in the literature agree with those validated on the EUREKAI patients we selected some particular subsets for whom the evaluation of the above parameters was much sensible.

i) Validation of r_0

The timing of testosterone concentration depends on the phase of the LHRH therapy, and in particular T can be assumed to be negligible after the initial flare.

Consequently, we selected 60 patients undergoing LHRH therapy for whom at least two values of the PSA dosage were available during the therapy.

Assuming that $T(t) = 0$ $r = r_0$ can be easily evaluated assuming an exponential tumour growth, independently of the value of S_{coeff} .

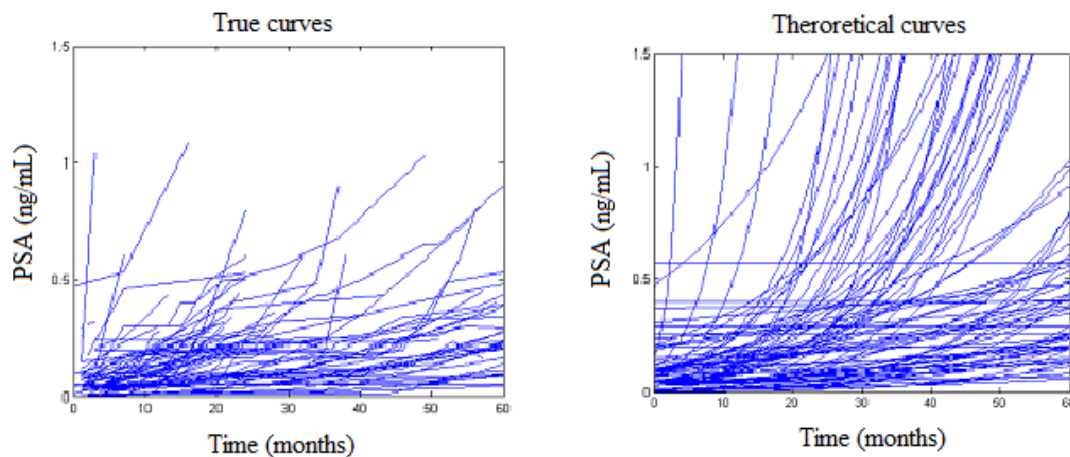
We found r_0 in the same range as expected from the literature and from UPENN model.

ii) Validation of pT without therapy

Assuming that no ADT was administered, we expect that both the testosterone production and its consumption for tumour growth are physiologically distributed on the population.

In order to estimate it on the EUREKA1 database, we selected 84 relapsed patients who didn't undergo any therapy and had at least 2 PSA values after RP.

Assuming $r_0 = 0.02 \text{ month}^{-1}$ we found $pT = (0.04 \pm 0.07) \text{ month}^{-1}$, which is compatible with the assumption of $p = 0.01 \pm 0.008 \text{ cell}^{-1}$ and a low value of testosterone (3.7 mg/day).



Figs 10a and 10b describe the 'true' and 'theoretical' curves respectively.

Figure 10a true curves; 10b theroretical curves.

iii) overall model validation

Among the 84 patients of EUREKA1 who underwent RP, had adjuvant hormone therapy for more than 6 months, no radiotherapy, no neo-adjuvant therapy, we selected the 5 patients with a

recurrence during the adjuvant therapy. Only 2 of them started with initial PSA value under the threshold of 0.2 mg/mL.

We used these 2 patients for a preliminary validation of the LHRH model (Fig 11a and 11b). Moreover, as a control, we selected a patient with no recurrence during ADT (Fig 11c).

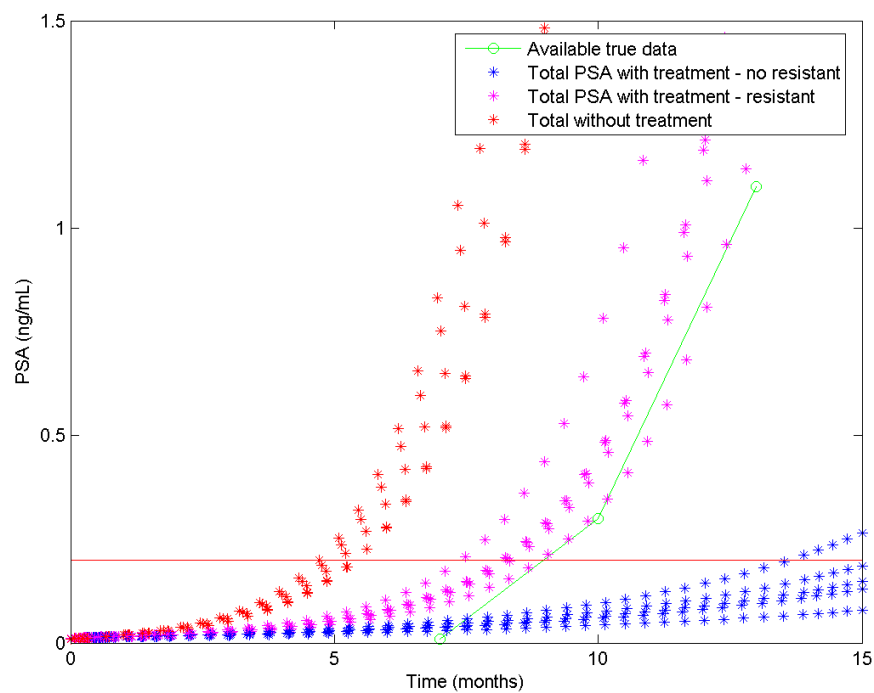


Fig 11a – Patient 1089 (no genetic information available)

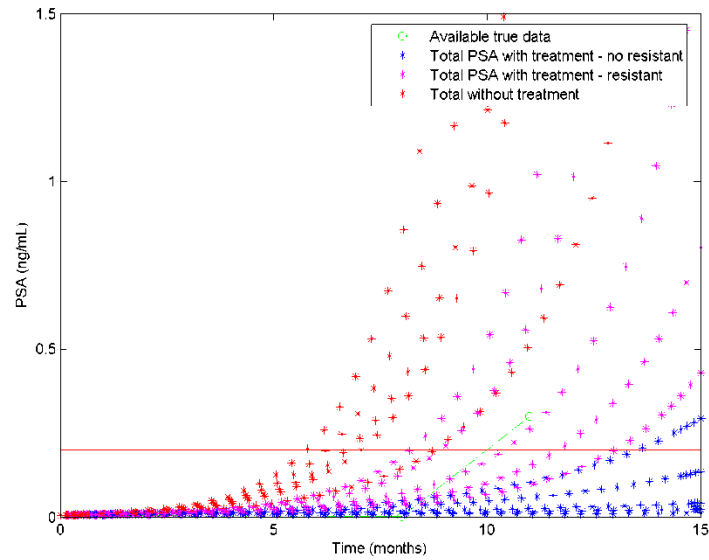


Fig I b – Patient 2284 (no genetic information are available)

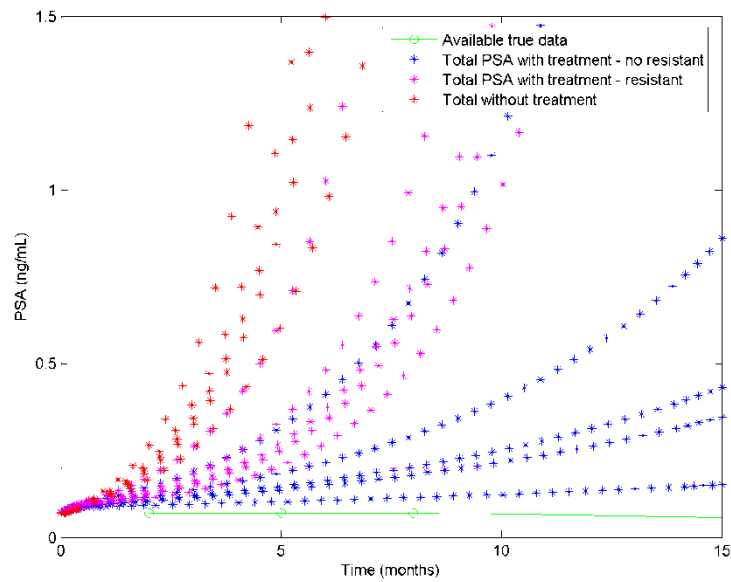


Fig I c– Patient AA65 – under ADT

Our model shows 3 different scenarios: PSA without therapy (red stars), PSA during ADT in case of the presence of a resistant clone before the start of the therapy (magenta stars) and PSA during ADT in case of no resistant clone before the start of the therapy. Green dots are the real data of the patients.

As we expected, the two patients (Fig. 11a and 11b) with a recurrence during ADT are compatible with a huge resistant clone before starting therapy (magenta stars), while the patients who do not relapse (Fig. 11c) follows the blue stars. The testosterone level comes from ICCS models.

Our model gives 5 different previsions for each scenario, changing the parameter values according to their ranges. This happens because we want to give an idea of the behaviour of the PSA, but we cannot expect to predict the exact future PSA values. If extra information is available, for example gene expression, the prediction can be more accurate and the most probable scenario can be easily selected.

References

- [1]. Feldman BJ, Feldman D “The development of androgen-independent prostate cancer,” *Nat Rev Cancer* . vol.1, pp.34–45, 2001
- [2]. C. Huggins and C. Hodges, “The effect of castration, of estrogen and of androgen injection on serum phosphatases in metastatic carcinoma of the prostate,” *Cancer Res.*, vol. 1, pp. 293–297, 1941.
- [3]. V. J. Assikis and J. W. Simons, “Novel therapeutic strategies for androgen-independent prostate cancer: an update,” *Semin Oncol*, vol. 31 Suppl.4, pp. 26–32, 2004.
- [4]. W. P. Harris, E. A. Mostaghel, P. S. Nelson, and B. Montgomery, “Androgen deprivation therapy: progress in understanding mechanisms of resistance and optimizing androgen depletion,” *Nat Clin Pr. Urol*, vol. 6, pp. 76–85, 2009.
- [5]. A. Katzenwadel and P. Wolf, “Androgen deprivation of prostate cancer: Leading to a therapeutic dead end,” *Cancer Lett.*, vol. 367, pp. 12–17, 2015.
- [6]. S. Kumar, M. Shelley, C. Harrison, B. Coles, T. J. Wilt, and M. D. Mason, “Neo-adjuvant and adjuvant hormone therapy for localised and locally advanced prostate cancer,” *Cochrane Database Syst. Rev.*, no. 4, p. CD006019, Oct. 2006.
- [7]. A. M. Ideta, G. Tanaka, T. Takeuchi, and K. Aihara, “A mathematical model of intermittent androgen suppression for prostate cancer,” *J. Nonlinear Sci.*, vol. 18, no. 6, pp. 593–614, 2008.
- [8]. M. Elishmereni et al., “Predicting time to castration resistance in hormone sensitive prostate cancer by

a personalization algorithm based on a mechanistic model integrating patient data,” *Prostate*, vol. 76, no. 1, pp. 48–57, 2016.

[9]. Y. Hirata, N. Bruchovsky, and K. Aihara, “Development of a mathematical model that predicts the outcome of hormone therapy for prostate cancer,” *J. Theor. Biol.*, vol. 264, no. 2, pp. 517–527, 2010.

[10]. J. D. Veldhuis, “Recent insights into neuroendocrine mechanisms of aging of the human male hypothalamic-pituitary-gonadal axis,” *J. Androl.*, vol. 20, no. 1, pp. 1–17, Feb. 1999.

[11]. R.W. Smith. Hypothalamic regulation of pituitary secretion of luteinizing hormone —II. feedback control of gonadotropin secretion. *Bull. Math. Biol.*, 42(1):57–78, 1980.

[12]. Churilov, A., Medvedev, A., & Shepeljavyi, A. (2009). Mathematical model of non-basal testosterone regulation in the male by pulse modulated feedback. *Automatica*, 45, 78–85

[13]. LZ Krsmanovic, SS Stojilkovic, F Merelli, SM Dufour, MA Virmani and KJ Catt. Calcium signalling and episodic secretion of gonadotropin-releasing hormone in hypothalamic neurons. *Proc. Nat. Acad. Sci. USA*, 89:8462-8466, 1992

[14]. Kumar P, Sharma A. Gonadotropin-releasing hormone analogs: Understanding advantages and limitations. *Journal of Human Reproductive Sciences*. 2014;7(3):170-174. doi:10.4103/0974-1208.142476.

[15]. PM Conn, WF Crowley Jr, Gonadotropin-releasing hormone and its analogs *Annu Rev Med*, 45 (1994), pp. 391–405

[16]. O. Ortmann, J. M. Weiss, and K. Diedrich, “Gonadotrophin-releasing hormone (GnRH) and GnRH agonists: mechanisms of action,” *Reprod. Biomed. Online*, vol. 5 Suppl 1, pp. 1–7, 2002.

[17]. Lim CN, Salem AH. A Semi-Mechanistic Integrated Pharmacokinetic/Pharmacodynamic Model of the Testosterone Effects of the Gonadotropin-Releasing Hormone Agonist Leuprolide in Prostate Cancer Patients. *Clinical Pharmacokinetics*. 2015;54:963–73.

[18]. M. Marberger et al., “Effectiveness, pharmacokinetics, and safety of a new sustained-release leuprolide a cetate 3.75-mg depot formulation for testosterone suppression in patients with prostate cancer: a Phase III, open-label, international multicenter study,” *Clin. Ther.*, vol. 32, no. 4, pp. 744–757, Apr. 2010.

[19]. A. A. Shafi, A. E. Yen, and N. L. Weigel, “Androgen receptors in hormone-dependent and castration-resistant prostate cancer,” *Pharmacol. Ther.*, vol. 140, no. 3, pp. 223–238, Dec. 2013.

[20]. M.-L. Zhu and N. Kyprianou, “Androgen receptor and growth factor signalling cross-talk in prostate cancer cells,” *Endocr. Relat. Cancer*, vol. 15, no. 4, pp. 841–849, Dec. 2008.

[21]. H. K. Lin, S. Yeh, H. Y. Kang, and C. Chang, “Akt suppresses androgen-induced apoptosis by phosphorylating and inhibiting androgen receptor,” *Proc. Natl. Acad. Sci. U. S. A.*, vol. 98, no. 13, pp. 7200–7205, Jun. 2001.

[22]. Z. Culig, “New possibilities for urinary molecular diagnostics,” *BJU Int.*, vol. 117, no. 4, pp. 547–548,

Apr. 2016.

[23]. M. V. Cronauer, W. A. Schulz, T. Burchardt, R. Ackermann, and M. Burchardt, “Inhibition of p53 function diminishes androgen receptor-mediated signalling in prostate cancer cell lines,” *Oncogene*, vol. 23, no. 20, pp. 3541–3549, Apr. 2004.

[24]. C. Guiot, P. G. Degiorgis, P. Delsanto, P. Gabriele, and T. Deisboeck, “Does Tumour growth follow a ‘universal law’?,” *J. Theor. Biol.*, vol. 225, pp. 147–151, 2003.

[25]. I. Stura, E. Venturino, and C. Guiot, “A two-clones tumour model: Spontaneous growth and response to treatment,” *Math. Biosci.*, vol. 10, no. 1, pp. 19–28, 2015.

[26]. H. Vierhapper, P. Nowotny, and W. Waldhäusl, “Determination of testosterone production rates in men and women using stable isotope/dilution and mass spectrometry,” *J. Clin. Endocrinol. Metab.*, vol. 82, no. 5, pp. 1492–1496, 1997.

[27]. J. Morken, A. Packer, R. Everett, J. Nagy, and Y. Kuang, “Mechanisms of resistance to intermittent androgen deprivation in patients with prostate cancer identified by a novel computational method,” *Cancer Res.*, vol. 74, no. 14, pp. 3673–3683, 2014.

CHAPTER DI: DISCUSSION

In this deliverable the methods developed and/or adopted by CHIC in order to carry out clinical adaptation and partial clinical validation of its highly innovative multiscale cancer hypermodels have been presented and analyzed. Important and extensive clinical adaptation and validation results, findings and remarks of special value for both the fundamental/basic science and the clinical communities have also been included.

The presented partial clinical validation of the developed hypermodels, largely based on retrospective imaging, histological, molecular and clinical data has demonstrated the great potential of cancer hypermodels and Oncosimulators to serve as clinical decision support systems (CDS) and/or cores of future *in silico* trial platforms. However, additional retrospective validation work for the developed hypermodels is needed in order to more fully substantiate and support their “candidacy” for undergoing validation through prospective clinical trials. This is a necessary step in order to definitely assess both their clinical validity and clinical value.

Further retrospective validation work will be carried out by specific former CHIC partners on a bilateral or small partner group basis.

Regarding the eventual prospective clinical validation of the hypermodels, certain exploratory steps have already been taken, including focused discussions within the framework of the International Society for Pediatric Oncology (SIOP).

CHAPTER CO: CONCLUSIONS

Based on the partial validation results and analyses that have been reported in this document, the highly innovative CHIC hypermodels and Oncosimulators appear to possess a great potential for serving as clinical decision support systems (CDS) and/or cores of future *in silico* trial platforms. However, additional retrospective validation work for the developed hypermodels and Oncosimulators is needed in order to more fully substantiate and support their “candidacy” for undergoing validation through prospective clinical trials. This is a necessary step in order to definitely assess both their clinical validity and clinical value. Further retrospective validation work will be carried out by specific former CHIC partners on a bilateral or small partner group basis. Regarding the eventual prospective clinical validation of the hypermodels, certain exploratory steps have already been taken, including focused discussions within the framework of the International Society for Pediatric Oncology (SIOP).

APPENDIX I: FREQUENT CHIC RELATED ABBREVIATIONS AND ACRONYMS

IMPORTANT NOTE Abbreviations and acronyms that are not included in this table may be deciphered using the “Find” facility which is provided by current pdf document readers. By locating the first instance of an abbreviation or an acronym in the document, the reader can also see its full name

AD	Androgen Dependent
ADC	Adenocarcinoma
ADSCC	Adenosquamous Cell Carcinoma
ADT	Androgen Deprivation Therapy
AJCC	American Joint Committee on Cancer
Akt	Protein kinase B (PKB)
ALK	Anaplastic Lymphoma Kinase
AMD	Advanced Microdevices
ANSI	American National Standards Institute
API	Application Program Interface
ATP	Adenosine Triphosphate
AUC	Area Under Curve
BED	University of Bedfordshire
bGS	biopsy Gleason Score
BMS	Bio-Mechanical Simulator
BS	Biomechanics Simulator
CGAL	Computational Geometry Algorithms Library
CHIC	Computational Horizons in Cancer
CINECA	Consorzio Interuniversitario del Nord Est Italiano Per il Calcolo Automatico (Interuniversity Consortium for High Performance Systems)
CKP	Cell Kill Probability
CKR	Cell Kill Rate
CNS	Central Nervous System
COSMIC	Catalog of Somatic Mutations in Cancer
CRAF	Clinical Research Application Framework (CRAF)
CS	Cell Simulator
CSF	Cerebrospinal Fluid
CSS	Cancer Stem Cell
CSV	Comma Separated Values

CT	Computed Tomography
DC	Dendritic Cell
DGM	Diffusion Coefficient of Grey Matter
DICOM	Digital Imaging and Communications in Medicine
DIFF	Terminally Differentiated Cell
DRE	Digital Rectal Examination
DWM	Diffusion Coefficient of White Matter
EAU	European Association of Urology
EBRT	External Beam Radiation Therapy
ED	Equivalent Dose
EGF	Epidermal Growth Factor
EGFR	Epidermal Growth Factor Receptor
ERBB2	erb-b2 Receptor Tyrosine Kinase 2
ERK	Extracellular Signal-Regulated Kinases
FEM	Finite Element Method
FORTH	Foundation for Research and Technology Hellas
GBM	Glioblastoma Multiforme
GF	Growth Fraction
GC	Geometrical Cell
GPSM	Gleason, PSA, Seminal Vesicle and Margin Status
GS	Gleason Score
GUI	Graphical User Interface
HE	Hypermodelling Editor
HER3	Human Epidermal Growth Factor Receptor 3
HTML	Hypertext Markup Language
ICCS or ICCS- NTUA	Institute of Communication and Computer Systems – National Technical University of Athens
IMRT	Intensity Modulated Radiation Therapy
ISO	International Organization for Standardization
KUL	Catholic University of Leuven
LADC	Lung Adenocarcinoma
LCC	Large Cell Carcinoma
LIMP	Limited Mitotic Potential
LQ	Linear Quadratic
LSCC	Lung Squamous Cell Carcinoma
MAPK	Mitogen-Activated Protein Kinase
MD	Molecular Dynamics
MRI	Magnetic Resonance Imaging
MUSCLE	Multiscale Coupling Library and Environment
MUT	Mutant

NBC	Number of Biological Cells
NCCN	National Comprehensive Cancer Network
NCI	National Cancer Institute
NGCT	Neighbour Geometrical Cells belonging to the Tumour
NIH	National Institutes of Health
NK	Natural Killer
NSCLC	Non Small Cell Lung Cancer
NSG	NOD- <i>scid</i> <i>IL2ry^{null}</i> Mouse Model of Human Skin
OER	Oxygen Enhancement Ratio
OFAT	One Factor at A Time
OS	Oncosimulator
OWL	Web Ontology Language
pAKT	phospho-AKT
PCa	Prostate Cancer
PDE	Partial Differential Equation
PSA	Prostate Specific Antigen
PUN	Phenomenological Universalities (Approach)
RDF	Resource Description Framework
RP	Radical Prostatectomy
RT	Radiotherapy
RTK	Receptor Tyrosine Kinase
SASA	Solvent Accessible Surface Area
SBML	Systems Biology Markup Language
SCC	Squamous Cell Carcinoma
SCID	Severe Combined ImmunoDeficient
SCLC	Small Cell Lung Cancer
SQL	Structured Query Language
STAT	Signal Transducer and Activator of Transcription or Signal Transduction And transcription
SVM	Support Vector Machines
TCGA	The Cancer Genome Atlas
TKI	Tyrosine Kinase Inhibitors
TRUS	Trans-Rectal Ultrasound
UBERN	University of Bern
UCL	University College London
ULC	Undifferentiated Large Cell Carcinoma
UML	Unified Modeling Language
UNITO	University of Turin
UOXF	University of Oxford
UPENN	University of Pennsylvania
USAAR	University of Saarland

USFD	University of Sheffield
VEGF	Vascular Endothelial Growth Factor
VPH	Virtual Physiological Human
VTk	Visualization ToolKit
WT	Wild Type
WT	Wilms Tumour = Nephroblastoma
XML	EXtensible Markup Language